Title
Metal Oxide Promotion of Cobalt-Based Fischer-Tropsch Synthesis Catalysts

Author
Johnson, Gregory Robert

Publication Date
2015

Peer reviewed|Thesis/dissertation

Metal Oxide Promotion of Cobalt-Based Fischer-Tropsch Synthesis Catalysts

by

Gregory Robert Johnson

A dissertation submitted in partial satisfaction of the

requirements for the degree of

Doctor of Philosophy

in

Chemical Engineering

in the

Graduate Division

of the

University of California, Berkeley

Committee in charge:

Professor Alexis T. Bell, Chair
Professor Alexander Katz
Professor T. Don Tilley

Fall 2015

Metal Oxide Promotion of Cobalt-Based Fischer-Tropsch Synthesis Catalysts

by

Gregory Robert Johnson

Abstract

Metal Oxide Promotion of Cobalt-Based Fischer-Tropsch Synthesis Catalysts

by

Gregory Robert Johnson

Doctor of Philosophy in Chemical Engineering

University of California, Berkeley

Professor Alexis T. Bell, Chair

Synthetic fuel production by means of Fischer-Tropsch synthesis (FTS) involves the catalytic hydrogenation of CO over Co-based catalysts. Often, these catalysts incorporate performance-enhancing additives known as promoters. Although not catalytically active for FTS by themselves, promoters can alter the structural and electronic properties of the active Co metal so as to improve catalyst activity, selectivity, or stability. Elements that form metal oxides have been studied for their ability to increase CO consumption rates and shift the product distribution toward higher molecular weight. Despite several decades of study of such elements, there remains limited understanding of the connections between these promotional effects and element properties. Accordingly, this dissertation focuses on clarifying the chemical basis for the effects of metal oxide promotion and making connections to periodic trends.

To understand the importance of physical contact between the promoter and the Co, the influence of Co-Mn spatial association on the magnitude of Mn promotional effects was investigated. Elemental maps obtained by STEM-EDS revealed that different catalyst pretreatment methods could control how closely associated the promoter and Co were at the nanoscale. By relating these results to catalytic reaction data, it was determined that higher extents of contact between the two elements were correlated with higher selectivities toward C5+ hydrocarbons. This work was extended to the elements Ce, Gd, La, and Zr, which are among the most commonly studied metal oxide-forming promoters. The presence of the promoter element suppressed methane formation and increased the FTS chain propagation probability, but the sensitivity of these effects toward promoter loading was different for each element. Elements that deposited preferentially onto the Co nanoparticles led to rapid shifts in the product distribution as the promoter loading increased, whereas elements that dispersed over the entire catalyst surface resulted in more gradual changes. For all promoters, the product selectivities became insensitive to loading when the loading reached a quantity nearly equivalent to that which would form a half monolayer of the promoter on the Co nanoparticle surface. These trends are characteristic of the formation of active sites along the interface between the Co and the promoter that exhibit improved product selectivity.

Structurally, the oxidation states and local coordination environments of the promoters were consistent with highly dispersed oxides. No evidence for the formation of bimetallic alloys or large promoter-containing crystallites was detected by either X-ray absorption spectroscopy or X-ray diffraction. These data suggest that small promoter oxide moieties decorate the surface of the Co metal nanoparticles so as to form metal-metal oxide interfaces. Under this model, the promotional effects increase in magnitude as the fraction of Co active sites that are adjacent to the promoter increases. When the Co surface is sufficiently covered by the promoter so that the fraction of active sites that are along the perimeter of the promoter moieties is nearly unity, the catalyst performance ceases to improve as a function of promoter loading. Guided by this reasoning, the catalytic properties of the promoted catalysts were investigated using samples in which the fraction of sites that were promoted was near unity.

Measurements of reaction kinetics were conducted to assess the impact of metal oxide promotion on the rate parameters governing FTS. The rates of CO consumption for both unpromoted and metal oxide-promoted catalysts followed a Langmuir-Hinshelwood rate law for which H-assisted CO dissociation is assumed to be the rate determining step. Each promoter increased the apparent rate constant and the CO adsorption constant that appear within the rate law. Thus, metal oxide promotion appears both to facilitate the cleavage of the C–O bond and to enhance the extent of CO adsorption onto the catalyst. This finding was reinforced by CO temperature programmed desorption experiments and an evaluation of the effects of Mn promotion on the rate of CO disproportionation. Owing to the appearance of the CO adsorption constant in the numerator and denominator of the rate law, it is possible for promoted catalysts to have both higher and lower turnover frequencies than unpromoted catalysts depending on the chosen operating pressure. As a consequence, an optimal promoter can be found for maximizing the turnover frequency at a given operating pressure. However, product selectivity, which is largely determined by the availability of adsorbed H, is invariably improved by a higher CO adsorption constant because it decreases the ratio of adsorbed H to CO on the Co surface.

Strong correlations between catalyst performance and the Lewis acidity of the promoter oxide suggest that Lewis acid-base interactions between the promoter and the adsorbed CO are the cause for the observed metal oxide promotional effects. Much of the experimental data presented in this work favors the hypothesis that CO can interact simultaneously with Co through the C atom and with the promoter cation through the O atom. These chemical interactions, in which the promoter serves as a Lewis acid, weaken the bond between C and O. Experimental evidence for this effect was observed in the lower activation barrier for CO hydrogenation over the ZrO_2-promoted catalysts and the appearance of adsorbed carbonyl species on the MnO-promoted catalyst with severely redshifted C–O stretching frequencies measured by in situ infrared spectroscopy. These results provide insight into the chemical mechanism by which metal oxides affect the reaction and identify Lewis acidity of the promoter as the relevant descriptor for quantitatively predicting metal oxide-based promotional effects over Co FTS catalysts.

Table of Contents

List of Figures and Schemes iv

List of Tables x

Acknowledgements xii

Chapter 1: Introduction 1

Chapter 2: Investigations of Element Spatial Correlation in Mn-Promoted Co-Based Fischer-Tropsch Synthesis Catalysts 7

Abstract 7

2.1 Introduction 7

2.2 Experimental Methods 9

2.3 Results and Discussion 13

2.3.1 TEM and HR-STEM Imaging 13

2.3.2 Acquisition of Elemental Maps by STEM-EDS 13

2.3.3 Correlation Analyses of Simulated Elemental Maps 15

2.3.4 Correlation Analysis of Co-Mn Catalysts 17

2.3.5 Catalytic Performance 19

2.4 Conclusions 20

Supporting Information 30

Chapter 3: An Investigation into the Effects of Mn-Promotion on the Activity and Selectivity of Co/SiO2 for Fischer-Tropsch Synthesis: Evidence for Enhanced CO Adsorption and Dissociation 43

Abstract 43

3.1 Introduction 43

3.2 Experimental Methods 44

3. Results 48

3.3.1 Microscopy 48

3.3.2 H_2 Chemisorption and O_2 Titration 49

3.3.3 X-ray Absorption Spectroscopy 49

3.3.4 CO Temperature-Programmed Desorption 50

3.3.5 Infrared Spectroscopy 51

3.3.6 Kinetics and Catalytic Performance 52

3.4 Discussion 55

3.4.1 Effects of Mn Promotion on Co Particle Size and Structure 55

3.4.2 Mn and Co Oxidation States 56
3.4.3 Spatial Distribution of Mn 57
3.4.4 Influence of Mn on the FTS Reaction and Surface Adsorbates 58
3.4.5 Origin of Mn Promotion Effects 60
3.5 Conclusions 61
Supporting Information 73
Chapter 4: The Role of ZrO_2 in Promoting the Activity and Selectivity of Co-Based Fischer-Tropsch Catalysts 98
Abstract 98
4.1 Introduction 98
4.2 Experimental Methods 99
4.3 Results 103
4.3.1 Temperature-Programmed Reduction 103
4.3.2 O_2 Titration and H_2 Chemisorption 103
4.3.3 In Situ X-Ray Absorption Spectroscopy 104
4.3.4 Electron Microscopy 105
4.3.5 CO Temperature-Programmed Desorption 106
4.3.6 Catalyst Activity 107
4.3.7 Catalyst Selectivity 108
4.4 Discussion 109
4.4.1 Effects of Zr Promotion on the Co Nanoparticle Structure 109
4.4.2 Structure and Chemical State of the Zr Promoter 110
4.4.3 Influence of Zr Promotion on Activity and the Reaction Mechanism 112
4.4.4 Relationship between Zr Promotion and Product Selectivity 113
4.4.5 Interaction between Zr and the Co Active Sites 114
4.5 Conclusion 115
Supporting Information 127
Chapter 5: Connections between the Lewis Acidity of Metal Oxide Promoters and the Catalytic Properties of Co-Based Fischer-Tropsch Synthesis Catalysts 138
Abstract 138
5.1 Introduction 138
5.2 Experimental Section 140
5.3 Results 142

5.3.1 Effects of Metal Oxide Promotion on Co Reduction 142
5.3.2 Effects of Metal Oxide Promotion on Co Nanoparticle Size 144
5.3.3 Effects of Metal Oxide Promotion on Co Nanoparticle Structure 144
5.3.4 Promoter Oxidation States and Structure 145
5.3.5 Spatial Association between Co and the Metal Oxide Promoters 146
5.3.6 Catalytic Activity 148
5.3.7 Catalytic Selectivity 149
5.4 Discussion 150
5.4.1 Lewis Acidity of the Promoter Oxides 150
5.4.2 Dependence of Catalytic Properties on Promoter Loading 151
5.4.3 Influence of Promoter Lewis Acidity on Catalyst Activity and Selectivity 153
5.5 Conclusion 155
Supporting Information 170

List of Figures and Schemes

Scheme 1.1 Simplified reaction pathways for Fischer-Tropsch synthesis..... 4

Figure 1.1 Representative FTS product distribution for a Mn-promoted Co catalyst (Mn/Co = 0.1) at 493 K, 10 bar, and 22% CO conversion..... 4

Scheme 1.2 Hypothesized interaction between adsorbed CO and metal oxide moieties..... 5

Figure 2.1 Bright-field TEM images of (A) Co and (B) Co-Mn (Mn/Co = 0.1) catalysts..... 22

Figure 2.2 HAADF-STEM images of a Co-Mn catalyst sample (Mn/Co=0.1) 23

Figure 2.3 Accumulation of damage to a Mn-promoted Co catalyst (Mn/Co = 0.1) by extended rastering with the electron beam in STEM mode..... 23

Figure 2.4 Elemental map of a Co-Mn catalyst (directly reduced, Mn/Co = 0.5) obtained by STEM-EDS..... 24

Figure 2.5 Simulated images and correlation analysis plots of Co-Mn nanoparticles with different levels of element segregation 25

Figure 2.6 STEM-EDS elemental maps and correlation analysis plots of Co-Mn catalysts (Mn/Co = 0.5) with different pretreatment conditions 27

Figure 2.7 Selectivities of methane and C_{5+} hydrocarbons for the Co and Co-Mn (Mn/Co = 0.5) catalysts under Fischer-Tropsch synthesis 29

Figure S2.1 Comparison of Co peak count maps using raw counts and the background-subtracted signal..... 30

Figure S2.2 Evaluation of X-ray count rates at different microscope operating conditions..... 30

Figure S2.3 Illustration of color depth in elemental map channels 32

Figure S2.4 Effect of lower color depth range on correlation analysis methods..... 34

Figure S2.5 Effect of additive Gaussian white noise on correlation analysis methods..... 37

Figure S2.6 Thermogravimetric analysis of Co-Mn (Mn/Co = 0.1) catalyst precursor decomposition 40

Figure 3.1 Bright-field TEM images of Co-Mn catalysts with different bulk Mn/Co atomic ratios 64

Figure 3.2 STEM-EDS elemental maps of Co-Mn catalysts with different bulk Mn/Co atomic ratios 65

Figure 3.3 Histograms of Co-Mn nanoparticle compositions for different bulk Mn/Co atomic ratios 66

Figure 3.4 XANES spectra at the Co K-edge for the Co-Mn catalysts 67

Figure 3.5 Mn K-edge XANES data for the Mn/Co = 0.1 catalyst 68

Figure 3.6 Mean temperature of the first chemisorbed CO desorption peak as a function of Mn loading 69

Figure 3.7 In situ IR spectra of adsorbed CO on the reduced Co-Mn catalysts measured at 493 K and 1 bar 69

Figure 3.8 Dependence of CO consumption rate on H_2 and CO partial pressures 70

Figure 3.9 Comparison of rates per gram of Co and turnover frequencies for different Mn/Co ratios at 493 K 71

Figure 3.10 Fractional carbon surface coverage resulting from CO dissociation as a function of exposure time to CO at 493 K for catalysts with different Mn/Co ratios 72

Figure 3.11 Comparison of CH_4 and C_{5+} selectivities as a function of pressure at 493 K for catalysts with different Mn/Co ratios 72

Figure S3.1 Histograms of nanoparticle compositions for the Co-Mn catalysts with different bulk Mn/Co atomic ratios 73

Figure S3.2 CO Temperature-Programmed Desorption for the unpromoted and Mn-promoted catalysts 74

Figure S3.3 FTIR measurements of hydrogenation over a CO-saturated Mn-promoted catalyst (Mn/Co = 0.1) 76

Figure S3.4 Cobalt-time yields for the Co-Mn catalysts with different bulk Mn/Co atomic ratios 77

Figure S3.5 Turnover frequencies for the Co-Mn catalysts with different bulk Mn/Co atomic ratios 79

Figure S3.6 Parity plots for the Co-Mn catalysts with different bulk Mn/Co atomic ratios..... 81

Figure S3.7 Product selectivities for the Co-Mn catalysts at atmospheric pressure and 493 K as a function of Mn loading 82

Figure S3.8 CH_4 selectivities for the Co-Mn catalysts with different bulk Mn/Co atomic ratios 83

Figure S3.9 C_2-C_4 selectivities for the Co-Mn catalysts with different bulk Mn/Co atomic ratios 85

Figure S3.10 C_{5+} selectivities for the Co-Mn catalysts with different bulk Mn/Co atomic ratios 87

Figure S3.11 X-ray diffraction patterns for the unpromoted, Mn/Co = 0.1, and Mn/Co = 0.5 catalysts 89

Scheme S3.1 Hypothesized structures of the Co-Mn catalysts with different Mn loadings..... 91

Scheme S3.2 Hypothesized interaction between a CO adsorbate and the Mn promoter 94

Figure 4.1 TPR profiles of the Co and Co-ZrO_2 (Zr/Co = 1.0) catalysts 118

Figure 4.2 In situ XANES spectra of the Co-ZrO_2 catalysts collected at the Zr K-edge 119

Figure 4.3 EXAFS spectra of Co and Co-ZrO_2 catalyst samples at the Zr K-edge and Co K-edge 120

Figure 4.4 STEM-EDS elemental map and nanoparticle composition histogram of the Co-ZrO_2 catalyst prepared with a Zr/Co = 1.0 atomic ratio..... 121

Figure 4.5 CO temperature-programmed desorption spectra for the Zr-promoted (Zr/Co = 1.0) and unpromoted (Zr/Co = 0) catalysts..... 121

Figure 4.6 Dependence of the CO consumption rate for the Zr-promoted catalyst (Zr/Co = 1.0) on H_2 and CO partial pressures..... 122

Figure 4.7 Dependence of FTS turnover frequencies on temperature and pressure for the Zr-promoted (Zr/Co = 1.0) and unpromoted catalysts 123

Figure 4.8 FTS turnover frequencies as a function of CO conversion for the catalyst prepared with Zr/Co = 1.0 123

Figure 4.9 Effect of Zr loading on product selectivities at 1 bar and 493 K 124

Figure 4.10 Comparison of CH_4 and C_{5+} selectivities as a function of pressure for Zr-promoted (Zr/Co = 1.0) and unpromoted (Zr/Co = 0) catalysts..... 125

Figure 4.11 Selectivities toward CH_4 and C_{5+} for the catalyst prepared with Zr/Co = 1.0 as a function of CO conversion 126

Scheme S4.1 Sequence of steps involved in the synthesis of the Co-Zr catalysts 127

Figure S4.1 TPR spectra of catalyst precursors 128

Figure S4.2 In situ XANES spectra of the reduced Co-Zr catalysts collected at the Zr K-edge for different loadings of Zr 129

Figure S4.3 Rates of CO consumption per gram Co as functions of temperature and pressure for the Zr-promoted (Zr/Co = 1.0) and unpromoted (Zr/Co = 0) catalysts 129

Figure S4.4 Parity plots for the Zr-promoted (Zr/Co = 1.0) and unpromoted (Zr/Co = 0) catalyst 130

Figure S4.5 Arrhenius plots for the Zr-promoted (Zr/Co = 1.0) and unpromoted (Zr/Co = 0) catalysts 131

Figure S4.6 Effect of pressure and temperature on product selectivities for the Zr-promoted (Zr/Co = 1.0) and unpromoted (Zr/Co = 0) catalysts..... 132

Scheme S4.2 Hypothesized structures an unpromoted Co nanoparticle, Zr-promoted nanoparticle with Zr/Co = 0.25, and Zr-promoted nanoparticle with Zr/Co = 1.0 134

Figure 5.1 TPR profiles of the unpromoted and metal oxide-promoted catalysts 158

Figure 5.2 EXAFS spectra of the Co and metal oxide-promoted catalyst samples at the Co K-edge 159

Figure 5.3 In situ XANES spectra of the catalysts prepared with La/Co = 0.1, Ce/Co = 2.0, and Gd/Co = 1.0 160

Figure 5.4 Representative HAADF-STEM images and STEM-EDS elemental maps for the catalysts prepared with La/Co = 0.1, Ce/Co = 2.0, and Gd/Co = 1.0 162

Figure 5.5 Nanoparticle composition histograms for catalysts prepared with La, Ce, and Gd promoters with promoter/Co ratios of 0.1 and 1.0..... 164

Figure 5.6 FTS turnover frequencies as a function of pressure for the unpromoted and metal oxide-promoted catalysts 166

Figure 5.7 Effects of promoter loading on the selectivity toward CH_4 and C_{5+} hydrocarbons at 493 K and 1 bar 167

Figure 5.8 Selectivities toward CH_4 and C_{5+} hydrocarbons as a function of pressure for the unpromoted and metal oxide-promoted catalysts 167

Figure 5.9 Correlations of the apparent rate coefficient and the CO adsorption constant with the relative Lewis acidity of the promoter oxide, represented by $N_M - 2\delta_M$ 168

Figure 5.10 Selectivities toward CH_4, C_2-C_4, and C_{5+} as a function of the promoter Lewis acidity 169

Figure S5.1 HAADF-STEM images of the catalysts prepared with La/Co = 0.1, Ce/Co = 2.0, and Gd/Co = 1.0 170

Figure S5.2 EXAFS spectra for the Mn-promoted catalyst and a MnO reference sample at the Mn K-edge..... 170

Figure S5.3 FTS turnover frequencies as a function of pressure for the unpromoted and metal oxide-promoted catalysts at 493 K 171

Figure S5.4 Fraction of active sites interfacing with the promoter determined by simulated deposition of promoter moieties onto Co 172

Figure S5.5 Parity plot for the unpromoted and metal oxide-promoted catalysts..... 173

Figure S5.6 Rates of CO consumption per gram Co as a function of pressure for the unpromoted and metal oxide-promoted catalysts 174

Figure S5.7 Correlation between the apparent rate constant and the relative Lewis acidity of the promoter oxide, represented by $N_M - 2\delta_M$ 175

Figure S5.8 FTS turnover frequencies for the unpromoted and metal oxide-promoted catalysts demonstrating that the optimal turnover frequency occurs with promoters of intermediate Lewis acidity 176

List of Tables

Table 2.1 Correlation metrics for simulated images of Co-Mn nanoparticles with different levels of segregation 22

Table 2.2 Correlation metrics for Co-Mn catalysts with different pretreatment conditions..... 22

Table S2.1 Parameters for time lapse videos of beam damage to the Co-Mn catalyst samples at different voltages, currents, and dwell times..... 31

Table S2.2 Correlation metrics for different levels of color depth in the Co and Mn channels .. 37

Table S2.3 Correlation metrics for different levels of noise in the Co and Mn channels 40

Table 3.1 Microscopy Characterization Data for the Co-Mn Catalysts 63

Table 3.2 H_2 Chemisorption and O_2 Titration Characterization Data for the Co-Mn Catalysts ... 63

Table 3.3 Oxidation State Data from XAS Measurements for the Co-Mn catalysts..... 63

Table 3.4 Kinetic Parameters for the Co-Mn Catalysts..... 64

Table S3.1 Indexed X-ray diffraction peaks corresponding to the data in Figure S3.11 90

Table 4.1 Physical characterization data for the Co-ZrO_2 catalysts..... 117

Table 4.2 Co extents of reduction, nanoparticle dispersions, and coverages of the nanoparticle surfaces by ZrO_2 117

Table 4.3 Fitted kinetics parameters for the Zr-promoted and unpromoted catalysts..... 117

Table S4.1 Fitted rate law parameters for the catalysts prepared with Zr/Co = 0 and Zr/Co = 1.0 130

Table 5.1 Physical characterization data for the metal oxide-promoted catalysts..... 156

Table 5.2 Extents of Co reduction, nanoparticle dispersions, and coverages of the nanoparticle surfaces by the metal oxide promoters..... 157

Table 5.3 Fitted kinetics parameters for the unpromoted and Zr-promoted catalysts..... 157

Table S5.1 Mean nanoparticle compositions for the metal oxide-promoted catalysts..... 171

Table S5.2 Relative Lewis acidities of the promoter elements 173

Acknowledgements

There are many individuals who contributed both directly and indirectly to my dissertation project to whom I am very grateful. First, Prof. Alex Bell was an excellent mentor during my years in graduate school. Through his guidance, I learned how to conduct hypothesis-driven research and gained a valuable set of professional skills that I look forward to using in my future career. At the start of my graduate studies, I worked with Dr. Arne Dinse, a postdoctoral researcher in the Bell Group who started our research project concerning metal oxide-promoted Fischer-Tropsch synthesis catalysts. Arne was the one who introduced me to heterogeneous catalysis reaction experiments, and I enjoyed working with him to tackle some of the engineering challenges pertaining to the fixed-bed reactor system used for this project. During my second year of studies, I started working with Dr. Sebastian Werner, another postdoctoral researcher, who was a very helpful mentor and scientific role model for me. Sebastian was the one who initiated our work with analytical electron microscopy and laid out the ground work for our approach using statistical analysis of elemental maps. The researchers at NCEM, especially Dr. Karen Bustillo and Dr. Peter Ercius, were excellent collaborators, and I am grateful to have had access to such microscopy expertise.

There were many Master's students and undergraduates who worked with me at various times during my project. Maxwell Aigner, Markus Ulbrich, and Sebastian Schulze assisted with the exploratory research into Mn promotion and the development of the FTS reactor during my first year. Markus Görlich spent a semester helping me with a side project on secondary reactions that occur during FTS over the promoted catalysts. Toward the end of my dissertation, I was joined in the lab by Tomohiro Ishiguro and David Koshy who were very helpful in taking over my experimental work so that I could focus on writing this dissertation.

My experience in grad school, both inside and outside the lab, was enriched by my fellow graduate students and researchers at UC Berkeley. I would like to acknowledge those who traveled to Illinois to assist with my XAS experiments at the APS: Andrew "Bean" Getsoian, Konstantinos Goulas, Adam Grippo, Chris Ho, John Howell, Rachel Licht, Lin Louie, Julie Rorrer, Alice Ye, and Zheng Zhai. I am also grateful to Ezra Clark, James Dombrowski, Joe Gomes, David Hanna, Amber Janda, Shannon Klaus, Yi-Pei Li, Shaama MS, Anton Mlinar, Shylesh Pillai, Eric Sacia, Will Vining, Alex Wang, and Jason Wu. All of these members of the Bell Group were great collaborators, sources of scientific discussions, and valued friends. I will always treasure the memories and friendships from my time in the Bell group.

Chapter 1

Introduction

For over a century, the transportation of people and goods across the world has depended on the availability of affordable hydrocarbon-based fuels. At present, these fuels are largely derived from petroleum, a finite resource of which over 90 million barrels per day are consumed worldwide.[1] Uncertainty about the longevity of petroleum reserves and the growing environmental impact of fuel emissions have been driving forces for research into alternative fuels.[2] Typically, synthetic fuel production has been envisioned to start with either biomass, coal, or natural gas as feedstocks. The motivations for using biomass are that it can be grown wherever there is arable land and has the potential to be a carbon-neutral feedstock. Although non-renewable, coal and natural gas are both appealing feedstocks owing to their abundance relative to petroleum in many regions of the world.[3] All of these feedstocks can be converted into synthesis gas, a mixture of CO and H_2 from which a variety of organic molecules can be formed via catalytic reactions. One of the most prominent examples of these reactions is Fischer-Tropsch synthesis (FTS), which converts synthesis gas to hydrocarbons.

Discovered in the mid-1920s,[4] FTS has been the subject of ongoing research and commercialization. Compared to other chemical processes for synthetic fuel production, FTS has the advantage of producing long-chain hydrocarbons that are compatible with existing internal combustion engines and fuel distribution infrastructure. Most Group VIIIB elements exhibit activity for CO hydrogenation,[5] but Co is widely regarded as offering the best compromise between affordability and catalytic performance.[6] Co-based FTS catalysts typically consist of Co metal nanoparticles supported on a high surface area support, such as SiO_2, Al_2O_3, or TiO_2. As depicted in Scheme 1.1, FTS begins with the adsorption of CO and H_2 onto the Co surface; however, the sequence of elementary steps that follow remain heavily debated.[7-9] As a simple consequence of producing hydrocarbons from CO, the bond between C and O must be cleaved during the catalysis. This step has been proposed to occur either by direct dissociation of the CO,[10] after the CO has been partially hydrogenated,[11] or even through an insertion mechanism.[12] Despite the controversy regarding the correct pathway by which the C–O bond is cleaved, there is consensus that FTS proceeds by the step-wise addition of C_1 monomers to growing alkyl chains.[13] Under this model, a growing chain containing n C atoms can either propagate to a chain of length $n + 1$ or terminate as either an alkane or alkene of length n. The alkenes can participate in various secondary reactions, such as re-adsorption and hydrogenation. Together, the network of elementary steps shown in Scheme 1.1 determines the FTS product distribution, which greatly influences the process economics for FTS.

A typical FTS product distribution for a Co-based catalyst is given in Figure 1.1. Although most of the C goes toward hydrocarbons suitable for direct use as liquid fuels and lubricants (i.e., the C_{5+} hydrocarbons), a sizeable fraction of the C exits the reactor as CH_4 and other light hydrocarbons. The C_2-C_4 alkenes can be upgraded to longer chain lengths via oligomerization or metathesis reactions,[14] but CH_4 and the C_2-C_4 alkanes have relatively low economic value without undergoing further processing.[15] Consequently, a principal focus of applied FTS research has

been finding ways to suppress the formation of the C_1-C_4 product fraction in favor of the C5+ hydrocarbons. To a limited extent, this goal can be addressed by changing the operating conditions of an FTS reactor. Lower temperature, higher pressure, and a lower synthesis gas H_2/CO ratio all increase the probability of chain propagation, shifting the product distribution to higher molecular weight.[16] Another strategy is to optimize the composition and structure of the catalyst used for FTS.

Substances that are not catalytically active for a given chemical reaction are occasionally used as additives in catalysts. Known as promoters, these additives can enhance catalyst performance including activity, selectivity, or stability. For Co-based FTS catalysts, the use of promoters is a well-investigated topic. Most studies have explored the use of noble metals to assist in the reduction of Co to the active metallic state.[17] However, these elements are typically reported to have limited or occasionally detrimental effects on the FTS product distribution.[18] Elements that form metal oxides under reaction conditions, such as early transition metals and lanthanides, represent a class of promoters that have been demonstrated to consistently decrease the selectivity toward CH_4 and shift the products toward higher molecular weights.[19-21] Reviews of the effects of these promoters are provided in Chapters 3, 4, and 5 for Mn, Zr, and various lanthanides, respectively. In general, existing studies consider the effects of each element in isolation and do not present a unified chemical basis for the effects of metal oxide promotion. Investigations concerning CO and CO_2 hydrogenation over metal oxide-promoted Rh have provided evidence that the promoter oxide may act as a Lewis acid to facilitate CO hydrogenation.[22,23] While these studies provide a starting point, these hypotheses have not been thoroughly investigated, especially in the context of FTS over Co-based catalysts.

Understanding the role of metal oxide promoters starts with identifying the relationship between the promotional effects and the spatial association between the Co nanoparticles and the promoters. Chapter 2 addresses this topic through a study of the effects of pretreatment conditions on element spatial correlation in Mn-promoted catalysts. Catalysts with the same weight loading of Mn were prepared and pretreated either by direct reduction in H_2 or by calcination in air. The elemental maps of these catalysts contained regions of both segregation and association between the Co and Mn, but without interpretable structures unique to each catalyst, it was challenging to identify by visual inspection of the elemental maps which catalyst exhibited more association between the Co and Mn. As a result, statistical methods were developed and employed to aggregate the data from multiple maps and reach conclusions about the degree of element association within these catalysts. These analyses indicated that a stronger spatial correlation between the Co and Mn occurred in the catalyst that was prepared by direct reduction in H_2. Since this catalyst had a higher selectivity toward C_{5+} hydrocarbons, these results establish a structure-performance relationship suggesting that physical contact between the Co and the promoter is essential for creating the promotional effects. This relationship is the first piece of evidence in this dissertation supporting the hypothesis that the promotion effects originate from the interface between the Co and the promoter.

Continuing on the topic of Mn promotion, Chapter 3 provides further evidence for the importance of metal-metal oxide interfaces for improving the performance of Co-based FTS catalysts. In this portion of the study, the influence of Mn/Co atomic ratio on catalyst selectivity

was examined in detail. Increases in the Mn loading up to Mn/Co = 0.1 resulted in lower CH_4 selectivity and higher C_{5+} selectivity. Above this critical atomic ratio, the product selectivities did not change with further increases in the Mn loading. This behavior is rationalized by the assumption that the active sites along the perimeter of MnO moieties decorating the Co surface are responsible for the improved selectivity. According to this model, the selectivity depends on the fraction of active sites belonging to the promoted and unpromoted groups. As the Mn/Co ratio increases up to Mn/Co = 0.1, the Co surface becomes increasingly covered by the promoter, which increases the fraction of sites that are at the Co-MnO interface. The critical atomic ratio at which the product distribution becomes insensitive to Mn loading corresponds to half monolayer coverage of the Co by the promoter. This finding is notable because simulations of promoter deposition suggest that the fraction of sites that are adjacent to the MnO approaches unity at half monolayer coverage. These trends between catalyst structure and selectivity provide strong evidence that the formation of the Co-MnO interface controls the emergence of the promotion effects.

Chapter 3 also examines the effects of Mn promotion on the FTS reaction mechanism. Measurements of CO consumption rates were used to identify a rate law describing the kinetics of CO consumption. FTS over both the Mn-promoted and unpromoted catalysts obeyed the same two-parameter Langmuir-Hinshelwood rate law, suggesting that H-assisted CO dissociation prevails on both catalysts. Mn promotion was found to increase the apparent rate coefficient for CO consumption and the CO adsorption constant appearing in the rate law. Higher values for these two parameters suggest that the promoted active sites adjacent to the MnO exhibit enhanced CO adsorption and dissociation relative to the active sites not in contact with the promoter. These interpretations were corroborated by CO temperature-programmed desorption experiments, measurements of CO disproportionation rates, and in situ infrared spectroscopy. These experiments suggest that the adsorbed CO can interact with the nearby promoter so as to weaken the carbonyl bond and strengthen the binding of the CO to the catalyst surface, as depicted in Scheme 1.2.

Chapter 4 extends these concepts to Zr-promoted catalysts, which were found to be largely analogous to the Mn-promoted catalysts. In contrast to Mn, which had a high affinity toward Co, Zr did not have a preference for associating with the Co nanoparticles. As a result, a loading of Zr/Co = 1.0 was required to form a half monolayer of the promoter over the catalyst surface. Another key difference between the two promoters is that the C_{5+} selectivity, apparent rate coefficient, and CO adsorption constant were all higher for the Zr-promoted catalyst compared to the optimal Mn-promoted catalyst. Since Zr^{4+} is more Lewis acidic than Mn^{2+}, these results suggest that the promoter and the adsorbed CO participate in a Lewis acid-base interaction. In Chapter 5, this hypothesis is tested by generalizing the study to other elements that form metal oxides under reaction conditions with the aim of establishing periodic trends. Here, the extent to which the product selectivities and rate law parameters shift using different promoters were compared to the Lewis acidities of these promoters. Strong correlations were observed between promoter Lewis acidity and both the decrease in CH_4 selectivity and increase in C_{5+} selectivity. Moreover, both the apparent rate coefficient for CO consumption and the CO adsorption constant increased with higher promoter Lewis acidity. These findings are consistent with the promoter metal cation acting as Lewis acid centers, possibly through a direct interaction with the

O atom of adsorbed CO as proposed in Scheme 1.2. In addition to providing insight into the chemical basis for metal oxide promotion effects, this dissertation establishes that Lewis acidity is the relevant descriptor for evaluating the potential of metal oxide-forming elements as promoters for Co-based FTS catalysts.

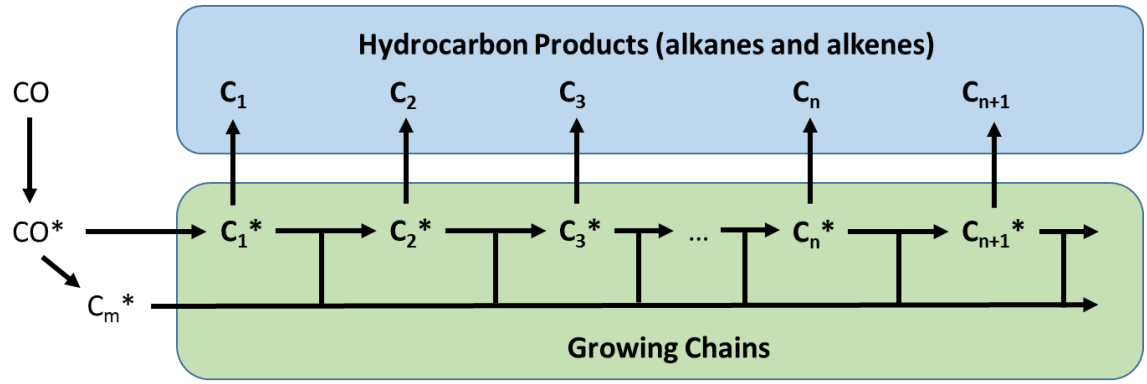

Scheme 1.1 Simplified reaction pathways for Fischer-Tropsch synthesis. Species that are adsorbed on the catalyst surface are denoted with an asterisk. C_m* is the monomer species that adds to the growing chains. The reversibility of adsorption for CO and alkenes is not shown.

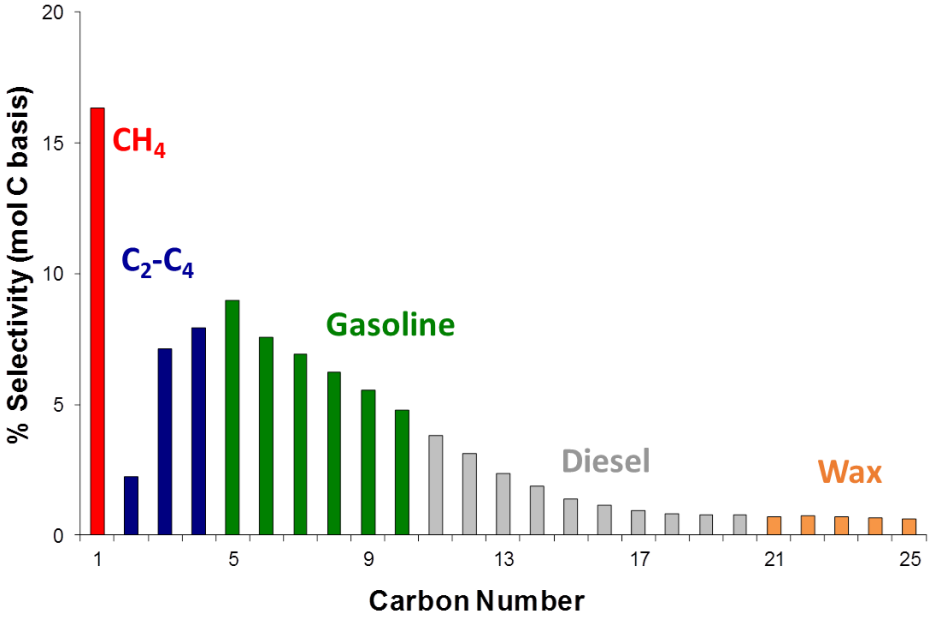

Figure 1.1 Representative FTS product distribution for a Mn-promoted Co catalyst (Mn/Co = 0.1) at 493 K, 10 bar, and 22% CO conversion. The figure is truncated to show only the selectivities for the C_1-C_{25} hydrocarbons (C_{25+} selectivity is 5.9%).

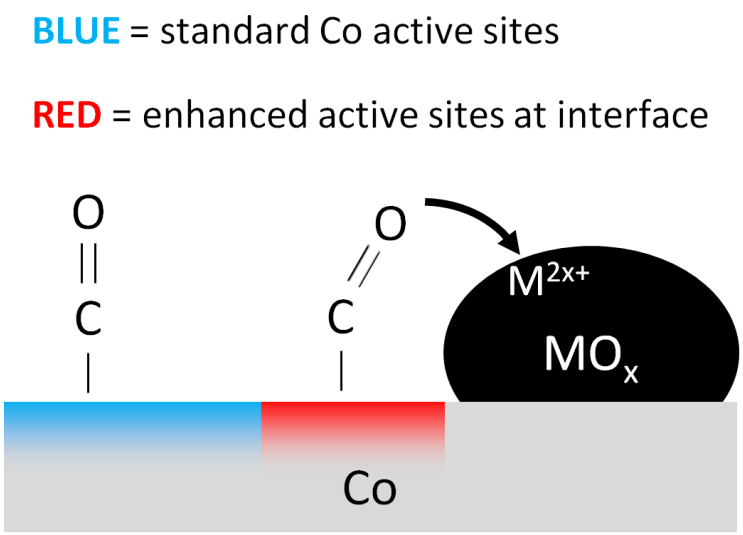

Scheme 1.2 Hypothesized interaction between adsorbed CO and metal oxide moieties. Co active sites along the perimeter of the promoter oxide (red) exhibit enhanced FTS activity and selectivity; active sites separate from the promoter (blue) behave the same as sites in unpromoted catalysts. Based on Ref. 24 with permission from the American Chemical Society.

References

1. Conti, J.; Holtberg, P.; Napolitano, S.; Schaal, A.M.; Doman, L.E.; Arora, V.; Singer, L. *International Energy Outlook 2014*; DOE/EIA-0484; U.S. Dept. of Energy: Washington, D.C., 2014.

2. Huber, G.W.; Iborra, S.; Corma, A. *Chem. Rev.* **2006**, *106*, 4044-4098.

3. *BP Statistical Review of World Energy 2015*; Technical Report for BP p.l.c., London: U.K., June 2015.

4. Fischer, F.; Tropsch, H. *Ber. Deut. Chem. Ges.* **1926**, *59*, 830-831.

5. Bell, A.T. *Catal. Rev. Sci. Eng.* **1981**, *23*, 203-232.

6. Khodakov, A.Y.; Chu, W.; Fongarland, P. *Chem. Rev.* **2007**, *107*, 1692-1744.

7. Dry, M.E. *Appl. Catal., A* **1996**, *138*, 319-344.

8. Schulz, H. *Appl. Catal., A* **1999**, *186*, 3-12.

9. Shetty, S.; van Santen, R.A. *Catal. Today* **2011**, *171*, 168-173.

10. Craxford, S.R.; Rideal, E.K. *J. Chem. Soc.* **1939**, 1604-1614.

11. Ojeda, M.; Nabar, R.; Nilekar, A. U.; Ishikawa, A.; Mavrikakis, M.; Iglesia, E. *J. Catal.* **2010**, *272*, 287-297.

12. Pichler, H.; Schulz, H. *Chem. Ing. Tech.* **1970**, *42*, 1162– 1174.

13. Anderson, R.B.; Friedel, R.A.; Storch, H.H. *J. Chem. Phys.* **1951**, *19*, 313-319.

14. Leitch, D.C.; Lam, T.C.; Labinger, J.A.; Bercaw, J.E. *J. Am. Chem. Soc.* **2013**, *135*, 10302-10305.

15. Periana, R.A.; Taube, D.J.; Gamble, S.; Taube, H.; Fuji, H. High Yield, Low Temperature Oxidation of Mathane to Methanol. In *Catalytic Activation and Functionalisation of Light Alkanes: Advances and Challenges;* Derouane, E.G.; Haber, J.; Lemos, F.; Ribeiro, F.R.; Guisnet, M., Eds.; Springer: n.p., 1998, pp 297-310.

16. Gibson, E.J.; Hall, C.C. *J. Appl. Chem.* **1954**, *4*, 49-61.

17. Diehl, F.; Khodakov, A.Y. *Oil Gas Sci. Technol.* **2009**, *64*, 11−24.

18. Chu, W.; Chernavskii, P.A.; Gengembre, L.; Pankina, G.A.; Fongarland, P.; Khodakov, A.Y. *J. Catal.* **2007**, *252*, 215−230.

19. Adachi, M.; Yoshii, K.; Han, Y.Z.; Fujimoto, K. *Bull. Chem. Soc. Jpn.* **1996**, *69*, 1509−1516.

20. Huber, G.W.; Butala, S.J.M.; Lee, M.L.; Bartholomew, C.H. *Catal. Lett.* **2001**, *74*, 45−48.

21. Moradi, G.R.; Basir, M.M.; Taeb, A.; Kiennemann, A. *Catal. Commun.* **2003**, *4*, 27−32.

22. Sachtler, W.M.; Ichikawa, M. *J. Phys. Chem.* **1986,** *90*, 4752-4758.

23. Boffa, A.B.; Lin, C.; Bell, A.T.; Somorjai, G.A. *Catal. Lett.* **1994**, *27*, 243-249.

24. Johnson, G.R.; Werner, S.; Bell, A.T. *ACS Catal.* **2015**, *5*, 5888-5902.

Chapter 2

Investigations of Element Spatial Correlation in Mn-Promoted Co-Based Fischer-Tropsch Synthesis Catalysts

Abstract

Making connections between performance and structure in bimetallic catalysts requires knowledge of how the two elements are spatially associated. Elemental maps obtained by analytical TEM methods are an invaluable tool for identifying the location of different elements, but for many samples, visual inspection of elemental maps is insufficient for assessing the degree of element spatial correlation. This is particularly true for beam-sensitive materials where short mapping acquisition times lead to images with high noise and low color depth. In these situations, statistical analysis of elemental maps can be used to identify spatial correlations among the elements in a sample. In this work, the relationship between catalyst performance and bimetallic spatial association was explored using Mn-promoted Co-based Fischer-Tropsch synthesis catalysts prepared by different pretreatment methods. Mn was used as a catalyst additive to suppress methane formation. Catalysts that underwent calcination before reduction produced more methane and fewer long-chain hydrocarbons than catalysts that were directly reduced. The extent to which Co and Mn were spatially associated was assessed using correlation metrics, colocation plots, and histograms generated using data from STEM-EDS maps. Although both catalysts yielded visually similar elemental maps, the results of statistical analysis suggested that the calcined catalyst exhibited greater spatial segregation between the Co and Mn. These findings support the hypothesis that having Mn in close proximity to the Co is essential for the manifestation of Mn promotion effects in Co-based FTS catalysts.

2.1 Introduction

Transmission electron microscopy (TEM) is a valuable tool for characterizing catalyst particles and has been widely applied in the field of heterogeneous catalysis to assess nanoparticle size and structure. This has been demonstrated for numerous systems containing Pt, Au, or other heavy transition metals.[1-3] However, for lighter transition metals such as Co and Cu, standard techniques such as bright-field TEM become more challenging due to the lower contrast of these elements against typical catalyst support materials such as silica, alumina, or titania. Scanning transmission electron microscopy with high-angle annular dark-field imaging (HAADF-STEM) produces images with contrast based on the atomic number of the material (Z-contrast), but this technique is of limited utility when investigating samples containing elements with similar atomic numbers, overlapping structures in projection, and uneven thickness.[4] For many catalyst systems, analytical electron microscopy methods such as energy dispersive spectroscopy (EDS) or electron energy-loss spectroscopy (EELS) are the only viable techniques for obtaining element-specific images with nanoscale resolution.

Acquiring elemental maps on particles or structures that are less than 10 nm in size means that the measured signal will be small. Particularly in EDS mapping, where X-ray generation by

core-electron relaxation after excitation with the incident beam is a low probability event, it is necessary to use more beam current than is typical for imaging or to use increased acquisition times for signal averaging.[5] However, small particles are often beam-sensitive, and the integrity of the map necessitates that the incident electrons do not impart enough energy to rearrange the material being mapped. The challenge then is to balance sample damage (requiring lower beam current or total dose) and spatial resolution with the collection of enough X-ray counts to make quantitative conclusions (requiring higher beam current or total dose). Even with proper optimization of map acquisition parameters, additional challenges exist pertaining to the interpretation of map data and the determination of how associated or segregated multiple elements are with respect to each other.

Often, the assessment of element spatial association relies upon visual inspection to identify structures of different compositions in the elemental maps.[6-8] However, this approach is insufficient when interpretable motifs do not exist or when the length scale of composition heterogeneity is similar to that of the map resolution. Moreover, comparisons among samples are difficult to make if the degree of element segregation varies throughout different regions of an individual sample. Statistical tools for analyzing image similarity represent a useful alternative approach, and there are abundant examples of these tools being applied toward microscopy research. Microbiologists have long made use of various correlation coefficients to quantify colocation of fluorescently labeled proteins within cells.[9] Using elemental maps obtained by energy-filtered TEM, Grogger et al. were able to infer the existence of various chemical phases in alloys and ceramics through multivariate histograms.[10-11] More recently, Parish and Brewer explored the application of principle component analysis toward STEM-EDS maps to count and identify distinct phases in ceramics.[12] Still, there has not been much evaluation of how statistical methods can be used to evaluate element segregation in samples for which sensitivity to beam damage is a prevailing concern.

These considerations about data interpretation are frequently present when studying industrially relevant catalysts, which often consist of a catalytically active metal and one or more catalytically inactive promoter elements that serve to increase the activity, selectivity, or stability of the active element.[13] For example, Co metal is known to be an active catalyst for Fischer-Tropsch synthesis (FTS) of hydrocarbons from CO and H_2, and transition metal oxide promoters are frequently employed to improve product selectivity.[14] While several studies have shown that the addition of Mn limits the undesired formation of methane and enhances the formation of long-chain hydrocarbons used in diesel fuel, the means by which Mn affects the catalytic properties of Co are not well understood.[15,16] Boffa et al. and Sachtler et al. have hypothesized that adsorbed CO can interact simultaneously with Co metal sites and nearby Mn cations so as to weaken the carbonyl bond and facilitate CO dissociation.[17,18] If such a scheme were true, then it would imply that Mn oxide must be in contact with Co metal nanoparticles. Testing such a hypothesis requires analytical electron microscopy in order to understand the degree of spatial association between Co and Mn within these catalysts. Through STEM-EELS imaging, Morales et al. determined that Mn preferentially locates close to Co in TiO_2-supported Co-Mn catalysts; however, these conclusions came from visual inspection of a small number of nanoparticles.[19] There are compelling motivations for developing ways to avoid the risks of basing conclusions on non-representative images and subjective interpretations. In this work, we adapt existing

methods and introduce new approaches for statistically evaluating the colocation of two elements from a set of EDS maps. We demonstrate that these methods can be used even when the total number of X-ray counts per pixel is low and where binning pixels would sacrifice too much spatial resolution. These methods are then used to analyze a Mn-promoted Co catalyst to show how changes in the pretreatment of this catalyst affect the spatial relationship of Mn and Co, which correlates with changes in catalyst product selectivity.

2.2 Experimental Methods

2.2.1 TEM Sample Preparation

Catalyst precursors were prepared by impregnating porous silica (PQ Corporation, CS-2129) with an aqueous solution of $Co(NO_3)_2{\cdot}6H_2O$ and $Mn(CH_3COO)_2{\cdot}4H_2O$ (Sigma-Aldrich, 99.999% purity) followed by drying at room temperature overnight. The dried catalyst precursors were then calcined in flowing air (Praxair, zero grade) at 673 K or reduced in flowing H_2 (Praxair, 99.999% purity) at 673 K for 2 hr with 4 K/min temperature ramps followed by passivation with 500 ppm O_2 in He (Praxair, 99.999% purity) at room temperature for 30 min. In this work, catalysts prepared by these two pretreatment methods are referred to as initially calcined and directly reduced catalysts, respectively. Co weight loading was kept constant at 10 wt% Co in all samples; Mn loading was varied to yield samples with Mn/Co atomic ratios of 0, 0.1, and 0.5. The bulk elemental compositions of all catalyst samples were verified by ICP-OES (Galbraith Laboratories).

TEM samples of the catalysts were prepared by grinding 5 mg of catalyst in a mortar for 30 s. The ground catalyst particles were then suspended in 1 mL of anhydrous hexane and ultrasonicated for 1 min. From this suspension, 5 µL aliquot was drop-cast onto an ultra-thin carbon film with lacey carbon support Cu TEM grid (Ted Pella). To remove solvent, the sample grid was dried in a vacuum oven at 373 K at less than 0.1 bar for 1 hr.

2.2.2 TEM and STEM Imaging

Bright-field TEM images of the Co-Mn catalysts were acquired to assess particle size statistics using an FEI Tecnai T12 microscope at the Electron Microscopy Lab at UC Berkeley operated with an accelerating voltage of 120 kV. For each catalyst sample, approximately 300 nanoparticles were used to generate particle size distributions. The surface mean diameters, also known as the Sauter mean diameters, of the nanoparticles were calculated according to eq. 2.1, where n_i is the number of particles with diameter d_i in a nanoparticle sample of size N:[20]

$$\bar{d} = \frac{\sum_i^N n_i d_i^3}{\sum_i^N n_i d_i^2} \tag{2.1}$$

More detailed imaging of the metal nanoparticles within the Co-Mn catalysts was done in STEM mode using an FEI Tecnai T20 microscope and an aberration-corrected FEI Titan 80-300 (TEAM I) at the Molecular Foundry at the Lawrence Berkeley National Laboratory. On both microscopes, images were collected using an accelerating voltage of 80 kV.

2.2.3 STEM-EDS Mapping

Hyperspectral elemental maps were recorded using a FEI Titan electron microscope equipped with a 4 segment silicon drift detector with a 0.7 steradian solid angle at the Molecular Foundry at the Lawrence Berkeley National Laboratory. Images were acquired in scanning transmission electron microscopy (STEM) mode with a probe convergence semi-angle (α) of 10 mrad. High-angle annular dark-field (HAADF) images were acquired with inner semi-angles (β) greater than 70 mrad. The X-ray spectrum at each pixel was recorded from 0-10 keV with an energy resolution of 140 eV and a dispersion of 10 eV per channel. For each map, close to 100 frames were collected using active drift compensation. The mapping was performed on regions near the edges of the silica support material that were thinner than 100 nm so as to avoid overlapping nanoparticles, which is necessary for proper determination of spatial correlation of elements. Optimization of mapping conditions was conducted to improve X-ray counts and minimize beam damage to the sample using the following parameter ranges: 80, 200, and 300 kV at beam currents of 0.1-1.0 nA with pixel dwell times between 50 and 150 µs. HAADF images were acquired during EDS mapping to monitor beam damage to the sample.

Bruker Esprit software was used to process and quantify the EDS maps using the following approach. First, a fit of the Bremsstrahlung background X-rays was subtracted from the hyperspectral images using pre-defined fitting regions where no characteristic X-ray peaks appeared. Corrections for escape peaks, pileup peaks, shelf, tail, and shift errors were applied. Contributions of X-rays from Fe and Cu to the Mn and Co peaks, which could come from the microscope column and Cu sample grids, were negligible. As an extra precaution, a peak deconvolution routine was used to remove any contribution from these elements from the spectra. Due to the high transparency of the sample to Cu and Fe K_α X-rays, contributions to the Co and Mn K_α peaks due to secondary fluorescence was assumed to be negligible. Elemental compositions were determined by integrating the Co K_α and K_β peaks at 6.93 keV and 7.6 keV and the Mn K_α and K_β peaks at 5.89 keV and 6.49 keV; Cliff-Lorimer factors were used to calculate percent compositions. Si was treated as the compound SiO_2 in these calculations to improve quantification accuracy.

Spectrum images using electron energy-loss spectroscopy (EELS) were acquired at 200kV on a FEI Tecnai F20. Although EELS data can often produce better spatial resolution with thin samples, the high energy of the K edges of Co and Mn and the lower scattering cross-section for the L edges produced inferior information as compared with the EDS spectrum images.

2.2.4 Data Analysis

Statistical analysis of element spatial association was performed using custom-written software, which was released as an open-source package called QMapTools.[21] First, X-ray count maps from which the background had been subtracted and detector effects removed, as described previously, were exported from the Bruker Esprit software. This was done separately for the Co and Mn channels with the data being exported as color-coded images with the convention of red representing Mn and green representing Co where pixel intensity scaled linearly with X-ray counts for the respective element. To improve the statistical significance of the correlation analysis, multiple images from different regions of the same sample were used. A variety of correlation metrics, scalar values that express the level of similarity between two numerical series, were then computed using the intensity maps. For all four of the correlation

metrics described below, possible values are decimal numbers ranging from -1 to 1, where 1 represents perfect positive correlation, 0 indicates no correlation, and -1 indicates perfect negative correlation between the two elements.

The Pearson product-moment correlation coefficient (PCC), which characterizes the linearity of the relationship between two variables, was calculated according to eq. 2.2.[22] Here, N is the total number of pixels in the combined elemental map; r_i and g_i are the intensities of the ith pixel for the Mn and Co channels, respectively; $\bar{r}$ and $\bar{g}$ are the mean pixel intensities of the Mn and Co channels, respectively; and s_r and s_g are the sample standard deviations of the Mn and Co channels, respectively. By normalizing using the mean intensity, differences in brightness between the two channels are controlled for, and the division by the standard deviations renders the metric insensitive to differences in image contrast.[23]

$$PCC = \frac{1}{(N-1)} \sum_{i=1}^{N} \left(\frac{r_i - \bar{r}}{s_r}\right)\left(\frac{g_i - \bar{g}}{s_g}\right) \tag{2.2}$$

If Mn were to form a shell-like layer over the Co nanoparticles, then the X-ray counts for the two metals would not scale linearly together. Since the PCC tests for a linear relationship between the concentrations of the two metals, the PCC may fail to properly account for spatial association other than alloy formation. For this reason, the Spearman rank correlation coefficient (SRCC), which tests for monotonicity between the Co and Mn pixels intensities, was also computed. The formula for the SRCC is given in eq. 2.3.[24] In this equation, R_i and G_i are the ordinal ranks of the Mn and Co pixel intensities at the ith pixel.

$$SRCC = 1 - \frac{6\sum_{i=1}^{N}(R_i - G_i)^2}{N(N^2-1)} \tag{2.3}$$

Within the field of life sciences, a commonly used metric to assess colocation of fluorescent dyes using confocal microscopy is the Manders colocalization coefficient (MCC).[25] This metric considers the fraction of pixels, weighted by intensity, containing one species that also contain the other species. For maps suffering from shot noise or low color depth, the magnitude of the signal intensities at a given location in the map may be quite unrelated to the actual element concentrations at that position. By making an assessment of element co-presence irrespective of relative channel intensities, the MCC should be relatively insensitive to these problems. In the context of this work, the fraction of Co-containing pixels that also contained Mn was calculated as demonstrated in the equation below:

$$MCC = \frac{\sum_i^N g_{i,coloc}}{\sum_i^N g_i} \tag{2.4}$$

where $g_{i,coloc} = g_i$ if $r_i > 0$, and $g_{i,coloc} = 0$ otherwise

A limitation of these correlation coefficients is that similarity between adjacent pixels is neglected in the calculations. Since this information has been assumed to be a key component of human visual perception, Wang et al. developed the structural similarity index method (SSIM) to quantify the similarity between two images using structural information.[26] Here, the similarity of

a small window of pixels is compared on both channels, and this calculation is repeated at every position in the image to generate a local SSIM value at each pixel. These values are then averaged to yield a scalar value expressing the similarity of the two images. By basing the metric on the comparison of groups of contiguous pixels, more weight should be given toward spatial correlation between the elements on length scales larger than the map resolution using the SSIM than with the other correlation metrics. The calculation of this metric was implemented using an 8 x 8 pixel window, a 1.5 pixel standard deviation for the Gaussian distribution applied to the window, and the same stabilizing constants as used by Wang et al.

Although the correlation metrics are relatively straightforward to interpret, information about how correlation scales as a function of channel intensities is not retained in the resulting scalar value. To investigate how much Mn was present where Co was least and most concentrated, plots showing the fractional Mn colocation versus normalized Co pixel intensity, referred to as colocation plots in this work, were constructed. First, the Mn and Co channels were divided by the highest Mn and Co pixel intensities in the map to yield a normalized map in which all pixel values on both channels ranged from 0 to 1. All pixels with a given normalized Co pixel intensity, g, were then grouped into a set of size N_g. The normalized Mn intensities at each pixel in this set, r_i/r_{max}, were then averaged according to eq. 2.5 to yield the fractional colocation of Mn for all pixels with a given Co intensity, $f_{Mn,g}$.

$$f_{Mn,g} = \frac{1}{N_g}\sum_i^{N_g}\frac{r_i}{r_{max}} \tag{2.5}$$

Two-dimensional histograms of Co and Mn pixel intensities were prepared by linearly scaling the pixel intensities in each channel separately so that the mean intensities were rescaled to be 0.5 for both channels. A scatterplot for scaled Mn versus scaled Co intensities was then created where each data point represented one pixel in the elemental map. The scatterplot was divided into 20 bins in both dimensions, and the number of data points in each bin was counted. These data were then used to make a heat map equivalent to a two-dimensional histogram where the number of pixels having a given pair of scaled Co and Mn intensities was represented by a color scale. The initial normalization placed images with different total X-ray counts onto a common scale and located the centroid of the histogram at the center of the plot. Scaling the Mn and Co in this manner made any datapoints that fell along the diagonal line running from the origin through the center of the plot have Mn/Co ratios equivalent to that of the bulk catalyst. By observing how much histogram intensity was located on or away from the diagonal parity line, a quick determination of the relative extents of segregation in different samples could be made. Even though data points could exist at any positive number along both axes of the histogram, the plotted axes were truncated at 1 because the number of data points with either scaled Mn or Co intensities above 1 was negligible for both the maps of the Co-Mn catalysts and those based on the simulated images.

Additionally, histograms of atomic composition on the basis of Co and Mn were constructed. These plots were prepared by calculating the relative concentrations of Co and Mn at each pixel using the Cliff-Lorimer method with 4 x 4 pixel binning to increase accuracy.[27] Cliff-

Lorimer factors for compositions in terms of atomic percent at the appropriate accelerating voltage were obtained from the Bruker Esprit software.

2.2.5 Catalytic Testing

Experiments to determine catalyst activity and selectivity were conducted using a fixed-bed microreactor. In a typical experiment, approximately 50 mg of passivated catalyst diluted with 100 mg of silica was mixed together and loaded into a quartz glass reactor. The reactor was then heated at 4 K/min from room temperature to 673 K in 100 ml/min H_2 at 1 bar to reduce the catalyst. After holding at 673 K for 120 min, the reactor was cooled to 493 K and the inlet feed was switched to syngas with H_2/Co = 2 (Praxair, CO 99.9% purity and H_2 99.999% purity) to start the Fischer-Tropsch reaction. Measurements were done at steady state at various CO conversions by manipulating the inlet feed volumetric flow rate. The chemical composition of the reactor outlet was determined using an Agilent 6890 gas chromatograph with FID and TCD detectors to measure hydrocarbons and CO, respectively.

2.3 Results and Discussion

2.3.1 TEM and HR-STEM Imaging

TEM images of the Co-Mn catalysts were collected to assess the size distribution and structure of the metal nanoparticles supported on silica. Typical bright-field TEM images for an unpromoted and Mn-promoted catalyst (Mn/Co = 0.1) are presented in Figure 2.1. Although the metal nanoparticles are visible against the silica support material, it is not possible to determine the relative abundance of the two metals within the nanoparticles owing to the similar atomic numbers of Co and Mn and the ambiguous nature of TEM contrast. The surface mean diameters of the unpromoted, Mn/Co = 0.1, and Mn/Co = 0.5 catalysts were calculated to be 9.4 ± 2.1 nm, 9.1 ± 1.8 nm, and 8.9 ± 2.6 nm, respectively. No significant differences in nanoparticle morphology were observed among the three catalyst samples; most nanoparticles had near-spherical geometry.

HAADF-STEM images provided better contrast of the metal nanoparticles against the silica support as shown in Figure 2.2. Although the atomic lattice of the metal nanoparticles was visible in images acquired under HRSTEM conditions (Figure 2.2B), it was not possible to infer the presence of Mn using these data. Since Co and Mn nanoparticles oxidize in air, all reduced catalyst samples were passivated with dilute O_2 at ambient temperature before immobilization on TEM sample grids. Various mixed oxide phases have been reported for Co and Mn so both the stoichiometry and crystal structure of the nanoparticles were indeterminate, and reliable phase identifications and calculation of lattice parameters were not possible.[28]

2.3.2 Acquisition of Elemental Maps by STEM-EDS

Elemental maps obtained by STEM-EDS proved to be a robust method for locating metal nanoparticles and distinguishing between Co and Mn. To optimize map acquisitions, the interplay between STEM-EDS imaging conditions, X-ray count rates, and effective map resolution was explored using reference materials and a Mn-promoted catalyst (Mn/Co = 0.1). Figure S2.2 of the Supporting Information shows the effect of accelerating voltage and beam current on the X-ray

count rate using a 60 nm-thick reference Cu foil, which was estimated to be of comparable mass thickness to the imaged regions of the Co-Mn catalyst samples. X-ray count rates increased linearly with beam current and decreased with higher accelerating voltages. These observations were consistent with the phenomenon of scattering cross sections decreasing as accelerating voltage increases.[29] In order to achieve sufficient beam current, the strength of the first condenser lens is reduced which results in a larger probe size than is typically used for high resolution STEM. Since accelerating voltage is inversely related to beam spreading, it can be inferred that effective map resolution would be poorer at higher beam currents because of the larger probe size and at lower accelerating voltages.[30] For this study, an accelerating voltage of 200 kV and beam current of about 0.6 nA was deemed to be an acceptable compromise between resolution and acquisition time, and most images were acquired at these conditions. Based on measurements in which oxide multilayers in a reference sample were resolved, the size of the electron probe was estimated to be 0.8 nm. Typically, 512x512 pixel maps were acquired with 0.54 nm pixel length, which gave dose rates of about 50,000 e/nm^2-s. The effective spatial resolution was estimated to be between 0.8 and 1.1 nm based on the single-scattering model.[31] Consequently, binning of the pixels was not performed, except for the composition histograms, so as not to discarded valid spatial information.

Beam damage was another factor that participated in the selection of operating parameters. It was observed that extended mapping times led to significant densification of the silica support, which placed an upper limit on elemental map acquisition times. As seen in Figure 2.3C, the porous structure of the silica support had collapsed appreciably after 45 min of scanning under the electron beam at 200 kV and 0.6 nA. Videos of beam damage to the support using various accelerating voltages, beam currents, and pixel dwell times are included in the Supporting Information. Descriptions of the imaging conditions for these videos are given in Table S2.1 of the Supporting Information. At identical total electron doses to the sample, similar levels of sample restructuring were observed when varying pixel dwell times and beam currents. These observations suggest that damage to the sample was more a function of total dose rather than dose rate in the tested range of parameters. Sample damage appeared to decrease slightly at higher accelerating voltages, which was consistent with the restructuring being caused by possibly a combination of radiolysis and diffusion.[29] To prevent sample damage from substantially affecting the elemental maps, the live HAADF-STEM image was monitored so that the mapping could be terminated before significant sample restructuring occurred (Figure 2.3B).

Silica particles began to move upon starting the beam rastering so inevitably there was a small amount of motion in the support during the mapping. Maps showing gross damage to the support were discarded. Of the maps that were analyzed, most features moved no more than 5 nm between the initial and final HAADF-STEM images. The use of active drift compensation, which tilts the beam to follow features of interest, was not relevant for averting the errors introduced by the motion of overlapping silica particles relative to each other. By itself, this phenomenon would limit the effective length scale at which segregation could be detected to perhaps no less than 5 nm. No evidence for knock-on damage was observed in these samples at the tested acceleration voltages. Particle sintering was an unlikely damage mechanism because the particle size distributions visible in STEM-EDS were comparable to those obtained from BF images. Another damage-related concern is the possibility of Oswald ripening, which has been

reported as a prominent mechanism for damage to nanoparticle specimens at high enough beam currents.[32] In this mechanism, atoms on the surface of small particles may become mobilized under the beam and diffuse to larger particles. By surface free energy arguments, most of the Mn should be located on the surface of the metal nanoparticles, so Oswald ripening may affect the nanoparticle compositions without appreciable changes in the particle sizes.[33] Using very low dose rates may help avoid this type of damage.[34] However, STEM-EDS map acquisition times would be impractically long for this system. Since this type of beam-sensitivity would not be readily visible in the HAADF-STEM images owing to the difficulty of identifying metal nanoparticles against the silica support in these images, Oswald ripening may be an additional contribution to the level of spatial association in the elemental maps.

Representative elemental maps of a Mn-promoted Co catalyst (Mn/Co = 0.5) are shown in Figure 2.4. Maps from multiple catalyst particles were acquired to confirm that these images were representative of the sample. The boxed region in the HAADF-STEM image (Figure 2.4A) shows the region over which the elemental maps were acquired. Although metal nanoparticles are visible in the HAADF-STEM image, identifying which features belong to the nanoparticles and to the edges of the overlapping support particles is challenging. However, the EDS maps for Co and Mn (Figs. 4C and 4D, respectively) clearly reveal the locations of the nanoparticles. By comparing spatial features in both the Co and Mn maps, it is apparent that there is a certain degree of correlation between the locations of the two elements because regions of higher Co intensity appear at regions of higher Mn intensity. The two maps are not identical though, and Mn appears to have dispersed over the silica support more so than the Co, which has been speculated to occur in related Co-Mn catalysts.[35] Without a single well-defined morphology, such as alloyed or separate Co and Mn nanoparticles, it would be difficult to make comparisons between catalyst samples. Consequently, statistical methods for determining the extent of Co-Mn spatial association were explored.

2.3.3 Correlation Analyses of Simulated Elemental Maps

To validate the ability of the statistical analysis methods to evaluate spatial correlation, simulated images of nanoparticles with various compositions and structures were generated. The maps were generated stochastically using a Poisson process to simulate the detection of X-ray counts. Three levels of spatial association between Co and Mn were considered (in order of increasing element segregation): nanoparticles with alloyed Co and Mn, small Mn nanoparticles decorating the surface of larger Co nanoparticles, and separate Co and Mn nanoparticles with uncorrelated positions. Representative images of these three test cases are shown in Figure 2.5A.

Correlation metrics computed using sets of 20 simulated images for each test case are given in Table 2.1. Values for the PCC, SRCC, MCC, and SSIM were close to unity for the alloying case, which represented maximal spatial correlation between the two elements. Lower values for the correlation metrics were found for the surface associated case, and the segregated case had the lowest value metrics. For the latter, the MCC and SSIM were less sensitive to segregation having relatively high values of 0.27 and 0.18, respectively, compared to the 0.03 and 0.02 of the PCC and SRCC. This would be expected for the MCC because a portion of the randomly distributed Co and Mn nanoparticles will always overlap when particle densities are sufficiently high. The SSIM may yield higher than expected estimates of similarity due to its incorporation of

information about adjacency. Nevertheless, all four metrics were shown to discriminate adequately among the test images.

Figure 2.5B shows colocation plots for the three test cases. In the case of alloyed nanoparticles, a slope of unity was observed because there were approximately equal intensities of Co and Mn at each location in the simulated elemental maps. Surface decorating Mn particles yielded a colocation plot with a smaller slope which showed a plateau at higher Co intensities. The Co nanoparticles were simulated as three-dimensional spheres so the pixels with maximum Mn intensities, which were used to normalize the data, were likely to have occurred near the edges of the projected area formed by the Co nanoparticles. This meant that fractional Mn colocation should be less than unity where Co intensities were highest, which was at the center of the projected area formed by the Co nanoparticles. The case of uncorrelated, separate Co and Mn nanoparticles resulted in a plot with a flat distribution, which was the expected result if Co and Mn intensities were not correlated. For this case, the average fractional Mn colocation was dictated by the density of nanoparticles in the simulated map, with fractional Mn colocation values increasing as nanoparticles density increased.

The two-dimensional histograms for Co and Mn intensities presented in Figure 2.5C gave characteristic patterns for different levels of element segregation. Intense histogram density along the diagonal parity line for the alloyed nanoparticles was consistent with all pixels having compositions similar to that of the bulk. With increasing segregation, more histogram density was observed away from the parity line and toward the axes. For the spatially uncorrelated nanoparticles, essentially all histogram intensity fell along the axes, which indicated most pixels contained either no Mn or no Co signal. The composition histograms shown in Figure 2.5D were consistent with the observed spatial distributions in the simulated maps. The alloyed nanoparticles with homogeneous composition gave a narrow, monomodal distribution. Surface decoration of the Co nanoparticles by smaller Mn nanoparticles, showed a broader composition distribution with the appearance of pixels with compositions near 0 and 100% Mn. The spatially uncorrelated nanoparticles showed strong signs of segregation with most histogram density close to either 0 or 100% Mn.

In situations where beam damage to the sample limits the permissible map acquisition times, elemental maps may have low color depth due to insufficient X-ray counts. Here, color depth refers to the number of distinct values for pixel intensities in a given channel, and an illustration of the concept is provided in Figure S2.3 of the Supporting Information. The effect of lower color depth on the output of the statistical methods was tested using the simulated images which were modified to have lower color depth. As shown in Figure S2.4 of the Supporting Information for the surface associated test case, the correlation metrics were quite insensitive to this degradation in data quality, and the colocation plot was unaffected provided that the Co channel had high color depth. Fewer intensity values translated to missing data points in the colocation plot if the Co channel was modified, and the two-dimensional histograms were severely impacted when the color depth of either the Mn or Co channels were lowered because this plot displays information about the pixel intensities of both channels. These results suggest that the correlation metrics could be used for assessing element segregation in maps with low

color depth. Since the colocation plot only required sufficient color depth in one channel, the plot could be an appropriate tool to use when one element is more dilute than the other.

Figure S2.5 of the Supporting Information shows the effects of Gaussian noise on the output of the statistical methods. With the exception of the MCC, increasing levels of noise caused the metrics to report lower levels of element spatial correlation, which was consistent with the noise being spatially uncorrelated. The PCC was least sensitive in the presence of low noise, but the SSIM demonstrated the best performance at high noise levels where the noise began to visually obscure the simulated signal from the nanoparticles. The slope of the colocation plots flattened as noise levels increased. Low levels of noise overwhelmed the real signal in the two-dimensional histograms owing to the greater number of pixels where no nanoparticles were located. A judicious pixel intensity cutoff or pixel mask could be used to remove the contribution of these pixels from the plot.

It must be emphasized that even though these analysis methods were tested on and could discriminate between very dissimilar structural patterns, the objective was not to identify the specific morphology of the nanoparticles. Rather, the intention was to extract a relative quantitative measure of how segregated the two elements were for the purpose of making comparisons between catalysts.

2.3.4 Correlation Analysis of Co-Mn Catalysts

STEM-EDS maps of the initially calcined and directly reduced catalysts after FTS reaction were acquired to determine how closely associated the Mn promoter was with respect to the active Co metal. Representative elemental maps for the two catalysts are presented in Figure 2.6A. From visual inspection of the maps, it is clear that there are Mn-rich and Mn-poor regions, but it is difficult to establish which catalyst exhibited a greater degree of spatial segregation between the two elements. This is complicated by the apparent tendency of the two metals to spread more evenly over the silica support after exposure to syngas, shown in Figure 2.6A, compared to samples that had not been exposed to syngas, represented by Figure 2.4. Scanning tunneling microscopy studies have provided evidence that Co surface atoms may become mobile under typical FTS conditions leading to catalyst restructuring.[36] Moreover, Prieto et al. reported that Co nanoparticles can flatten during reaction so as to increase the area of contact between the nanoparticles and support.[37] Such restructuring would be similar to the phenomenon observed in the catalysts of this work. A more precise determination of element spatial correlation was made using the statistical methods introduced previously.

Correlation metrics for these catalysts based on a set of over 10 map images for each catalyst are presented in Table 2.2. The directly reduced sample had relatively high correlation values of 0.74 (PCC), 0.78 (SRCC), and 0.56 (SSIM); lower values of 0.28 (PCC), 0.34 (SRCC), and 0.26 (SSIM) were calculated for the initially calcined sample. The PCC and SRCC metrics had similar values for the directly reduced sample, which suggests that the relationship between the Co and Mn intensities in this sample were relatively linear. This is visually evident in the 2D histograms discussed later in this section in which most histogram intensity fell along the diagonal parity line. These two metrics also had similar values for the initially calcined sample, although the difference between the two metrics was slightly larger. The PCC metric probes the more

stringent criterion of linearity between the Co and Mn intensities rather than monotonicity as does the SRCC, which would make the PCC respond more sensitively to higher segregation. The lower value of the PCC metric compared to the SRCC was likely due to segregation breaking the linearity of the relationship between the Co and Mn intensities more so than the monotonicity of the relationship. Although the SSIM metric differentiated between the two catalysts, this metric consistently gave lower values than the PCC and SRCC metrics, which was a behavior also seen with the simulated images. Making a direct comparison between the magnitude of the SSIM values and those of the other metrics for the same sample would not be informative because the SSIM is a fundamentally different calculation which aims to quantify differences in images as perceived by the human eye, whereas the PCC and SRCC only assess the relationship between the Co and Mn intensities at each pixel. In general, the metrics should be viewed as ordinal values rather than cardinal values. The magnitude of each metric increases with higher spatial correlation so comparing the same metric for different samples yields information about which sample exhibits more spatial association. However, there is no inherent meaning to the absolute value of the metric other than the limiting values of -1, 0, and 1. The MCC values were close to unity for both catalysts due to the baseline Mn signal over much of the catalyst support. An intensity cutoff could be used to remove regions of fewer Mn X-ray counts from the MCC calculation, but this would be a subjective correction that could introduce biases that overstate element segregation. Without any guide for an appropriate cutoff threshold, the MCC proved to be an unsuitable measure of element spatial association in these samples. Nevertheless, the PCC, SRCC, and SSIM metrics all indicated that the initially calcined sample had a larger degree of spatial segregation between the Co and Mn compared to the directly reduced sample.

Colocation plots for the two Mn-promoted catalysts are included in Figure 2.6B. A much steeper slope in the plot for the directly reduced compared to that for the initially calcined catalyst was observed. This can be interpreted as indicating a higher correlation between the Co and Mn concentrations in the directly reduced sample. A related aspect of these plots is the higher fractional Mn colocation at low Co pixel intensities in the plot for the initially calcined catalyst, which is consistent with there being more Mn-rich pixels. Interestingly, neither plot shows high fractional Mn colocation at high Co pixel intensities, which indicates the presence of regions with high concentrations of Co without significant Mn co-presence in both catalysts. The representative elemental maps (Figure 2.6A), which both contain several bright green regions on the scale of 10-40 nm, are consistent with this interpretation of the colocation plots.

Two-dimensional histograms, shown in Figure 2.6C, provided further evidence of greater element spatial correlation in the directly reduced sample compared to the initially calcined sample. Most of the histogram distribution for the directly reduced sample was located more closely to the diagonal parity line, which indicates that a relatively high fraction of pixels had compositions close to that of the bulk. In contrast, more of the histogram distribution for the initially calcined catalyst, which suggests there were more pixels that were enriched in either Co or Mn. These interpretations are also evident in the atomic composition histograms for the two catalysts, which are presented in Figure 2.6D. A narrower composition distribution was observed for the directly reduced catalyst. Local maxima are present in the composition histograms at 0 and 100% Mn. These features are due to there being pixels for which no X-ray counts were recorded at the Mn or Co peaks, respectively, which was likely a consequence of baseline noise

over holes in the specimen. For both catalysts, the mean of the composition histograms was equivalent to the bulk Mn/Co ratio determined by ICP to within 5%.

Taken together, the results of the correlation analyses imply that the initially calcined catalyst demonstrated greater spatial segregation between the Co and Mn. However, it is important to recognize that beam damage to the sample could be a contribution to the observed levels of element association in the samples. Any motion of overlapping silica particles and Oswald ripening of the Co-Mn nanoparticles would likely inflate the estimates of element spatial correlation. Nevertheless, a rationalization of the greater observed segregation in the initially calcined can be made by analogy to studies of the thermal decomposition of Co precursors in silica-supported catalysts. Girardon et al. reported that the decomposition of $Co(CH_3COO)_2$ in air led to greater formation of Co silicates than if $Co(NO_3)_2$ was used as the precursor.[38] This phenomenon was attributed to the acetate decomposition being exothermic and the nitrate decomposition being endothermic. Thermogravimetric analysis of the Co-Mn catalyst precursor in air (Figure S2.6 of the Supporting Information) confirmed that the decomposition of $Mn(CH3COO)_2$ was also exothermic, and the decomposition of $Mn(CH_3COO)_2$ in H_2 has been reported as being endothermic.[39] Compared to a direct reduction of the catalyst precursor, an oxidative pretreatment step may provide localized heat that facilitates dispersal of the Mn over the support and contributes to partial integration of the Mn into the silica.

Similar observations of more extensive bimetallic interactions after direct reduction pretreatment compared to calcination have been reported for Pt-Re catalysts based on catalytic data.[40] Higher segregation between metals due to calcination was also inferred from infrared spectroscopy of adsorbates on Pt-Ru catalysts.[41] With regard to Co-Mn catalysts, den Breejen et al. acquired elemental maps of Co-Mn-Pt catalysts calcined with either NO or air and found pretreatment in NO to promote higher dispersions of the both Co and Mn.[42] Other studies of Co-Mn catalysts using analytical electron microscopy techniques have been published, but data interpretation only consisted of visual inspection of a small number of nanoparticles.[15,19,43]

2.3.5 Catalytic Performance

A comparison of the FTS product selectivities for the initially calcined and directly reduced Mn-promoted catalysts (Mn/Co = 0.5) is presented in Figure 2.7. Selectivity data for an unpromoted catalyst (Mn/Co = 0) prepared by direct reduction is included for reference. For the unpromoted catalyst, the selectivity toward methane was 33% on a molar carbon basis. The presence of Mn in the catalyst was found to decrease the methane selectivity, but to different extents depending on the catalyst preparation method. The Mn-promoted catalyst that was initially calcined had a methane selectivity of 26%, whereas the directly reduced counterpart had a more favorable selectivity of 21%. Selectivities toward C_{5+} hydrocarbons, a product fraction which includes all hydrocarbons containing five or more carbon atoms, followed the opposite trend. The unpromoted reference catalyst had a C_{5+} selectivity of 36%, the initially calcined Co-Mn catalyst had a selectivity of 41%, and the directly reduced Co-Mn catalyst had a selectivity of 48%. An initially calcined unpromoted catalyst was found to give similar selectivities to those of the directly reduced unpromoted catalyst (34% methane and 34% C_{5+}). All catalysts exhibited constant carbon number product selectivities as a function of CO conversion up to conversions

of 25%, which was consistent with our previous findings for these catalysts when operating at atmospheric pressure.[16]

Using the correlation analysis results from the elemental maps, a connection can be made between catalyst performance and the spatial association between Co and Mn. The least methane was produced by the promoted catalyst exhibiting the highest level of spatial correlation between Co and Mn. This suggests that the selectivity promotion effects emerge from the two elements being in close proximity; specifically, the required proximity is likely to be at or smaller than the map resolution, which is what is tested by the correlation analysis. The comparable selectivities for the unpromoted catalysts prepared by initial calcination and direct reduction support the interpretation that differences in Mn spatial distribution are responsible for the observed selectivity differences in the promoted catalysts rather than any inherent property of the pretreatment steps on the Co. The possibility that the observed selectivity differences for the three catalysts were due to nanoparticle size effects is unlikely given that the surface mean diameters of the catalysts were similar. Moreover, FTS on Co-based catalysts has been shown to be insensitive to particle size above diameters of about 6 nm, which was the case for all catalysts in this work.[44]

2.4 Conclusions

As demonstrated by this investigation of Co-Mn FTS catalysts, non-analytical TEM techniques can be insufficient for distinguishing between elements when atomic numbers are similar or when nanoparticles are dispersed over irregularly structured supports. Elemental mapping can reliably identify the location of these multi-metal nanoparticles, but acquisition times long enough to generate sufficient X-ray counts for traditional quantification are often not feasible due to beam damage. Low color depth and low signal-to-noise ratios can lead to erroneous composition histograms unless significant pixel binning is used. However, such measures reduce the resolution at which variations in composition can be detected. To make comparisons about element segregation among beam-sensitive catalysts, a variety of statistical methods can be employed.

Thorough testing of the statistical methods using simulated elemental maps demonstrated that the methods could serve as quantitative descriptors of element segregation. Of the correlation metrics considered in this work, the PCC proved to be the most sensitive to changes in element segregation. However, under high noise conditions, the SSIM performed the best. Colocation plots required high color depth in the map for at least one channel; two-dimensional histograms required sufficient color depth in both channels. In general, it was observed that the statistical methods that conveyed more information about the co-presence of the two elemental had more demanding data quality requirements.

These methods were used to assess metal segregation in Co-Mn FTS catalysts that had the same bulk composition, but where one catalyst was calcined in air and the other reduced in H_2 during the decomposition of the Co and Mn precursors at elevated temperature. Although the elemental maps for both catalysts were visually similar, it was determined by statistical analysis that the directly reduced catalyst exhibited a greater degree of spatial association between Co and Mn. It is possible that beam-induced damage to the sample, both by support densification

and Oswald ripening of the nanoparticles, affected the observed element spatial correlation so as to limit the resolution at which element segregation was detectable. However, the elemental maps displayed composition variations at length scales larger than 20 nm. Equivalent loadings of Mn promoter were added to both catalysts, but the directly reduced catalyst demonstrated the lowest methane selectivity and highest C_{5+} selectivity. These findings suggest that a performance-structure relationship may exist whereby higher spatial association between the Co and Mn is linked to improved product selectivities. This connection is consistent with the guiding hypothesis that Co and Mn must be in close proximity for cooperative interactions between the metals and adsorbed CO.

Acknowledgements

Funding for this work was provided by BP through the XC^2 program. Microscopy experiments were performed at the UC Berkeley Electron Microscopy Lab and the Molecular Foundry, Lawrence Berkeley National Lab, which is supported by the U.S. Department of Energy under Contract # DE-AC02-05CH11231. The authors acknowledge helpful discussions with Dr. Jim Ciston and Dr. Cheng-Yu Song.

Table 2.1 Correlation metrics for simulated images of Co-Mn nanoparticles with different levels of segregation. Representative images of the three patterns are given in Figure 2.5A. An explanation of each metric is given in the experimental methods section.

Pattern	PCC	SRCC	MCC	SSIM
Alloying	0.99	1.00	1.00	0.99
Surface Associated	0.75	0.73	0.81	0.78
Segregated	0.03	0.02	0.18	0.27

Table 2.2 Correlation metrics for Co-Mn catalysts with different pretreatment conditions. The initially calcined catalyst was calcined in air at 673 K and then reduced in H_2 at 673 K. The directly reduced catalyst was reduced in H_2 at 673 K. An explanation of each metric is given in the experimental methods section.

Sample	PCC	SRCC	MCC	SSIM
Initially Calcined	0.28	0.34	0.99	0.26
Directly Reduced	0.74	0.78	1.00	0.56

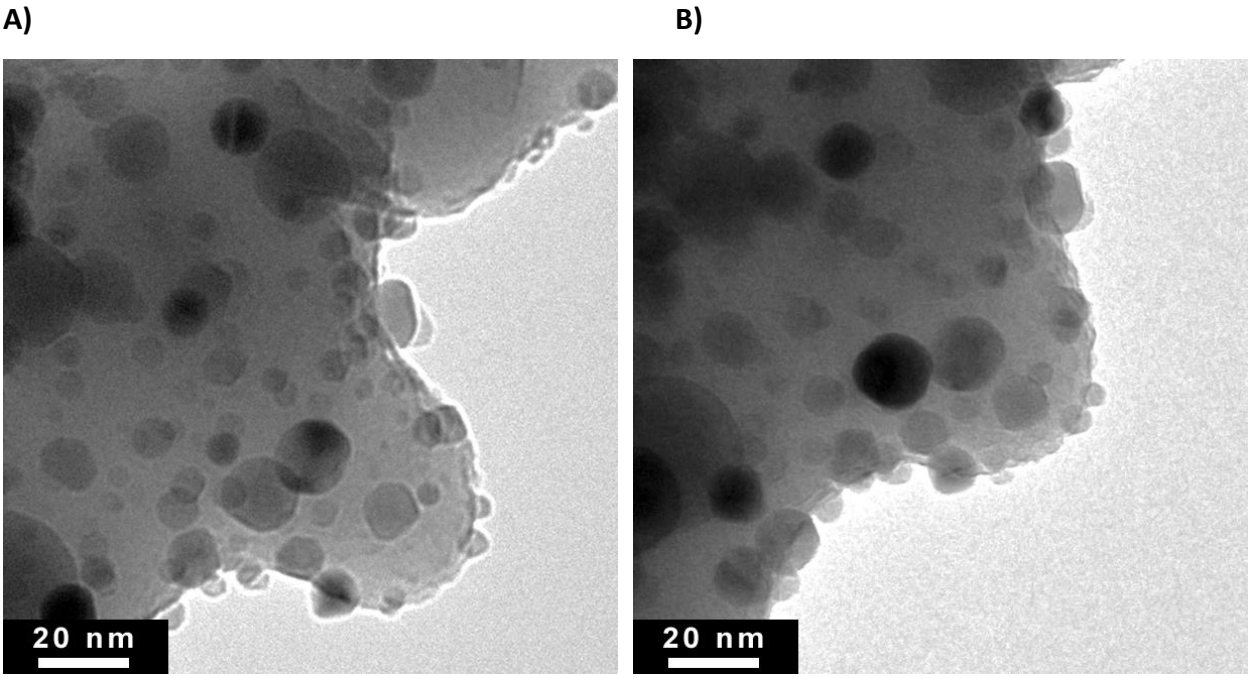

Figure 2.1 Bright-field TEM images of (A) Co and (B) Co-Mn (Mn/Co = 0.1) catalysts. Images were acquired using an FEI Tecnai F12 at 120kV. Although metal nanoparticles can be identified against the silica support material, it is not possible to distinguish unambiguously between Co and Mn.

A) B)

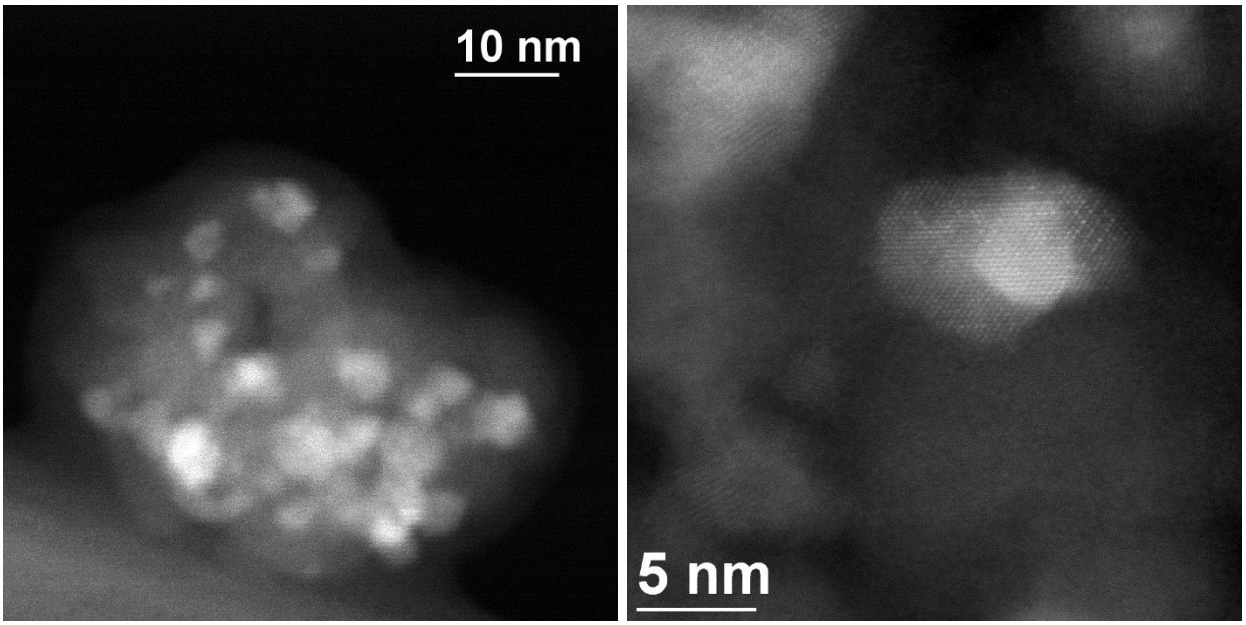

Figure 2.2 HAADF-STEM images of a Co-Mn catalyst sample (Mn/Co=0.1) taken in an (A) FEI Tecnai T20 and (B) the TEAM I, both at 80kV. It is not obvious where the Co and Mn are located with respect to each other even upon examining the lattice of the metal nanoparticles.

A) B) C)

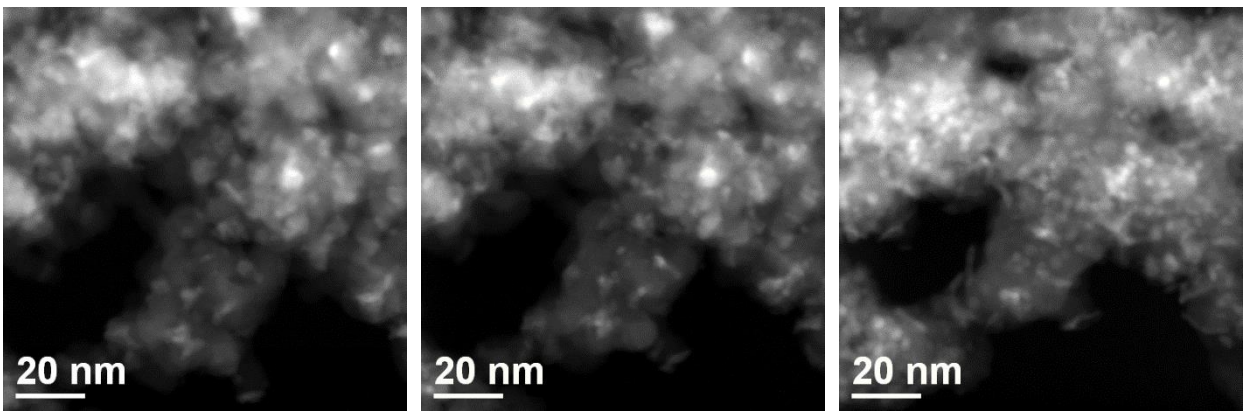

Figure 2.3 Accumulation of damage to a Mn-promoted Co catalyst (Mn/Co = 0.1) by extended rastering with the electron beam in STEM mode. Images were acquired in succession at 200 kV, 0.6 nA beam current, and 50 µs dwell time. (A) initial catalyst image; (B) catalyst image after 8 min (typical mapping time); and (C) catalyst image after 45 min. Comparisons of accelerating voltage, beam current, and dwell time are included in Table S2.1 of the Supporting Information.

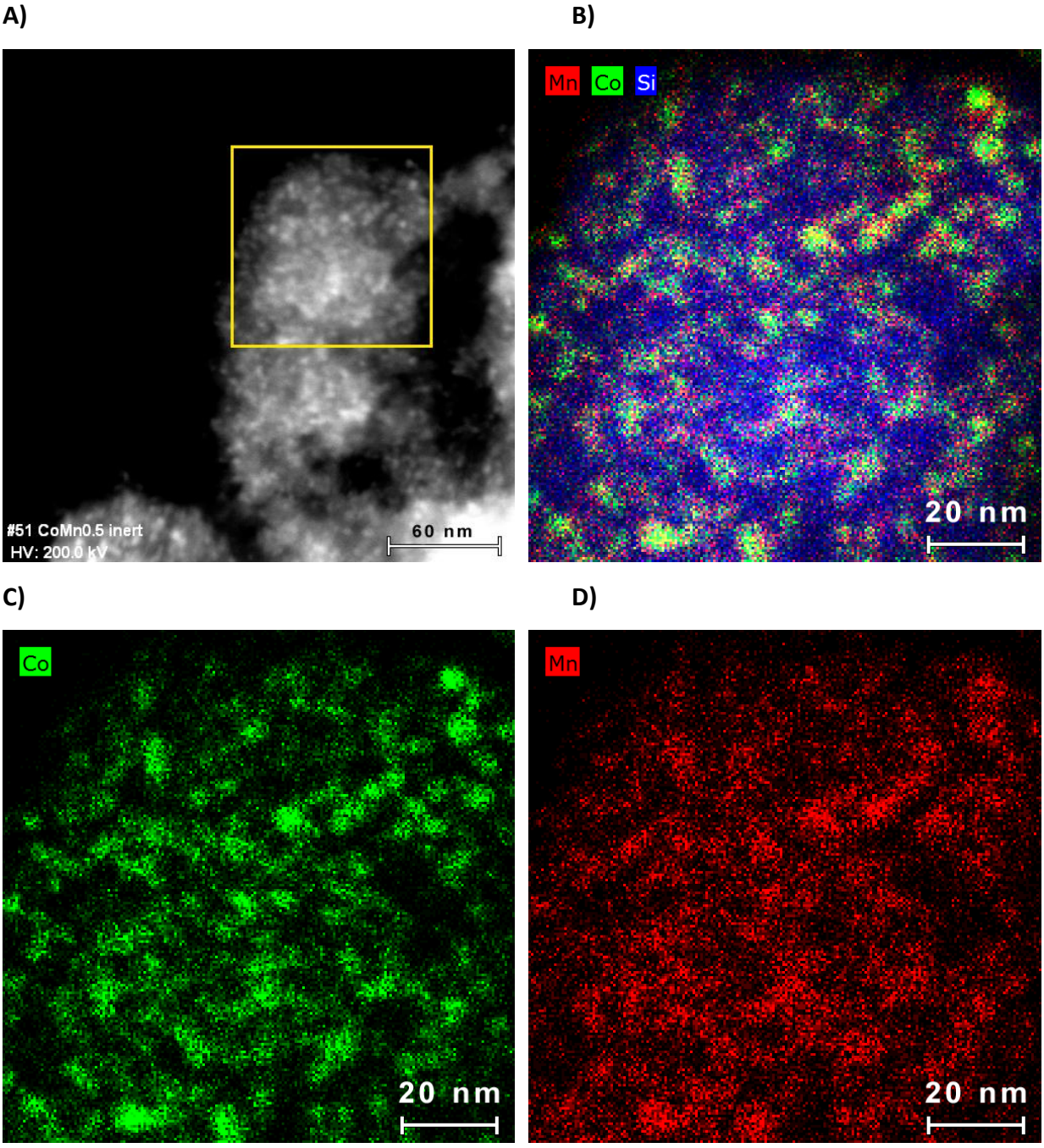

Figure 2.4 Elemental map of a Co-Mn catalyst (directly reduced, Mn/Co = 0.5) obtained by STEM-EDS. (A) HAADF image of catalyst particle with boxed region indicating where the elemental map was acquired; (B) STEM-EDS elemental map; (C) Co channel; and (D) Mn channel. Images were acquired at 200 kV accelerating voltage and 0.6 nA beam current.

Alloyed **Surface Associated** **Segregated**

A)

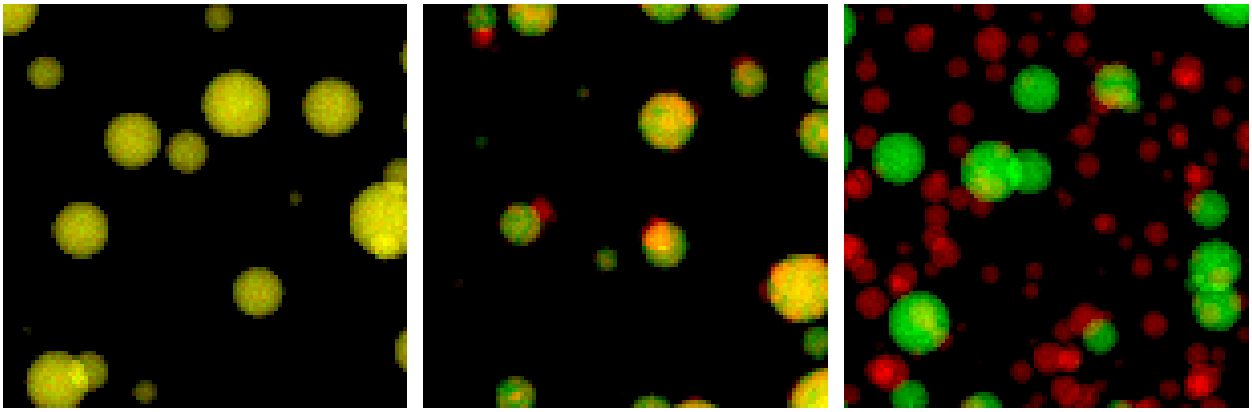

B)

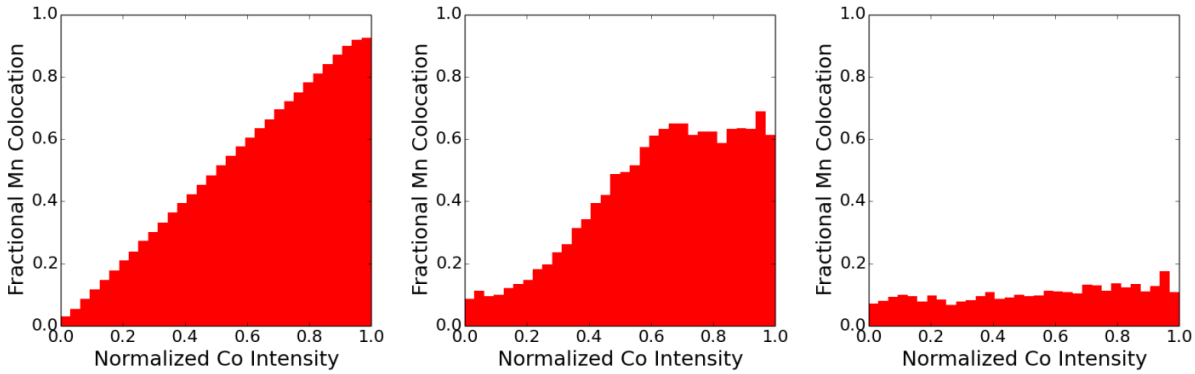

C)

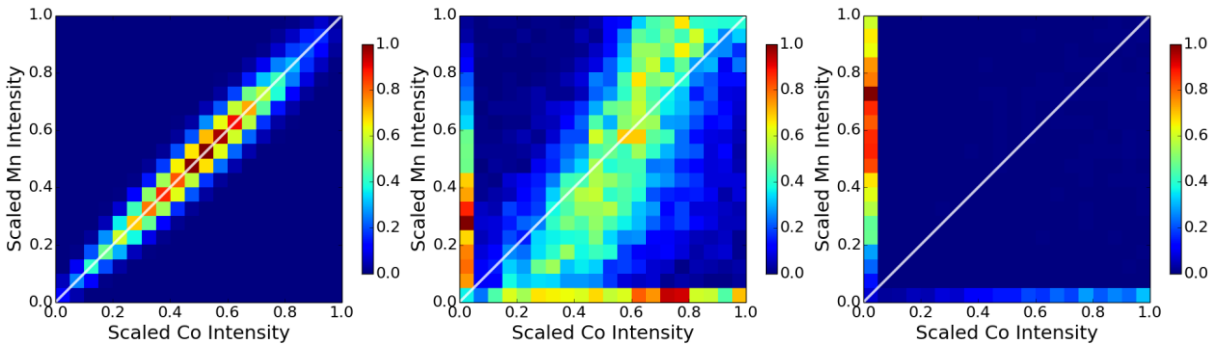

D)

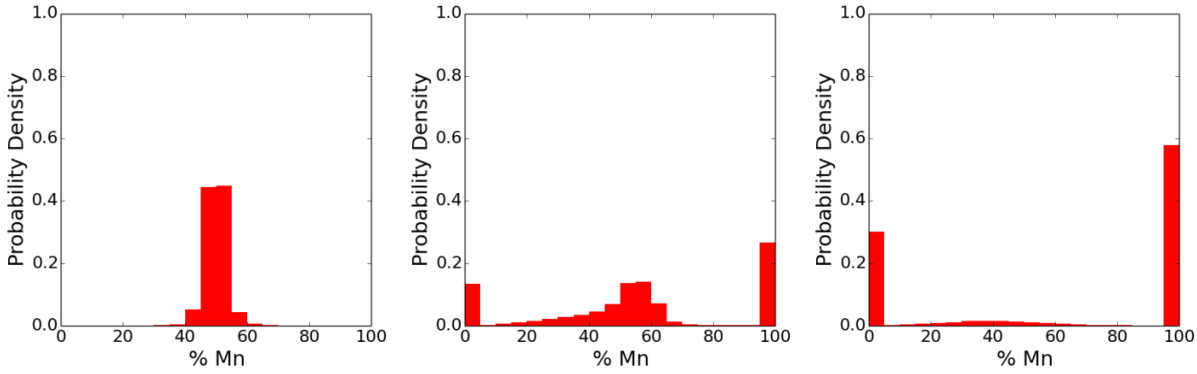

Figure 2.5 Simulated images and correlation analysis plots of Co-Mn nanoparticles with different levels of element segregation. Left column: alloying; middle column: surface association; right column: complete segregation. (A) Representative simulated images depicting different extends of element association; (B) colocation probability plots; (C) 2D histograms; and (D) composition histograms.

Initially Calcined **Directly Reduced**

A)

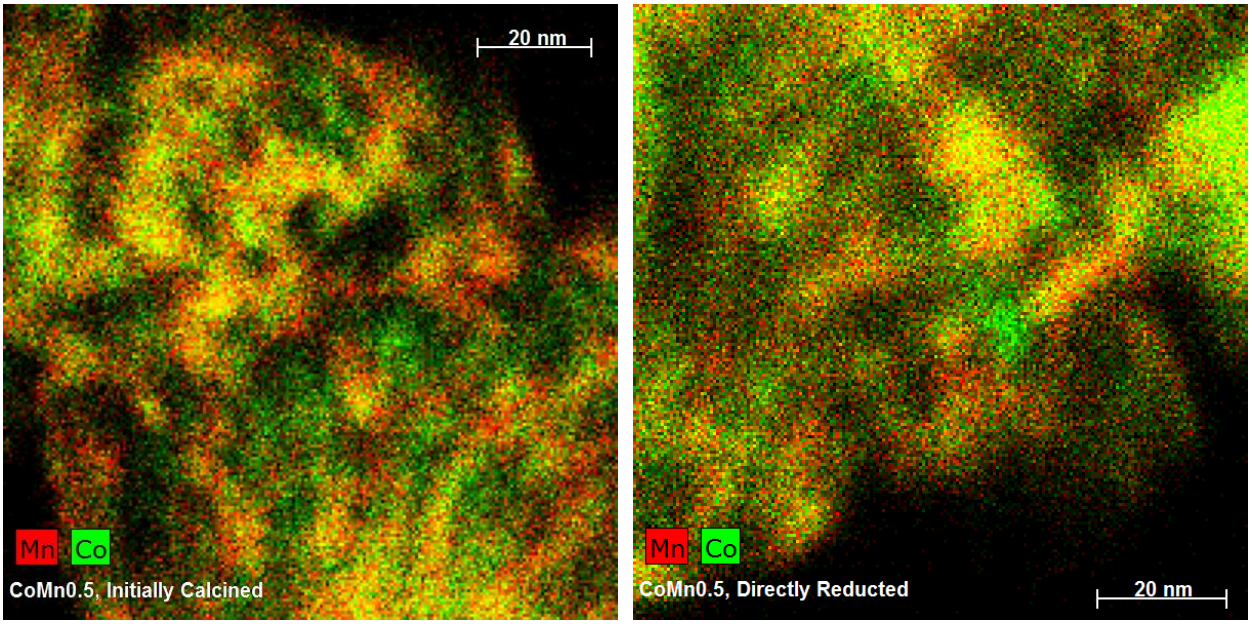

B)

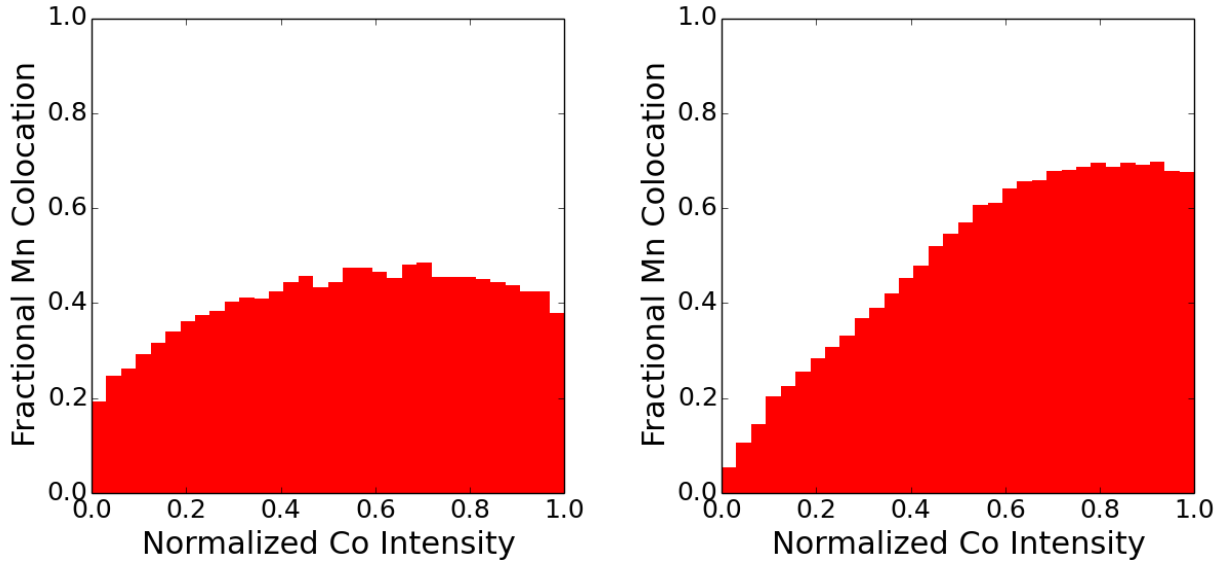

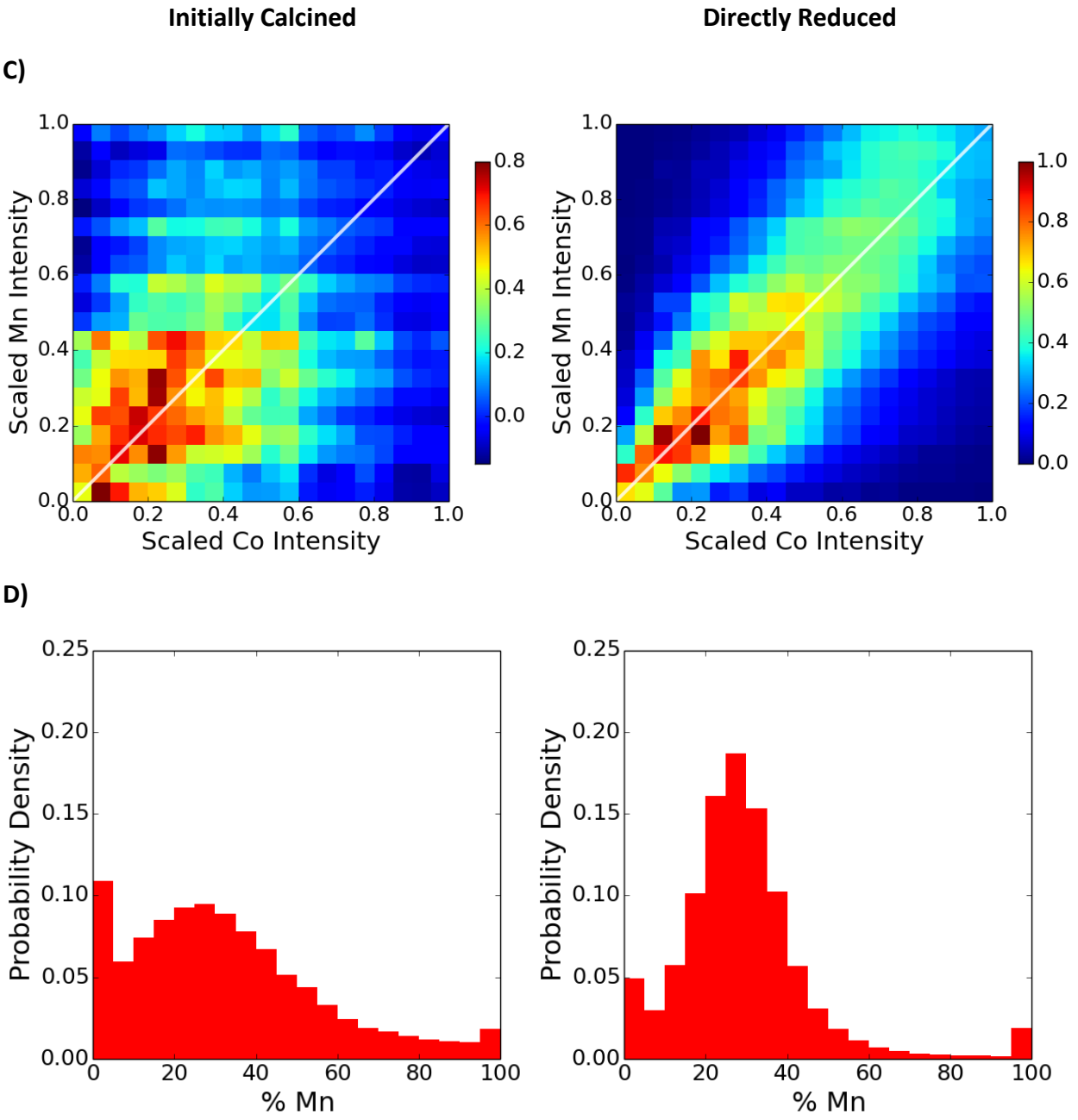

Figure 2.6 STEM-EDS elemental maps and correlation analysis plots of Co-Mn catalysts (Mn/Co = 0.5) with different pretreatment conditions. Left column: catalyst was initially calcined at 673 K and then reduced at 673 K; right column: catalyst was directly reduced at 673 K. (A) Representative elemental maps; (B) colocation probability plots; (C) 2D histograms; and (D) composition histograms.

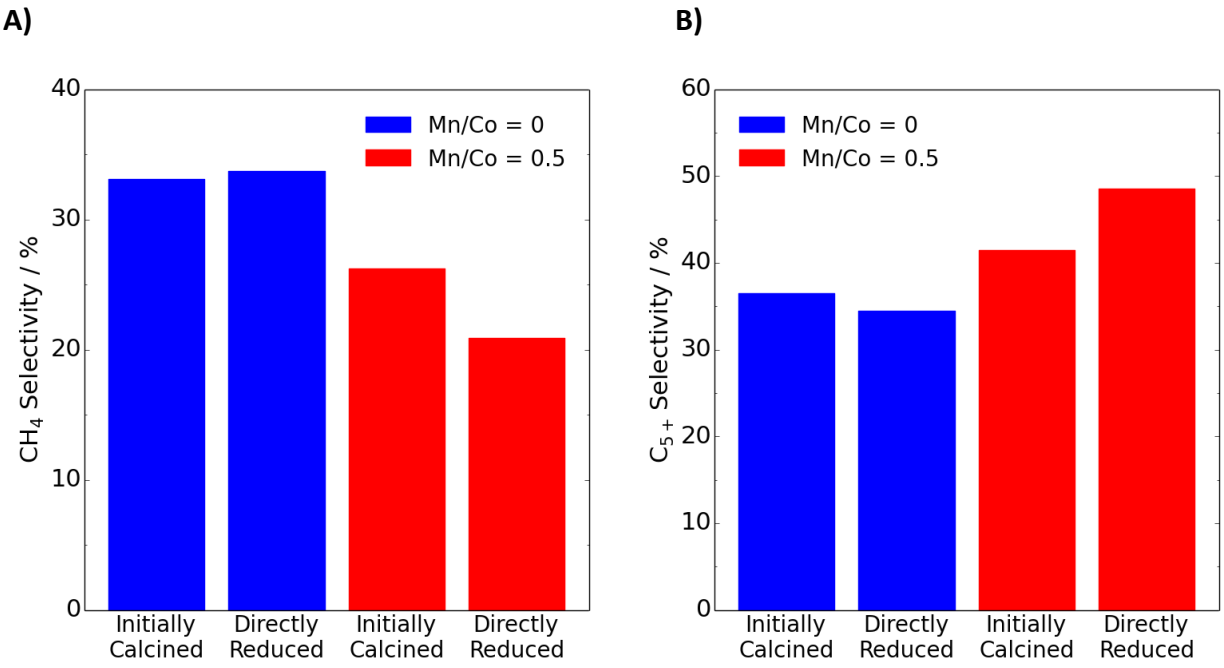

Figure 2.7 Selectivities of (A) methane and (B) C_{5+} hydrocarbons for the Co and Co-Mn (Mn/Co = 0.5) catalysts under Fischer-Tropsch synthesis. Measurements were taken at 1 bar, 493 K, and $H_2/CO = 2$, and the data were extrapolated to 0% CO conversion. The plotted data is product selectivity on a molar carbon basis.

A) B)

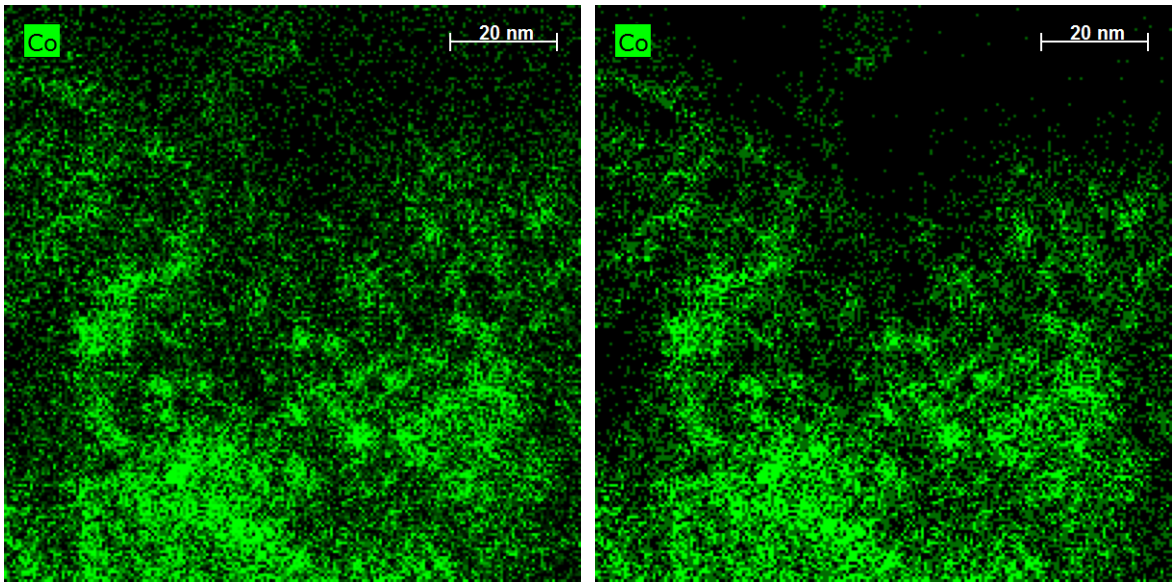

Figure S2.1 Comparison of Co peak count maps using (A) raw counts and (B) the background-subtracted signal. The reduction in baseline counts across the map after background removal is most visible in the thinner regions of the imaged sample. These data were obtained using a Co catalyst with an acceleration voltage of 200 kV.

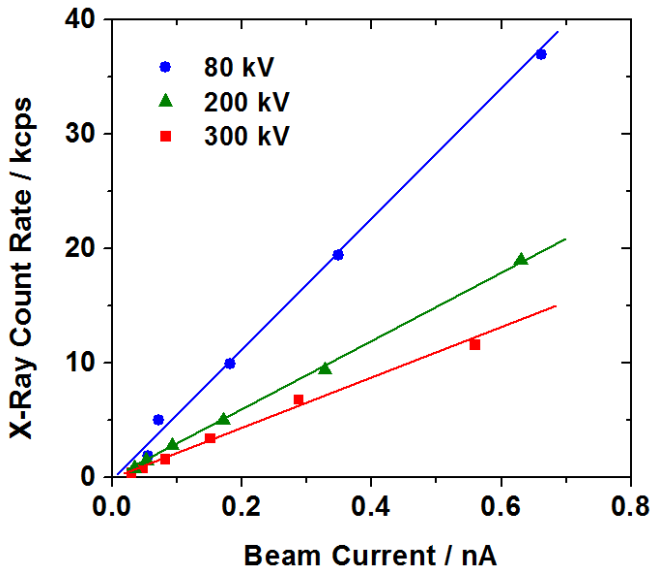

Figure S2.2 Evaluation of X-ray count rates at different microscope operating conditions. Data were collected using a 60 nm-thick Cu reference foil. It was found that in the investigated regime, count rates were linearly proportional to beam current and decreased as accelerating voltage increased.

Table S2.1 Parameters for time lapse videos of beam damage to the Co-Mn catalyst samples at different voltages, currents, and dwell times. All videos were acquired at 512x512 pixels, and the video frame rates were scaled to a constant dose rate per pixel. The videos are available on the Journal of Catalysis website at DOI: doi:10.1016/j.jcat.2014.12.011

Comparison of Accelerating Voltage

File Name	Voltage (kV)	Current (nA)	Dwell Time (µs)	Playback FPS
A.avi	300	0.45	50	27
B.avi	200	0.60	50	20
C.avi	80	0.40	50	30

Comparison of Beam Current

File Name	Voltage (kV)	Current (nA)	Dwell Time (µs)	Playback FPS
D.avi	200	0.60	50	20
E.avi	200	0.31	50	39
F.avi	200	0.17	50	70

Comparison of Dwell Time

File Name	Voltage (kV)	Current (nA)	Dwell Time (µs)	Playback FPS
G.avi	200	0.59	150	20
H.avi	200	0.60	100	20
I.avi	200	0.59	50	20

A)

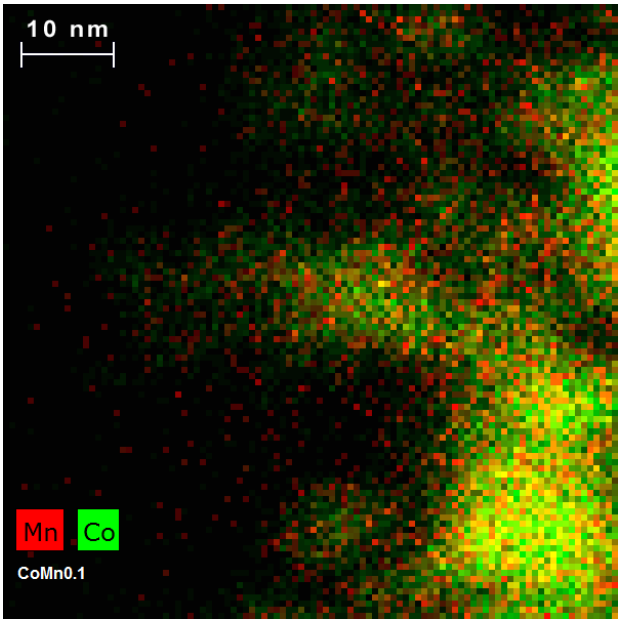
10 nm
Mn
Co
CoMn0.1

B)

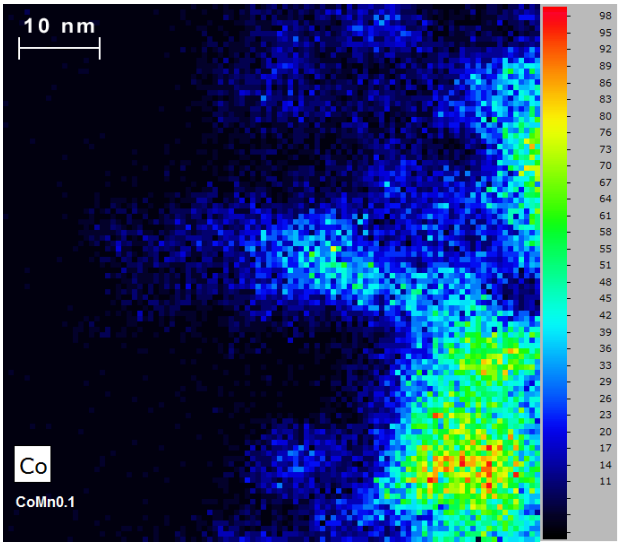
10 nm
Co
CoMn0.1
98
95
92
89
86
83
80
76
73
70
67
64
61
58
55
51
48
45
42
39
36
33
29
26
23
20
17
14
11

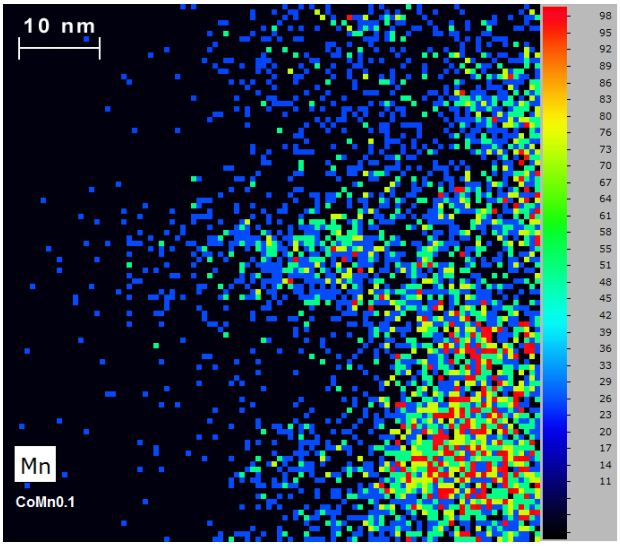
10 nm
Mn
CoMn0.1
98
95
92
89
86
83
80
76
73
70
67
64
61
58
55
51
48
45
42
39
36
33
29
26
23
20
17
14
11

C)

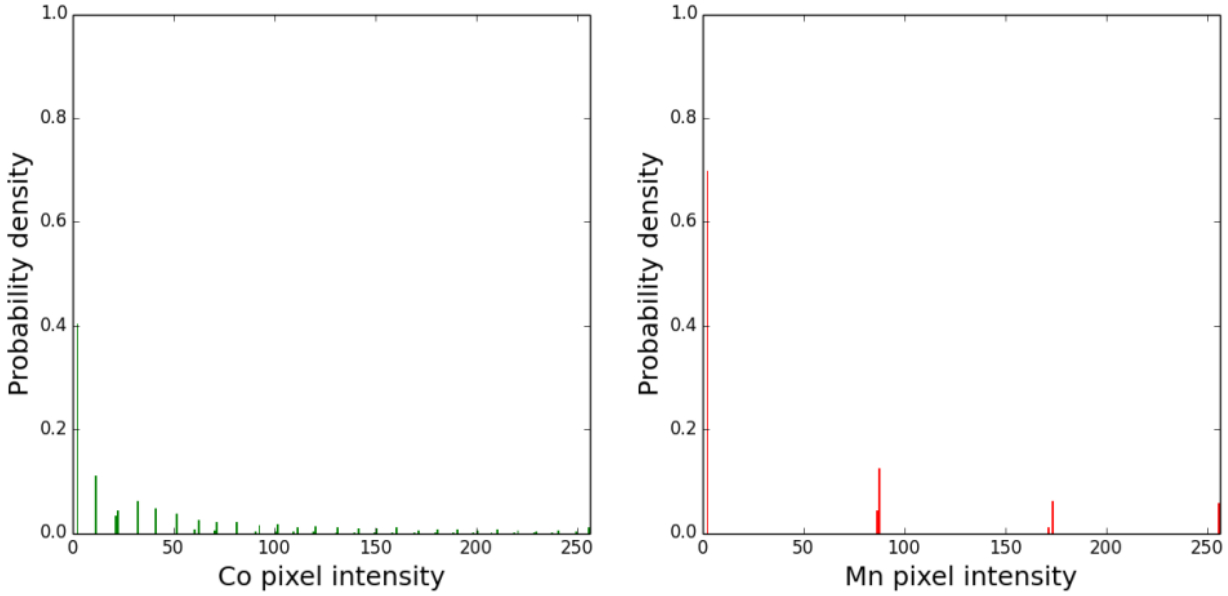

Figure S2.3 Illustration of color depth in elemental map channels. (A) elemental map of Co-Mn catalyst (Mn/Co = 0.1); (B) Co (left) and Mn (right) element channel color coded by X-ray count intensity; and (C) histograms of pixel intensity for Co (left) and Mn (right). The Co channel has 46 distinct levels of intensity, whereas the Mn channel has only 6 levels.

High Co and Mn CD **High Co and Low Mn CD** **Low Co and Mn CD**

A)

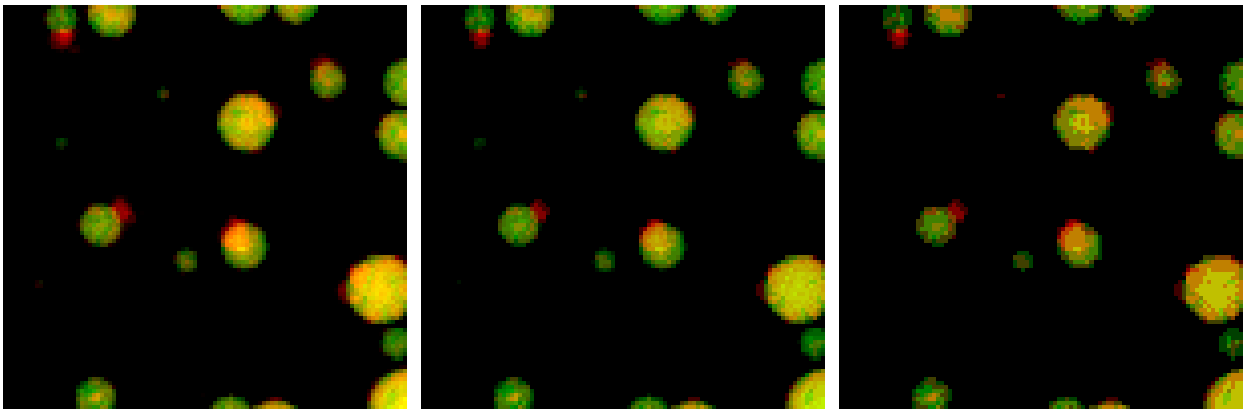

Lower color depth had the appearance of there being fewer distinct colors in the simulated elemental maps. The original images consisted of pixel intensities covering all integer values between 0 and 255. To generate images with lower color depth, a list of new pixel intensities was generated where certain values in the original range were skipped. Lower color depth corresponded to more skipped values. Pixels of the same intensity in the original images were grouped into sets, and assigned new intensity values. The value reassigned to each set was the value in the list of new pixel intensities closest to the original intensity of each set. This operation, which could be applied separately to the Co and Mn channels, had the effect of consolidating the number of colors in the map into a smaller number.

B)

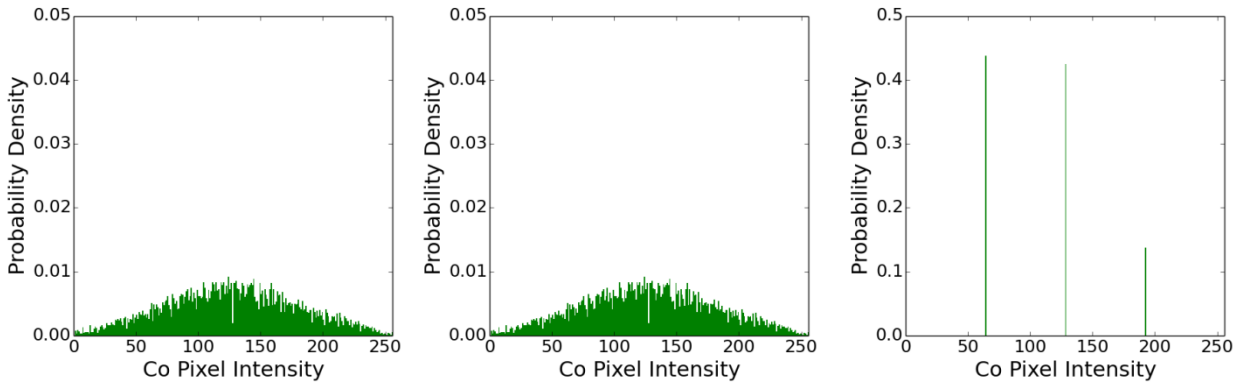

The histograms of pixel intensities for the Co channel show the number of pixel intensities in the Co channel. The original images (left column) had 255 distinct levels of intensity. In the middle column, the Co channel was left unmodified. In the right column, the reduction in color depth was applied.

C)

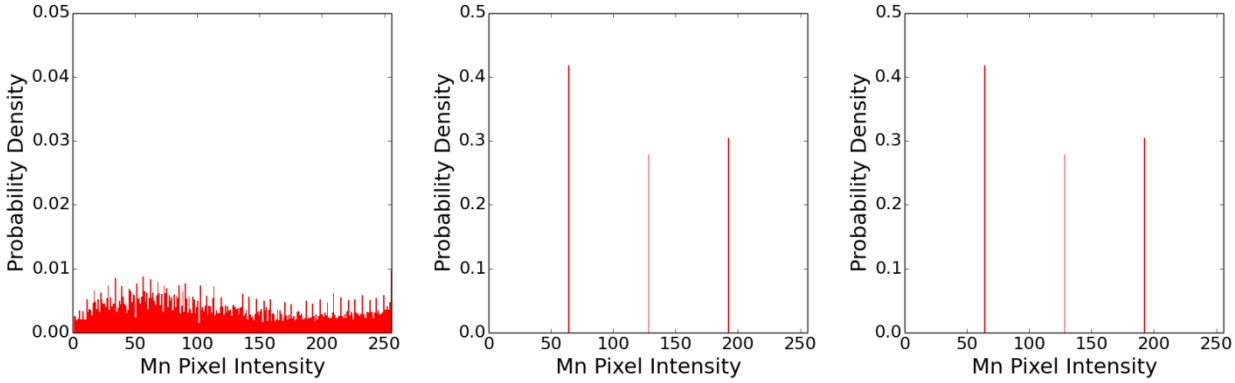

The histograms of pixel intensities for the Mn channel show the number of pixel intensities in the Mn channel. The original images (left column) had 255 distinct levels of intensity. In the middle column, the Mn channel was reduced to only 3 non-zero levels of intensities. In the right column, the same reduction in color depth was applied.

D)

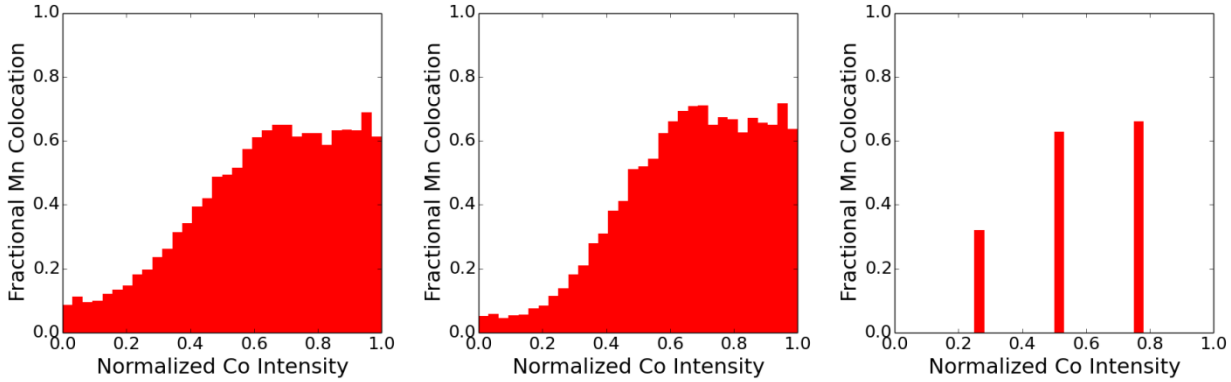

The reduction in color depth of the Mn channel had minimal effect on the colocation plot (middle column), but once the color depth of the Co channel was lowered, the structure of the plot was severely degraded (right column). An insufficient number of distinct Co pixel intensities caused there to be missing datapoints in the colocation plot.

E)

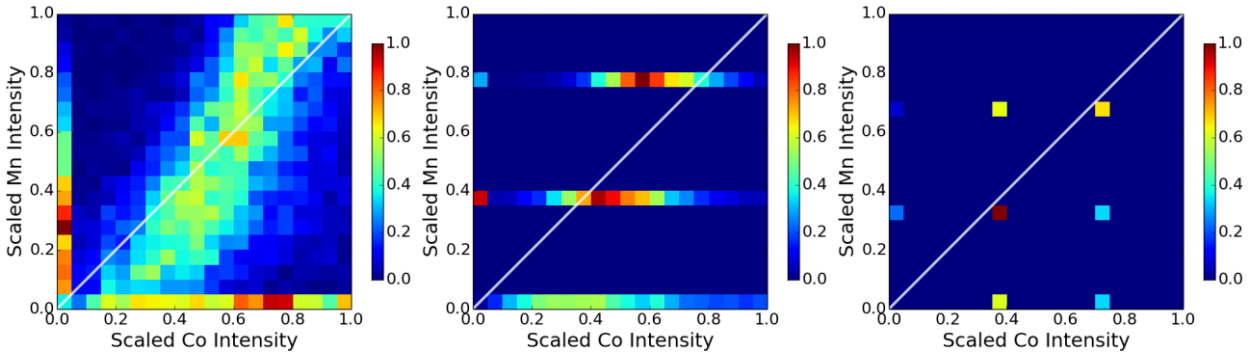

Lower color depth in either channel made the two-dimensional histograms of Co and Mn pixel intensities unrecognizable compared to the original. This was seen in the case of lowered Mn color depth as missing datapoints vertical axis (middle column). With the color depth lowered on both channels, there were missing data along both axes (right column).

F)

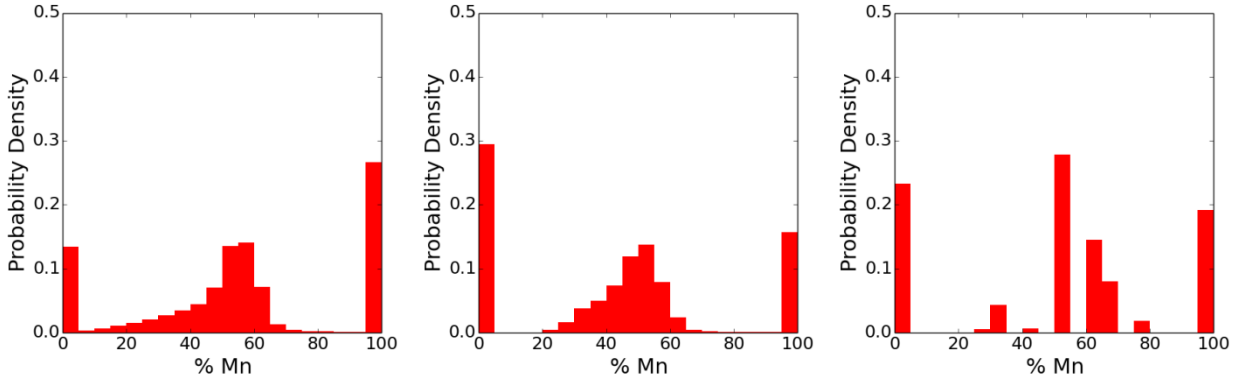

Lower color depth had the effect of making the composition calculation at each pixel coarser in resolution. With a reduction in the Mn color depth, inaccuracies developed in the composition histogram even though the shape of the distribution remained the same (middle column). With the addition of lowered Co color depth, certain ratios of Mn to Co intensities became forbidden so as to create gaps in the histogram (right column).

Figure S2.4 Effect of lower color depth range on correlation analysis methods. Simulated images for surface associated Mn and Co nanoparticles were rendered with reduced color depths for the Co and Mn channels. Left column: High Co and Mn color depth; middle column: high Co and low Mn color depth; right column: low Co and Mn color depth. (A) Representative simulated images of surface associated Co-Mn nanoparticles with varying color depth; (B) histograms of Co pixel intensities; (C) histograms of Mn pixel intensities; (D) colocation probability plots; (E) 2D histograms; and (F) composition histograms.

Table S2.2 Correlation metrics for different levels of color depth in the Co and Mn channels. The adjustments to the color depths correspond to those in Figure S2.4. An explanation of each correlation metric is given in the experimental methods section.

Sample	PCC	SRCC	MCC	SSIM
Surf. Assoc., high CD	0.75	0.73	0.81	0.78
Surf. Assoc., low Mn CD	0.74	0.69	0.85	0.76
Surf. Assoc., low CD	0.72	0.71	0.83	0.77

No Noise (SNR = ∞) **Low Noise (SNR = 4.5)** **High Noise (SNR = 1.3)**

A)

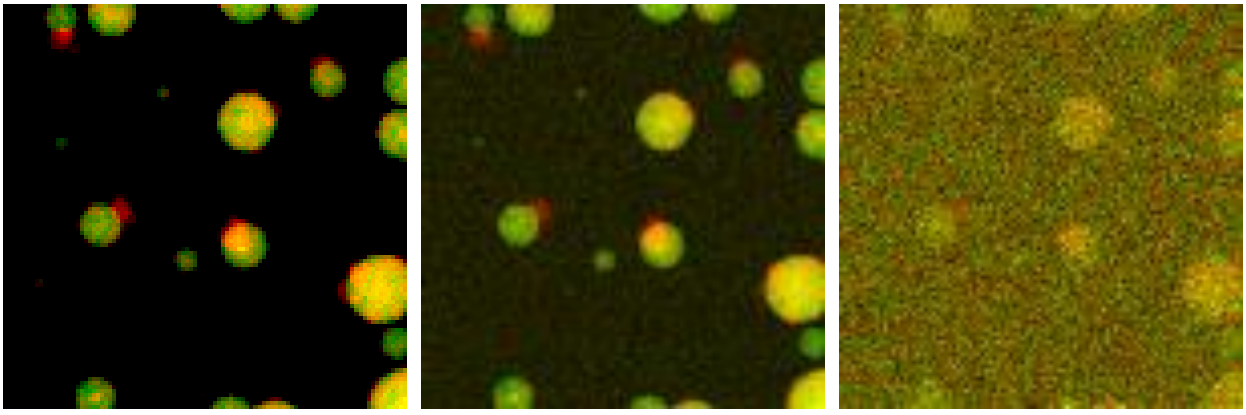

White Gaussian noise was added to the original simulated images using a multiplier to adjust the intensity of the noise relative to the signal from the nanoparticles. The presence of noise became evident first in the pixels where no nanoparticles were located (middle column). As noise levels increased (right column), the intensity of the pixels became more characteristic of a white noise pattern.

B)

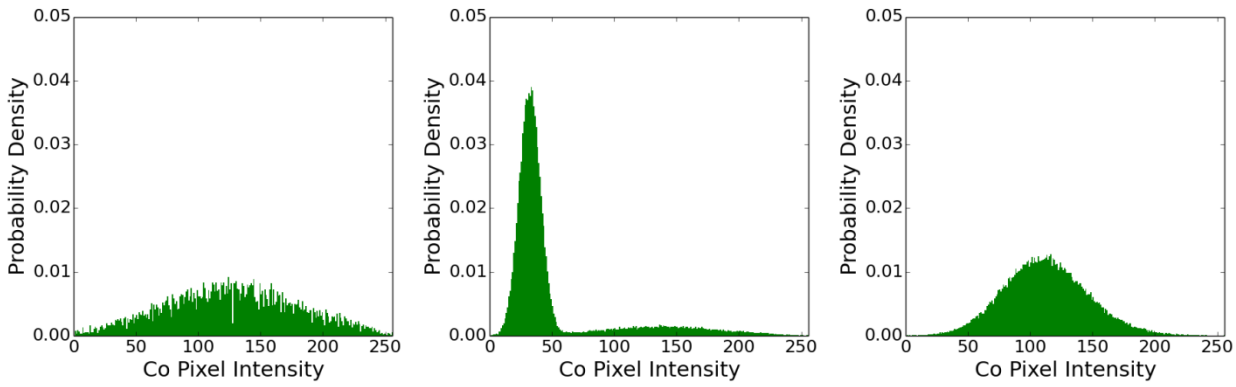

C)

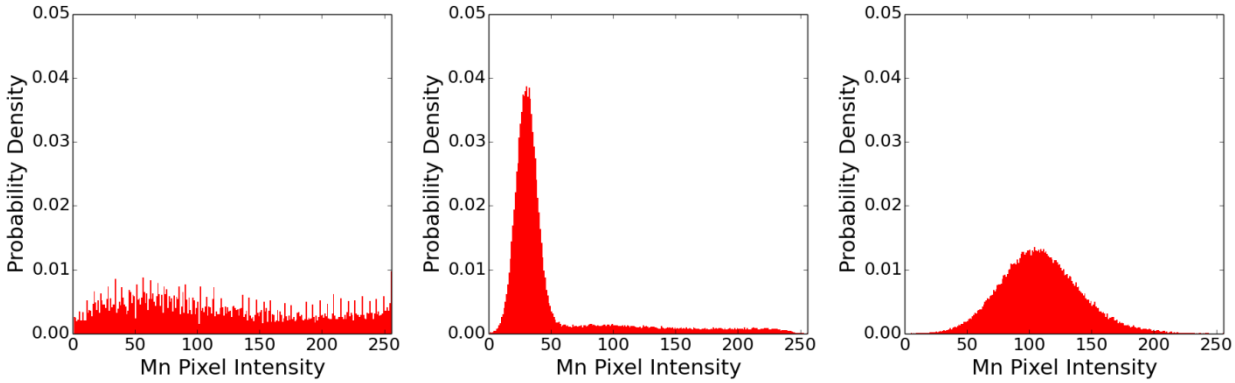

The presence of low intensity noise (SRN = 4.5, middle column) resulted in large Gaussian peaks in the low intensity regions of the Co and Mn pixel intensity histograms (middle column). These peaks were due to pixels having randomized, low intensity Co and Mn values that were black in the original simulated image in the left column. As the intensity of the noise increased (right column), the Gaussian peaks shifted to higher intensities and masked the signal from the simulated sample.

D)

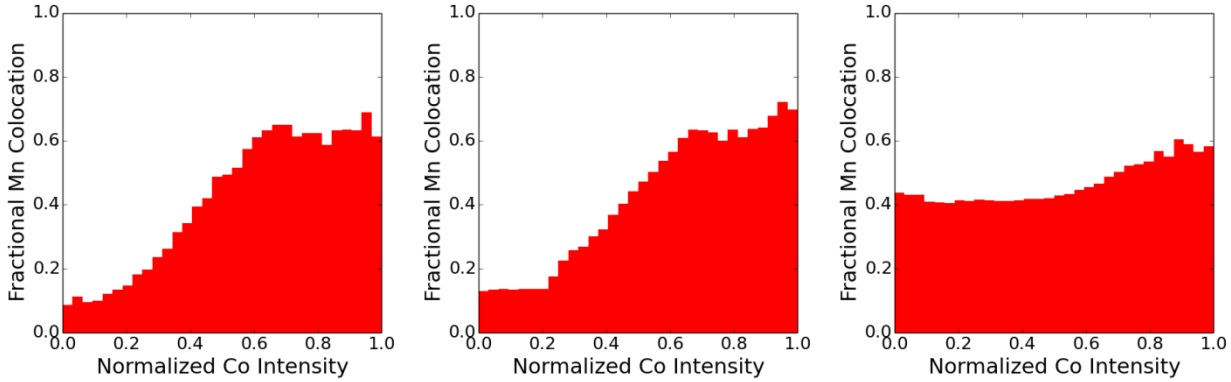

The consequence of this addition of noise in the colocation plots was the appearance of a flat region at low Co intensities that moved rightward as the noise level increased. In the middle column, the low level noise overpowered the signal from the sample up to a normalized Co intensity of about 0.2. In the right column, this extended to a normalized Co intensity of about 0.7.

E)

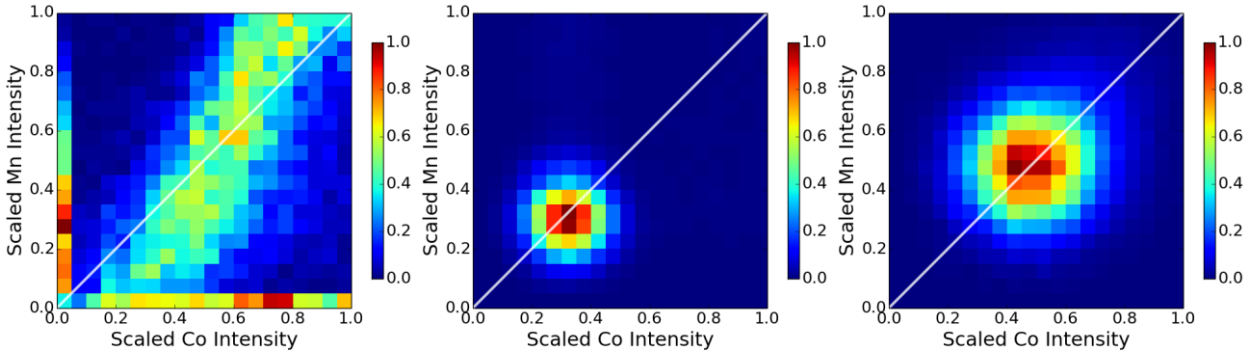

The presence of noise caused a circular region of intensity to appear in the two-dimensional histograms of Co and Mn pixel intensities. This was consistent with all contributing to the histogram. In the middle column, the region was shifted toward the origin because of the contribution of higher intensity pixels from the simulated sample. The mean intensity in all three histograms was always 0.5 in both channels after the scaling operation.

F)

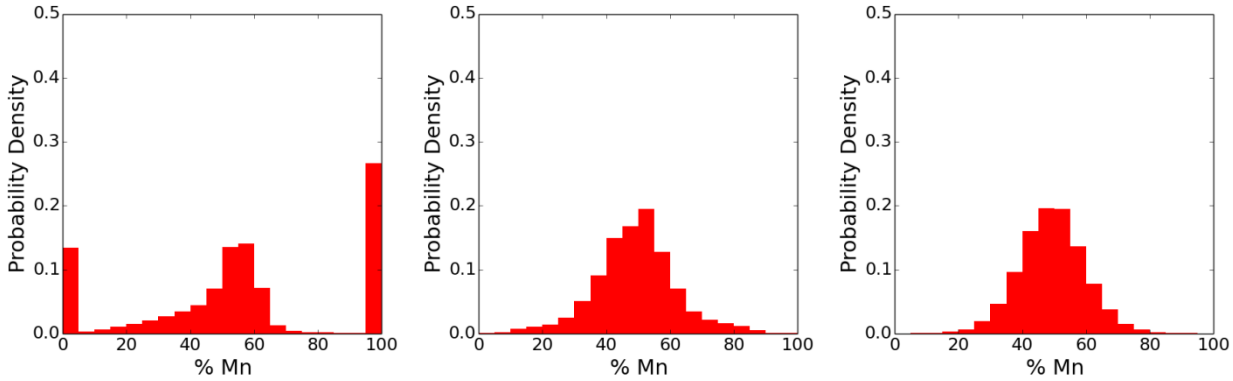

Upon introducing low-level noise, the histogram immediately showed a Gaussian peak without any evidence of the segregation found in the original plot. In practice, an intensity-based cutoff for contributing pixels would need to be used to remove pixels where no nanoparticles were located. As noise levels increase, this correction would become increasing difficult to apply.

Figure S2.5 Effect of additive Gaussian white noise on correlation analysis methods. Simulated images for surface associated Mn and Co nanoparticles were rendered with various signal to noise ratios for the Co and Mn channels. The signal to noise ratios were calculated by dividing the mean intensity of the pixels where the nanoparticles were located by the standard deviation of the intensities of the pixels where the nanoparticles were not located. Left column: No noise; middle column: low noise (SNR = 4.5); right column: high noise (SNR = 1.3). (A) Representative simulated images of surface associated Co-Mn nanoparticles with various levels of noise; (B) histograms of Co pixel intensities; (C) histograms of Mn pixel intensities; (D) colocation probability plots; (E) 2D histograms; and (F) composition histograms.

Table S2.3 Correlation metrics for different levels of noise in the Co and Mn channels. The adjustments to the noise correspond to those in Figure S2.5. An explanation of each correlation metric is given in the experimental methods section.

Sample	PCC	SRCC	MCC	SSIM
Surf. Assoc., SNR = ∞	0.75	0.73	0.81	0.78
Surf. Assoc., SNR = 4.5	0.74	0.31	1.00	0.61
Surf. Assoc., SNR = 1.3	0.16	0.12	1.00	0.58

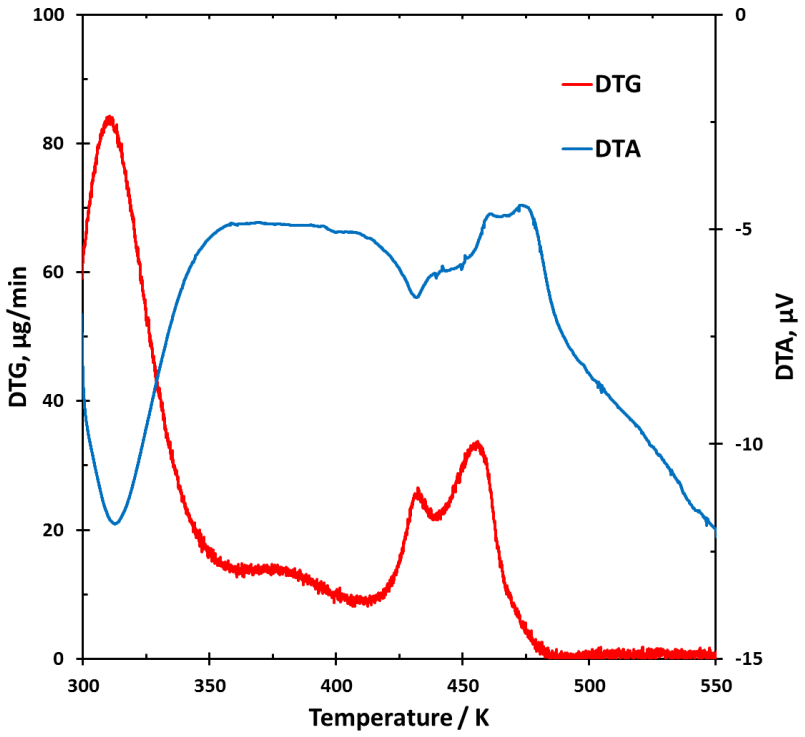

Figure S2.6 Thermogravimetric analysis of Co-Mn (Mn/Co = 0.1) catalyst precursor decomposition. The measurements were done in air with a 2 K/min temperature ramp rate. The plotted signals are the time derivative of sample weight (DTG) and the voltage applied to the heating element (DTA), which is a proxy for the rate of heat transfer to and from the sample. The signal from 300 to 400 K corresponds to removal of water. The peak that starts at 423 K corresponds to the decomposition of $Co(NO_3)_2$, which was shown to be endothermic by the DTA data. The decomposition of $Mn(CH_3COO)_2$ followed at about 450 K, which was an exothermic process.

References

1. Liu, Z.; Ling, X.Y.; Su, X.; Lee, J. Y. *J. Phys. Chem. B* **2004**, *108*, 8234-8240.

2. Wolf, A.; Schüth, F. *Appl. Catal., A* **2002**, *226*, 1-13.

3. Ritschel, M.; Leonhardt, A.; Elefant, D.; Oswald, S.; Büchner, B. *J. Phys. Chem. C* **2007**, *111*, 8414-8417.

4. Klenov, D.O.; Stemmer, S. *Ultramicroscopy* **2006**, *106*, 889-901.

5. Parish, C.M.; Brewer, L.N. *Microsc. Microanal.* **2010**, *16*, 259-272.

6. Zhu, T.; Flytzani-Stephanopoulos, M. *Appl. Catal., A* **2001**, *208*, 403-417.

7. Sayah, E.; Brouri, D.; Wu, Y.; Musi, A.; Da Costa, P.; Massiani, P. *Appl. Catal., A* **2011**, *406*, 94-101.

8. Xiao, K.; Bao, Z.; Qi, X.; Wang, X.; Zhong, L.; Fang, K.; Lin, M.; Sun, Y. *J. Mol. Catal. A-Chem.* **2013**, *378*, 319-325.

9. Dunn, K.W.; Kamocka, M.M.; McDonald, J.H. *Am. J. Physiol-Cell Ph.* **2001**, *300*, C723-C742.

10. Grogger, W.; Hofer, F.; Kothleitner, G. *Micron* **1998**, *29*, 43-51.

11. Grogger, W.; Krishnan, K.M. *IEEE T. Magn.* **2001**, *37*, 1465-1467.

12. Parish, C.M.; Brewer, L.N. *Ultramicroscopy* **2010**, *110*, 134-143.

13. Jacobs, G.; Das, T.K.; Zhang, Y.; Li, J.; Racoillet, G.; Davis, B.H. *Appl. Catal., A* **2002**, *233*, 263-281.

14. Khodakov, A.Y.; Chu, W.; Fongarland, P. *Chem. Rev.* **2007**, *107*, 1692-1744.

15. Bezemer, G.; Radstake, P.; Falke, U.; Oosterbeek, H.; Kuipers, H.; van Dillen, A.; de Jong, K. *J. Catal.* **2006**, *237*, 152-161.

16. Dinse, A.; Aigner, M.; Ulbrich, M.; Johnson, G.R.; Bell, A.T. *J. Catal.* **2012**, *288*, 104-114.

17. Sachtler, W.M.H.; Shriver, D.F.; Hollenberg, W.B.; Lang, A.F. *J. Catal.* **1985**, *92*, 429-431.

18. Boffa, A.B.; Lin, C.; Bell, A.T.; Somorjai, G.A. *Catal. Lett.* **1994**, *27*, 243-249.

19. Morales, F.; Grandjean, D.; de Groot, F.M.F.; Stephan, O.; Weckhuysen, B.M. *Phys. Chem. Chem. Phys.* **2005**, *7*, 568-572.

20. Datye, A.K.; Xu, Q.; Kharas, K.C.; McCarty, J.M. *Catal. Today* **2006**, *111*, 59-67.

21. Werner, S.; Johnson, G.R. *QMapTools*, version 1.0.0; University of California, Berkeley: Berkeley, CA, 2014.

22. Pearson, K. *Philos. Trans. R. Soc. Lond. Ser. A* **1896**, *187*, 253-318.

23. Goshtasby, A.A. *Image Registration: Principles, Tools, and Methods*; Springer: London, 2012.

24. Myers, J.L.; Well, A.D.; Lorch, R.F., Jr. *Research Design and Statistical Analysis*, 3rd ed.; Routledge: New York, 2010.

25. Manders, E.M.M.; Verbeek, F.J.; Aten, J.A. *J. Microsc.* **1993**, *169*, 375-382.

26. Wang, Z.; Bovik, A.C.; Sheikh, H.R.; Simoncelli, E.P. *IEEE T. Image Process.* **2004**, *13*, 600-612.

27. Cliff, G.; Lorimer, G.W. *J. Microsc.* **1975**, *103*, 203-207.

28. Yankin, A.M.; Balakirev, V.F. *Inorg. Mater.* **2002**, *38*, 391-402.

29. Williams, D.B.; Carter, C.B. *Transmission Electron Mircroscopy*; Springer: New York, 2009.

30. Pennycook, S.J.; Nellist, P.D. *Scanning Transmission Electron Microscopy*; Springer: New York, 2011.

31. Jones, I.P.; *Chemical Microanalysis Using Electron Beams*; Institute of Materials: London, 1992.

32. Kisielowski, C.; Specht, P.; Gygax, S. M.; Barton, B.; Calderon, H.A.; Kang, J.H.; Cieslinski, R. *Micron* **2015**, 68, 186-193.

33. Tyson, W.R.; Miller, W.A. *Surf. Sci.* **1977**, 62, 267-276.

34. Zhu, Y.; Ramasse, Q.M.; Brorson, M.; Moses, P.G.; Hansen, L.P.; Kisielowski C.F.; Helveg, S. *Angew. Chem. Int. Edit.* **2014**, *53*, 10723-10727.

35. Tan, B.J.; Klabunde, K.J.; Sherwood, P.M.A. *J. Am. Chem. Soc.* **1991**, *113*, 855-861.

36. Wang, Z.-J.; Yan, Z.; Liu, C.-J.; Goodman, D.W. *ChemCatChem* **2011**, *3*, 551-559.

37. Prieto, G.; Martínez, A.; Concepción, P.; Moreno-Tost, R. *J. Catal.* **2009**, *266*, 129-144.

38. Girardon, J.-S.; Lermontov, A.S.; Gengembre, L.; Chernavskii, P.A.; Griboval-Constant, A.; Khodakov, A.Y. *J. Catal.* **2005**, *230*, 339-352.

39. Mohamed, M.A.; Halway, S.A. *Thermochim. Atca.* **1994**, *242*, 173-186.

40. Pieck, C.L.; Parera, J.M. *Stud. Surf. Sci. Catal.* **1997**, *111*, 433-438.

41. Blanchard, G.; Charcosset, H.; Chenebaux, M.T.; Primet, M. *Stud. Surf. Sci. Catal.* **1979**, *3*, 197-210.

42. den Breejen, J.P.; Frey, A.M.; Yang, J.; Holmen, A.; van Schooneveld, M.M.; de Groot, F.M.F.; Stephan, O.; Bitter, J.H.; de Jong, K.P. *Top. Catal.* **2011**, 54, 768-777.

43. Feltes, T.E.; Zhao, Y.; Klie, R.F.; Meyer, R.J.; Regalbuto, J.R. *ChemCatChem* **2010**, 2, 1065-1068.

44. Bezemer, G.L.; Bitter, J.H.; Kuipers, H.P.; Oosterbeek, H.; Holewijn, J.E.; Xu, X. ; Kapteijn, F.; van Dillen, A.J.; de Jong, K.P. *J. Am. Chem. Soc.* **2006**, 128, 3956-3964.

Chapter 3

An Investigation into the Effects of Mn-Promotion on the Activity and Selectivity of Co/SiO_2 for Fischer-Tropsch Synthesis: Evidence for Enhanced CO Adsorption and Dissociation

Abstract

Mn is an effective promoter for improving the activity and selectivity of Co-based Fischer-Tropsch synthesis (FTS) catalysts, but the mechanism by which this promoter functions is poorly understood. The work reported here was aimed at defining the manner in which Mn interacts with Co and determining how these interactions affect the activity and selectivity of Co. Detailed measurements are reported for the kinetics of FTS as a function of Mn/Co ratio, temperature, and reactant partial pressure. These data are described by a single, two-parameter rate expression. Mn-promotion was found to increase both the apparent rate constant for CO consumption and the CO adsorption constant. Further evidence for enhanced CO adsorption and dissociation was obtained from measurements of temperature-programmed desorption of CO and CO disproportionation rates, respectively. Quantitative analysis of elemental maps obtained by STEM-EDS revealed that the promoter accumulates preferentially on the surface of Co nanoparticles at low Mn loadings, resulting in a rapid onset of improvements in the product selectivity as the Mn loading increases. For catalysts prepared with loadings higher than Mn/Co = 0.1, the additional Mn accumulates in the form of nanometer-scale particles of MnO on the support. In situ IR spectra of adsorbed CO show that Mn promotion increases the abundance of adsorbed CO with weakened C–O bonds. It is proposed that the cleavage of the C–O bond is promoted through Lewis acid-base interactions between the Mn^{2+} cations located at the edges of MnO islands covering the Co nanoparticles and the O atom of CO adsorbates adjacent to the MnO islands. The observed decrease in selectivity to CH_4 and the increased selectivity to C_{5+} products with increasing Mn/Co ratio are attributed to a decrease in the ratio of adsorbed H to CO on the surface of the supported Co nanoparticles.

3.1 Introduction

Of the elements that are known to improve the Fischer-Tropsch synthesis (FTS) product selectivity when added as promoters to Co-based catalysts, Mn is among the most frequently discussed in the literature. Early studies concerning the use of MnO as a support material demonstrated that this support decreased the selectivity to methane and increased the olefin to paraffin ratio of light hydrocarbons in comparison to more conventional supports.[1-3] Within the past decade, research by Morales et al.[4-6] and de Jong et al.[7,8] have explored the use of Mn as a promoter for Co FTS catalysts. In addition to observing selectivity and rate enhancements in the promoted catalysts, these researchers found evidence that Mn forms a variety of oxide structures, parts of which were associated with the active Co phase. Feltes et al. studied the effect of catalyst preparation methods using impregnation solvent pH to guide the selective deposition of the Mn promoter onto the Co[9,10]. This strategy was reported to yield promotion

effects comparable to those obtained by dry impregnation but requiring smaller quantities of the Mn promoter owing to the improved contact between the Mn and the Co. Relatedly, we have carried out quantitative analyses of elemental maps of catalysts prepared by different pretreatment conditions and demonstrated that Mn promotion effects are correlated with the degree of spatial colocation between Mn and Co.[11] Dinse et al. have examined the activity and selectivity of silica-supported Co-Mn catalysts and rationalized the promotion effects in terms of H availability and CO coverage.[12] More recently, several studies have reported measurements of the CO hydrogenation kinetics over Mn-promoted Co FTS catalysts, but these investigations have not provided much additional insight into how Mn participates in the FTS chemistry.[13-15]

While the effects of Mn promotion on FTS over Co are now well-documented, the manner by which Mn promotion affects catalyst activity and selectivity remains speculative and untested. The most frequently cited explanation for the effects of metal oxide promoters on CO hydrogenation over Rh assumes that CO adsorbed at the metal-metal oxide interface can interact both with the metal through the C atom and with a cation of the oxide through the O atom.[16,17] The promoter is hypothesized to serve as a Lewis acid that weakens the C–O bond and facilitates its dissociation. By analogy to Rh catalysts, a direct interaction between the CO and promoter cation at interface sites has been invoked as an explanation for the promotion effects seen in Co-based catalysts.[18] Nevertheless, there have been no attempts to determine whether the CO adsorption at the metal-promoter interface results in stronger CO adsorption and enhanced dissociation of the C–O bond other than by inferences drawn from observations of the effects of oxide promoters on FTS kinetics. We report here an investigation of Mn-promoted Co-based FTS catalysts that combines detailed catalyst characterization data with measurements of the reaction kinetics. These efforts were undertaken with the aim of clarifying the chemical basis for the observed effects of Mn promotion of Co. In addition to determining how Mn affects the FTS rate law, connections were established between catalyst structure and performance that explain the dependence of FTS activity and selectivity on promoter loading. These findings strongly favor the hypothesis that active sites near the Co-MnO interface are responsible for the improved activity and C_{5+} selectivity of Mn-promoted Co catalysts.

3.2 Experimental Methods

3.2.1 Catalyst Synthesis

The catalysts were prepared by incipient wetness impregnation of silica powder (PQ Corp., CS-2129). Typically, 2.5 mL of an aqueous solution of $Co(NO_3)_2{\cdot}6H_2O$ and $Mn(CH_3COO)_2{\cdot}4H_2O$ (Sigma-Aldrich, 99.999% purity) was added dropwise to 1 g of the support material, which was constantly stirred. The quantities of dissolved Co and Mn precursors in the solution were adjusted so as to keep the loading of Co fixed at 10 wt% with respect to the sum of silica and cobalt and to achieve various molar ratios of Mn to Co between 0 and 0.5. After the catalyst precursor was dried overnight at room temperature, the dried material was passed through a 60 mesh sieve and the retained particles were discarded. The silica containing the metal precursor was then heated to 673 K in H_2 as described in the Supporting Information in order to decompose the precursors and reduce the Co. The catalyst was then cooled to room

temperature and passivated. Catalyst compositions were verified by ICP-EOS (Galbraith Laboratories).

3.2.2 TEM Imaging

The passivated catalysts were prepared for analysis by electron microscopy by drop-casting ethanol suspensions of ground catalyst onto lacey carbon Cu TEM grids (Ted Pella). A complete description of this protocol is given in the Supporting Information. To determine size distributions of the catalyst nanoparticles, bright-field transmission electron microscopy (BF-TEM) images of the Co-Mn catalysts were acquired at the Electron Microscopy Lab at the University of California, Berkeley using an FEI Tecnai T12 electron microscope. Imaging was done with an accelerating voltage of 120 kV. Nanoparticle size distributions for each sample were determined using samples of approximately 300 nanoparticles. The surface mean diameter for the nanoparticles in a catalyst sample was calculated according to eq. 3.1, where n_i is the number of particles with diameter d_i in a nanoparticle sample of size N:[19]

$$\bar{d} = \frac{\sum_i^N n_i d_i^3}{\sum_i^N n_i d_i^2} \tag{3.1}$$

3.2.3 STEM-EDS Elemental Mapping

Elemental maps of the catalysts were acquired using scanning transmission electron microscopy with energy dispersive spectroscopy (STEM-EDS). The samples for this analysis were prepared using the same protocol as was used for preparing the BF-TEM samples. STEM-EDS measurements were done using an FEI Titan electron microscope at the National Center for Electron Microscopy at the Lawrence Berkeley National Laboratory. The microscope was operated with an accelerating voltage of 200 kV and fluorescent X-rays were collected using a Bruker four-segment silicon drift detector. A complete description of the spectrometer settings and analysis methods is given in the Supporting Information.

3.2.4 Chemisorption and Titration Characterizations

Static H_2 chemisorption measurements were acquired using a Micromeritics 3Flex surface characterization analyzer. Passivated catalyst samples were placed inside a quartz sample tube and heated to 673 K in H_2 to reduce the Co. After flowing H_2 at this temperature for 2 h, the sample tubes were evacuated and cooled to 373 K, which was the temperature at which the adsorption isotherms were measured. This choice of adsorption temperature was based on the published finding that 373 K leads to maximum H_2 uptake for Co supported on silica.[20] The total H_2 uptake from the isotherm was used to calculate the number of metallic Co atoms exposed on the surface of the nanoparticles for a given catalyst sample. On the basis of published results for similar catalysts, it was assumed that the H/Co adsorption stoichiometry was 1/1.[20,21]

O_2 titration was used to assess the extent of Co reduction in the reduced catalyst samples. These measurements were done by monitoring the effluent of a quartz glass reactor with an MKS Spectra Minilab quadrupole mass spectrometer. Catalyst samples were loaded into the reactor and reduced at 673 K in H_2. Using a sample loop, pulses of air were injected into the reactor using He as a carrier gas. The O_2 peaks in the mass spectrometry data were integrated to obtain O_2 uptake values due to oxidation of the Co and Mn. On the basis of data from X-ray absorption

spectroscopy, it was assumed that the Co initially consisted of a mixture of Co(0) and CoO that was oxidized completely to Co_3O_4 and that all the Mn underwent an oxidation from MnO to MnO_2. Accordingly, the extent of reduction of the Co was calculated as shown in eq. 3.2:

$$frac.\,Co\ reduced = \frac{2(O_2\ molar\ uptake) - (moles\ Mn) - \left(\frac{4}{3} - 1\right)(moles\ Co)}{moles\ Co} \qquad (3.2)$$

CO temperature-programmed desorption experiments were conducted using a Micromeritics AutoChem II 2920 instrument. Passivated catalyst samples were reduced at 4 K/min to 673 K in H_2 with a 2 h hold at 673 K and then cooled to 213 K with He flowing through the system. After the temperature had stabilized, CO pulses were introduced to the sample using He as the carrier gas while the flow downstream of the sample was monitored using the instrument thermal conductivity detector. The CO pulses continued until the sample showed no further CO uptake, and the sample tube was flushed for 10 min to clear any CO in the gas phase. The temperature was then ramped to 1073 K at 10 K/min to desorb chemisorbed CO from the catalyst surface.

3.2.5 X-ray Diffraction

Powder X-ray diffraction (XRD) patterns were collected at beamline 11-BM at the Advanced Photon Source synchrotron at Argonne National Laboratory using the mail-in service. Passivated catalyst samples were reduced at 673 K in H_2 and then rapidly cooled to 298 K under flowing He. Under an inert atmosphere, the reduced samples were then transferred into Kapton sample tubes and sealed with epoxy. XRD measurements were conducted at ambient temperature using 28.3 keV X-rays over a 2θ range of 0.5 to 50° with a 0.001° step size.

3.2.6 In Situ X-ray Absorption Spectroscopy

X-ray absorption spectroscopy (XAS) data were collected in transmission mode at beamline 10-BM at the Advanced Photon Source synchrotron at Argonne National Laboratory.[22] Sample pellets were placed inside a quartz in situ cell that was surrounded by a tube furnace for temperature control and connected to a gas manifold for controlling gas composition and flow. Further details concerning the beamline setup and sample preparation methods can be found in the Supporting Information. X-ray absorption near-edge structure (XANES) spectra of the passivated Co-Mn catalysts with Mn/Co atomic ratios of 0, 0.01, 0.05, 0.1, and 0.5 were measured at both the Mn K-edge (6,539 eV) and Co K-edge (7,709 eV) under ambient conditions. Reduction of the catalysts was then performed by heating the in situ cell at 4 K/min in flowing H_2 to 673 K, holding at 673 K for 2 h, and cooling to 493 K. XANES spectra of the reduced catalysts were then collected at 493 K at both the Mn and Co K-edges. Syngas (H_2/CO 2/1) was then introduced into the in situ cell, and the catalyst was aged for 6 h, which was determined by reaction experiments to be adequate for reaching a stable activity. XANES spectra of the catalysts under reaction conditions were then measured at both the Mn and Co K-edges. The XAS data were analyzed using the Demeter software family, which uses IFEFFIT internally.[23,24]

3.2.7 Infrared Spectroscopy

Fourier transform infrared spectroscopy (FTIR) measurements were made using a Thermo Scientific Nicolet 6700 FTIR spectrometer equipped with an MCT detector cooled by liquid N_2.

Spectra were collected in transmission mode from 1200 to 4000 cm^{-1} with 1 cm^{-1} resolution. For each spectrum, 32 scans were averaged to improve the signal to noise ratio. The catalyst samples were pressed into thin wafers and loaded into an in situ cell containing CaF_2 windows. The cell was flushed for 30 min with He flowing at 100 ml/min before reducing the catalyst at 623 K for 2 h under a 100 mL/min flow of H_2. Then, the cell was flushed with He and cooled to 493 K before introducing adsorbates. IR spectra were collected at different partial pressures of CO by adjusting the volumetric flow rates of CO and He diluent. Measurements in syngas were made with a 2/1 ratio of H_2 to CO. All spectra were collected at 493 K and 1 bar of total pressure, and for a given condition, measurements were repeated until the spectra demonstrated negligible changes over 30 min. Control measurements were also made using blank silica and Mn on silica samples.

3.2.8 Catalytic Reactions

The activity and selectivity of the catalysts for Fischer-Tropsch synthesis were determined by carrying out reactions in a fixed-bed reactor. An Agilent 6890N gas chromatograph was used to measure the hydrocarbons, H_2, Ar, and CO in the reactor effluent. A full description of the reactor apparatus is provided in the Supporting Information. In a typical experiment, 50 mg of catalyst and 150 mg of calcined silica diluent were mixed together and loaded into the reactor. The catalyst was then heated at 4 K/min to 673 K with flowing H_2. After it was held at 673 K for 2 h, the reactor was cooled at 10 K/min to the desired reaction temperature with flushing He. The composition of the gas feed to the reactor was gradually switched from He to syngas over 10 min to prevent runaway conditions. For most experiments, the syngas had a 2/1 ratio of H_2 (Praxair, 99.999% purity) to CO (Praxair, 99.9% purity) with 7% Ar (Praxair, 99.999% purity) included as an internal standard. Variations of reactant partial pressures were done by blending separate streams of H_2 and CO using calibrated mass flow controllers. The CO supply contained 20% Ar as an internal standard. The CO conversion was adjusted by changing the total gas flow rate through the reactor.

Before conducting the reaction experiments, the background activity of the empty reactor, silica support, and Mn deposited onto silica were all verified to be negligible. It was determined that internal transport limitations could be neglected under all operating conditions by means of the Weisz-Prater criterion.[25] The absence of external transport limitations was verified by a series of exploratory measurements at different space velocities and bed loadings. As reported previously, conversion of the CO to hydrocarbons was calculated both on the basis of CO consumed and on the basis of hydrocarbons produced.[12] The former allowed determination of the C_{5+} product selectivity without measuring the individual components of the liquid product fraction, while the latter proved to be more accurate at low conversions and under operating conditions that led to negligible wax production. Under all tested reaction conditions, the production of CO_2 was not detected and the selectivity toward oxygenates on a molar carbon basis was less than 1%.

Catalytic activity for the Boudouard reaction, in which CO dissociates to form surface carbon and CO_2, was assessed by reducing a given catalyst in a quartz reactor and exposing the catalyst to CO at 493 K and 1 bar for a fixed time ranging from 15 min to 3 h. The reactor was then flushed with He at 673 K for 15 min to remove the gas phase and molecularly adsorbed CO. The yield of dissociated CO was then determined by flushing the reactor with H_2 and monitoring

the reactor effluent for methane using an MKS Minilab mass spectrometer. A makeup flow of He with a 1% Ar internal standard was present during the methanation to account for any changes in volumetric flow.

3. Results

3.3.1 Microscopy

To assess the size distributions of the Co nanoparticles within the catalysts, TEM images were acquired for each catalyst sample. Representative TEM images for the unpromoted, low Mn loading (Mn/Co = 0.1), and high Mn loading (Mn/Co = 0.5) catalysts are shown in Figure 3.1. For all levels of Mn loading, the nanoparticles were approximately spherical in shape and had particle sizes ranging from about 5 to 20 nm. The surface mean diameters, presented in Table 3.1, were close to 10 nm for all loadings; however, the standard deviation of the particle size distributions increased with higher Mn loadings. Elemental maps obtained via STEM-EDS were necessary for discriminating between Co and Mn in the catalyst samples. Figure 3.2 contains representative elemental maps for Mn/Co atomic ratios of 0, 0.01, 0.05, 0.1, and 0.5. In these images, the colors red, green, and blue correspond to Mn, Co, and Si, respectively. The relative pixel intensities of the Co and Mn channels were scaled according to the total X-ray counts for each channel. A notable feature of the samples with Mn/Co atomic ratios of 0.01 and 0.05 was the absence of Mn-rich agglomerates. At a loading of Mn/Co = 0.1, the presence of Mn became apparent in the weighted elemental map, but there remained no evidence for separate, Mn-rich particles comparable in size to the Co nanoparticles. Only at a high loading of Mn/Co = 0.5 was there visual evidence for Mn-rich particles with diameters greater than several nanometers.

The compositions of individual nanoparticles were determined by selecting circular regions around a Co nanoparticle and any adjacent Mn in the STEM-EDS elemental maps. The X-ray counts for Co and Mn in each quantification region were totaled and converted to a Mn/Co atomic ratio. This process was repeated for over 100 nanoparticles in each sample to generate nanoparticle composition statistics for all Mn loadings, which are reported in Table 3.1. The average nanoparticle composition was almost identical to the bulk composition for the Mn/Co = 0.01 catalyst, but catalysts with higher promoter loadings exhibited average nanoparticle compositions substantially lower than the corresponding bulk compositions. Figure 3.3 shows histograms of the nanoparticle compositions and illustrates the broadening of the composition distribution with higher Mn loading. The shapes of the histograms are more evident in Figure S3.1 of the Supporting Information in which the horizontal axes were rescaled to cover six standard deviations in the Mn/Co ratio. From these data, it is apparent that the distributions are modeled well by Gaussian functions, and that the distributions have similar relative standard deviations. These values were between 20 and 25% for the catalysts with bulk Mn/Co ratios of 0.05, 0.1, and 0.5. The Mn/Co = 0.01 catalyst had a higher relative standard deviation of 36%, but this may have been due to the contribution of instrument error near the detection limit of STEM-EDS.

3.3.2 H_2 Chemisorption and O_2 Titration

The results from the static chemisorption experiments with H_2 are presented in Table 3.2. These data demonstrate that the total exposed surface area of the metallic Co nanoparticles decreased monotonically as the Mn loading increased. For the unpromoted catalyst, the mean particle size and dispersion determined by H_2 uptake were 12 nm and 8%, respectively, which are in good agreement with the values determined by TEM imaging of 11 nm and 9%. However, the H_2 uptake of the catalyst prepared with Mn/Co = 0.5 was about 1 order of magnitude less than that of the unpromoted catalyst, suggesting blockage of the Co surface by Mn species. Control samples of the silica support with and without Mn showed no evidence for H_2 chemisorption, which implies that all observed H_2 uptake was due to adsorption onto the surface of Co nanoparticles unless spillover from the Co onto the MnO_x were to occur. Although we cannot rule out the occurrence of spillover from the H_2 uptake data alone, this phenomenon seems unlikely given that the stoichiometric ratio of H to linearly adsorbed CO determined by CO TPD was about 1/1 for all Mn loadings.

O_2 uptake values from the O_2 titration experiments are also provided in Table 3.2. These data were used to calculate the extent of Co reduction as a function of Mn loading. These calculations account for pre-existing CoO and the co-oxidation of the promoter, which are often neglected in the literature and, if not corrected for, can lead to substantial overestimation of the Co extent of reduction at high Mn loadings. The oxidation states of the Mn and Co before and after the O_2 titrations were inferred from the XANES measurements and published phase diagrams.[26] The data reveal that the fraction of Co in a metallic state following reduction decreased as the Mn loading increased, which is consistent with reports of Mn impeding Co reduction.[27]

3.3.3 X-ray Absorption Spectroscopy

Figure 3.4 displays the X-ray absorption spectra near the Co K-edge for the passivated and reduced Co-Mn catalysts at various Mn loadings. The edge energies of the passivated catalysts were located between those of the CoO and Co_3O_4 standards. Additionally, linear combination fits of the XANES regions were most consistent with the assumption that Co present in the passivated catalysts is a mixture of CoO and Co_3O_4. After reduction in H_2 at 673 K, the catalysts exhibited a shift in the Co edge toward lower energies closer to the edge of the Co(0) standard. The magnitude of this shift decreased with increasing Mn loading, suggesting that the addition of Mn impeded the reduction of Co to the metallic state. Linear combination fitting of the Co XANES spectra revealed that the Co species in the reduced catalysts were a mixture of Co(0) and CoO. This analysis was also used to estimate the extent of Co reduction. The results given in Table 3.3 indicate that the extent of Co reduction decreased with increasing Mn loading. Although the estimates of Co reduction from XANES are lower than the values determined by oxygen titration, the same influence of Mn loading on the Co reduction was observed by both methods. After exposure to syngas at 493 K for 6 h, the Co edges exhibited a small shift to lower energies, which suggests that several percent of the Co continued to reduce during the first 6 h of time on stream.

XANES data were collected at the Mn K-edge for all catalysts in a passivated state under ambient conditions and after reduction in H_2 at 673 K for 2 h. The reduced catalysts were then

exposed to syngas at 493 K for 6 h and measured again. Data collected at the Mn K-edge for a representative catalyst with Mn/Co = 0.1 are presented in Figure 3.5. The XANES spectra shown in Figure 3.5A indicate that the edge energy for the passivated catalyst was located between those of the Mn_2O_3 and MnO_2 standards. After reduction, the catalyst Mn edge energy shifted to an energy close to that of the MnO standard. Exposing the catalyst to syngas did not cause major changes to the spectrum. A more quantitative approach for determining apparent oxidation states from XANES data involves constructing a linear relationship between oxidation state and the centroid of the 1s to 3d pre-edge feature.[28] This method, depicted in Figure 3.5B for the catalyst with Mn/Co = 0.1, yielded the same conclusions as inspecting the edge energy shifts. The apparent Mn oxidation states for catalysts with various promoter loadings in the passivated, reduced, and reacted states are given in Table 3.3. All loadings showed evidence of Mn being in an oxidized state between 2+ and 3+ after the reduction pretreatment step.

3.3.4 CO Temperature-Programmed Desorption

Several CO desorption peaks were observed in the TPD data for the Mn-promoted and unpromoted catalysts (Figure S3.2A of the Supporting Information). In each run, a peak near 265 K was observed, which was attributed to physisorbed CO because the same peak appeared in control measurements done with the silica support. No additional CO desorption peaks were measured on either the silica or Mn deposited on silica control samples. The first chemisorbed CO peak on the catalyst samples occurred near 450 K, and higher temperature desorption peaks were observed between 600 and 700 K. Using the Redhead model[29] with an assumed pre-exponential factor of 10^{13} s^{-1}, the lower temperature peaks were calculated to correspond to CO with desorption activation energies near 95 kJ/mol and the more strongly bound CO had energies between 130 and 150 kJ/mol. The binding energy for the low-temperature peak falls within the range of energies reported by multiple studies for linearly adsorbed CO at high CO surface coverages.[30,31] The literature on CO adsorbed at bridge sites is less extensive, but surface studies by Lahtinen et al. and Carlsson et al. assert that these species desorbed at temperatures lower than those for the linearly adsorbed CO.[32,33] This suggests that the signal from bridged CO species may be superimposed with the tail of the physisorbed CO peak. The high-temperature desorption peaks have similarities to those observed by Bridge et al. of CO desorption from Co surfaces incorporating oxygen.[34] Accordingly, it is proposed that these higher temperature peaks correspond to CO adsorbed in contact with the MnO promoter. Any peaks that may have occurred at temperatures higher than 723 K would have been obscured by dehydroxylation of the silica support.

As shown in Figure 3.6, the temperature of the first chemisorbed CO desorption peak maximum increased with higher Mn loading for Mn/Co atomic ratios between 0 and 0.1. A catalyst prepared with Mn/Co = 0.25 had a CO desorption temperature similar to that of the Mn/Co = 0.1 catalyst. Notably, these data points followed the same pattern as product selectivity: sensitivity to the promoter at low Mn loadings followed by a plateau for Mn/Co > 0.1. TPD experiments using catalysts prepared with Mn/Co ratios higher than 0.25 were not possible owing to the lower chemisorption uptake per gram of catalyst of these materials. The area ratios of the higher to lower temperature CO desorption peaks increased linearly with Mn loading (Figure S3.2B of the Supporting Information), which indicates that a greater fraction of the CO

adsorbate pool was bound in the more strongly interacting sites when Mn was present. By a comparison of the CO desorption peak areas to the H_2 static chemisorption uptakes, it was determined that the 1/1 CO/Co adsorption stoichiometry for sites corresponding to the lower temperature desorption peak was not affected by the presence of Mn. Overall, these findings are consistent with CO adsorbing both onto Co metal sites weakly affected by the Mn promoter and onto sites in direct contact with the MnO promoter and support.

3.3.5 Infrared Spectroscopy

In situ IR spectra revealed the presence of CO adsorbates on the catalyst surface when the reduced catalysts were exposed to CO at reaction temperature. In Figure 3.7A, the IR spectrum for the unpromoted catalyst shows a peak at 2077 cm^{-1} corresponding to linearly adsorbed CO.[35] The Mn promoter induced a shift of this peak toward lower wavenumbers such that the Mn/Co = 0.5 catalyst had a peak position of 2068 cm^{-1}. Additionally, there was a slight increase in the peak area of bridging CO (1880–1890 cm^{-1}) relative to the linearly adsorbed CO as Mn loading increased. The most prominent difference between the spectra was the appearance of a peak at 1588 cm^{-1} when Mn was present.

Red-shifting of the linearly adsorbed CO peak is consistent with stronger binding of CO to the Co surface, but the connection of this feature to Mn remains ambiguous. In their study of ambient-temperature CO adsorption onto Mn-promoted Co catalysts, Morales et al. identified two linearly adsorbed CO peaks at 2030 and 2050 cm^{-1} and found that higher Mn loading increased the prominence of the lower wavenumber peak relative to the higher wavenumber peak.[6] Since the withdrawal of electron density from the Co by the MnO promoter would decrease π^* back-donation to the adsorbed CO and hence increase the carbonyl stretching frequency, structural effects were suggested as the probable explanation for the differences between the unpromoted and Mn-promoted catalyst IR spectra. den Breejen et al. reported the same result for related catalysts.[8] The catalyst preparation methods used in both studies resulted in smaller Co particles as the Mn loading increased, which means that the findings could be a simple consequence of size effects. Smaller particles would also explain the lower intensity of bridging CO observed in the Mn-promoted catalysts, which differs from the findings of the present study. Catalysts with particle sizes close to 10 nm were used in the present study, which rules out Mn affecting CO adsorption through particle size effects alone, but it remains possible that the MnO promoter led to the formation of surface structures, possibly involving undercoordinated Co atoms, that resulted in CO adsorbates with comparatively weakened carbonyl bonds.

The peak at 1588 cm^{-1} is similar to those found in the IR spectra of various FTS catalysts, which have been attributed most frequently to carbonate species interacting with the catalyst support.[35,36] The absence of the peak from the unpromoted catalyst suggests that these species were adsorbates interacting with the MnO and not the silica. Moreover, these adsorbates were not observed in the spectra for the control sample consisting of MnO supported on silica, suggesting that an interface between Co and MnO_x was necessary for the appearance of these species. Given that the peak area scaled linearly with Mn loading, it is likely that this peak incorporated spillover of the CO onto the MnO rather than exclusively species at the Co-promoter interface. Nevertheless, this peak has a frequency similar to those of carbonyl complexes in which

separate metal atoms are bound to both the C and O atoms of the CO.[37] By analogy to these complexes, it has been proposed for various heterogeneous catalyst systems that adsorbed CO may bind simultaneously to the metal and an oxophilic component of the promoter through the C and O atoms, respectively.[38] With a vastly weakened carbonyl bond, such species would presumably undergo C–O dissociation much more readily than CO not at the interface with the metal oxide promoter.

To understand the relative reactivity of these species toward hydrogenation, IR spectra under transient conditions were collected for the catalyst prepared with Mn/Co = 0.1 as follows. The reduced catalyst was exposed to flowing CO at 493 K to saturate the catalyst surface with carbonyl adsorbates, and then the flow through the in situ cell was switched to H_2 to start the hydrogenation of the adsorbed species. It was observed that the linearly adsorbed CO, bridging CO, and the species giving rise to the peak at 1588 cm^{-1} disappeared on the same time scale in the presence of H_2 (Figure S3.3). Additionally, a peak centered at 1619 cm^{-1} remained after 1 h exposure to H_2. Although not identifiable in the steady-state spectra shown in Figure 3.7, this peak was present before the hydrogenation was started and its magnitude did not change significantly during the exposure to H_2. These results demonstrate that an inert carbonyl species associated with MnO_x forms on the promoted catalysts. However, there is also sufficient evidence to conclude that the IR peak at 1588 cm^{-1} is associated with a separate species that can undergo hydrogenation.

Flowing syngas over the reduced catalysts led to changes in the IR spectra as shown in Figure 3.7B. The copresence of H_2 broadened and red-shifted the peaks corresponding to linearly adsorbed CO. These shifts were 13 and 5 cm^{-1} for the unpromoted and Mn/Co = 0.5 catalysts, respectively. The red-shifting of the CO peak due to H_2 has been attributed to either repulsive interactions between coadsorbed CO and H[39] or the contribution of electron density from the H to the Co metal that can increase the extent of π^* back-donation to the CO.[40] The smaller magnitude of the shift in the Mn-promoted catalyst cannot be explained with certainty, but this effect may result from there being less H_2 adsorbed on the Mn-promoted catalysts. Interestingly, the intensity of the 1588 cm^{-1} peak relative to the linearly adsorbed CO peak for the Mn/Co = 0.5 catalyst did not change under syngas. However, a broad peak at the same frequency emerged in the spectrum for the unpromoted catalyst. Formate species have been suggested to form on FTS catalysts with vibrational frequencies between 1300 and 1600 cm^{-1},[35] which could account for this peak, but it cannot be determined whether the species exists on the Co metal or on the silica support. Peaks from C-H bonds (2855, 2927, and 2960 cm^{-1}) became visible when the catalyst was exposed to syngas. These peaks validate that hydrocarbons were forming on the catalyst surface during the measurements but did not reveal any differences between the promoted and unpromoted catalysts. No discernible signal for CO_2 or for alcohol -OH groups was observed, which is consistent with the absence of alcohols in the product distributions observed in experiments conducted with a packed-bed reactor.

3.3.6 Kinetics and Catalytic Performance

The dependencies of CO consumption rate on the partial pressures of H_2 and CO found for the unpromoted, low Mn loaded (Mn/Co = 0.1), and high Mn loaded (Mn/Co = 0.5) catalysts at 493 K and extrapolated to 0% CO conversion are displayed in Figure 3.8. With fixed CO partial

pressure, a linearly proportional relationship was found to exist between the rate and the partial pressure of H_2 for both catalysts (Figure 3.8A). Variation of the CO partial pressure with fixed H_2 partial pressure led to rate maxima being observed for both catalysts (Figure 3.8B). It was not possible to assign an unambiguous CO partial order dependence at CO partial pressures below which the rate maximum occurred owing to the narrow pressure range of this regime. However, at higher CO partial pressures beyond which the rate maximum occurred, the rate clearly exhibited a negative first-order dependence on CO partial pressure, which is consistent with inhibition due to molecularly adsorbed CO. These data for both catalysts are consistent with the most commonly used rate law for describing FTS kinetics on Co-based catalysts, given as eq. 3.3.[41] Here, $-r_{CO}$ is the rate of CO consumption, P_{CO} is the CO partial pressure, P_{H_2} is the H_2 partial pressure, the parameter a is an apparent rate constant, and the parameter b is the CO adsorption constant. Although this Langmuir-Hinshelwood-type expression has its origins in empirical fitting, this rate law can be derived mathematically starting from the assumption of CO dissociation following a hydrogen-assisted pathway.[42]

$$-r_{CO} = \frac{abP_{CO}P_{H_2}}{(1+bP_{CO})^2} \tag{3.3}$$

CO consumption rates as a function of pressure for catalysts prepared with various Mn loadings are presented in Figure 3.9. These data were collected at 493 K using a 2/1 H_2/CO syngas composition with extrapolation to 0% CO conversion. Figure 3.9A shows the data normalized by the weight loading of Co in each sample. Here, a Mn/Co atomic ratio of 0.01 increased the activity relative to that of the unpromoted catalyst by about 50%. Higher loadings of promoter decreased the rate such that the Mn/Co = 0.05 catalyst had a specific activity similar to that of the unpromoted catalyst and the Mn/Co = 0.5 catalyst was about a factor of 5 less active than the unpromoted catalyst. The turnover frequencies for CO consumption (Figure 3.9B) obtained by normalizing the specific activities by the number of Co atoms accessible to H_2 chemisorption, increased as the Mn/Co ratio increased. The one exception to this trend is the catalyst with Mn/Co = 0.5, which did not have the highest turnover frequency, but this could be an artifact of the high uncertainty of the H_2 uptake measurement for this catalyst.

All tested catalysts deactivated by about 30% within the first several hours of time on stream. After this initial deactivation, the activities were stable to within 10% over the course of the experiments, which lasted up to 1 week. Consequently, all reported data were collected after an initial 12 h aging period. Interestingly, no selectivity changes were detected within the aging period for any catalyst. This suggests that the deactivation involved a decrease in the number of active sites rather than an alteration to the intrinsic activity of the sites. Such a phenomenon would lead to the turnover frequencies reported in Figure 3.9B being underestimated because the H_2 uptake measurements were performed using catalyst that had not been exposed to syngas. However, the qualitative conclusions from these data should not be affected because the percent deactivations of all catalysts after aging were similar.

Nonlinear least-squares regression was used to obtain parameters for the rate law, and these are given in Table 3.4. The parameters a and b increased by factors of about 4 and 3, respectively, as the Mn/Co atomic ratio increased from 0 to 0.5. Kinetics data at various temperatures and pressures for each catalyst (Figures S3.4 and S3.5 of the Supporting

Information) were collected in an attempt to extract estimates of pre-exponential factors and energies from the parameters a and b. This procedure required simultaneously fitting four parameters, and owing to cumulative error and the coupling between a and b that occurs as the pressure increases, accurate estimates could not be obtained. However, at high pressures, molecularly adsorbed CO becomes the most abundant surface species, and the rate law simplifies to eq. 3.4 and an apparent rate constant equivalent to $\frac{a}{b}$ appears. The apparent pre-exponential factor and activation energy for this apparent rate constant calculated using kinetics data at 16 bar are reported in Table 3.4 as A_{app} and $E_{A,app}$, respectively. Parity plots showing the agreement between the experimental and predicted values are included in Figure S3.6 of the Supporting Information.

$$-r_{CO} = \frac{aP_{H_2}}{bP_{CO}} \tag{3.4}$$

The effect of Mn promotion on CO disproportionation via the Boudouard reaction was investigated by exposing reduced catalysts to CO at 493 K and 1 bar. Although the concentration of CO_2 in the reactor effluent was not high enough to be measured reliably by online mass spectrometry, carbon on the catalyst surface was quantified by clearing the catalyst surface of adsorbed CO and then flushing H_2 through the reactor at 493 K to produce methane. The m/z = 16 signal was attributed to methane and not atomic O because the m/z 15 signal, corresponding to CH_3 fragments, was proportional to the m/z 16 signal. Moreover, the m/z 16 signal was assumed to result from methanation of surface carbon rather than hydrogenation of undissociated CO because no increase in the m/z 18 signal, corresponding to water, was observed when flushing the reactor with H_2. Figure 3.10 shows the quantity of methanated carbon normalized by the number of surface Co metal atoms as a function of CO exposure time for catalysts with different Mn loadings. A sample of 5 wt% MnO on silica did not yield any measurable methane signal even after 24 h of CO exposure. As seen by the trend of increasing slope through the data points with higher Mn loading, the presence of Mn facilitated the CO disproportionation reaction. However, for all catalysts, the CO disproportionation rates were about 3 orders of magnitude lower than the FTS turnover frequencies.

Dinse et al. demonstrated that at atmospheric pressure silica-supported catalysts have lower methane and higher C_{5+} selectivities on promotion with a Mn/Co atomic ratio close to 0.1 and that higher Mn/Co ratios lead to no further improvements to the product selectivity.[12] However, the regime of Mn/Co ratios between 0 and 0.05 was not investigated in detail. In the present study, measurements of catalysts prepared by the same method but with lower loadings of promoter (Figure S3.7 of the Supporting Information) confirmed that Mn-induced improvements in the product selectivity reached a maximum at Mn/Co = 0.1. Moreover, this asymptotic trend of product selectivity as a function of Mn loading was confirmed to occur at high pressures (Figure 3.11). However, this optimal loading of Mn/Co = 0.1 should not be considered to be a universal optimum applicable for all catalyst synthesis methods. The extent to which an interface forms between the Co and MnO_x may vary depending on the materials and procedures used for catalyst preparation. This may account for the lack of an optimal promoter loading for silica-supported Co-Mn catalysts that were prepared using different pretreatment methods.[8]

The disparity between the product selectivities of the unpromoted and Mn-promoted catalysts decreased with increasing pressure. At 1 bar, the unpromoted catalyst had a methane selectivity close to 40%, whereas the catalyst for which Mn/Co = 0.1 had a methane selectivity of 20%. At 16 bar, this performance difference decreased to less than 5% as the product distribution shifted to higher molecular weights for all catalysts. Additional selectivity data at various temperatures and pressures is included in Figures S3.8, S3.9, and S3.10 of the Supporting Information.

3.4 Discussion

3.4.1 Effects of Mn Promotion on Co Particle Size and Structure

The TEM images of the catalysts show that the inclusion of Mn in the catalyst formulation does not affect the mean diameters of the nanoparticles significantly. Consequently, it is unlikely that the changes to catalyst activity and selectivity observed upon Mn promotion are attributable to particle size effects. Moreover, the surface mean diameters were all close to 10 nm, and multiple researchers have reported that the turnover frequency for FTS on Co becomes insensitive to particle size above 6-10 nm.[43-45] This reported phenomenon has been rationalized by the relative abundance of corner and edge sites to terrace sites as a function of particle size. The ratio of undercoordinated to terrace Co atoms reaches a plateau at about 6 nm, assuming cuboctohedral nanoparticle geometry.[46] Hence, it has been proposed that the terrace atoms are more active for FTS than the corner and edge atoms in a Co nanoparticle, and these undercoordinated sites possibly become poisoned by binding species too strongly.[47] More recently, theoretical investigations by van Santen et al. have posited that lower CO dissociation barriers exist for Co sites at step edges or on corrugated surfaces and that these sites may form in abundance only on nanoparticles above a certain size.[48,49] Prior studies on Co-Mn FTS catalysts have suggested that Mn can cause a decrease in the size of the Co nanoparticles formed relative to that of unpromoted Co.[6,9] These studies and our own previous work with Co-Mn catalysts reported that the size of Co nanoparticles decreases with increasing Mn content, on the basis of powder XRD line broadening measurements.[12] We note, however, that such measurements may not yield an accurate measure of nanoparticle size owing to Mn-induced crystal defects in the Co nanoparticles, which would increase the prevalence of particles composed of several smaller domains.

Phase diagrams for bulk Co-Mn alloys indicate that at 673 K, the temperature used in this study for catalyst reduction, a transition from the hexagonal close-packed (hcp) crystal structure to face-centered cubic (fcc) occurs in the region of low Mn/Co ratios where product selectivities are a strong function of promoter loading.[50] Consequently, the possibility that the promotion effects were caused by a Mn-induced transition from hcp to fcc structure needs to be considered. XRD measurements of reduced catalyst samples sealed in inert gas revealed the presence of diffraction peaks corresponding to hcp Co metal in the unpromoted and Mn-promoted catalysts (Figure S3.11 and Table S3.1 of the Supporting Information). No peaks exclusively attributable to fcc Co metal or Mn oxides were detected. An analysis of the Co K-edge EXAFS data was not able to distinguish between these two Co metal crystal structures. In addition to this lack of experimental evidence for a crystal structure transition, there is consensus in the literature that

runs counter to the hypothesis. It has been reported that the FTS turnover frequency of hcp Co nanoparticles is higher than that of fcc Co nanoparticles.[51,52] With regard to product selectivity, it is reported either that there is little difference in the product distribution for the two crystal structures or that fcc Co yields higher methane levels.[53,54] These findings lead to a prediction that a transition from the hcp to the fcc crystal structure would result in a decrease in site activity and possibly higher methane selectivity, which is contrary to what are the observed effects of Mn promotion.

3.4.2 Mn and Co Oxidation States

Co-Mn catalysts are invariably reported to have Mn in an oxidized state under FTS operating conditions. Studies by Tan et al. suggest that Mn forms MnO and Mn_2O_3 after catalyst reduction.[55,56] A series of in situ XAS studies of Mn-promoted, titania-supported Co catalysts by Morales et al. have shown that the promoter adopts a 2+ oxidation state and that there is an assortment of mixed oxides of Mn with the Co and Ti.[4,27,57] These experiments provide a basis for invoking Mn oxide in rationalizing the promotion effects, but the quantity of promoter relative to Co in the catalysts studied by Morales et al. exceeded the threshold described in the present study at which catalyst performance became insensitive to Mn loading. High loadings of promoter that lead to the formation of spectator Mn oxide particles and the plethora of other Mn-containing species could obscure the signal from the Mn that is responsible for promotion effects. The rapid improvement followed by a plateau in the product selectivities as a function of Mn loading seen in the present study suggest that the state in which Mn exists up to a Mn/Co atomic ratio of 0.1 is vital for the observed promotion effects, whereas the Mn that accumulates at higher loadings effectively does not participate in the catalysis.

One hypothesis that was considered to explain the trends in catalyst performance as a function of promoter loading was the possible formation of an alloy of metallic Mn with Co on the nanoparticle surface, which may occur at the low Mn loadings where selectivity is highly sensitive to promoter loading. Since the surface free energy of Mn metal is much lower than that of Co, the Mn would be expected to locate preferentially on the nanoparticle surfaces.[58] Furthermore, the Mn loading at which C_{5+} selectivity reaches a plateau is approximately equivalent to the amount necessary to form a monolayer on the nanoparticle surfaces (Mn/Co = 0.1). The saturation of the nanoparticle surfaces by Mn could explain why C_{5+} selectivity did not continue to improve beyond Mn/Co atomic ratios of 0.1. Although these trends are phenomenologically consistent, no evidence for metallic Mn was observed for the Co-Mn catalysts investigated in this study. XANES measurements at the Mn-edge revealed that a partial reduction of the Mn species occurred after reducing the catalysts in H_2 at 673 K. This is evident in both the shift of the Mn K-edge to lower energies upon reduction (Figure 3.5A) and the energy of the pre-edge features in the XANES spectra (Figure 3.5B). In the passivated catalyst, the apparent oxidation state of the Mn was closest to that of 4+ cations, and after reduction, the promoter formed species with a mixture of 2+ and 3+ cations. Consequently, Mn is likely present as an oxide for Mn/Co ratios below 0.1.

From the extents of reduction data, it is apparent that a portion of the Co in the unpromoted catalyst (~20%) remains unreduced, most likely as highly dispersed CoO or Co silicate. The presence of Mn also contributes to lower extents of Co reduction, suggesting that

the MnO_x overlayer may incorporate Co to form Co-Mn mixed metal oxides. The Mn/Co stoichiometry of this mixed oxide cannot be quantified readily because it is unknown whether the Mn oxide affects Co silicate formation or inhibits the reduction of the CoO nanoparticles without forming mixed-metal oxides. If a portion of the Mn is dispersed over the support along with Co, this could account for the lower extent of Co reduction without being detectable by XRD, chemisorption, or microscopy.

3.4.3 Spatial Distribution of Mn

The absence of large agglomerates of MnO in the STEM-EDS images of the catalysts with Mn/Co atomic ratios of less than 0.1 (Figs. 2A and 2B) demonstrates that the promoter is finely dispersed over the Co. For this regime, it is also noted that the mean of the nanoparticle composition histogram for each catalyst sample is very close to the bulk Mn/Co ratio, and no nanoparticles in these catalysts have a Mn/Co ratio more than 3 standard deviations away from the value for the bulk catalyst. It can also be shown through material balance arguments that segregation of Mn away from the Co nanoparticles would result in Mn/Co ratios determined from STEM-EDS maps having an average value lower than the bulk catalyst composition. Hence, the close match between the compositions of the bulk and the individual nanoparticles is a reliable indicator of a preferential spatial association between the Mn and Co. From these findings, it can be inferred that an energetic interaction between the two metals exists which balances the entropic tendency of the promoter to disperse across the support, for which there is more surface area than on the Co nanoparticles.

Previous studies of Mn-promoted Co catalysts have reported that Mn accumulates selectively onto the Co nanoparticles. In their studies of titania-supported Co-Mn catalysts, Morales et al. found that although migration of the promoter onto the support occurred during catalyst pretreatment, MnO nanoparticles were visibly adjacent to Co nanoparticles in STEM-EELS images of the catalyst.[5] Bezemer et al. have also reported contact between Co and Mn domains in reduced catalysts, although their catalysts were prepared with carbon nanofiber supports with which the MnO had limited chemical interaction.[7] More recent studies by Feltes et al.[9] and Zhao et al.[59] have explored how preparing titania-supported Co-Mn catalysts by the strong electrostatic adsorption (SEA) method could enhance the spatial association between the two elements. It remains unclear how readily these findings can be translated to silica supports, especially given that these researchers found the Mn spatial distribution relative to the Co to be highly sensitive to changes in catalyst preparation methods. Moreover, these studies did not attempt to quantify the relative amount of Mn associated with individual Co nanoparticles.

At Mn/Co = 0.01, the average nanoparticle Mn/Co ratio is 0.0096, which is 96% of the bulk catalyst composition. However, as Mn loading increases, the discrepancy between the average nanoparticle composition and the bulk composition grows. The average nanoparticle compositions for bulk Mn/Co ratios of 0.05, 0.1, and 0.5 are 92, 86, and 74% of their bulk compositions, respectively. This trend indicates that spatial segregation between the Co nanoparticles and the Mn begins to occur as the Mn loading increases. This does not mean that less Mn is present near the Co nanoparticle surfaces in the catalysts with higher promoter loadings, but rather that the additional Mn in these catalysts has a tendency to accumulate separately from the Co nanoparticle surfaces. Evidence for this phenomenon is clearly seen by

the presence of small Mn oxide particles in the elemental map of the catalyst for which Mn/Co = 0.5 (Figure 3.2D).

Evidence for coverage of the Co nanoparticle surfaces by Mn can be extracted from a comparison of the H_2 uptake data to the Co nanoparticle surface area determined from TEM particle size estimates and O_2 titration uptakes. Eq. 3.5 expresses how the fractional coverage of Co metal by Mn species was calculated using these data. To account for Co metal that was inaccessible to H_2 adsorption owing to nanoparticle contact with the silica support, the fraction of the nanoparticle surface covered by the silica support was included in the calculation via the parameter ε. Using the characterization data for the unpromoted catalyst, this correction factor was calculated according to eq. 3.6 and determined to be 15%. It is assumed that the fraction of the nanoparticle surface that was covered by silica is the same for each sample, which is a reasonable approximation given the similar Co nanoparticle sizes and shapes for all tested catalysts.

$$frac.\,Mn\ coverage = 1 - \frac{2(H_2\ uptake)}{(moles\ Co)(frac.\ Co\ reduced)(frac.\ dispersion)(1-\varepsilon)} \quad (3.5)$$

$$\varepsilon = 1 - \frac{2(H_2\ uptake)_{unpromoted}}{(moles\ Co)_{unpromoted}\,(frac.\ Co\ reduced)_{unpromoted}\,(frac.\ dispersion)_{unpromoted}} = 0.15 \quad (3.6)$$

The calculated percent surface coverages of Co nanoparticles by MnO reported in Table 3.2 indicate that higher Mn loadings lead to greater blockage of the Co metal surface. A Mn/Co atomic ratio of 0.01 results in only 9% of the surface becoming inaccessible, and at a loading of Mn/Co = 0.5, 83% of the nanoparticle surface is estimated to be covered by MnO species. At the loading where product selectivities become relatively insensitive to increasing Mn loading (Mn/Co = 0.1), the estimated Mn coverage is 48%. These data do not reveal information about the perimeter between the Co metal and the islands of Mn oxide that decorated the nanoparticle surfaces. However, the coverage estimates are notable, considering that Williams et al. have reported through simulations that the perimeter between a surface and randomly deposited islands is maximized at approximately half a monolayer coverage.[60] These trends between catalyst selectivity and surface coverage of the Mn over the Co nanoparticles support the hypothesis that Co active sites close to the interface with the Mn are responsible for the promotion effects.

3.4.4 Influence of Mn on the FTS Reaction and Surface Adsorbates

The agreement of the kinetics data with eq. 3.3 suggests that FTS on the unpromoted and Mn-promoted catalysts follow reaction mechanisms that yield the same rate law. Although it cannot be inferred whether the same species appear in the sequence of elementary steps leading from CO and H_2 to the hydrocarbon products, the results are consistent with FTS proceeding by the H-assisted dissociation of CO for all catalysts. The principal effect of the Mn promoter on the rate law is through the magnitude of the parameters a and b in eq. 3.3, which represent the apparent rate constant and CO adsorption constant, respectively. Increased values for these two parameters imply that Mn both facilitates the dissociation of CO, which is presumed to be the rate-determining step for FTS, and increases the extent to which adsorbed CO covers the Co metal surface. Qualitatively, the impact of Mn on the parameter a manifests in the generally

higher turnover frequencies for the promoted catalysts at a given pressure (Figure 3.9B); the decreased sensitivity of turnover frequency to pressure at higher Mn loadings (Figure 3.9B) illustrates the impact of Mn on the parameter b. The turnover frequencies increased nearly monotonically with Mn loading owing to the interplay between the apparent rate constant and the CO adsorption constant which appear in the numerator and denominator of the rate law given as eq. 3.4, respectively. As Mn loading increased, the apparent activation energy, $E_{A,app}$, at 16 bar increased substantially (Table 3.4). However, the activation energy of the rate-determining step could not be isolated because the apparent rate constant is a composite of several equilibrium constants along with the rate constant of the rate-determining step. These circumstances preclude making meaningful inferences from the trend in the pre-exponential factors. The increase in $E_{A,app}$ with Mn loading could be due to larger CO heats of adsorption on the promoted catalysts, a phenomenon that is corroborated by the CO TPD and IR spectroscopy data, but this hypothesis remains speculative without information about the magnitudes of the other contributions to $E_{A,app}$.

With regard to product composition, the higher CO adsorption constant and apparent rate constant due to Mn promotion are consistent with the lower methane and higher C_{5+} selectivity of the promoted catalysts. A greater coverage of CO on the catalyst surface would decrease H availability, assuming competitive adsorption takes place between H_2 and CO, so as to favor chain growth at the expense of methanation and hydrogenation termination reactions. Moreover, a decrease in the abundance of vacant sites may impede the rate of alkyl chain termination to olefins through β-hydride abstraction. These changes in surface adsorbate abundances are also consistent with increased olefin to paraffin product ratios observable in the C_2-C_4 product fraction.[12] Facilitated C–O bond cleavage would lead to the more frequent appearance of C_1 monomers that could scavenge H to further promote chain growth over termination. Mn promotion led to selectivity improvements at all operating conditions although there were diminishing returns at high pressure. In general, Mn promotion had an impact on the FTS selectivity analogous to operating at a higher partial pressure of CO, which follows from the larger CO adsorption constant of the Mn-promoted catalysts. The selectivities for all catalysts converged as the pressure increased, which is an expected outcome under the assumption that the differences in product selectivities among the catalysts were primarily due to differences in adsorbate coverages and that the CO surface coverage would reach saturation at high pressure. As previously reported,[12] higher C_{5+} selectivities are obtainable with these catalysts at higher CO conversions, which highlights the importance of secondary reactions and water for tuning the product distribution.

The effects of Mn promotion on the FTS kinetics and selectivity are consistent with enhanced CO adsorption being an important contributor, and evidence for this trait was also observed in the experimental data that probed the surface adsorbates. Larger heats of adsorption on the Mn-promoted catalysts were seen by the shift of the linearly adsorbed CO TPD peak to higher temperatures and the relative growth of the higher temperature CO desorption peak at higher promoter loadings. The clustering of the desorption profile into two distinct desorption temperatures is an expected feature if there were a mix of “unpromoted” Co sites far from the interface with the promoter and “promoted” Co sites at these interfaces, respectively. From these data, it can be deduced that the higher temperature desorption peak cannot be solely

from CO bound simultaneously to Co and MnO because the unpromoted catalyst also shows desorption at this temperature. Hence, the higher temperature peak may involve CO interacting with the silica support. Since the peak area scaled relatively linearly with the total quantity of the promoter, the peak also shows signs of spillover onto the MnO. It was observed during exploratory measurements that flowing undiluted syngas through a bed of freshly reduced catalyst resulted in a reactor temperature spike. This is expected if CO suddenly adsorbs onto the catalyst surface without sufficient time for the reactor to dissipate the released heat and remain isothermal. While this temperature spike was on the order of 10 K for the unpromoted catalyst, beds of the Mn-promoted catalyst with identical total Co metal surface area led to spikes of over 100 K. Although no quantitative reasoning can be done with these observations, these experimental curiosities are consistent with the CO heat of adsorption being higher when using Mn promoters.

The higher turnover frequencies and apparent rate constants on the promoted catalysts strongly suggest that CO dissociation is intrinsically faster on the Mn-promoted catalysts, but it must be conceded that changes to H_2 adsorption or the equilibrium constants of intermediate steps could be confounding variables. CO disproportionation rates provide a simpler view of the ease by which CO dissociates on these catalysts, and these rates were found to increase with increasing Mn loading. This finding suggests that direct CO dissociation is facilitated by the presence of the promoter, which is consistent with the hypothesis that the promoter acts as Lewis acid to help break apart CO. Interestingly, these observations are similar to those of Sachtler and Ichikawa, who found that the temperature at which CO_2 production was detectable decreased on Rh catalysts that had been promoted with Mn oxide.[16]

3.4.5 Origin of Mn Promotion Effects

Given the absence of MnO_x peaks in the XRD spectra and the lack of visible MnO particles at low promoter loadings (Mn/Co ≤ 0.1), MnO_x is presumed to be highly dispersed over the surface of the Co nanoparticles, resulting in a large fraction of the surface Co atoms being in contact with the promoter. The proposed formation of a finely dispersed MnO_x oxide overlayer for Mn/Co ratios less than 0.1 followed by the appearance of larger, segregated Mn oxide particles at higher loadings mirrors the onset of promotion effects at low promoter loadings followed by insensitivity of the product selectivity to promoter loading at Mn/Co ratios greater than 0.1. A conceptual framework for connecting these phenomena starts with the hypothesis that the interface between the Co metal and the Mn oxide promoter is responsible for the observed promotion effects.

As depicted in Scheme S3.1 of the Supporting Information, the Co metal sites can be partitioned into two ensembles: unpromoted sites that are not close to MnO (blue) and promoted sites that are adjacent to MnO (red). For a catalyst without any Mn promoter, the surface of a Co nanoparticle consists entirely of unpromoted sites, which is indicated by the blue shell surrounding the Co nanoparticle in Scheme S3.1A. A small loading of promoter (Scheme S3.1B, Mn/Co = 0.01) results in some surface Co atoms becoming adjacent to the MnO_x, as shown by the sites that are highlighted in red. Although these sites are proposed to have improved activity and selectivity, the unpromoted sites are much more abundant; thus, the catalyst with Mn/Co = 0.01 performs only marginally better than the unpromoted catalyst. As the promoter

loading increases, the ratio of promoted to unpromoted Co sites should increase, provided the promoter is well-distributed over the Co surface so as to form abundant interface sites. Accordingly, the product selectivity of the catalyst should improve with higher Mn loading until the fraction of sites that are promoted begins to dominate, as depicted in Schemes S3.2C and S3.2D. Once the fraction of sites that are promoted approaches unity (Mn/Co = 0.1), further addition of promoter to the catalyst would begin to cover up the Co surface such that CO consumption rates per gram of Co would decrease simply by there being fewer active sites. This is depicted in Scheme S3.1E for the catalyst with Mn/Co = 0.5, where larger patches of MnO_x cover the catalyst surface.

Previous studies have conjectured that the CO might bind to metal oxides through the O atom while being simultaneously bound to the metal through the C atom. In this scheme, the Mn would act as a Lewis acid drawing electron density from the O atom of the adsorbed CO (Scheme S3.2 of the Supporting Information). If CO dissociation occurred at such a site, the Mn may participate in a redox reaction whereby the Mn cation accepts the O atom and subsequently undergoes a reduction to regenerate the active site, which is a mechanism that has been proposed for rare-earth oxide promoters.[61] However, the first-order rate dependence on H_2 suggests that direct CO dissociation moderated by Mn^{2+} is not the primary pathway by which dissociation of the C–O bond occurs under typical FTS conditions. Further supporting this conclusion is the observation that the rate of C deposition via CO disproportionation in the absence of H_2 occurs at a rate that is 10^3 slower than the rate of FTS at the same temperature. Therefore, we propose that MnO dispersed on the surface of Co weakens the C–O bond, but C–O bond dissociation does not occur until the CO molecule is partially hydrogenated.

3.5 Conclusions

By combining detailed kinetics data with nanoscale characterization methods, new relationships between catalyst structure and performance can be determined for Mn-promoted Co-based FTS catalysts. The inclusion of Mn in the catalyst formulation did not lead to significant changes in Co particle size or crystal structure, which suggests that the role of the promoter was more than structural. Particle composition distributions obtained from quantitative STEM-EDS analysis revealed that there was evidence for the preferential spatial association between Mn and Co and that Mn was finely dispersed over the Co nanoparticles at low catalyst Mn/Co ratios. At higher promoter loadings, larger Mn oxide particles formed, which did not influence the catalysis apart from decreasing the fraction of exposed Co metal surface area. These structural trends closely matched the dependence of product selectivity on the catalyst Mn/Co ratio. Notably, the Mn loading yielding the least methane and the most C_{5+} was close to the half-monolayer promoter loading that would be expected to maximize the number of Co metal surface sites in contact with the MnO promoter. These findings were consistent with the hypothesis that sites along the interface between Co and Mn were responsible for the promotion effects.

Active sites with altered affinity for CO adsorption and FTS reactivity were observed in the Mn-promoted catalysts. Signs of enhanced CO adsorption on Mn-promoted catalysts were observed via the higher CO desorption temperatures and larger CO adsorption constant inferred

from fitting the FTS kinetics data. Additionally, in situ infrared spectroscopy experiments revealed that the Mn-promoted catalysts have a relative abundance of CO adsorbates with weakened carbonyl stretching energies in comparison to the unpromoted catalyst. Although the extent to which these adsorbates participate in the FTS reaction remains unclear, these characterization data are consistent with the larger FTS apparent rate constant and the higher CO disproportionation activity observed with the Mn-promoted catalysts. Higher CO surface coverage and facilitation of CO dissociation are also qualitatively consistent with a heavier hydrocarbon product distribution owing to less H availability for methanation and paraffin chain termination as well as more rapid C_1 monomer generation. Mn promotion led to higher FTS turnover frequencies although the cobalt-time yields decreased with increasing Mn loading because the promoter covered an increasing fraction of the Co surface. These findings demonstrate that an optimally promoted catalyst requires a Mn loading that balances the maximization of the interface between Co metal and MnO with the avoidance of blockage of the Co active sites by MnO.

Acknowledgements

This work was funded by the BP XC^2 program. Work at the Molecular Foundry was supported by the Office of Science, Office of Basic Energy Sciences, of the U.S. Department of Energy under Contract No. DE-AC02-05CH11231. This research used resources of the Advanced Photon Source, a U.S. Department of Energy (DOE) Office of Science User Facility operated for the DOE Office of Science by Argonne National Laboratory under Contract No. DE-AC02-06CH11357. We are grateful for discussions and TEM instrument training provided by Dr. Karen C. Bustillo. We acknowledge assistance with the XAS experiments from Dr. John Katsoudas, Dr. Joshua Wright, Dr. Andrew “Bean” Getsoian, Dr. Konstantinos Goulas, John Howell, Christopher Ho, and Alice Yeh. Furthermore, we acknowledge Dr. Konstantinos Goulas for collecting the CO TPD data presented in this work.

Table 3.1 Microscopy Characterization Data for the Co-Mn Catalysts.

Bulk Mn/Co Ratio	Avg. Particle Mn/Co Ratio[a]	d(Co)[b] (nm)	Dispersion[c] (%)
0.00	–	11 ± 2	9 ± 2
0.01	0.001 ± 0.003	10 ± 2	10 ± 2
0.05	0.05 ± 0.01	10 ± 3	10 ± 3
0.10	0.09 ± 0.02	10 ± 3	9 ± 3
0.50	0.4 ± 0.1	12 ± 4	8 ± 3

[a] The average Mn/Co ratios of the nanoparticles within the catalysts were determined by quantifying the composition of individual nanoparticles observed in the STEM-EDS elemental maps.
[b] Surface mean diameter.
[c] Particle dispersion was determined using TEM imaging assuming a site density of 14.6 Co atoms/nm^2 for supported nanoparticles.[20]

Table 3.2 H_2 Chemisorption and O_2 Titration Characterization Data for the Co-Mn Catalysts.

Bulk Mn/Co Ratio	H_2 Uptake[a] (mmol g^{-1})	O_2 Uptake[b] (mmol g^{-1})	Co(0)[c] (%)	MnO Coverage[d] (%)
0.00	0.051 ± 0.006	0.93 ± 0.04	79 ± 5	–
0.01	0.045 ± 0.005	0.89 ± 0.03	74 ± 4	10 ± 20
0.05	0.032 ± 0.007	0.91 ± 0.05	76 ± 6	40 ± 20
0.10	0.021 ± 0.005	0.86 ± 0.04	64 ± 5	50 ± 20
0.50	0.005 ± 0.002	1.01 ± 0.06	58 ± 8	80 ± 10

[a] H_2 uptake per gram catalyst was determined by static chemisorption.
[b] O_2 uptake per gram catalyst was measured by pulse titration of the reduced catalysts with 10% O_2 in He.
[c] Percentage of Co in the metallic state after pretreatment assuming that the catalysts initially consisted of a mixture of Co(0), CoO, and MnO and that full oxidation of Co and CoO to Co_3O_4 and Mn to MnO_2 occurred.
[d] Estimate of the percentage of the total metallic Co nanoparticle surface covered by MnO according to eq. 3.5 using the H_2 uptake data and TEM dispersions (Table 3.1).

Table 3.3 Oxidation State Data from XAS Measurements for the Co-Mn catalysts.[a]

Bulk Mn/Co Ratio	Co(0)[b] (%)	Passivated Mn Oxidation State	Reduced Mn Oxidation State	FTS Reaction Mn Oxidation State
0.00	55	–	–	–
0.01	51	4.2	2.5	2.0
0.05	43	4.5	2.2	2.0
0.10	28	4.2	2.2	2.5
0.50	23	4.5	2.7	2.7

[a] The apparent oxidation states of Mn were estimated by the position of the pre-edge feature in the Mn K-edge spectra.
[b] Percentage of Co in the metallic state after pretreatment estimated by linear combination fitting of the Co K-edge XANES spectra using the spectra of Co foil, CoO, and Co_3O_4 as references.

Table 3.4 Kinetic Parameters for the Co-Mn Catalysts.[a]

Bulk Mn/Co Ratio	*a* at 493 K ($bar^{-1}s^{-1}$)	*b* at 493 K (bar^{-1})	A_{app} ($bar^{-1}s^{-1}$)	$E_{A,app}$ (kJ/mol)
0.00	0.071	1.6	1×10^{8}	88
0.01	0.11	1.7	6×10^{9}	101
0.05	0.14	2.1	1×10^{13}	134
0.10	0.35	3.6	4×10^{15}	157
0.50	0.30	4.6	2×10^{16}	163

[a] The parameters *a* and *b* correspond to those in the rate law given as eq. 3.3. The apparent pre-exponential factors and activation energies were calculated using kinetics data at 16 bar where the rate law simplifies to eq. 3.4.

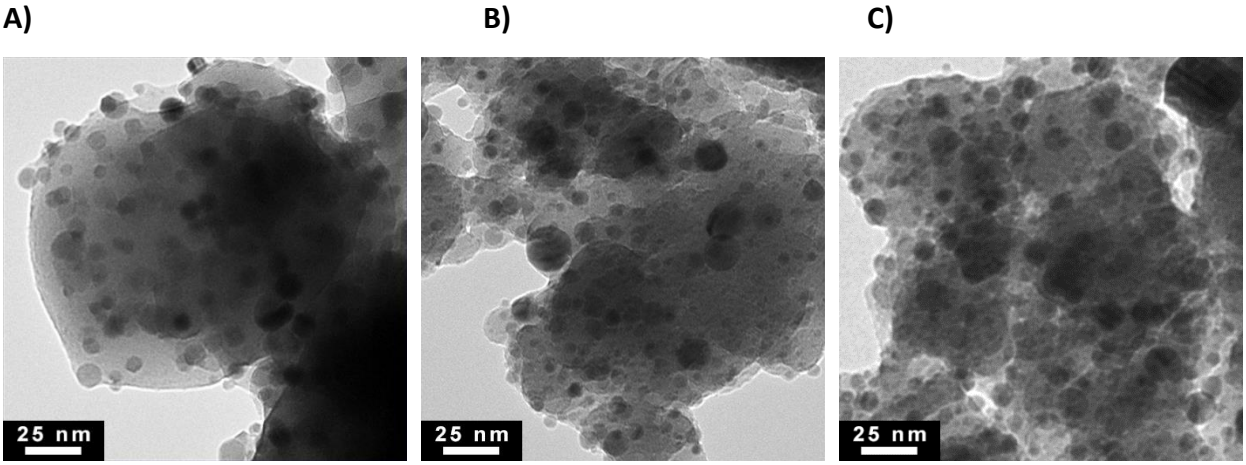

Figure 3.1 Bright-field TEM images of Co-Mn catalysts with bulk Mn/Co atomic ratios of (A) Mn/Co = 0, (B) Mn/Co = 0.1, and (C) Mn/Co = 0.5. For all catalysts, the Co loadings were 10 wt% relative to Co and silica. Particle size distribution statistics are reported in Table 3.1.

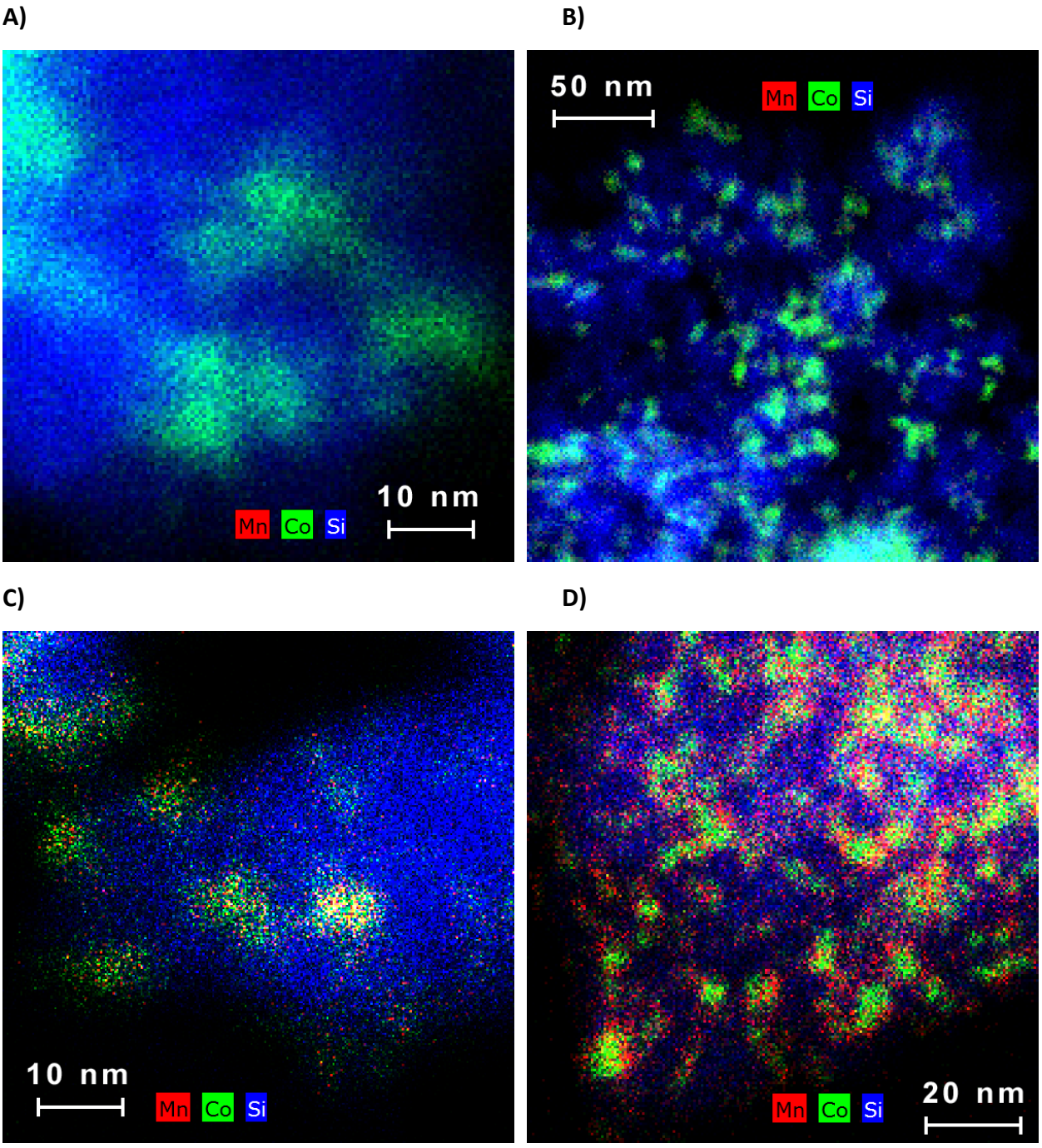

Figure 3.2 STEM-EDS elemental maps of Co-Mn catalysts with bulk Mn/Co atomic ratios of (A) Mn/Co = 0.01, (B) Mn/Co = 0.05, (C) Mn/Co = 0.1, and (D) Mn/Co = 0.5.

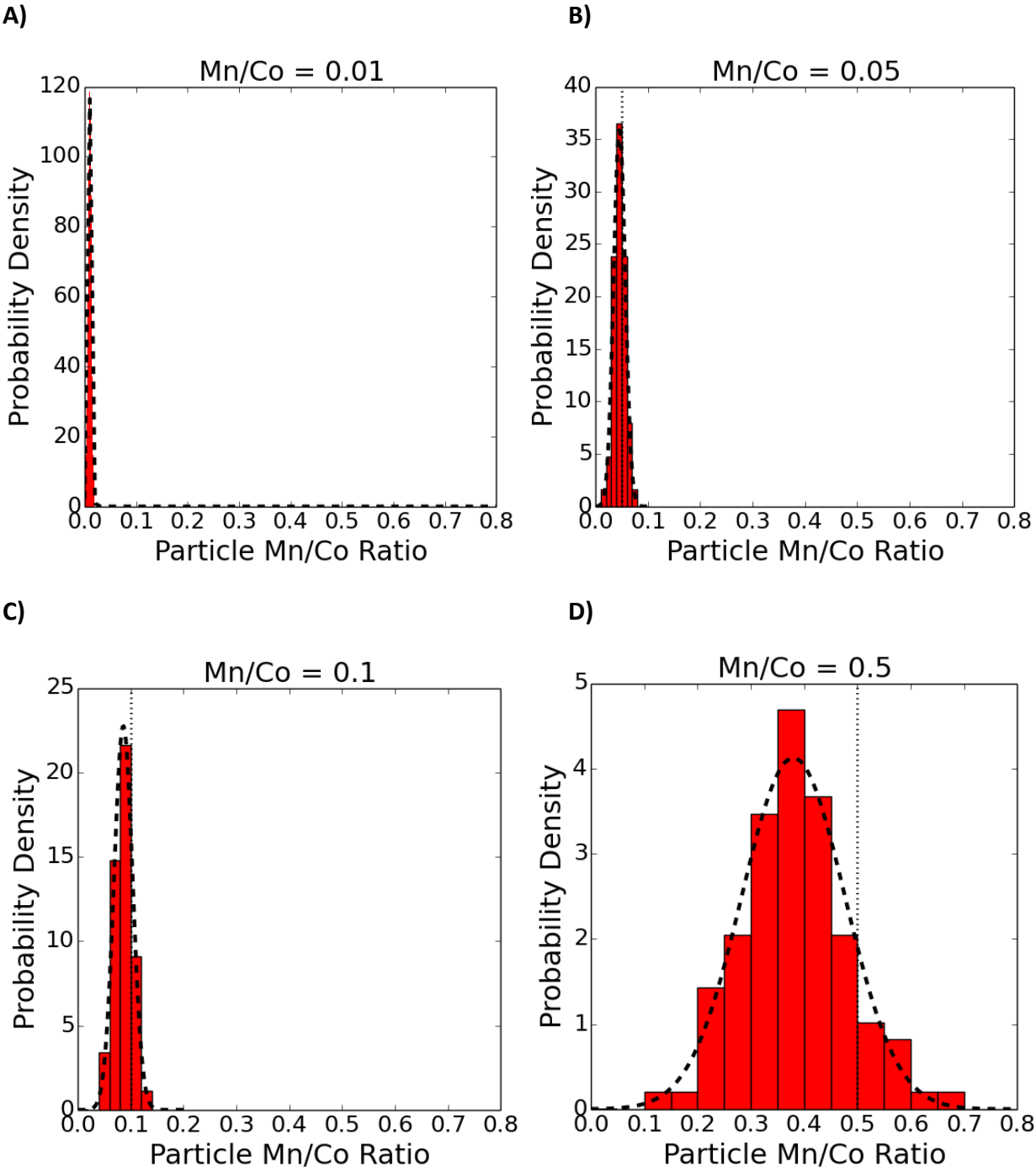

Figure 3.3 Histograms of Co-Mn nanoparticle compositions for bulk Mn/Co atomic ratios of (A) 0.01, (B) 0.05, (C) 0.1, and (D) 0.5. The dashed curve in each plot is a Gaussian function fitted to the data, and the vertical dotted line indicates the bulk catalyst composition.

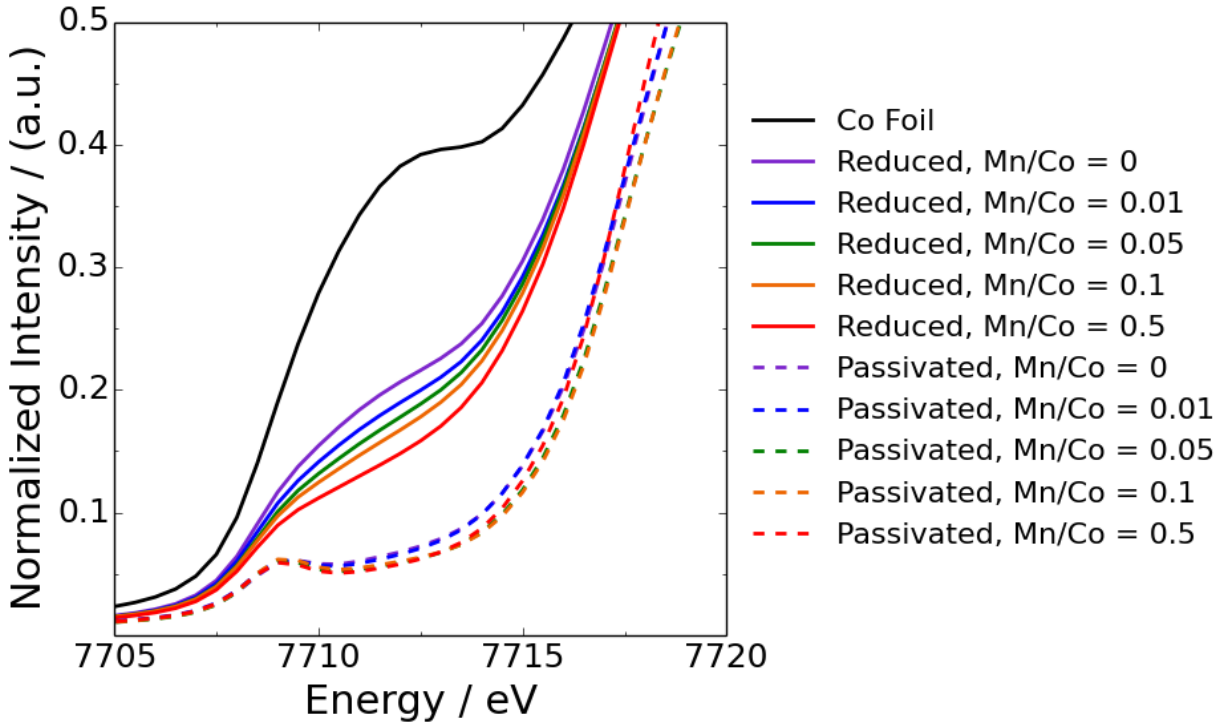

Figure 3.4 XANES spectra at the Co K-edge for the Co-Mn catalysts. After the spectra for the catalysts in a passivated state were collected under ambient conditions, the samples were reduced at 673 K in H_2 for 2 h. Spectra were then collected for the catalysts in the reduced state.

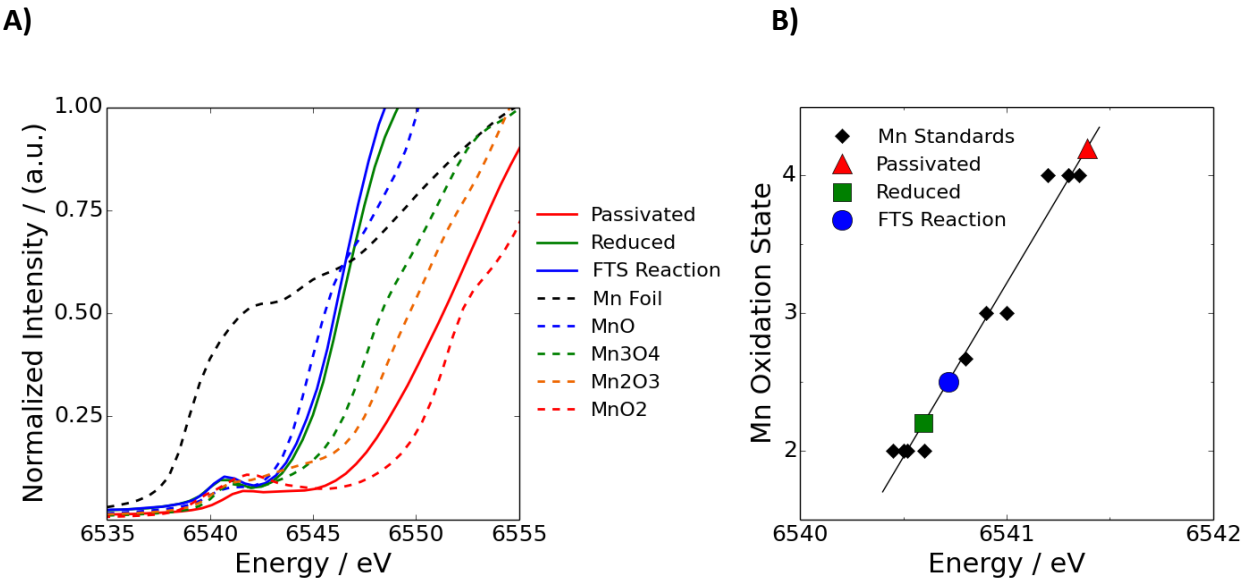

Figure 3.5 Mn K-edge XANES data for the Mn/Co = 0.1 catalyst: (A) XANES spectra of Mn oxide standards and the catalyst in the passivated state, after reduction, and during reaction; (B) linear relationship between apparent Mn oxidation state and the pre-edge feature centroid. The black line is the least-squares fit to the data points obtained from various Mn compounds of known oxidation state. The catalyst apparent oxidation states were inferred using this regression line. Estimates of the Mn apparent oxidation states for the catalysts with other Mn/Co ratios are reported in Table 3.3. The reduced catalyst data were acquired after reducing the catalysts at 673 K in H_2 for 2 h. The FTS reaction measurements were acquired after exposing the reduced catalysts to syngas at 493 K for 6 h.

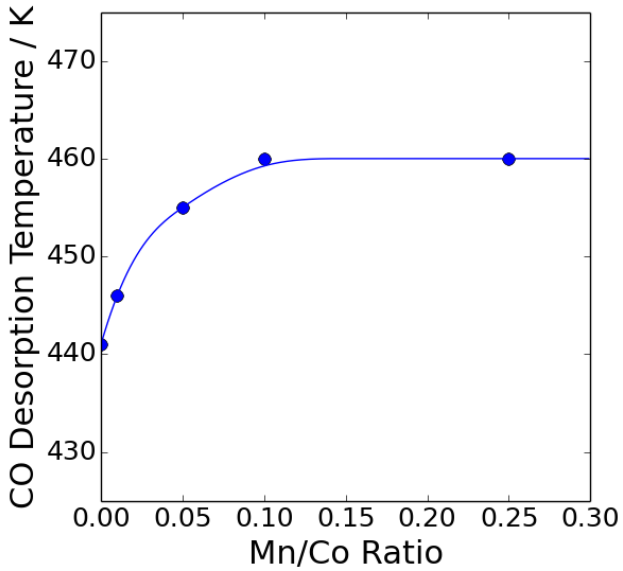

Figure 3.6 Mean temperature of the first chemisorbed CO desorption peak as a function of Mn loading. CO was adsorbed onto the catalyst at 213 K by pulse titration, and the temperature ramp rate for the desorption step was 10 K/min.

A) **B)**

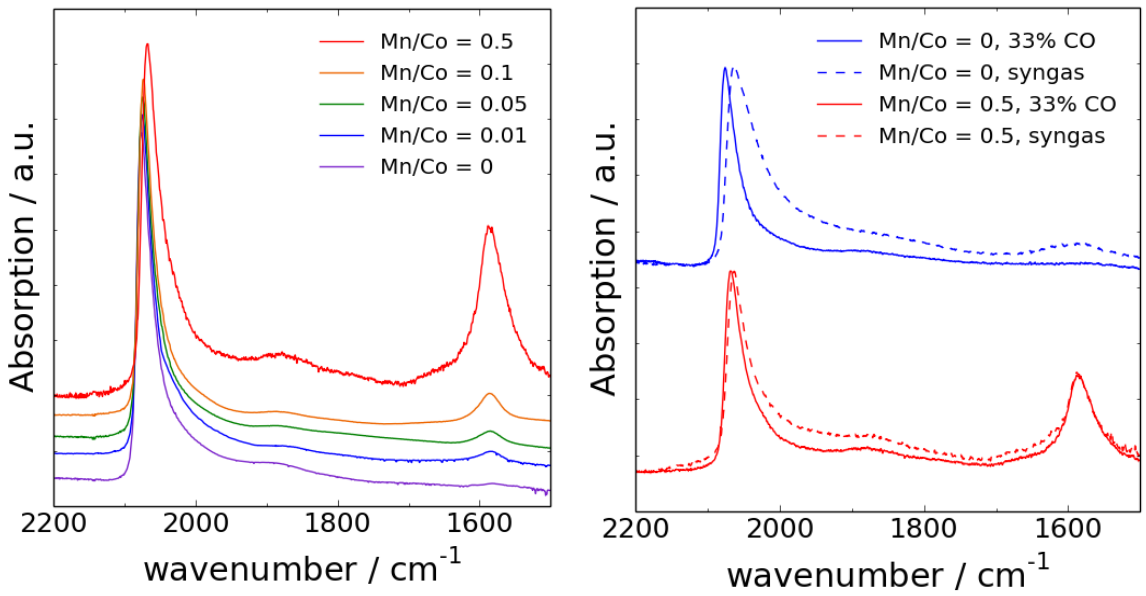

Figure 3.7 In situ IR spectra of adsorbed CO on the reduced Co-Mn catalysts measured at 493 K and 1 bar: (A) comparison of Mn loadings with 100% CO; (B) comparison of the Mn/Co = 0 and Mn/Co = 0.5 catalysts with 33% CO and either 67% He or 67% H_2 (syngas). In this figure, the signals were scaled so that the heights of the major peak near 2070 cm^{-1} are the same for each catalyst, and background subtraction was performed to remove contributions to the spectra from the catalysts and gas-phase CO.

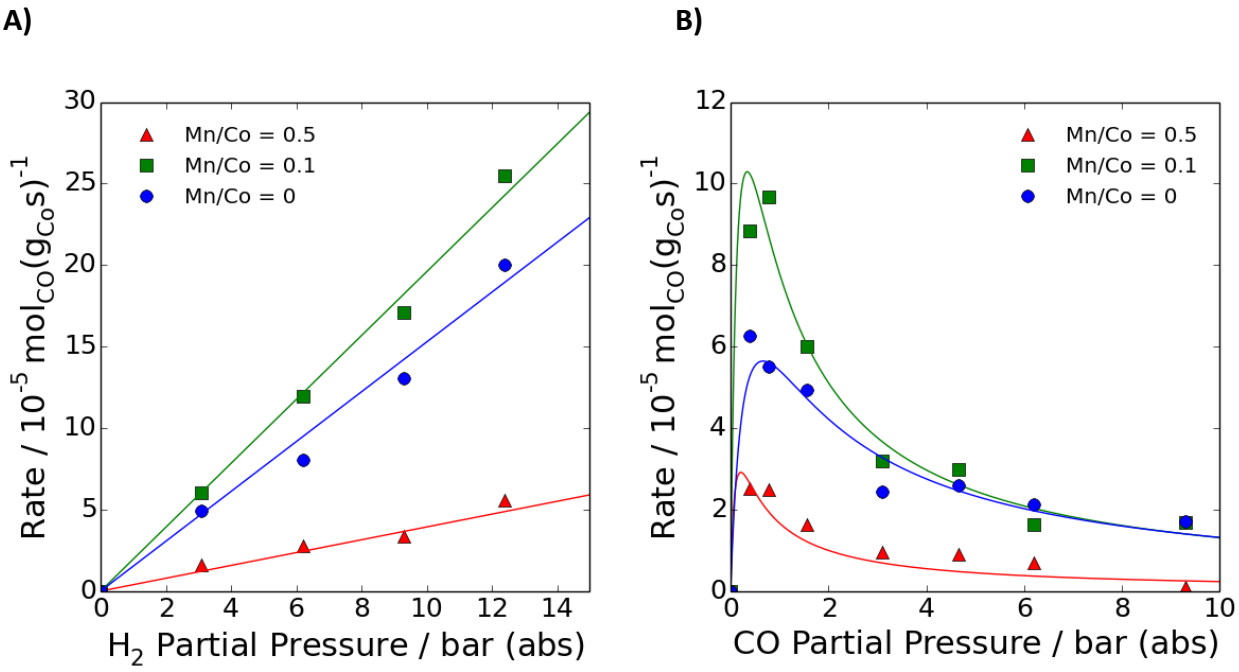

Figure 3.8 Dependence of CO consumption rate on (A) H_2 and (B) CO partial pressures. The variation of H_2 partial pressure was done with a constant CO partial pressure of 1.55 bar; the variation of CO partial pressure was done with a constant H_2 partial pressure of 3.1 bar. The data for both figures were collected at 493 K and were extrapolated to 0% conversion. The curves in the plots correspond to the rate law from eq. 3.3 fitted to the data.

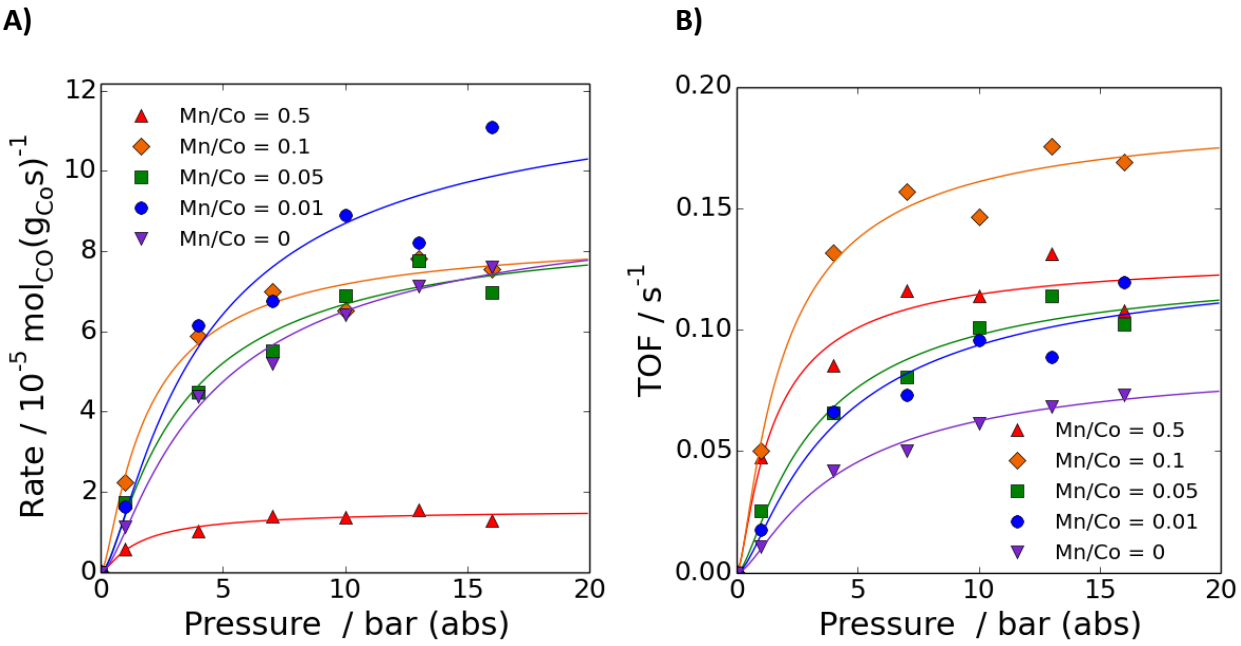

Figure 3.9 Comparison of (A) rates per gram of Co and (B) turnover frequencies for different Mn/Co ratios at 493 K. The data are based on CO consumption at 0% conversion. The curves in the plots correspond to the rate law from eq. 3.3 fitted to the data.

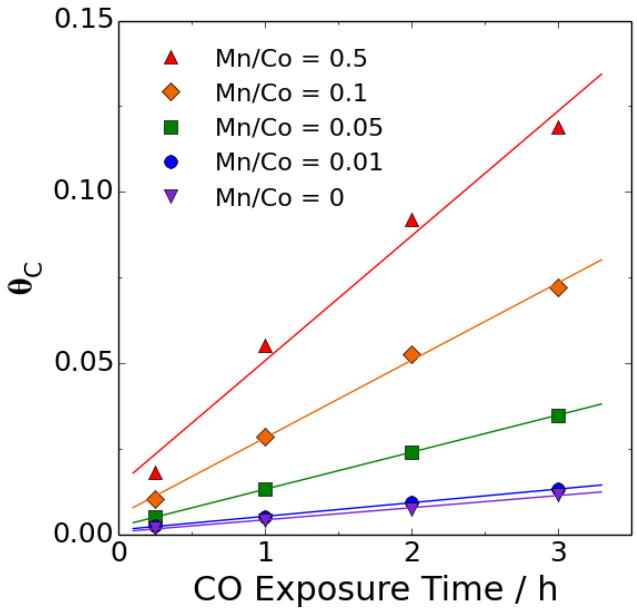

Figure 3.10 Fractional carbon surface coverage resulting from CO dissociation as a function of exposure time to CO at 493 K for catalysts with different Mn/Co ratios. The data are presented as the fraction of surface Co metal covered by carbon using H_2 uptake values as the basis for normalization.

A) **B)**

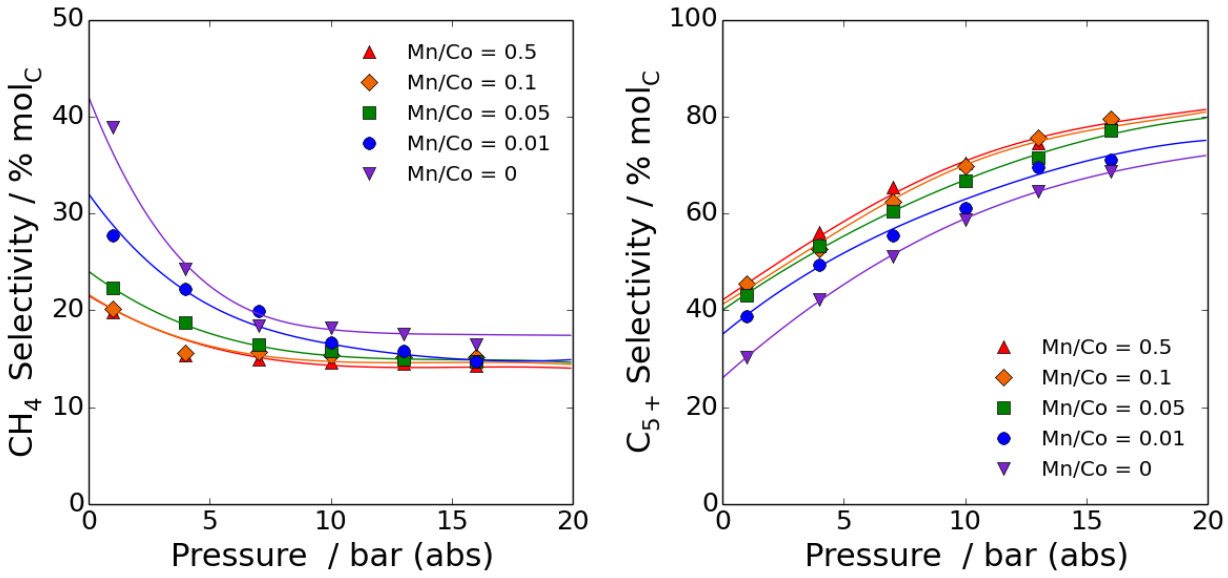

Figure 3.11 Comparison of (A) CH_4 and (B) C_{5+} selectivities as a function of pressure at 493 K for catalysts with different Mn/Co ratios. The data were extrapolated to 0% conversion. The curves in the plots are cubic splines intended for visual aid.

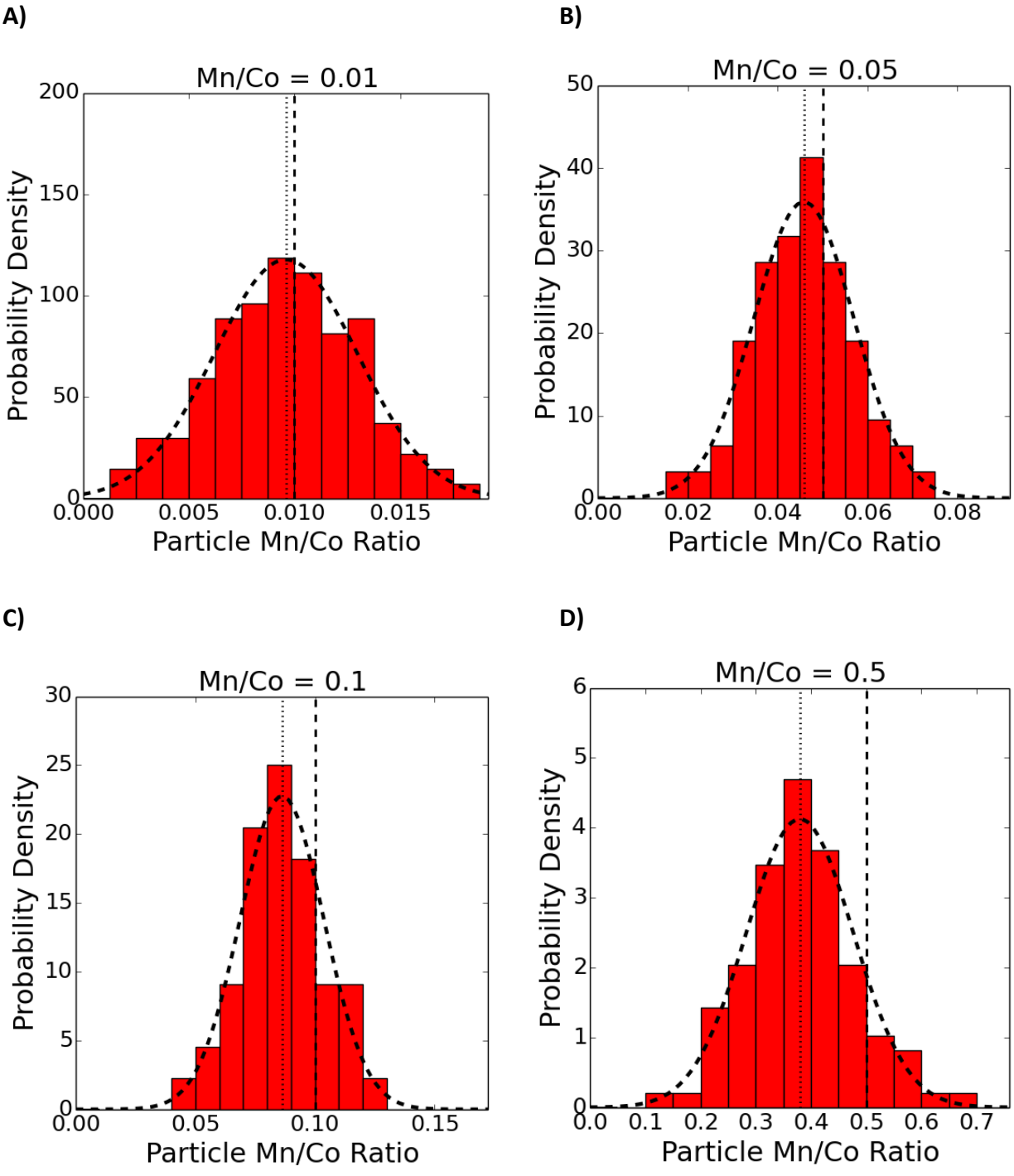

Figure S3.1 Histograms of nanoparticle compositions for the Co-Mn catalysts with bulk Mn/Co atomic ratios of (A) 0.01, (B) 0.05, (C) 0.1, and (D) 0.5. The dashed curve in each plot is a Gaussian function fitted to the data, and the vertical lines indicate the mean nanoparticle compositions (thin dotted) and the bulk catalyst compositions (thick dashed).

A)

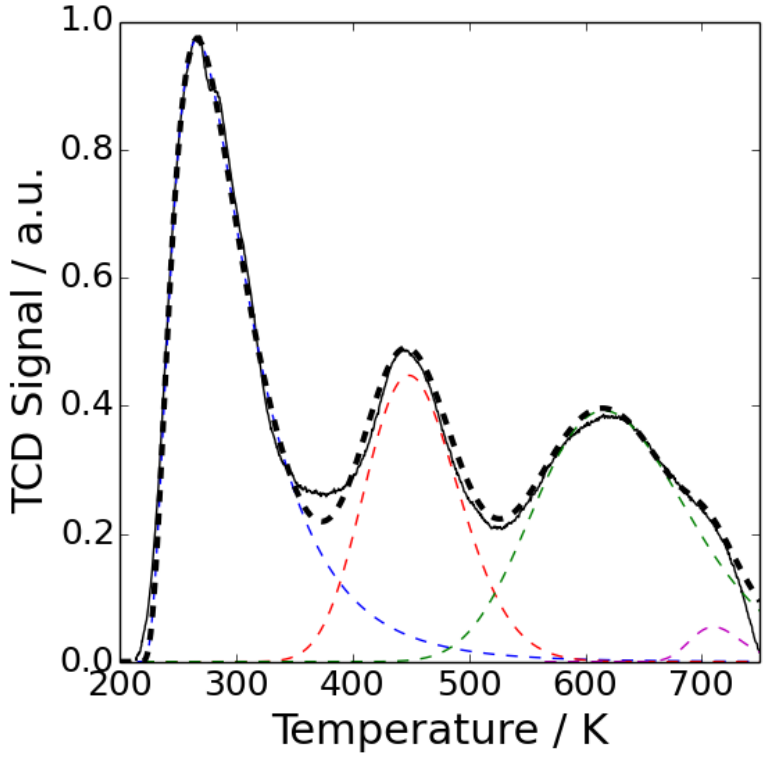
TCD Signal / a.u.
Temperature / K
0.0
0.2
0.4
0.6
0.8
1.0
200
300
400
500
600
700

B)

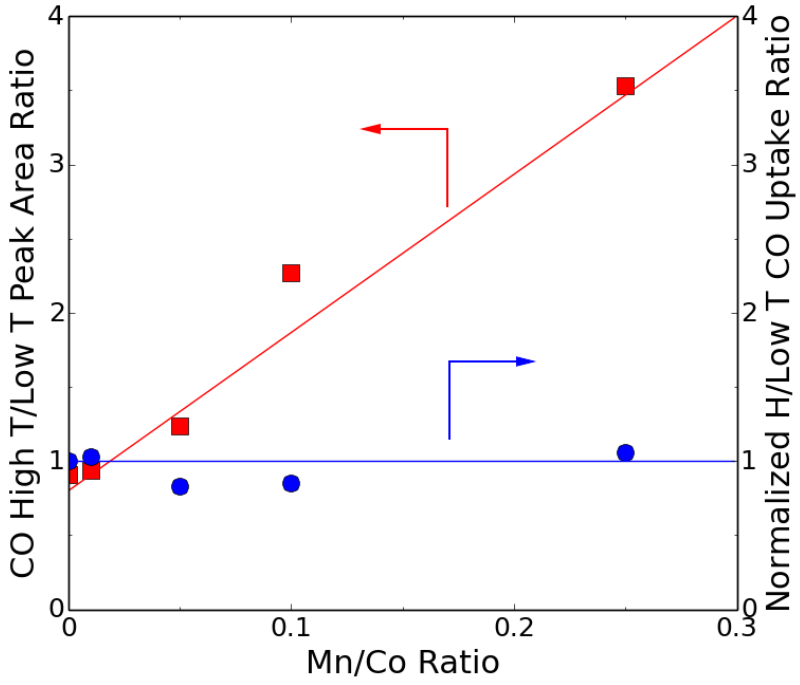
CO High T/Low T Peak Area Ratio
Normalized H/Low T CO Uptake Ratio
Mn/Co Ratio
0
1
2
3
4
0
0.1
0.2
0.3

Figure S3.2 CO Temperature-Programmed Desorption for the unpromoted and Mn-promoted catalysts.

(A) TCD signal (solid black line) as a function of temperature for the catalyst with Mn/Co = 0.1. The TCD signal was fitted using four log-normal peaks, which are shown as the dashed, colored lines, and the dashed, black line is the summation of the fitted peaks. The first peak (blue) was attributed to physisorbed CO, and the second (red) and third (green) peaks were attributed to chemisorbed CO. The fourth peak (purple), which appears as a shoulder of the third peak, was combined with third peak for the peak area analysis in Figure S3.2B.

(B) For various loadings of Mn, the ratio of the sum of the third and fourth CO chemisorption peak area to the second CO chemisorption peak area was calculated. This expression quantifies the amount of CO bound through stronger adsorption modes, including those involving interactions with MnO_x, to linearly adsorbed CO. In the figure below, these data are plotted in red using the left axis. The positive slope of these data indicates that higher promoter loading was associated with a larger fraction of the adsorbed CO being bound at sites with an affinity for CO that was stronger than that of the unpromoted sites.

Additionally, the ratio of H chemisorption molar uptake to the area of linearly adsorbed CO desorption peak was calculated for these catalysts using the equation below. Here, a normalization was performed using the ratio for the unpromoted catalyst so that the unpromoted catalyst had a normalized ratio of 1. This procedure is equivalent to assuming a 1/1 CO/Co adsorption stoichiometry for the unpromoted catalyst. The flat slope of the normalized H to low temperature CO (i.e., the second TPD peak) data suggests that the CO/Co adsorption stoichiometry did not change as a function of promoter loading.

$$normalized\ \frac{H}{Low\ T\ CO}\ Ratio = \frac{H\ chemisorption\ uptake}{Low\ T\ CO\ Peak\ Area} * \left(\frac{Low\ T\ CO\ Peak\ Area}{H\ uptake}\right)_{\frac{Mn}{Co}=0}$$

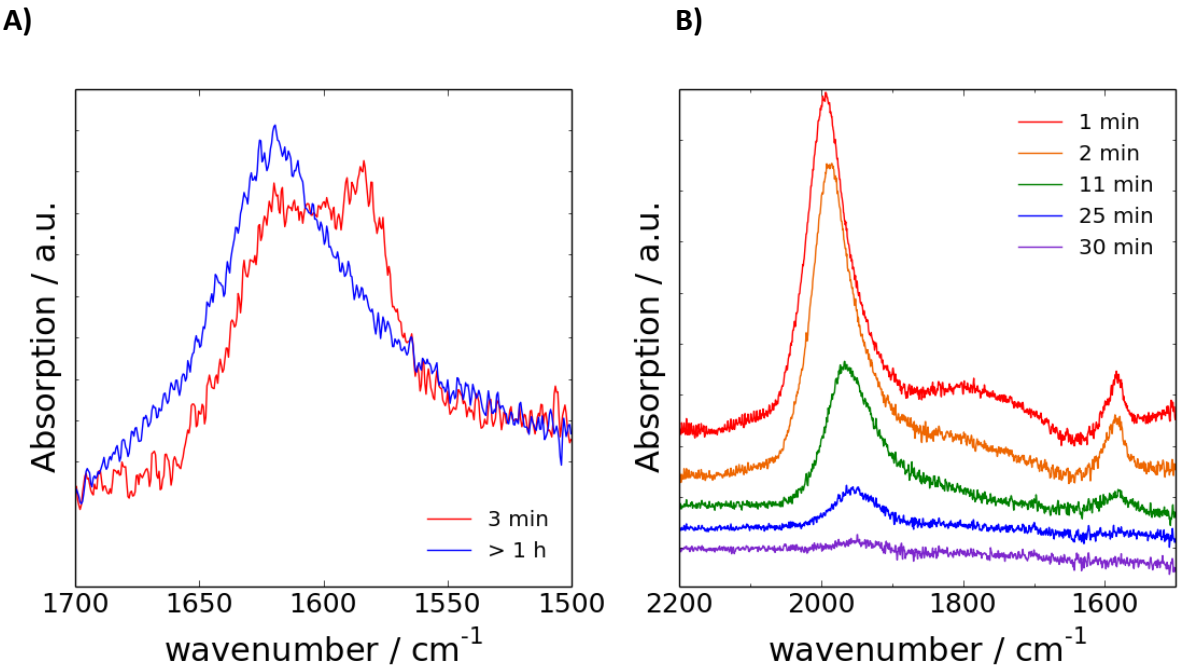

Figure S3.3 FTIR measurements of hydrogenation over a CO-saturated Mn-promoted catalyst (Mn/Co = 0.1). After reducing the catalyst at 673 K in H2 , the in situ cell was flushed with He and cooled to 493 K. CO was then flushed through the reactor to saturate the catalyst surface with carbonyl adsorbates. The flow through the in situ cell was then switched to H2 and FTIR measurements were collected at various times. The spectra are referenced in minutes elapsed after switching to H2 flow. (A) The peak at 1588 cm-1 decreased in intensity as time elapsed. At intermediate times (~3 min), this peak was distinguishable from a peak centered at 1619 cm-1. The peak at 1619 cm-1 remained visible after long durations of exposure to H2. (B) IR spectra of carbonyl adsorbates as a function of exposure time to H2. In this figure, the spectrum after 1 h of exposure to H2 was subtracted as a background removal. This removed the peak at 1619 cm-1, which was inactive toward hydrogenation. Linearly adsorbed CO, bridging CO, and the species giving rise to the peak at 1588 cm-1 were all labile under hydrogenation.

A)

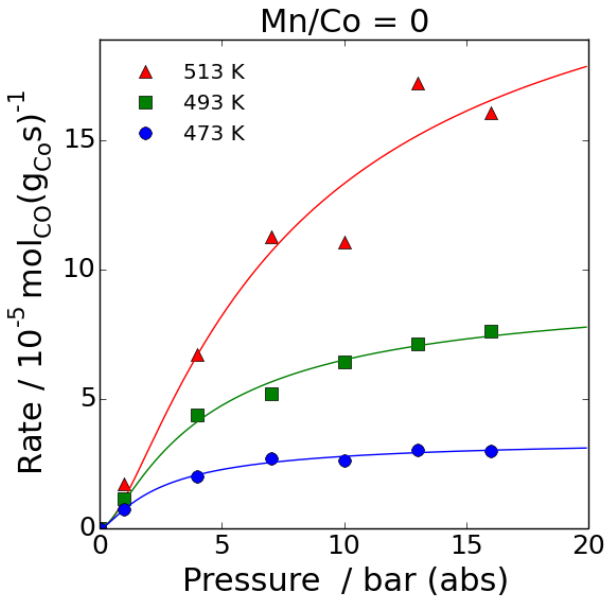
Mn/Co = 0
513 K
493 K
473 K
Rate / 10-5 molCO(gCos)-1
Pressure / bar (abs)

B)

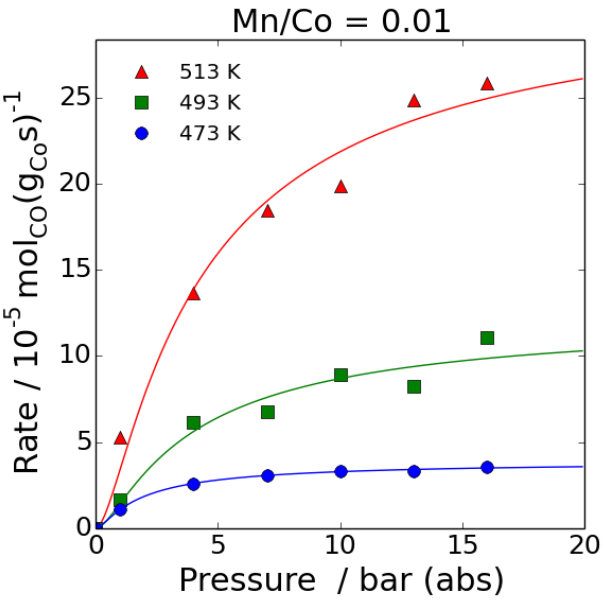
Mn/Co = 0.01
513 K
493 K
473 K
Rate / 10-5 molCO(gCos)-1
Pressure / bar (abs)

C)

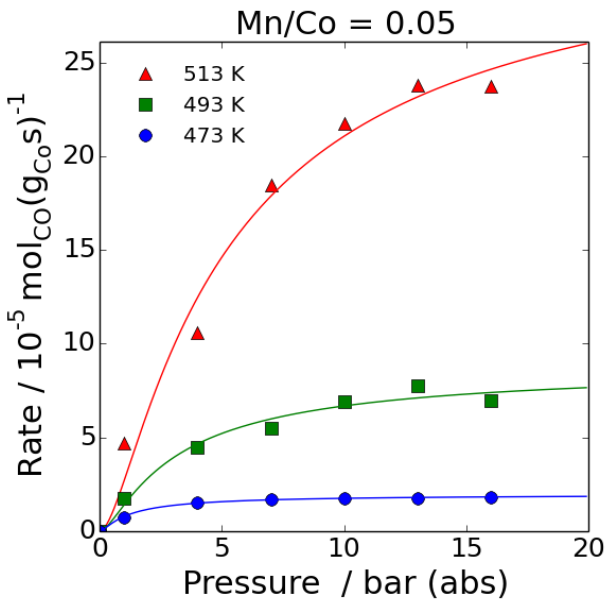
Mn/Co = 0.05
513 K
493 K
473 K
Rate / 10-5 molCO(gCos)-1
Pressure / bar (abs)

D)

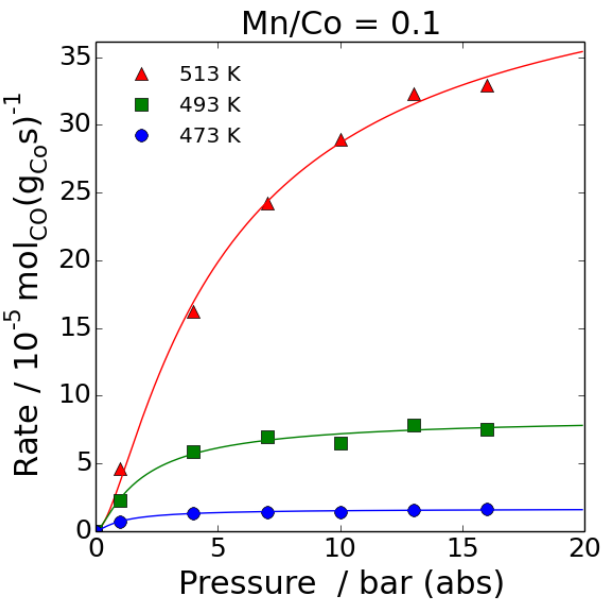
Mn/Co = 0.1
513 K
493 K
473 K
Rate / 10-5 molCO(gCos)-1
Pressure / bar (abs)

E)

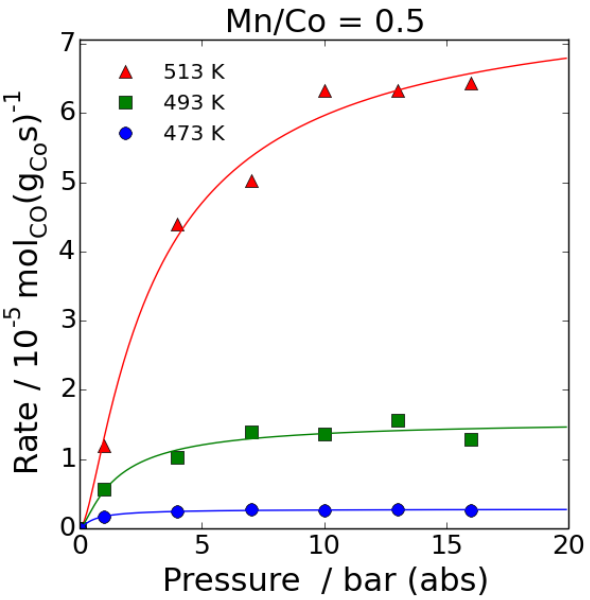

Figure S3.4 Cobalt-time yields for the Co-Mn catalysts with bulk Mn/Co atomic ratios of (A) Mn/Co = 0, (B) Mn/Co = 0.01, (C) Mn/Co = 0.05, (D) Mn/Co = 0.1, and (E) Mn/Co = 0.5. The data are based on CO consumption and were extrapolated to 0% conversion. The curves in each plot correspond to the rate law from eq. 3.3 fitted to the data at a given temperature.

A)

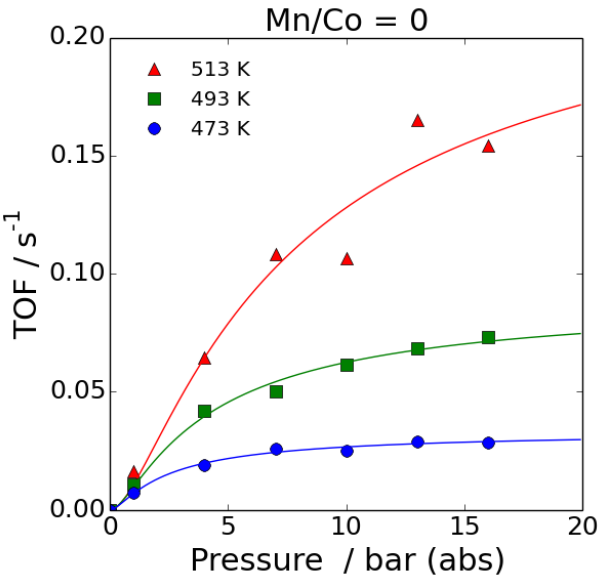
Mn/Co = 0
513 K
493 K
473 K
TOF / s-1
Pressure / bar (abs)
0.00
0.05
0.10
0.15
0.20
0
5
10
15
20

B)

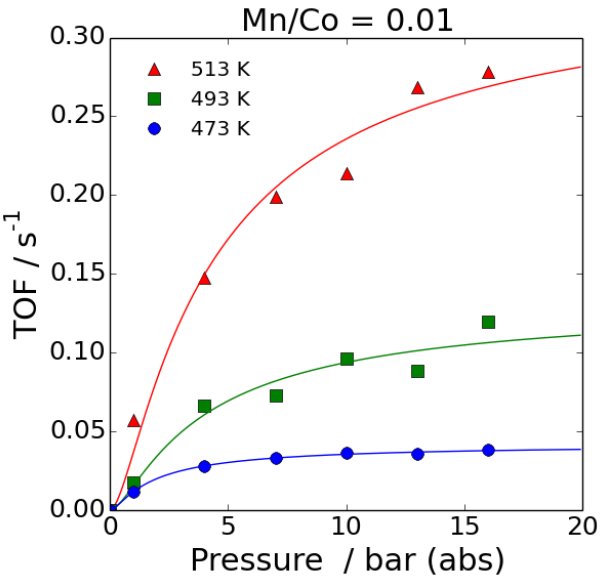
Mn/Co = 0.01
513 K
493 K
473 K
TOF / s-1
Pressure / bar (abs)
0.00
0.05
0.10
0.15
0.20
0.25
0.30
0
5
10
15
20

C)

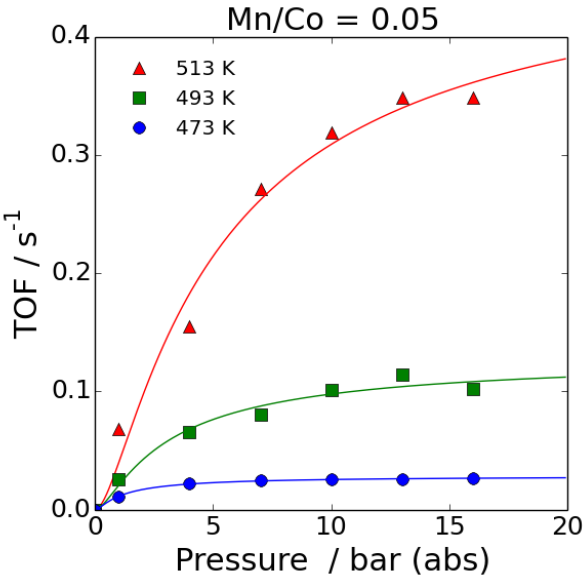
Mn/Co = 0.05
513 K
493 K
473 K
TOF / s-1
Pressure / bar (abs)
0.0
0.1
0.2
0.3
0.4
0
5
10
15
20

D)

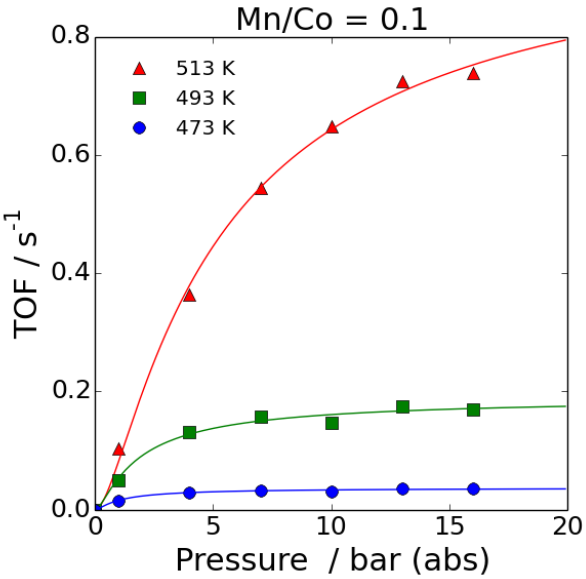
Mn/Co = 0.1
513 K
493 K
473 K
TOF / s-1
Pressure / bar (abs)
0.0
0.2
0.4
0.6
0.8
0
5
10
15
20

E)

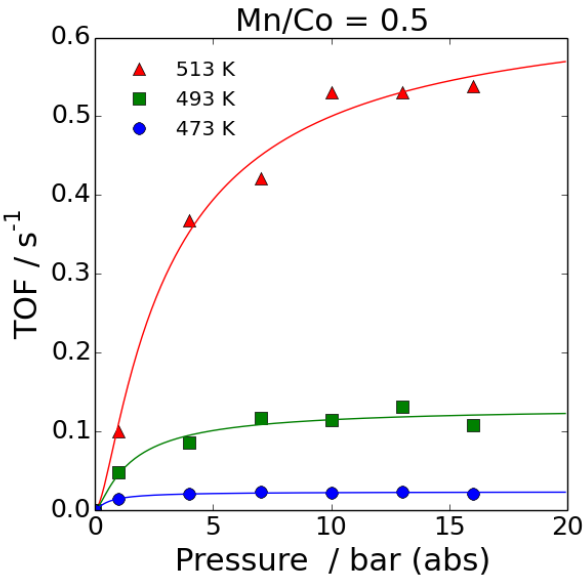

Figure S3.5 Turnover frequencies for the Co-Mn catalysts with bulk Mn/Co atomic ratios of (A) Mn/Co = 0, (B) Mn/Co = 0.01, (C) Mn/Co = 0.05, (D) Mn/Co = 0.1, and (E) Mn/Co = 0.5. The data are based on CO consumption and were extrapolated to 0% conversion. The curves in each plot correspond to the rate law from eq. 3.3 fitted to the data at a given temperature.

A)

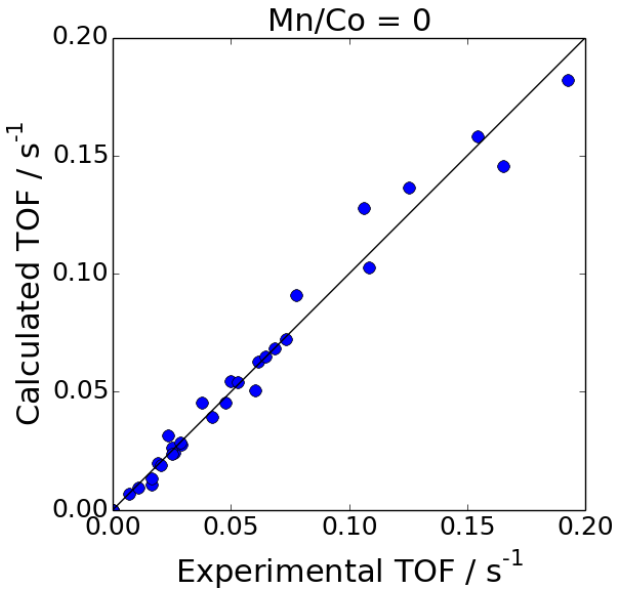
Mn/Co = 0
Calculated TOF / s-1
Experimental TOF / s-1
0.00
0.05
0.10
0.15
0.20

B)

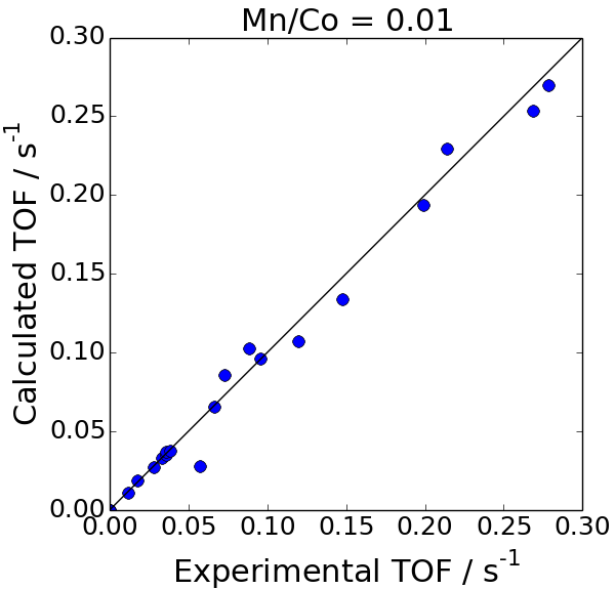
Mn/Co = 0.01
Calculated TOF / s-1
Experimental TOF / s-1
0.00
0.05
0.10
0.15
0.20
0.25
0.30

C)

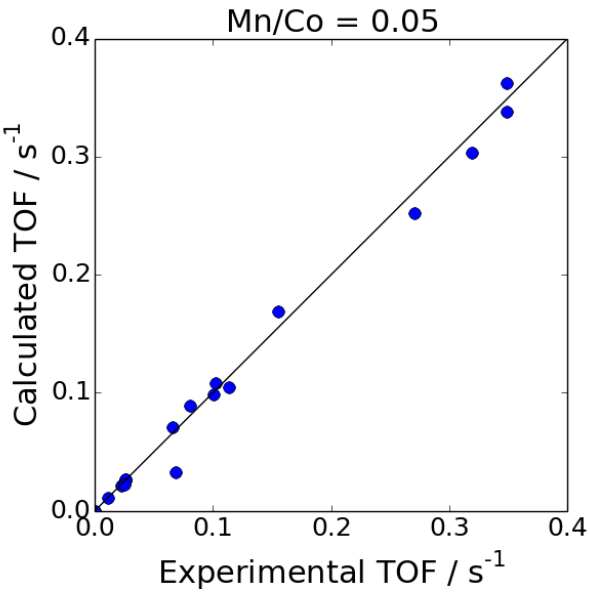
Mn/Co = 0.05
Calculated TOF / s-1
Experimental TOF / s-1
0.0
0.1
0.2
0.3
0.4

D)

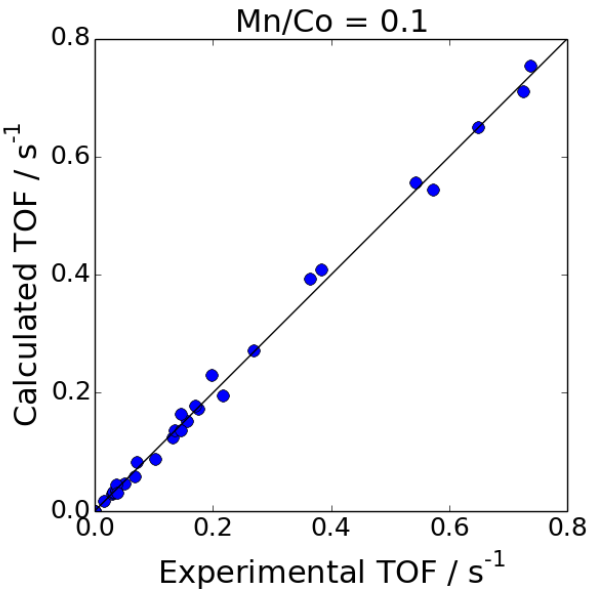
Mn/Co = 0.1
Calculated TOF / s-1
Experimental TOF / s-1
0.0
0.2
0.4
0.6
0.8

E)

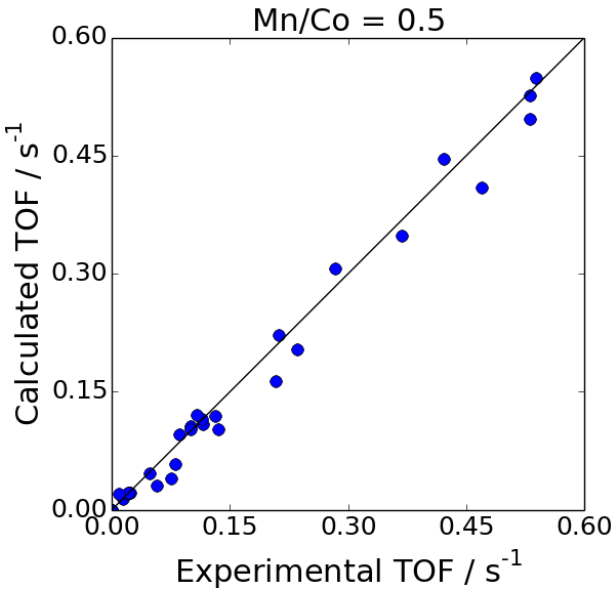

Figure S3.6 Parity plots for the Co-Mn catalysts with bulk Mn/Co atomic ratios of (A) Mn/Co = 0, (B) Mn/Co = 0.01, (C) Mn/Co = 0.05, (D) Mn/Co = 0.1, and (E) Mn/Co = 0.5.

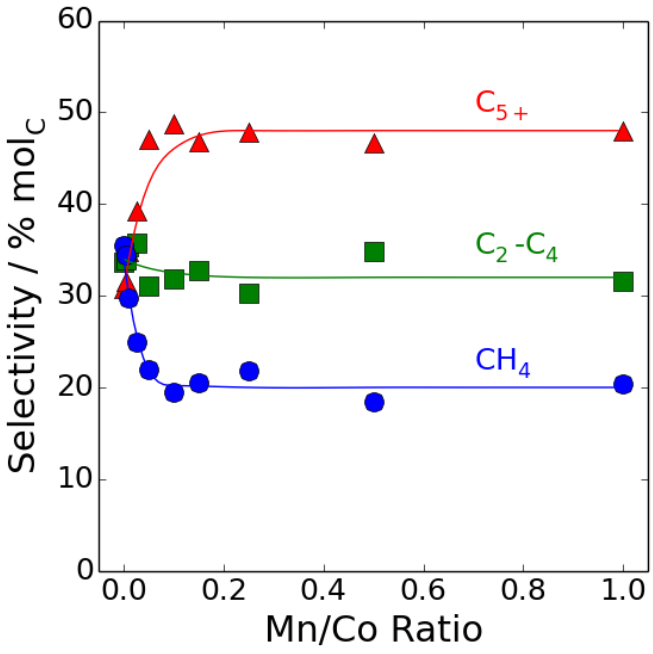

Figure S3.7 Product selectivities for the Co-Mn catalysts at atmospheric pressure and 493 K as a function of Mn loading. The data were extrapolated to 0% conversion. The curves in the plot are cubic splines intended for visual aid.

A)

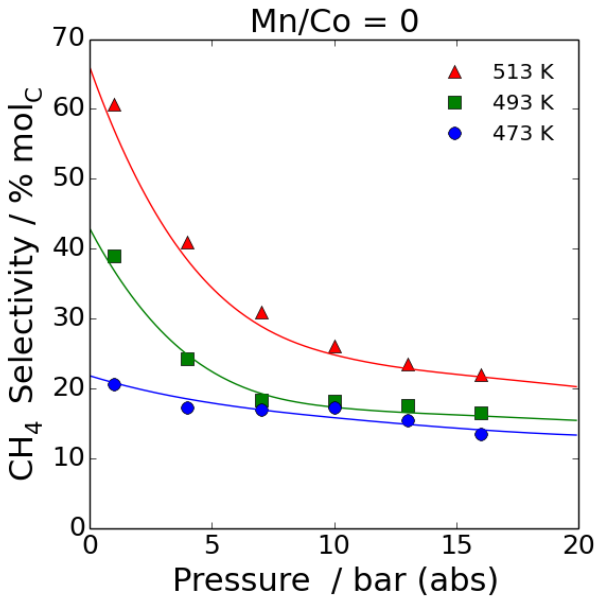
Mn/Co = 0
513 K
493 K
473 K
CH_4 Selectivity / % mol_C
Pressure / bar (abs)
0
10
20
30
40
50
60
70
0
5
10
15
20

B)

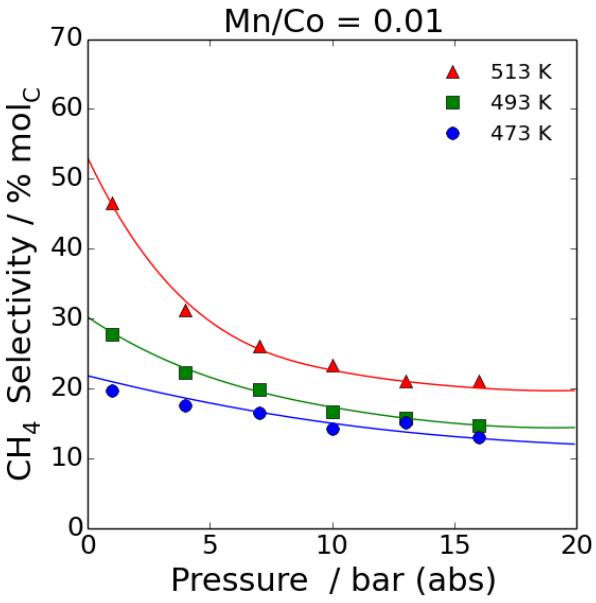
Mn/Co = 0.01
513 K
493 K
473 K
CH_4 Selectivity / % mol_C
Pressure / bar (abs)
0
10
20
30
40
50
60
70
0
5
10
15
20

C)

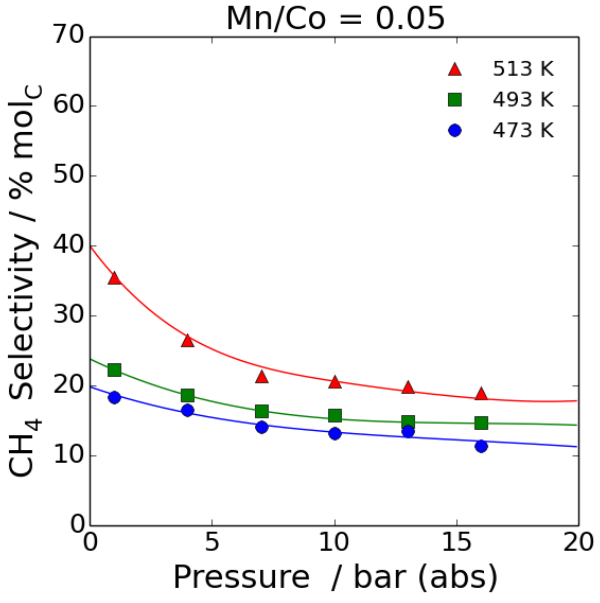
Mn/Co = 0.05
513 K
493 K
473 K
CH_4 Selectivity / % mol_C
Pressure / bar (abs)
0
10
20
30
40
50
60
70
0
5
10
15
20

D)

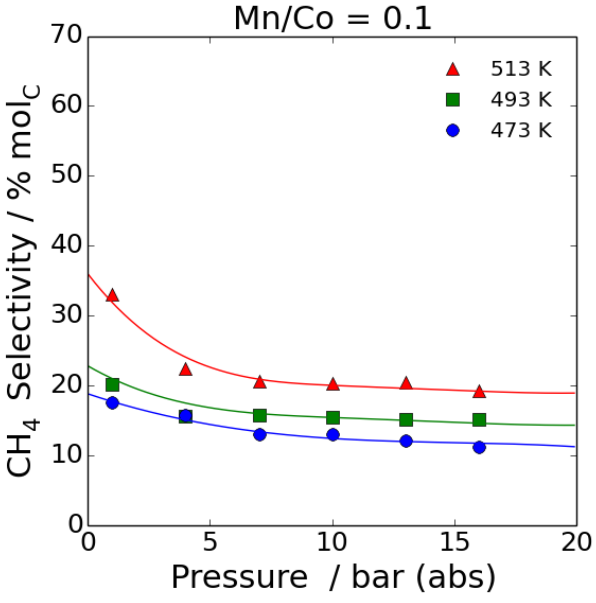
Mn/Co = 0.1
513 K
493 K
473 K
CH_4 Selectivity / % mol_C
Pressure / bar (abs)
0
10
20
30
40
50
60
70
0
5
10
15
20

E)

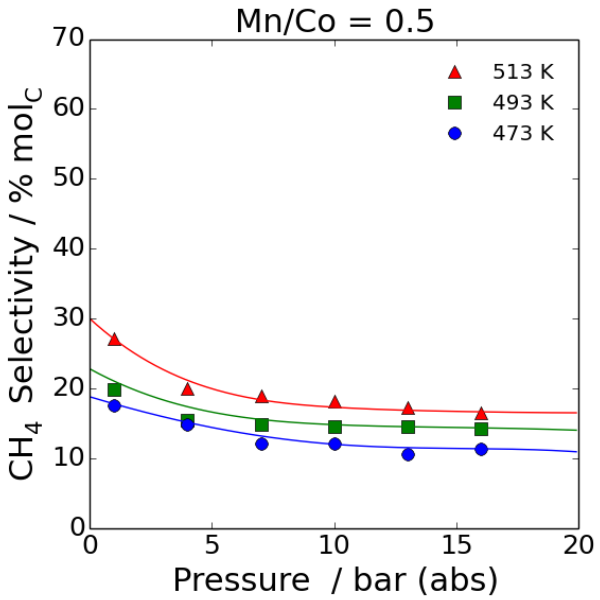

Figure S3.8 CH_4 selectivities for the Co-Mn catalysts with bulk Mn/Co atomic ratios of (A) Mn/Co = 0, (B) Mn/Co = 0.01, (C) Mn/Co = 0.05, (D) Mn/Co = 0.1, and (E) Mn/Co = 0.5. The data were extrapolated to 0% conversion. The curves in each plot are cubic splines intended for visual aid.

A)

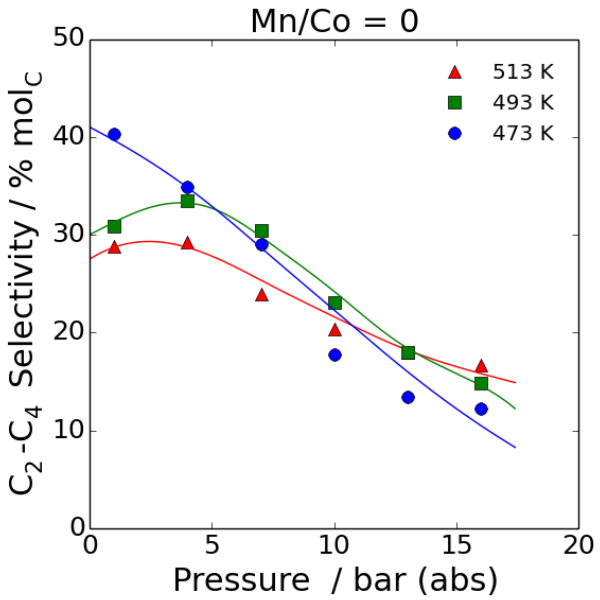
Mn/Co = 0
513 K
493 K
473 K
C_2-C_4 Selectivity / % mol_C
Pressure / bar (abs)
0
10
20
30
40
50
0
5
10
15
20

B)

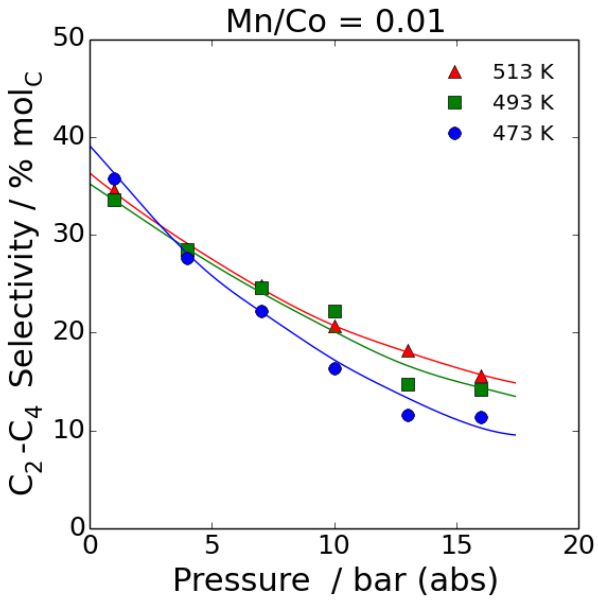
Mn/Co = 0.01
513 K
493 K
473 K
C_2-C_4 Selectivity / % mol_C
Pressure / bar (abs)
0
10
20
30
40
50
0
5
10
15
20

C)

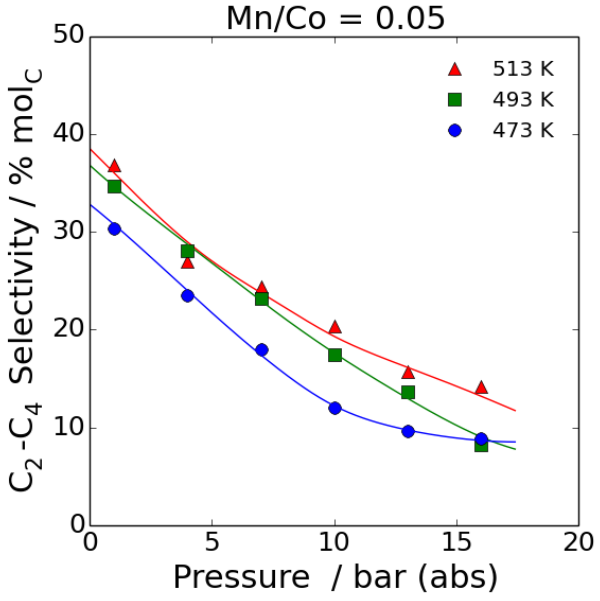
Mn/Co = 0.05
513 K
493 K
473 K
C_2-C_4 Selectivity / % mol_C
Pressure / bar (abs)
0
10
20
30
40
50
0
5
10
15
20

D)

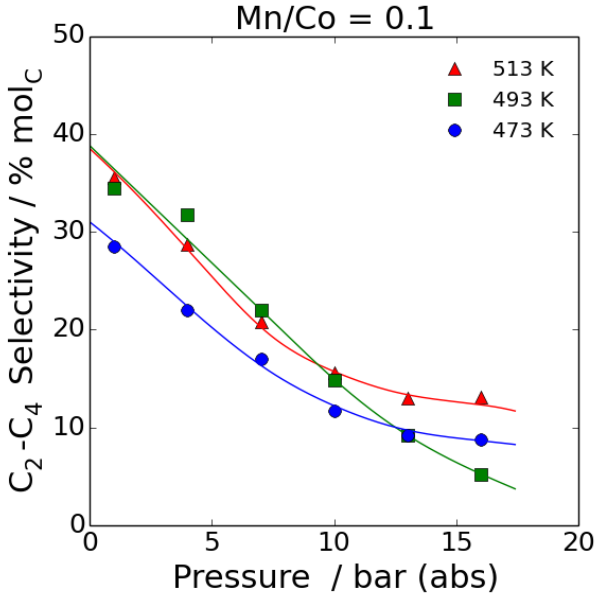
Mn/Co = 0.1
513 K
493 K
473 K
C_2-C_4 Selectivity / % mol_C
Pressure / bar (abs)
0
10
20
30
40
50
0
5
10
15
20

E)

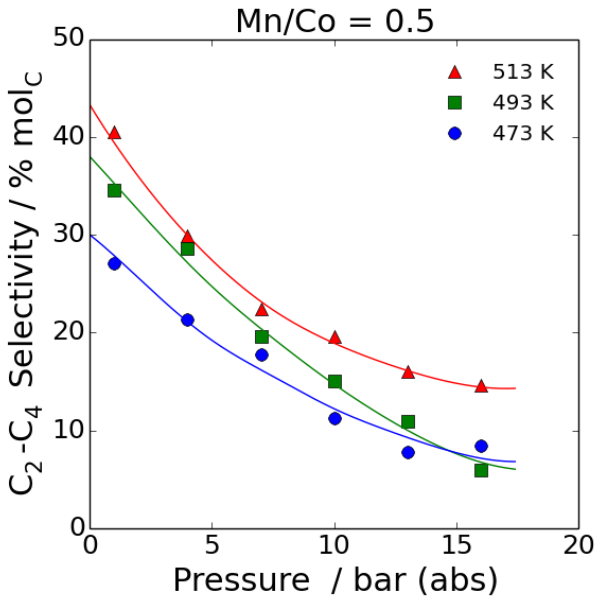

Figure S3.9 C_2-C_4 selectivities for the Co-Mn catalysts with bulk Mn/Co atomic ratios of (A) Mn/Co = 0, (B) Mn/Co = 0.01, (C) Mn/Co = 0.05, (D) Mn/Co = 0.1, and (E) Mn/Co = 0.5. The data were extrapolated to 0% conversion. The curves in each plot are cubic splines intended for visual aid.

A)

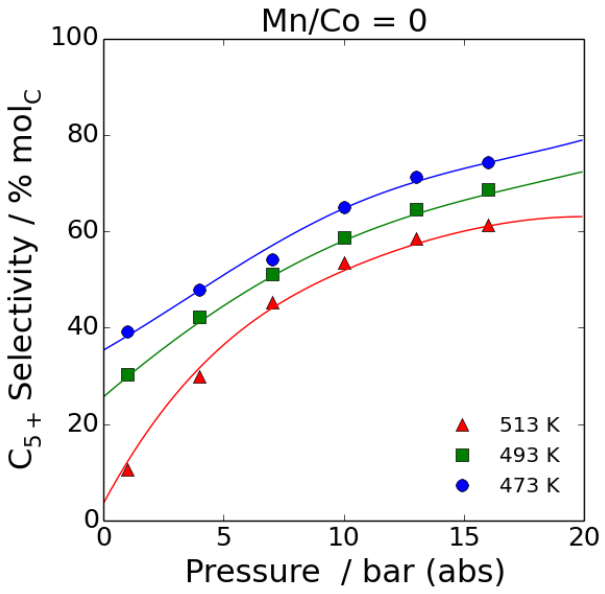
Mn/Co = 0
C_{5+} Selectivity / % mol_C
Pressure / bar (abs)
513 K
493 K
473 K

B)

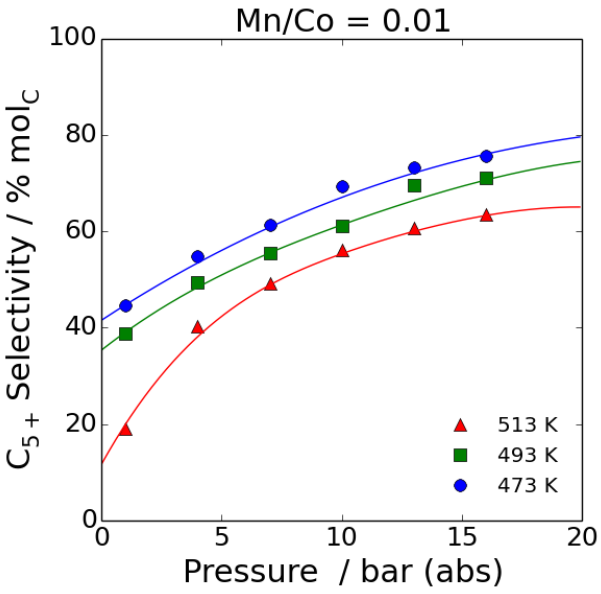
Mn/Co = 0.01
C_{5+} Selectivity / % mol_C
Pressure / bar (abs)
513 K
493 K
473 K

C)

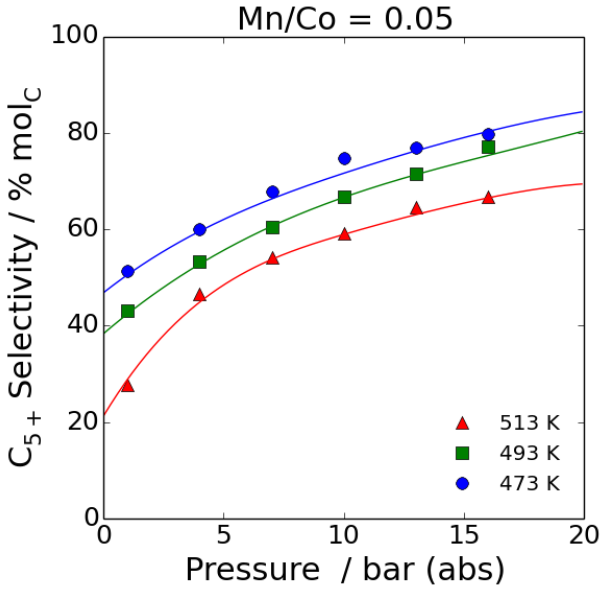
Mn/Co = 0.05
C_{5+} Selectivity / % mol_C
Pressure / bar (abs)
513 K
493 K
473 K

D)

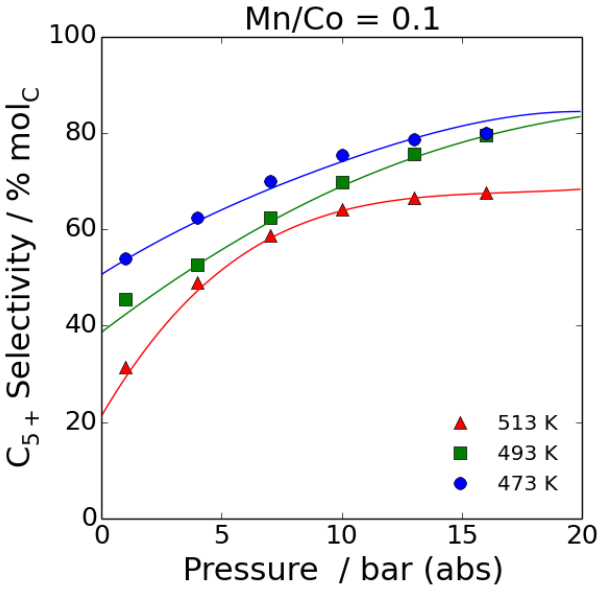
Mn/Co = 0.1
C_{5+} Selectivity / % mol_C
Pressure / bar (abs)
513 K
493 K
473 K

E)

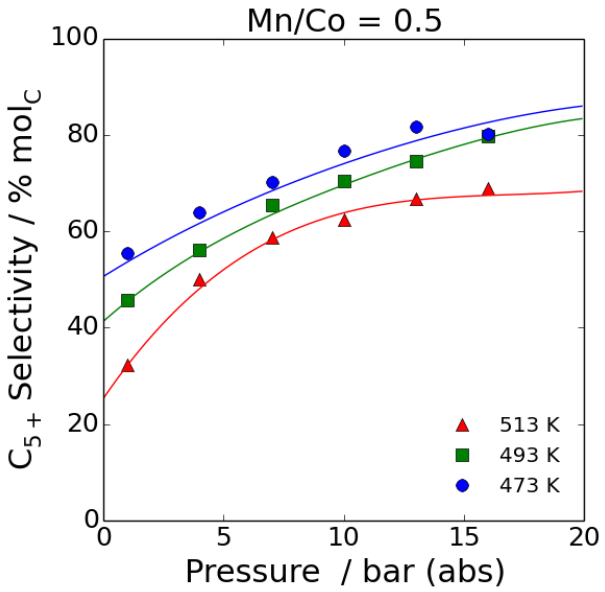

Figure S3.10 C_{5+} selectivities for the Co-Mn catalysts with bulk Mn/Co atomic ratios of (A) Mn/Co = 0, (B) Mn/Co = 0.01, (C) Mn/Co = 0.05, (D) Mn/Co = 0.1, and (E) Mn/Co = 0.5. The data were extrapolated to 0% conversion. The curves in each plot are cubic splines intended for visual aid.

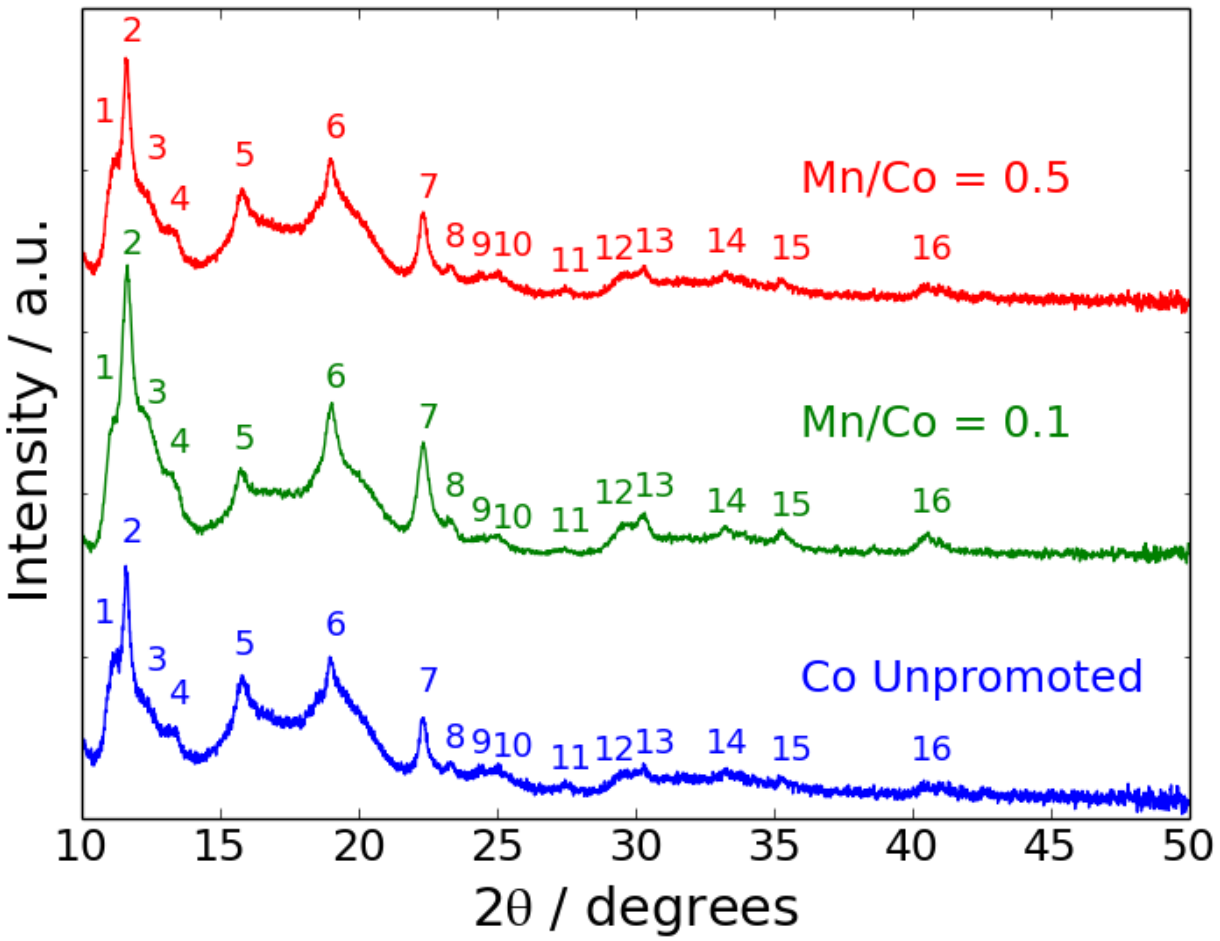

Figure S3.11 X-ray diffraction patterns for the unpromoted, Mn/Co = 0.1, and Mn/Co = 0.5 catalysts. The catalyst samples were reduced in H_2 at 493 K and sealed in Kapton tubes under inert gas. The data were collected at ambient temperature using 28.3 keV X-rays over a 2θ range of 0.5 to 50° with a 0.001° step size. Data at 2θ < 10° were difficult to interpret owing to a rapidly changing background signal in this region. Peak assignments for the 10° ≤ 2θ ≤ 50° region are given in Table S3.1.

Table S3.1 Indexed X-ray diffraction peaks corresponding to the data in Figure S3.11.

Marker Number	2θ (degrees)	Crystal	Orientation
1	11.14	CoO	<200>
2	11.62	Co (hcp)	<002>
3	12.40	Co (hcp)	<101>
4[a]	13.2		
5	15.78	CoO	<220>
6	19.01	Co (hcp)	<110>
7	22.34	Co (hcp)	<112>
8	23.33	Co (hcp)	<004>
9	24.43	CoO	<331>
10[b]	25.02	Co (hcp)	<202>
		CoO	<420>
11	27.51	CoO	<422>
12[b]	29.60	Co (hcp)	<211>
		CoO	<511>
			<333>
13	30.30	Co (hcp)	<114>
14	33.25	Co (hcp)	<300>
15	35.33	Co (hcp)	<302>
16[b]	40.57	Co (hcp)	<311>
		CoO	<551>

[a] Does not match any tabulated crystal structures containing Co, Mn Si, or O (possible instrument/sample holder background).

[b] Composite of peaks from Co (hcp) and CoO.

BLACK = MnO_x and $Co_{1-x}Mn_xO_y$

BLUE = unpromoted active sites not adjacent to oxide overlayer

RED = promoted active sites adjacent to oxide overlayer

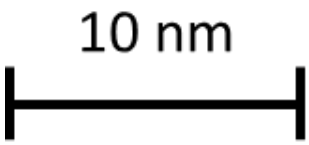

A) Mn/Co = 0

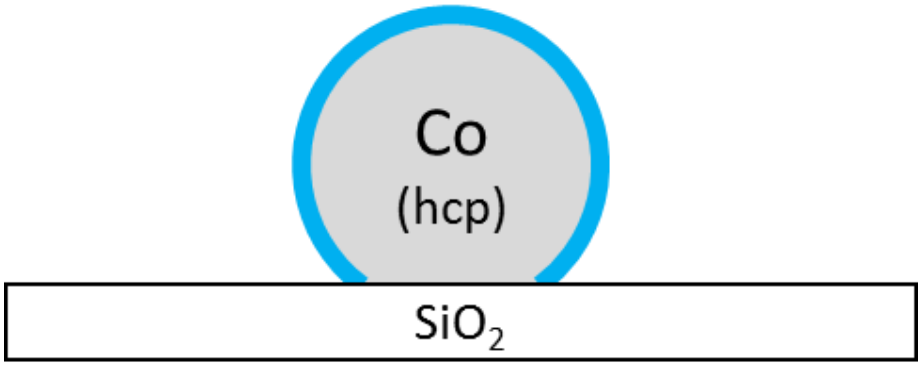

- 85% of the nanoparticle surface is available for catalysis
- All active sites are unpromoted

B) Mn/Co = 0

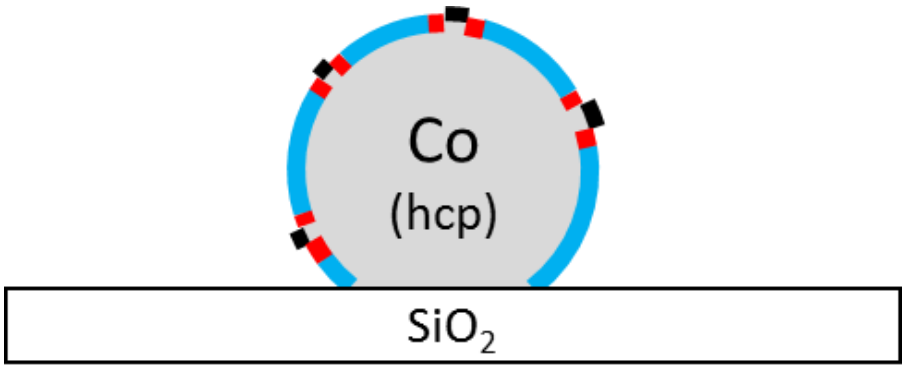

- Mn accumulates as highly dispersed MnO_x on the nanoparticle surface
- 77% of the nanoparticle surface is available for catalysis
- The majority of active sites remain unpromoted so catalyst selectivity and activity are similar to those of the Mn/Co = 0 catalyst

C) Mn/Co = 0.05

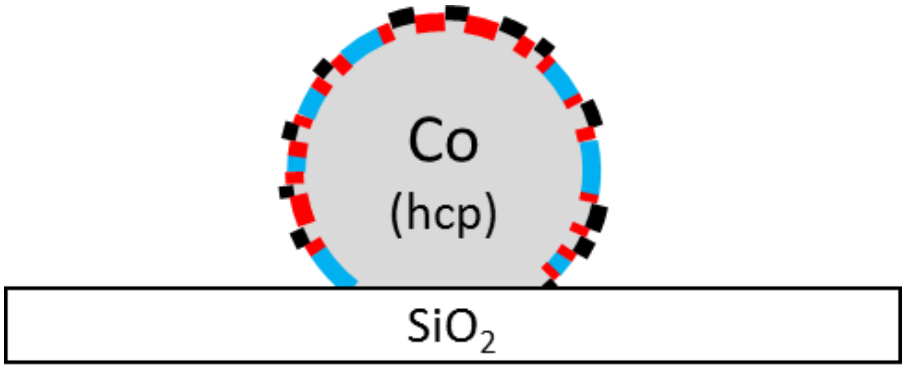

- Mn continues to deposit onto the nanoparticle surface
- 52% of the nanoparticle surface is available for catalysis
- Catalyst turnover frequency and selectivity improve as the promoted active sites constitute a substantial fraction of the total active sites

D) Mn/Co = 0.1

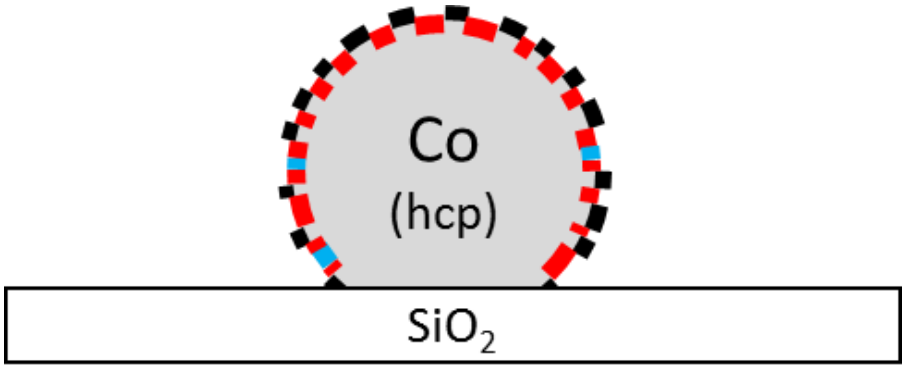

- Mn continues to deposit onto the nanoparticle surface
- Lower extent of reduction indicates incorporation of Co into a $Co_{1-x}Mn_xO_y$ phase
- 44% of the nanoparticle surface is available for catalysis
- Nearly all active sites are promoted by being adjacent to the surface oxide layer

E) Mn/Co = 0.5

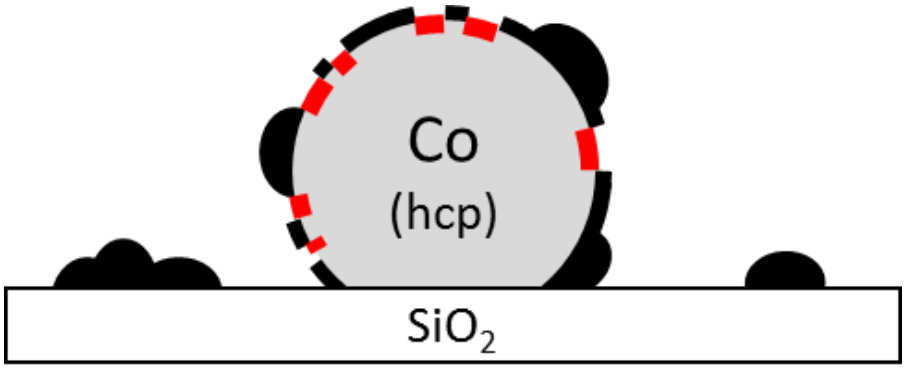

- $Co_{1-x}Mn_xO_y$ on nanoparticle surface grows outward rather than completely encapsulates the Co nanoparticle
- MnO_x deposits on the SiO_2 support
- 15% of the nanoparticle surface is available for catalysis
- Nearly all active sites are promoted by being adjacent to the MnO_x
- Selectivity remains the same as the Mn/Co = 0.1 catalyst because active sites are all promoted in both catalysts, but the fewer sites in the Mn/Co = 0.5 catalyst results in a much lower activity per gram Co

Scheme S3.1 Hypothesized structures of the Co-Mn catalysts with promoter loadings of (A) Mn/Co = 0, (B) Mn/Co = 0.01, (C) Mn/Co = 0.05, (D) Mn/Co = 0.1, (E) Mn/Co = 0.5. These cartoons are drawn as 2D cross-sections through nanoparticles. The black particles decorating the surface of the Co nanoparticles are MnOx. The outer layers of the Co nanoparticles are color-coded according to whether the Co active sites are separate from (blue) or adjacent to (red) the promoter.

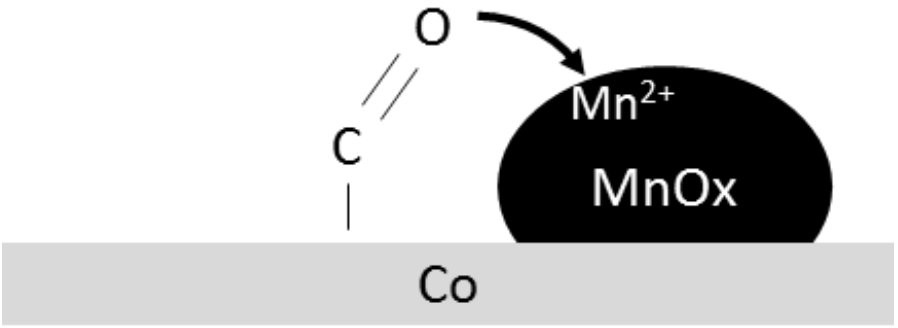

Scheme S3.2 Hypothesized interaction between a CO adsorbate and the Mn promoter. Mn cations may participate as Lewis acids and withdraw electron density from the CO oxygen. This phenomenon would result in a weakening of the C-O bond and a facilitation of CO dissociation.

References

1. Varma, R.L.; Dan-Chu, L.; Mathews, J.F.; Bakhshi, N.N. *Can. J. Chem. Eng.* **1985**, *63*, 72-80.

2. Colley, S.; Copperthwaite, R.G.; Hutchings, G.J.; van der Riet, M. *Ind. Eng. Chem. Res.* **1988**, *27*, 1339-1344.

3. Hutchings, G.J.; van der Riet, M.; Hunter, R.J. *Chem. Soc. Faraday Trans. 1* **1989**, *85*, 2875-2890.

4. Morales, F.; de Groot, F.M.F.; Glatzel, P.; Kleimenov, E.; Bluhm, H.; Hävecker, M.; Knop-Gericke, A.; Weckhuysen, B.M. *J. Phys. Chem. B* **2004**, *108*, 16201-16207.

5. Morales, F.; de Groot, F.M.F.; Gijzeman, O.L.J.; Mens, A.; Stephan, O.; Weckhuysen, B. M. *J. Catal.* **2005**, *230*, 301-308.

6. Morales, F.; de Smit, E.; de Groot, F.M.F.; Visser, T.; Weckhuysen, B.M. *J. Catal.* **2007**, *246*, 91-99.

7. Bezemer, G.L.; Radstake, P.B.; Falke, U.; Oosterbeek, H.; Kuipers, H.P.C.E.; van Dillen, A.J.; de Jong, K.P. *J. Catal.* **2006**, *237*, 152-161.

8. den Breejen, J.P.; Frey, A.M.; Yang, J.; Holmen, A.; van Schooneveld, M.M.; de Groot, F.M.F.; Stephan, O.; Bitter, J.H.; de Jong, K.P. *Top. Catal.* **2011**, *54*, 768-777.

9. Feltes, T.E.; Espinosa-Alonso, L.; de Smit, E.; D'Souza, L.; Meyer, R.J.; Weckhuysen, M.M.; Regalbuto, J.R. *J. Catal.* **2010**, *270*, 95-102.

10. Feltes, T.E.; Zhao, Y.; Klie, R.F.; Meyer, R.J.; Regalbuto, J.R. *ChemCatChem* **2010**, *2*, 1065-1068.

11. Johnson, G.R.; Werner, S.; Bustillo, K.C.; Ercius, P.; Kisielowski, C.; Bell, A.T. *J. Catal.* **2015**, *328*, 111-122.

12. Dinse, A.; Aigner, M.; Ulbrich, M.; Johnson, G.R.; Bell, A.T. *J. Catal.* **2012**, *288*, 104-114.

13. Atashi, H.; Siami, F.; Mirzaei, A.A.; Sarkari, M. *J. Ind. Eng. Chem.* **2010**, *16*, 952-961.

14. Thiessen, J.; Rose, A.; Meyer, J.; Jess, A.; Curulla-Ferré, D. *Microporous Mesoporous Mater.* **2012**, *164*, 199-206.

15. Mansouri, M.; Atashi, H.; Tabrizi, F. F.; Mirzaei, A. A.; Mansouri, G. *J. Ind. Eng. Chem.* **2013**, *19*, 1177-1183.

16. Sachtler, W.M.; Ichikawa, M. *J. Phys. Chem.* **1986**, *90*, 4752-4758.

17. Boffa, A.B.; Lin, C.; Bell, A.T.; Somorjai, G.A. *Catal. Lett.* **1994**, *27*, 243-249.

18. Guerrero-Ruiz, A.; Sepúlveda-Escribano, A.; Rodríguez-Ramos, I. *Appl. Catal., A* **1994**, *120*, 71-83.

19. Datye, A.K.; Xu, Q.; Kharas, K.C.; McCarty, J.M. *Catal. Today* **2006**, *111*, 59-67.

20. Reuel, R.C.; Bartholomew, C.H. *J. Catal.* **1984**, *85*, 63-77.

21. Bartholomew, C.H. *Catal. Lett.* **1991**, *7*, 27-51.

22. Kropf, A.J.; Katsoudas, J.; Chattopadhyay, S.; Shibata, T.; Lang, E.A.; Zyryanov, V.N.; Ravel, B.; McIvor, K.; Kemner, K.M.; Scheckel, K.G.; Bare, S.R.; Terry, J.; Kelley, S.D.; Bunker, B.A.; Segre, C.U. *AIP Conf. Proc.*, **2009**, 299-302.

23. Ravel, B.; Newville, M.J. *Synchrotron Radiat.* **2005**, *12*, 537-541.

24. Newville, M.J. *Synchrotron Radiat.* **2001**, *8*, 96-100.

25. Weisz, P.B.; Prater, C.D. *Adv. Catal.* **1954**, *6*, 143-196.

26. Yankin, A.M.; Balakirev, V.F. *Inorg. Mater.* **2002**, *38*, 309-319.

27. Morales, F.; Grandjean, D.; Mens, A.; de Groot, F.M.F.; Weckhuysen, B.M. *J. Phys. Chem. B* **2006**, *110*, 8626-8639.

28. Chalmin, E.; Farges, F.; Brown, G. E., Jr. *Contrib. Mineral. Petrol.* **2009**, *157*, 111-126.

29. Redhead, P.A. *Vacuum* **1962**, *12*, 203-211.

30. Couble, J.; Bianchi, D. *Appl. Catal., A* **2012**, *445-446*, 1-13.

31. Patanou, E.; Tveten, E.Z.; Chen, D.; Holmen, A.; Blekkan, E.A. *Catal. Today* **2013**, *214*, 19-24.

32. Lahtinen, J.; Vaari, J.; Kauraala, K. *Surf. Sci.* **1998**, *418*, 502-510.

33. Carlsson, A.F.; Naschitzki, M.; Bäumer, M.; Freund, H.-J. *J. Phys. Chem. B* **2003**, *107*, 778-785.

34. Bridge, M.E.; Comrie, C.M.; Lambert, R.M. *Surf. Sci.* **1977**, *67*, 393-404.

35. Fredriksen, G.R.; Blekkan, E.A.; Schanke, D.; Holmen, A. *Chem. Eng. Technol.* **1995**, *18*, 125-131.

36. Liao, L.F.; Lien, C.F.; Shieh, D.L.; Chen, M.T.; Lin, J.L. *J. Phys. Chem. B* **2002**, *106*, 11240-11245.

37. Sachtler, W.M.H.; Shriver, D.F.; Hollenberg, W.B.; Lang, A.F. *J. Catal.* **1985**, *92*, 429-431.

38. Nonneman, L.E.Y.; Ponec, V. *Catal. Lett.* **1991**, *7*, 197-203.

39. Beitel, G.A.; de Groot, C.P.M.; Oosterbeek, H.; Wilson, J.H. *J. Phys. Chem. B* **1997**, *101*, 4035-4043.

40. Sato, K.; Inque, Y.; Kojima, I.; Miyazaki, E.; Yasumori, I. *J. Chem. Soc., Faraday Trans. 1* **1984**, *80*, 841-850.

41. Yates, I.C.; Satterfield, C.N. *Energy Fuels* **1991**, *5*, 168-173.

42. Ojeda, M.; Nabar, R.; Nilekar, A.U.; Ishikawa, A.; Mavrikakis, M.; Iglesia, E. *J. Catal.* **2010**, *272*, 287-297.

43. Iglesia, E. *Appl. Catal., A* **1997**, *161*, 59-78.

44. Bezemer, G.L.; Bitter, J.H.; Kuipers, H.P.C.E.; Oosterbeek, H.; Holewijn, J.E.; Xu, X.; Kapteijn, F.; van Dillen, A.J.; de Jong, K.P. *J. Am. Chem. Soc.* **2006**, *128*, 3956-3964.

45. Zeng, B.; Hou, B.; Jia, L.; Wang, J.; Chen, C.; Sun, Y.; Li, D. *ChemCatChem* **2013**, *5*, 3794-3801.

46. Umpierre, A.P.; de Jesús, E.; Dupont, J. *ChemCatChem* **2011**, *3*, 1413-1418.

47. den Breejen, J.P.; Radstake, P.B.; Bezemer, G.L.; Bitter, J.H.; Frøseth, V.; Holmen, A.; de Jong, K.P. *J. Am. Chem. Soc.* **2009**, *131*, 7197-7203.

48. van Santen, R.A.; Ghouri, M.M.; Shetty, S.; Hensen, E.M.H. *Catal. Sci. Technol.* **2011**, *1*, 891-911.

49. Joos, L.; Filot, I.A.W.; Cottenier, S.; Hensen, E.J.M.; Waroquier, M.; Speybroeck, V.V.; van Santen, R.A. *J. Phys. Chem. C* **2014**, *118*, 5317-5327.

50. Ishida, K.; Nishizawa, T. *Bull. Alloy Phase Diagrams.* **1990**, *11*, 125-137.

51. Enache, D.I.; Rebours, B.; Roy-Auberger, M.; Revel, R. *J. Catal.* **2002**, *205*, 346-353.

52. Sadeqzadeh, M.; Karaca, H.; Safonova, O.V.; Fongarland, P.; Chambrey, S.; Roussel, P.; Griboval-Constant, A.; Lacroix, M.; Curulla-Ferré, D.; Luck, F.; Khodakov, A.Y. *Catal. Today* **2011**, *164*, 62-67.

53. Ducreux, O.; Rebours, B.; Lynch, J.; Roy-Auberger, M.; Bazin, D. *Oil Gas Sci. Technol.* **2009**, *64*, 49-62.

54. Gnanamani, M.K.; Jacobs, G.; Shafer, W.D.; Davis, B.H. *Catal. Today* **2013**, *215*, 13-17.

55. Tan, B.J.; Klabunde, K.J.; Tanaka, T.; Kanai, H.; Yoshida, S. *J. Am. Chem. Soc.* **1988**, *110*, 5951-5958.

56. Tan, B.J.; Klabunde, K.J.; Sherwood, P.M.A. *J. Am. Chem. Soc.* **1991**, *113*, 855-861.

57. Morales, F.; Grandjean, D.; de Groot, F.M.F.; Stephan, O.; Weckhuysen, B.M. *Phys. Chem. Chem. Phys.* **2005**, *7*, 568-572.

58. Tyson, W.R.; Miller, W.A. *Surf. Sci.* **1977**, *62*, 267-276.

59. Zhao, Y.; Feltes, T.E.; Regalbuto, J.R.; Meyer, R.J.; Klie, R.F. *Catal. Lett.* **2011**, *141*, 641-648.

60. Williams, K.J.; Boffa, A.B.; Lahtinen, J.; Salmeron, M.; Bell, A.T.; Somorjai, G.A. *Catal. Lett.* **1990**, *5*, 385-394.

61. Barrault, J.; Guilleminot, A. *Appl. Catal.* **1986**, *21*, 307-312.

Chapter 4

The Role of ZrO2 in Promoting the Activity and Selectivity of Co-Based Fischer-Tropsch Catalysts

Abstract

The effects of Zr promotion on the structure and performance of Co-based Fischer-Tropsch synthesis (FTS) catalysts were investigated. Inclusion of Zr in the catalysts was found to increase the FTS turnover frequency and the selectivity to C_{5+} hydrocarbons and to decrease the selectivity to methane under most operating conditions. These improvements to the catalytic performance are a function of Zr loading up to an atomic ratio of Zr/Co = 1.0, above which the product selectivity is insensitive to higher concentrations of the promoter. Characterization of the Co nanoparticles by different methods demonstrated that the optimal Zr loading corresponds to half monolayer coverage of the Co surface by the promoter. Measurements of the rate of FTS at different pressures and temperatures established that the kinetics data for both the Zr-promoted and unpromoted catalysts are described by a two-parameter Langmuir-Hinshelwood expression. The parameters used to fit this rate law to the experimental data indicate that the apparent rate coefficient and the CO adsorption constant for the Zr-promoted catalysts are higher than those for the unpromoted catalyst. Elemental mapping by means of STEM-EDS provided evidence that Zr is highly dispersed over the catalyst surface and has limited preference for association with the Co nanoparticles. In situ X-ray absorption spectroscopy confirmed the absence of mixing between the Zr and Co in the nanoparticles. These results suggest that Zr exists as a partial layer of ZrO_2 on the surface of the Co metal nanoparticles. Accordingly, it is proposed that Zr promotion effects originate from sites of enhanced activity at the interface between Co and ZrO_2. The possibility that ZrO_2 acts as a Lewis acid to assist in CO dissociation as well as to increase the ratio of CO to H adsorbed on the catalyst surface is discussed.

4.1 Introduction

Fischer-Tropsch synthesis (FTS) continues to be an attractive option for the production of synthetic fuels.[1] Much of the interest in FTS originates from the wide variety of carbon sources that can be used to produce synthesis gas, such as biomass, coal, or natural gas.[2] Additionally, the hydrocarbons produced by FTS are compatible with existing vehicles and transportation infrastructure. Recent efforts have focused on the development of Co-based catalysts, which are ideal for producing the unbranched, long-chain hydrocarbons found in diesel fuels.[3] A long-standing objective of this research is suppressing the formation of methane while shifting the product distribution toward C_{5+} hydrocarbons. To this end, extensive work has been devoted to exploring the effects of metal oxides as promoters. Particular interest has been devoted to ZrO_2, dating back to the 1980s.[4-6] These early patents, which are well-summarized by Oukaci et al.,[7] mention the role of Zr in moderating Co-support interactions and improving the catalyst stability. The suitability of ZrO_2 as a support[8,9] or support modifier[10-12] has also been reported as well as the use of Zr as a promoter deposited along with the Co precursor onto supports during the

catalyst preparation. For example, using catalysts in which Co and Zr precursors were impregnated onto SiO_2, Ali et al. found that Zr increased the turnover frequency for CO consumption and that at high promoter loadings, the presence of Zr resulted in improvements to the product selectivity.[13] Similar studies have also demonstrated the ability of Zr promoters to enhance the activity and selectivity of Co-based FTS catalysts.[14-16] However, it has also been reported that Zr promotion did not cause significant changes to the intrinsic activity of the catalyst[17,18] and the product distribution.[19] Without detailed information about the catalyst structure, especially regarding the structural and electronic interactions between Co and Zr, it remains difficult to fully reconcile these conflicting accounts.

At present, the effects of Zr promoters on catalyst performance remain ambiguous, and few studies have attempted to address the deeper question of whether Zr has any role beyond being a structural promoter. Ali et al. speculated that Co active sites at the interface with ZrO_2 may exhibit enhanced activity toward CO hydrogenation,[13] a hypothesis that originates from studies of metal oxide-promoted Rh catalysts.[20,21] This hypothesis has also been used to rationalize the catalyst structure-performance relationships resulting from Mn promotion of Co-based FTS catalysts.[22,23] In this study, we demonstrate that Zr promotes the catalyst activity and selectivity in a manner analogous to promotion by Mn. Activity and selectivity data were collected over a range of operating conditions to assess the impact of Zr promotion on the intrinsic activity and CO adsorption properties of the catalyst. The composition and structure of the catalyst was probed by elemental mapping and X-ray absorption spectroscopy to determine the extent to which the Zr promoter interacts with the Co nanoparticles within the catalysts. These data are consistent with the formation of highly dispersed nanoclusters of ZrO_2 over the surface of the Co nanoparticles, which produces interface sites that have higher activity toward FTS and interact more strongly with CO than unpromoted Co sites. ZrO_2 was determined to be a more effective promoter for improving product selectivity than MnO when the fraction of Co active sites at interface with the metal oxide promoter was close to unity. Since ZrO_2 is a stronger Lewis acid than MnO, these findings support the hypothesis that the role of the metal oxide promoter is to facilitate the binding and dissociation of CO through Lewis acid-base interactions.

4.2 Experimental Methods

4.2.1 Catalyst Synthesis

All catalysts were prepared by incipient wetness impregnation of porous SiO_2 (PQ Corporation) using aqueous solutions of $Co(NO_3)_2$ and $ZrO(NO_3)_2$ (Sigma-Aldrich, 99.999% purity). The concentration of the solutions were adjusted so as to achieve the targeted Zr/Co atomic ratio and a Co loading of 10 wt% with respect to the sum of the weights of SiO_2 and Co. On a watch glass, 1 g of the SiO_2 was spread evenly and about 1 mL of the metal impregnation solution was then added dropwise to the SiO_2. The SiO_2 powder was then kneaded using a spatula until the SiO_2 had a dry, homogenous appearance, and the impregnation step was repeated until all the solution had been absorbed into the support. The SiO_2 with the deposited metals, henceforth referred to as the catalyst precursor, was dried for at least 12 h at ambient conditions. The catalyst precursor was then heated at 5 K/min in flowing H_2 to 723 K to decompose the deposited nitrates. After holding at 723 K for 2 h, the catalyst was cooled to ambient temperature, exposed

to 500 ppm O_2 to passivate the metallic Co, and stored in a desiccator until use. ICP-OES (Galbraith Laboratories, Inc.) was used to confirm the Co and Zr loadings. The sequence of catalyst preparation steps is depicted as a flow diagram in Scheme S4.1 of the Supporting Information.

4.2.2 Temperature-Programmed Reduction

Temperature-programmed reduction (TPR) was conducted in a quartz tube reactor by heating the reactor from 298 K to 850 K at 5 K/min under a flow of 1% H_2, 1% Ar, and 98% He (30 mL/min). The effluent from the reactor was analyzed by an MKS Minilab quadrupole mass spectrometer. The Ar in the feed was used as an internal standard to correct for variation in the reactor outlet flow rate during the temperature ramp. TPR measurements were made on the catalyst precursors and the passivated catalysts (i.e., prior to the first and second pretreatment steps). Control measurements were made with SiO_2 and $ZrO(NO_3)_2$ deposited onto SiO_2.

4.2.3 O_2 Titration

The extent of Co reduction was assessed by O_2 titrations of the passivated catalysts using the same apparatus that was used for TPR. For these measurements, pulses of air were dosed into the reactor and the reactor effluent was monitored by the mass spectrometer. In a typical experiment, a passivated catalyst sample was loaded into the reactor and subsequently reduced in H_2 at 723 K for 2 h. The system was then flushed with He to remove H_2. Once the H_2 signal on the mass spectrometer returned to baseline values, a pulse of air was injected into the reactor using a sample loop on a 6-port valve. This step was repeated until O_2 peaks with equivalent area were observed. The O_2 signal as a function of time was integrated to calculate O_2 uptake.

4.2.4 H_2 Chemisorption

The exposed surface area of the metallic Co nanoparticles after reduction was quantified by static H_2 chemisorption using a Micromeritics 3Flex surface characterization analyzer. The catalysts were reduced in H_2 at 723 K, evacuated below 0.01 mbar for 2 h, and then cooled to 373 K. A known quantity of H_2 was then introduced into the sample tube and the pressure was allowed to equilibrate. This step was repeated until the pressure within the sample tube reached 0.66 bar in order to collect an H_2 adsorption isotherm. The adsorption temperature of 373 K was selected based on reports of this temperature being optimal for H_2 chemisorption measurements on Co.[24] Moreover, the full H_2 uptake of a single adsorption isotherm, rather than the difference between initial and repeat isotherms, was used to determine metallic Co surface area because this method has been reported to correspond more closely to dispersions determined by TEM imaging and the expected 1/1 H/Co adsorption stoichiometry.[24]

4.2.5 In Situ X-Ray Absorption Spectroscopy

The oxidation state of the promoter and the local environments of Co and Zr were probed by in situ X-ray absorption spectroscopy (XAS) experiments. These data were collected at beamlines 5-BM (DND-CAT) and 10-BM (MRCAT) at the Advanced Photon Source synchrotron at Argonne National Laboratory.[25] All measurements were conducted in transmission mode using gas ionization detectors. A Si(111) crystal monochromator, which was detuned to reject higher harmonics, was used to adjust the energy of the X-ray beam. Metal references foils were used

for energy calibration and sample spectra alignment. For these experiments, the passivated catalysts were pressed into pellets inside a sample holder that was placed into an in situ reactor cell. The cell was heated by a clamshell tube furnace and connected to a gas inlet manifold to flow He, H_2, and CO over the samples. After measuring spectra of the catalysts in the passivated state at ambient temperature, the catalysts were reduced in H_2 at 723 K. Spectra of the reduced catalysts were collected at 723 K and at ambient temperature. The samples were then re-heated to 493 K and exposed to syngas (2/1 H_2/CO) for 6 h before measuring a final set of spectra. Data analysis of the XAS spectra was performed using the Demeter software family,[26] which uses IFFEFIT internally.[27]

4.2.6 STEM Imaging and Elemental Mapping

The passivated catalysts were prepared for imaging by electron microscopy by grinding the catalysts with a mortar and pestle, suspending the ground catalysts in ethanol, and then drop-casting 5 µl of the suspensions onto lacey carbon Cu TEM grids (Ted Pella, Inc.). The TEM grids were dried in a vacuum oven at 383 K for 1 h to fully evaporate the solvent. High-angle annular dark-field (HAADF) images of the Co nanoparticles were obtained using an FEI Titan electron microscope at the Molecular Foundry at the Lawrence Berkeley National Laboratory. Elemental maps were obtained by energy dispersive spectroscopy (EDS) using the same microscope, which was equipped with a Bruker, four-segment, silicon drift detector that collected the fluorescent X-ray spectrum from 0-20 keV with an energy resolution of 140 eV and a dispersion of 10 eV per channel. All imaging and mapping was done in scanning transmission mode with a 200 kV accelerating voltage. The Bruker Esprit software program was used to process and quantify the elemental map data using the Cliff-Lorimer method.[28]

4.2.7 CO Temperature-Programmed Desorption

CO temperature-programmed desorption (TPD) measurements were made using a Micromeritics AutoChem II 2920 instrument. First, a catalyst sample was loaded into a sample tube and reduced in H_2 at 723 K. The sample was then cooled under He to 323 K and a series of 10% CO pulses were injected into the He carrier gas that was flowing through the sample tube. After saturating the catalyst surface with adsorbed CO, the system was flushed with He for 15 min to allow physisorbed CO to desorb and to clear the apparatus of gas phase CO. Then, the temperature of the sample was ramped at 10 K/min to 873 K while the thermal conductivity of the sample tube effluent was monitored.

4.2.8 Catalytic Reactions

Fischer-Tropsch synthesis was performed using a fix-bed reactor to assess the effects of Zr promotion on catalyst activity and selectivity. A quartz reactor was used for experiments at atmospheric pressure, and a 316 stainless steel reactor was used for experiments at elevated pressure. Each reactor was heated using a tube furnace, and the reactor temperature was regulated by a PID control loop incorporating a thermocouple inserted into the catalyst bed. Gas flow through the reactors were regulated by mass flow controllers. Pressure in the stainless steel reactor was measured with an electronic pressure transducer and controlled by a diaphragm back-pressure regulator. Sample collection vessels, maintained at 403 K, were installed below both reactors to collect liquid products, and the gaseous products were routed to an Agilent

6890N gas chromatograph for online composition analysis. The inlet and outlet of the reactors as well as all tubing between the liquid collection vessels and the gas chromatograph were heated to 503 K to prevent condensation of water and long-chain hydrocarbons.

Each experiment started with loading passivated catalyst into the reactor. The catalyst was reduced in H_2 by heating from 298 K to 723 K at the rate of 5 K/min. The reactor was then flushed with He and cooled to 493 K before starting the FTS reaction. The catalyst was aged for 12 h in syngas (2/1 H_2/CO), after which the catalyst activity had stabilized. Following the aging step, measurements were conducted at various reaction conditions to observe the effects of temperature, reactant partial pressures, and space velocity. The background activities of the reactor, SiO_2, and ZrO_2 deposited onto SiO_2 were found to be negligible, and the absence of transport limitations was determined by satisfying the Weisz-Prater criterion[29] and by carrying out a series of activity measurements at different space velocities and catalyst bed loadings. CO_2 production rates were below detectable levels, and oxygenates were less than 1% of the product fraction on a molar carbon basis.

The conversion of CO based on CO consumed, X_{CO}^{CO}, was calculated according to eq. 4.1, where C_{CO} and C_{Ar} are the molar concentrations of CO and Ar in the reactor effluent, respectively, and C_{CO}^0 and C_{Ar}^0 are the molar concentrations of the same species in the reactor inlet feed. The conversion was used to calculate the rate of CO consumption per gram of Co, given as $-r_{CO}$ in eq. 4.2, where Q_{in} is the volumetric flow rate of the reactor inlet feed and W_{Co} is the mass of Co in the catalyst bed. Ar was used as an internal standard and the concentrations of CO and Ar were determined using from the thermal conductivity detector response of the gas chromatograph.

$$X_{CO}^{CO} = \frac{\left(C_{CO}^0/C_{Ar}^0\right) - C_{CO}/C_{Ar}}{C_{CO}^0/C_{Ar}^0} \tag{4.1}$$

$$-r_{CO} = \frac{X_{CO}^{CO} CO_{CO}^0 Q_{in}}{W_{Co}} \tag{4.2}$$

The CO conversion based on products formed, X_{CO}^{HC}, and the rate of hydrocarbon production per unit mass of Co on a molar C basis, r_{HC}, was determined from eqs. 4.3 and 4.4, respectively. Here, Q_{out} is the volumetric flow rate of the reactor effluent and C_i is the molar concentration of hydrocarbons containing i carbon atoms. CO consumption rates were relied upon for reaction conditions giving high conversions and significant liquid product selectivities, whereas the hydrocarbon production rates were more accurate at low conversions and conditions where the selectivity to wax products was negligible.

$$X_{CO}^{HC} = \frac{Q_{out} \sum_{i=1}^{n} i C_i}{Q_{in} C_{CO}^0} \tag{4.3}$$

$$r_{HC} = \frac{Q_{out} \sum_{i=1}^{n} i C_i}{W_{Co}} \tag{4.4}$$

4.3 Results

4.3.1 Temperature-Programmed Reduction

The consumption of H_2 during the first and second reduction steps of the Zr-promoted (Zr/Co = 1.0) and unpromoted (Zr/Co = 0) catalysts is shown in Figure 4.1, and data for the byproducts formed are provided in Figure S4.1 of the Supporting Information. As shown in Figure S4.1C, the decomposition of Co nitrate deposited onto SiO_2 produces peaks corresponding to NO, H_2O, and NO_2 between 430 K and 580 K. When Zr oxynitrate was deposited onto SiO_2 along with the Co nitrate, these decomposition product peaks occurred at higher temperatures between 450 K and 620 K, which provides evidence for chemical interactions occurring between the Co and Zr precursors. The appearance of a peak at 395 K in the TPR profile for the co-impregnated catalyst precursor corresponds to Zr oxynitrate decomposition, which was observed in the profile for the control sample consisting of the Zr precursor deposited onto SiO_2 (Figure S4.1D). Interestingly, the TPR data for the control sample containing Zr oxynitrate had a peak 652 K, which was not present in the data for the co-impregnated catalyst precursor. On the basis of thermal gravimetric analysis, this peak has been attributed to restructuring of decomposed Zr precursor into crystalline ZrO_2.[30] However, the mass spectrometry data of the present study show evidence for NO production at this temperature, which demonstrates that full decomposition of Zr oxynitrate requires temperatures above 700 K. The absence of this peak from the co-impregnated catalyst precursor may indicate that the presence of the Co precursor lowers the temperature at which the Zr precursor fully decomposes.

The TPR profiles for the second reduction step of the Zr-promoted and unpromoted catalysts, which involved the pretreatment of the passivated catalysts prior to conducting FTS reactions, are shown in Figure 4.1. For the unpromoted catalyst, a single peak corresponding to the formation of Co metal is observed at 571 K. The data for the Zr-promoted catalyst showed two reduction events, possibly related to Co_3O_4 reduction to CoO and CoO reduction to Co metal at 485 and 680 K, respectively. Both catalysts also consumed H_2 over a broad temperature range starting at 650 K for the unpromoted catalyst and 775 for the promoted catalyst. Since slightly higher extents of reduction for the unpromoted catalyst were observed when the second reduction took place at 723 K compared to 673 K, it is reasonable to assume that this additional H_2 consumption is associated with the reduction of Co species that interacted strongly with the support (or the promoter for the Zr-promoted catalyst). This interpretation is corroborated by studies of Co reduction on both SiO_2[31] and Al_2O_3,[32] which report the formation of mixed oxides of Co and the support that require similar temperatures to reduce. On the basis of the temperature required to decompose the Zr precursor and to form Co metal in the Zr-promoted catalyst, a reduction temperature of 723 K was chosen for both catalyst pretreatment steps used in this study.

4.3.2 O_2 Titration and H_2 Chemisorption

O_2 titration uptakes for the reduced Co-ZrO_2 catalysts are presented in Table 4.1, and the corresponding extents of Co reduction are given in Table 4.2. To calculate the fraction of Co in the metallic state following the reduction step, it was assumed that the reduced catalysts consisted of Co(0) and CoO, which were fully oxidized to Co_3O_4 during the O_2 titrations.

Additionally, the promoter was assumed to be in the form of ZrO_2 and to not undergo partial reduction during the pretreatment step, which was confirmed by XANES. Accordingly, the fraction of Co that was metallic after reduction, $f_{Co,metal}$, was calculated from eq. 4.5 where U_{O_2} is the O_2 molar uptake and N_{Co} is the total moles of Co in the catalyst. For the unpromoted catalyst, 87% of the Co was reduced to Co metal following the second reduction pretreatment step. The extents of reduction decreased monotonically with Zr loading such that only 54% of the Co in the catalyst prepared with Zr/Co = 1.0 was metallic following reduction.

$$f_{Co,metal} = \frac{2U_{O_2} - \left(\frac{4}{3} - 1\right)N_{Co}}{N_{Co}} \tag{4.5}$$

H_2 uptake values followed a more complex trend possibly owing to H spillover onto the promoter, a documented phenomenon for metal nanoparticles in contact with ZrO_2.[13,33,24] No uptake of H_2 onto control samples consisting of SiO_2 and ZrO_2 deposited onto SiO_2 was measured, but the interface between Co and ZrO_2 in the promoted catalysts may provide sites through which H can transfer onto the ZrO_2. For catalysts with Zr/Co ratios between 0.01 and 0.1, the H_2 uptakes per gram of catalyst were comparable to that for the unpromoted catalyst. Taking into account the lower extents of reduction of these catalysts, the H_2 uptakes per mole of metallic Co were up to 10% higher than that of the unpromoted catalyst despite all catalysts having similar average nanoparticle sizes. This is an expected result if H spillover onto the ZrO_2 occurred. Nevertheless, the catalyst prepared with Zr/Co ratios greater than 0.25 showed a decrease in H_2 uptake as Zr loading increased, which is consistent with blockage of the Co surface by ZrO_2. Assuming this blockage effect dominated over spillover at high Zr loading, it would make the most sense to use the total H_2 uptake when determining the number of Co active sites for catalysts within this loading regime, which is the approach used for this work. We note that this assumption may underestimate the turnover frequencies of the Zr-promoted catalysts with Zr/Co ratios greater than 0.25.

4.3.3 In Situ X-Ray Absorption Spectroscopy

Figure 4.2 shows the X-ray absorption near-edge structure (XANES) spectra at the Zr K-edge for the Zr-promoted Co catalysts acquired after passivation, reduction, and reaction. For all Zr loadings, the Zr edge energies for the passivated catalysts were consistent with that for the ZrO_2 standard, which implies that the apparent oxidation state of the Zr in these catalysts is 4+. Furthermore, no shifts in the Zr edge energy were observed following the reduction at 723 K or after subsequent exposure to syngas at 493 K for 6 h. This confirms that the ZrO_2 did not reduce, which is expected considering that unsupported ZrO_2 does not reduce in H_2 even at much higher temperatures.[35] However, there were noticeable differences in the shape of the XANES spectra as a function of Zr loading. Although the spectra of the catalysts with higher Zr loadings (e.g., Zr/Co = 1.0) matched that of the monoclinic ZrO_2 standard reasonably well, the lower loading sample (Zr/Co = 0.1) had a more prominent edge feature at 18,003 eV and differences in the relative peak heights immediately after the edge. These features are consistent with the reported XANES spectrum for tetragonal ZrO_2.[36] Hence, Zr appears to adopt a tetragonal crystal structure at low loadings, which is perhaps related to Zr being atomically dispersed over the SiO_2 surface, and higher loadings result in the emergence of monoclinic ZrO_2 structures. The transition of the

XANES spectrum from that corresponding to the tetragonal structure to that for a predominantly monoclinic structure as a function of Zr loading is shown with greater detail in Figure S4.2 of the Supporting Information.

Analysis of the extended X-ray absorption fine structure (EXAFS) was carried out to gain additional structural information about the Co and Zr atoms in the catalysts. The EXAFS spectra for a Zr-promoted catalyst (Zr/Co = 1.0) and for an unpromoted catalyst, both in the reduced state, are shown in Figure 4.3. Fits of the data, represented by the dashed black lines, were performed for the data points within the shaded gray region of the plots. The modeling was done using a single energy shift for all paths and symmetric path expansion terms (i.e., $k*r_{eff}$) for each crystal structure present in the fit. False peaks at radial distances less than 1 Å are visible in the Zr K-edge data, but it was not possible to remove them by changing the background function parameters without significantly attenuating the amplitude of the Zr-O scattering path. In Figure 4.3A, the spectra collected at the Co K-edge for the both catalysts contain peaks corresponding to scattering paths in Co metal (Co-Co at R = 2.1 Å) and CoO (Co-O at R = 1.6 Å and Co-Co at R = 2.6 Å). In the case of the Zr-promoted catalyst, a satisfactory fit was achieved without needing to substitute Zr atoms into the Co metal and CoO structures used to calculate the scattering paths. This finding is consistent with the Zr promoter not intermixing into the Co-containing phases in significant quantities. A major difference between the spectra for the two catalysts is that the magnitude of the peaks due to scattering in CoO are much larger relative to the magnitude of the peak for the first coordination shell of Co metal in the Zr-promoted catalyst than in the unpromoted catalyst. This feature suggests that a greater fraction of Co in the unpromoted catalyst was in the metallic state than in the Zr-promoted catalyst, reinforcing the conclusion based on O_2 titrations that the Zr-promoted catalyst had a lower extent of reduction following pretreatment.

Figure 4.3B shows a comparison between the Zr K-edge EXAFS spectrum and that of monoclinic ZrO_2. Both spectra contain two major peaks in the shaded region corresponding to the first and second shell scattering paths. For the reference material, these peaks were clearly attributed to the Zr-O (R = 1.58 Å) and Zr-Zr (R = 3.01 Å) scattering paths of ZrO_2. The first peak of the spectrum for the Zr-promoted catalyst matches expectations for the Zr-O scattering path, but the second shell peak is highly attenuated relative to the magnitude of the first peak. The smaller second peak suggests that there are fewer neighboring Zr atoms in this shell compared to the structure of bulk ZrO_2, which would be the case if the Zr in the promoted sample were highly dispersed. Hence, these data suggest that even at this relatively high loading of promoter, the Zr did not form appreciable quantities of multilayered ZrO_2.

4.3.4 Electron Microscopy

Electron microscopy was used to gain information about the size and structure of the Co nanoparticles as well as the location of the promoter relative to that of the Co. Table 4.1 lists the surface mean diameters of the Co nanoparticles as determined by TEM imaging for catalysts prepared with various loadings of Zr. The average particle sizes and the standard deviations of the size distributions were found to be independent of Zr loading. For all catalysts, the particle sizes were close to 10 nm, which corresponds to Co dispersions of about 9%. Despite having a much larger atomic number than Co and Si, Zr was not identifiable in the HAADF-STEM images,

which necessitated the use of analytical TEM imaging to locate the promoter. A representative image of the Zr-promoted catalyst prepared with Zr/Co = 1.0 is provided as Figure 4.4A. In this STEM-EDS elemental map, a number of Co nanoparticles, appearing as green clusters, are dispersed over a relatively thin region of the SiO_2 support. The promoter, which is represented visually by the color red, is shown to be spread across the support without correlation with the positions of the Co nanoparticles. Preferential spatial association between Co and Zr was not found in the catalysts prepared with lower loadings of Zr relative to Co. This qualitative finding was observed in all the elemental maps acquired for this study, and no evidence for homogenous, bimetallic nanoparticles was observed.

The conclusion that Zr does not associate preferentially with the Co was reinforced by the quantification of the nanoparticle compositions. For this analysis, the pixels constituting a Co nanoparticle and a 1 nm buffer around the nanoparticle were selected and the X-ray spectrum of these pixels were quantified by the Cliff-Lorimer method to determine the composition of the nanoparticle. The data from a set of images giving a sample size of over 100 nanoparticles were used to construct a histogram of nanoparticle compositions. This is presented in the form of nanoparticle Zr/Co atomic ratios for the catalyst prepared with Zr/Co = 1.0 in Figure 4.4B. The nanoparticle composition distribution is modeled accurately by a Gaussian function, and the median of the distribution is 0.63. The discrepancy between the average nanoparticle composition (Zr/Co = 0.63) and the bulk composition (Zr/Co = 1.0) indicates that a significant portion of the Zr promoter was not in contact with the Co nanoparticles. With the tendency of the Zr to spread over the support, a material balance calculation would overestimate the amount of promoter in contact with the Co given that the EDS maps are two-dimensional projections of a three-dimensional, porous material. Nevertheless, this analysis agrees well with the qualitative conclusions derived from visual inspection of the elemental maps.

4.3.5 CO Temperature-Programmed Desorption

The CO TPD profiles for a Zr-promoted catalyst (Zr/Co = 1.0) and for an unpromoted catalyst are shown in Figure 4.5. A profile for the SiO_2 support was also collected and used for background subtraction to remove the contribution from SiO_2 dehydroxylation, which occurred at temperatures above 700 K. ZrO_2 deposited onto SiO_2 did not show any CO uptake or additional desorption peaks. The unpromoted catalyst exhibited CO desorption peaks at 435 and 560 K, which establishes that there are at least two distinct Co sites on which CO can adsorb. Estimates of CO heats of adsorption were made using the Redhead model[37] assuming a typical pre-exponential factor of 10^{13} s^{-1}. These calculations suggest that the first desorption peak corresponds to a desorption activation energy of 93 kJ/mol whereas the higher temperature peak corresponds to 119 kJ/mol. The Zr-promoted catalyst had a prominent desorption peak at 460 K, which corresponds to a desorption activation energy of 98 kJ/mol. A smaller desorption peak also appeared at 680 K. The latter peak, which corresponds to a desorption activation energy of 143 kJ/mol, indicates the presence of a much more strongly bound CO species when the catalyst is Zr-promoted. While the desorption activation energies of the unpromoted catalyst are similar to typical CO heats of adsorption on Co, the activation energy for desorption of the strongly bound CO on the Zr-promoted catalyst is significantly higher than that reported for unpromoted Co.[38,39]

4.3.6 Catalyst Activity

Measurements were made of the rate of FTS at 493 K under differential conversion using different partial pressures of H_2 and CO in order to determine the rate law for the kinetics of CO consumption over Zr-promoted catalysts. As shown in Figure 4.6 for the catalyst prepared with Zr/Co = 1.0, it was found that CO consumption rates scaled linearly with the H_2 partial pressure and had a negative first-order dependence on the CO partial pressure. Within the data set for the CO partial pressure variation, the CO consumption rates increased monotonically as the CO partial pressure decreased. Since the rate must go to zero as P_{CO} approaches zero, a rate maximum must exist, which the data suggest occurs between 0 and 0.5 bar. All of these observations are in accordance with the two-parameter, Langmuir-Hinshelwood expression given by eq. 4.6.[40] In this equation, $-r_{CO}$ is the rate of CO consumption, a is an apparent rate coefficient, b is the CO adsorption constant, P_{CO} is the CO partial pressure, and P_{H_2} is the H_2 partial pressure. The unpromoted catalyst follows the same rate law as reported in our recent studies of similar catalysts.[23]

$$-r_{CO} = \frac{abP_{CO}P_{H_2}}{(1+bP_{CO})^2} \tag{4.6}$$

Using this rate law, the dependence of CO consumption rates on total pressure and temperature was investigated. The unpromoted catalyst was found to be more active than the catalyst with Zr/Co = 1.0 at most conditions when compared on the basis of rates of CO consumption per gram Co (Figure S4.3 of the Supporting Information). This was most evident in the high pressure regime because the Zr-promoted catalyst was subject to stronger CO inhibition than the unpromoted catalyst. However, a different perspective is revealed when the H_2 uptake data from Table 4.1 is used to express the rates in terms of turnover frequencies on the basis of the number of Co atoms accessible to H_2 chemisorption. These data are shown in Figure 4.7 for the Zr-promoted (Zr/Co = 1.0) and unpromoted (Zr/Co = 0) catalysts. For most conditions, the Zr-promoted catalyst exhibits higher turnover frequencies than the unpromoted catalyst, which demonstrates that the promoter increases the intrinsic activity of the active sites that participate in FTS.

A deeper understanding of the effect of Zr on the rate law parameters was obtained by examining the parameters a and b appearing in the rate law. These parameters were obtained by nonlinear least-squares regression of the rate data, the fits are represented by the solid lines in Figures S4.3 and 4.7. The appropriateness of the rate law for modeling these kinetics data was confirmed by the high R^2 values of the parity plots in Figure S4.4 of the Supporting Information. The apparent rate coefficients and CO adsorption constants for the Zr-promoted catalyst (Zr/Co = 1.0) and unpromoted catalyst at 483, 493, and 503 K are given in Table S4.1 of the Supporting Information. At all temperatures, the apparent rate coefficients for the Zr-promoted catalyst are 3-4 times larger than those for the unpromoted catalyst, which demonstrates that CO consumption per Co atom is faster on the promoted catalyst. The CO adsorption constants for the Zr-promoted catalyst are substantially larger than those of the unpromoted catalyst, which implies that the presence of the Zr leads to a stronger interaction between the adsorbed CO and the catalyst surface.

Arrhenius plots of the apparent rate coefficients and CO adsorption constants, presented in Figure S4.5 of the Supporting Information, were used to obtain estimates of the pre-exponential and energetic parameters of the constants according to eqs. 4.7 and 4.8. In these equations, A is the pre-exponential factor for the apparent rate coefficient, E_A is the apparent activation energy, $K_{CO,0}$ is the pre-exponential factor for the adsorption constant, Q_{CO} is the CO heat of adsorption, R is the ideal gas constant, and T is the reaction temperature. Table 4.3 shows that the apparent activation energy for the unpromoted catalyst is about 15 kJ/mol larger than that of the Zr-promoted catalyst and the CO heat of adsorption for the Zr-promoted catalyst is about 27 kJ/mol larger than that of the unpromoted catalysts. The pre-exponential factors for the Zr-promoted catalyst were smaller than those for the unpromoted catalyst

$$a = Ae^{\frac{-E_A}{RT}} \tag{4.7}$$

$$b = K_{CO,0}e^{\frac{Q_{CO}}{RT}} \tag{4.8}$$

Although the rate law used in this study modeled the catalyst activity quite well in the limit of 0% CO conversion, discrepancies emerged at higher conversion. The rate law implies that CO consumption should decrease as conversion increases owing to the depletion of the CO and H_2. As shown in Figure 4.8, this behavior was observed qualitatively with the Zr-promoted catalyst at 1 bar; however at 10 bar, the catalyst activity was independent of CO conversion. These findings are similar to those previously reported for unpromoted and Mn-promoted Co-based catalysts.[41] A likely explanation for these effects is the higher partial pressure of water encountered when operating the reactor at a higher total pressure. Multiple researchers have reported that the formation of water has a positive effect on FTS activity for certain ranges of water partial pressure.[42,43] Additionally, the re-adsorption of olefins onto the catalyst surface and their incorporation into or initiation of chain growth may contribute to the positive deviation from the rate law as conversion increases. We have demonstrated previously that this reaction pathway is negligible at low pressure and significant at high pressure for Co/SiO_2 and Mn-promoted Co/SiO_2.[41]

4.3.7 Catalyst Selectivity

The dependence of catalyst selectivity on Zr loading was explored at 1 bar and 493 K under differential conversions using a series of catalysts prepared with Zr/Co ratios between 0 and 2 (Figure 4.9). It was found that methane selectivity decreased from about 35% to 14% as the Zr/Co ratio increased from 0 to 1.0. Over this range of Zr loading, the C_{5+} selectivity increased from 31% to 59%. Figure 4.9B shows the increase in the carbon number-weighted olefin to paraffin ratio of the C_2-C_4 fraction as a function of Zr loading. Both the carbon number selectivities and the olefin to paraffin ratio became insensitive to the promoter loading at a Zr/Co ratio close to 1. This diminishment in the effects of the promoter with increasing promoter loading is quite similar to that reported for Mn-promoted catalysts.[23] However in the case of Zr promotion, ten times as much promoter on an atomic basis is required to reach the selectivity plateau.

Experiments at elevated pressure and different temperatures were also conducted. As shown in Figure 4.10, selectivity toward methane decreased and that for C_{5+} increased as total

pressure increased from 1 bar to 10 bar for both catalysts. The effect was more pronounced for the unpromoted catalyst, which has about twice the selectivity toward methane and half as much toward C_{5+} at 1 bar compared to the Zr-promoted catalyst. Increasing the pressure gave diminishing improvements to the product distribution, and at 10 bar the carbon number selectivities were relatively insensitive to pressure. Still, the Zr-promoted catalyst had a lower methane selectivity (10%) and higher C5+ selectivity (79%) than the unpromoted catalyst (16% and 73%, respectively) at 10 bar. More detailed presentations of the methane, C_2-C_4, and C_{5+} selectivity data for the Zr-promoted and unpromoted catalysts are given in Figure S4.6 of the Supporting Information. Higher temperature elevated the selectivity toward methane at the expense of C_{5+} selectivity for both catalysts, and the effects of pressure on the carbon number selectivities were similar at all temperatures.

The effects of CO conversion on product selectivity were dependent on the total pressure at which the reaction was operated. Figure 4.11 shows the dependence of methane and C_{5+} selectivities on CO conversion at pressures ranging from 1 bar to 10 bar for the Zr-promoted catalyst. At atmospheric pressure, the selectivities did not change as CO conversion increased, which is identical to the behavior seen with the unpromoted and Mn-promoted catalysts.[41] At higher pressures, the methane selectivity decreased and C_{5+} selectivity increased as the conversion increased. This effect was quite substantial at 10 bar for which methane selectivity decreased from 10 % to 5.3% and C_{5+} selectivity increased from 80% to 89%. An extrapolation of these data suggest that C_{5+} selectivities higher than 95% could be achieved by operating at a CO conversion higher than 50%, which is quite typical for industrial FTS reactors.

4.4 Discussion

4.4.1 Effects of Zr Promotion on the Co Nanoparticle Structure

The empirical evidence presented above shows that promotion of Co/SiO_2 with ZrO_2 has an effect on the intrinsic activity of Co and on the distribution of products. To identify the cause for these effects, it is important to first consider whether or not ZrO_2 affects the Co nanoparticle size and morphology. It is well-established that turnover frequencies and product selectivities are sensitive to particle size when the Co nanoparticle diameters are smaller than 6 to 10 nm.[44-46] Accordingly, it is important to have the average Co particle size close to 10 nm in order to maximize activity per gram Co while avoiding particle size effects. The catalysts used for this study were prepared by co-impregnation of Co and Zr precursors onto SiO_2 followed by direct reduction in H_2. This catalyst preparation strategy was motivated by our recent investigations of Co-MnO catalysts which have demonstrated that this approach results in spherical Co nanoparticles that are insensitive to promoter loading and are close to 10 nm in diameter.[23] The same phenomenon was observed for the Co-ZrO_2 catalysts of the present study where the average particle sizes for all catalysts were within 2 nm of 10 nm and the predominant nanoparticle geometry was spherical. Hence, the absence of particle size and shape differences as a function of Zr loading eliminates one source of structural promotion effects.

Another aspect of the Co nanoparticle structure that must be considered is the oxidation state of Co and whether or not the presence of Zr leads to the formation of mixed phases of Co and Zr. The local environment of the Co atoms in the Zr-promoted catalyst as determined by

EXAFS is consistent with the Co being a mixture of CoO and Co metal phases. Thus, there are no indications of neighboring Zr atoms within the coordination shells around the Co atoms. Likewise, the Zr spectra did not show signs of neighboring Co atoms. These data suggest that the presence of Co-Zr mixed oxides after reduction does not appear to be substantial. Any ZrO_2 in contact with the Co would likely be on the surface of the nanoparticles rather than mixed into the nanoparticle bulk. Evidence for this morphology in the Co EXAFS spectrum is not detectable because only about 5% of the Co was on the surface of Co metal nanoparticles. Even if the Co nanoparticles were encapsulated by ZrO_2, the signals from the oxidized Co and the subsurface metallic Co would obscure the signal from the Co that coordinates with ZrO_2. The Zr EXAFS spectrum would also not reveal signs for this morphology because the tendency of the Zr to disperse over the SiO_2 support would result in Si rather than Co atoms dominating in the second coordination shell of Zr. Nevertheless, interactions between the Co and Zr could be inferred from the TPR profiles in which the temperature of Co reduction increased markedly with inclusion of the Zr promoter.

The higher Co reduction temperature and lower Co extent of reduction for the Zr-promoted catalyst is unexpected given the abundance of literature reporting that Zr facilitates the reduction of Co. Feller et al.[14] and Moradi et al.[15] have shown that Zr promotion resulted in substantial improvements to the extents of Co reduction for SiO_2-supported Co. These observations were rationalized in terms of the replacement of Co-Si interactions by weaker Co-Zr interactions, thereby permitting Co atoms to separate more readily from the oxide phase and form metallic nanoparticles. More recently, these reducibility trends were observed for Co on Al_2O_3.[17] However, not all reports claim that Zr improves Co reducibility. For example, Ali et al. have noted that the addition of Zr to SiO_2-supported Co catalysts did not cause significant changes to the TPR profiles and extents of Co reduction.[13] Likewise, Rohr et al. have reported that no improvements in Co reducibility result from Zr promotion of Al_2O_3-supported catalysts.[18] Variations in the level of interaction between Co and Zr due to differences in catalyst preparation methods or pretreatment conditions could account for the assortment of effects that Zr promotion has been reported to have on Co reducibility. In the present study, the coverage of the Co nanoparticle surface by a partial layer of ZrO_2 likely impedes the reduction of Co.

4.4.2 Structure and Chemical State of the Zr Promoter

Prior work on Zr promotion has assumed, either by chemical intuition or thermodynamics calculations, that Zr forms ZrO_2. However, it has been reported that Zr can undergo partial reduction in certain systems so it is important to verify whether ZrO_2 persists following reduction and during reaction.[47] As demonstrated by the in situ XANES data, the Zr promoter had an apparent oxidation state of 4+, which did not change during pretreatment in H_2 or with exposure to syngas. These data indicate that, within the limits of detection by XANES, the promoter was present as oxide structures, for which ZrO_2 is the most likely candidate at all levels of Zr promotion. On the basis of the edge features in the Zr XANES spectrum, it appears that the promoter transitions from a tetragonal to monoclinic structure as its loading increases. However, this phenomenon is not obviously connected to the observed effects of Zr promotion. Measurable improvements in the product distribution occurred as the Zr loading increased while ZrO_2 was present in the tetragonal phase, and the ZrO_2 became predominantly monoclinic before the product selectivity became insensitive to Zr loading at higher loadings.

The monoclinic structure of the promoter at a Zr/Co ratio of 1.0 was consistent with analysis of the EXAFS data (Figure 4.3). The diminished intensity of the second shell peak relative to the first shell peak is consistent with the ZrO_2 being highly dispersed. However, the fit of the second peak in the spectrum of the Zr-promoted catalyst was of notably lower quality than that of the first shell. Various alternative structures to monoclinic ZrO_2 were considered as a result. Working from the assumption that the Zr was highly dispersed over the SiO_2 support, substitutions of Si for Zr atoms in the second shell of ZrO_2 were made. For these fits, additional parameters for the path degeneracy, path expansion length, and mean squared displacement of the Si were introduced. Substitution of Si atoms into the ZrO_2 structure yielded minor improvements to the fit, which is expected considering the presence of additional fitting parameters. With no clear boundary between meaningful fit improvements and overfitting of the data, the identity and position of the second shell neighboring atoms remains ambiguous. Nevertheless, the most plausible fits involving Si yielded second shell path degeneracies that were about half of the values for the bulk structure, which is suggestive of monolayer, or near monolayer, coverage of ZrO_2 over the catalyst surface.

The hypothesis that Zr is highly dispersed over the entire catalyst surface agrees well with the elemental maps obtained by STEM-EDS. The representative map shown in Figure 4.4A illustrates the lack of spatial association between the Zr and Co as well as an absence of ZrO_2 nanoparticles. Most studies of Zr-promoted Co catalysts report a similar lack of large ZrO_2 domains, which generally has been inferred from the lack of peaks corresponding to ZrO_2 in XRD spectra.[48] The extent to which ZrO_2 associates with the Co versus the support has been investigated less rigorously though. The nanoparticle composition histogram given in Figure 4.4B indicates that less Zr is in contact with the nanoparticles than would be expected from the bulk Zr/Co ratio of the catalyst, which is a clear sign that partial segregation between the Co and ZrO_2 occurred. While quantitative elemental mapping is quite useful in this regard, the technique is less than adequate for inferring what fraction of the nanoparticle surface was covered by the promoter. To address this question, H_2 uptake and TEM particle size data were used to estimate θ_{Zr}, the fraction of the nanoparticle surface that was inaccessible for H_2 chemisorption due to coverage by ZrO_2. These values were calculated for catalysts with different Zr loadings using eq. 4.9, where U_{H_2} is the molar H_2 uptake and D is the Co nanoparticle dispersion determined by TEM imaging. The unpromoted catalyst showed good agreement between the dispersion determined by TEM and by H_2 chemisorption so no corrections were applied for blockage of the nanoparticle surface by the support.

$$\theta_{Zr} = 1 - \frac{2U_{H_2}}{N_{Co} f_{Co,metal} D} \tag{4.9}$$

As reported in Table 4.2, the fraction of the nanoparticle surface covered by ZrO_2 increases with Zr loading such that the catalyst prepared with Zr/Co = 1.0 is half covered by the promoter. The apparent lack of ZrO_2 coverage in the catalysts prepared with Zr/Co ratios less than 0.25 may have been an artifact of H_2 spillover onto the ZrO_2. While this effect would also be present in the catalysts prepared with higher Zr loading, the decreased Co metal surface area of these catalysts appears to dominate. To determine whether these coverage estimates are reasonable, a separate validation was performed using N_2 adsorption isotherms. Here, the

surface area that ZrO_2 would occupy assuming it forms a partial monolayer was compared to the total catalyst surface area determined by BET surface area analysis. The quantity of Zr in the Zr/Co = 1.0 catalyst would have a surface area of 112 m^2/g_{cat} if it were in the form of single layer of ZrO_2, and the surface area of the unpromoted catalyst was determined to be 238 m^2/g_{cat}. These values suggest that 47% coverage of the catalyst surface by ZrO_2, which is quite close to being a half monolayer in agreement with the estimates from TEM and chemisorption data.

The primary motivation for direct reduction of the catalyst precursors in H_2, rather than first calcining them in air, was our finding that the former pretreatment leads to better spatial association between Co and MnO in Mn-promoted Co/SiO_2.[22] In contrast to Zr, Mn has a high affinity for Co and deposits almost exclusively onto the Co nanoparticle surface until a significant fraction of the surface is covered. While the same catalyst pretreatment approach was used in the present work, it was found that Zr has a much lower affinity for associating with Co compared with SiO_2. We propose that the limited association between the two metals may be related to the relative inability of their precursors to form mixed oxide phases. Co(II) and Zr(IV) have similar ionic radii so there is more reason to think that lattice mismatches may play a role in this phenomenon. CoO and MnO both adopt the rock salt structure, but ZrO_2 has a monoclinic crystal structure under most conditions. With a sufficiently high loading of Zr, the weaker tendency of the ZrO_2 to associate with the Co can be overcome and a substantial interface between Co and the ZrO_2 can form.

4.4.3 Influence of Zr Promotion on Activity and the Reaction Mechanism

Although the activity for Zr-promoted Co-based catalysts at atmospheric[13,17] and elevated[14] pressure has been reported previously, the evaluation of rate laws with the aim of identifying the effects of the promoter on the rate parameters has not been conducted yet. In this study, it was determined that the Zr-promoted catalyst kinetics follow a rate law that is consistent with H-assisted CO dissociation as the rate-limiting step. As reported previously, the same rate law holds for the unpromoted catalyst.[23] Differences in the activities of the Zr-promoted and unpromoted catalysts originate from differences in the apparent rate coefficients and CO adsorption constants. For the Zr-promoted catalyst, both these parameters, a and b, are larger than those for the unpromoted catalyst. The larger apparent rate coefficient, a, suggests that ZrO_2 near the Co plays a role in facilitating CO dissociation, but this parameter combines the rate constant for the rate determining step along with the H_2 adsorption constant and the equilibrium constants for any quasi-equilibrated elementary reactions in the mechanism that occur prior to the rate determining step. Consequently, it is difficult to attribute the large apparent rate coefficient for the Zr-promoted catalyst solely to accelerated CO dissociation. A more important contributor to the differences in the turnover frequencies is the CO adsorption constant, which was 3 to 4 times larger with Zr promotion depending on the reaction temperature.

The appearance of the CO adsorption constant in the numerator of the rate law results in a significant increase of the turnover frequency for the Zr-promoted catalyst at low pressures. At 10 bar, the CO adsorption constant in the denominator of the rate law dominates such that Zr promotion yields turnover frequencies comparable to those for the unpromoted catalyst, especially at lower temperatures. These trends demonstrate that whether the promoter

increases or decreases the catalytic activity depends significantly on the temperature and pressure at which the system is operated. The heat of CO adsorption on the Zr-promoted catalyst, determined by parameter fitting of the kinetics data, is twice the magnitude of that for the unpromoted catalyst. However, these values are much smaller than the heats of adsorption inferred from the CO TPD profiles by the Redhead model. These differences likely result from the differences in CO surface coverages that occur during steady-state FTS and TPD measurements. Whereas the Co surface is largely saturated by CO under FTS, the catalyst surface becomes comparatively vacant during a desorption profile. Lateral interactions between neighboring CO adsorbates on the CO saturated surface are responsible for the lower heat of CO adsorption deduced from the FTS data.[49] Nevertheless, both perspectives are in qualitatively agreement that CO binds more strongly to the Zr-promoted catalyst compared to the unpromoted catalyst.

While there is consensus in the literature that Zr promotion of Co-based FTS catalysts increases rates of CO consumption per gram Co, there is less certainty regarding whether this is due to enhanced activity of the active sites or simply a greater abundance of active sites. Based on SSITKA experiments, Jongsomjit et al. concluded that Zr promotion increases the number of active surface intermediates without changing the average surface residence time of these intermediates.[17] Similarly, Rohr et al. found no improvements to the intrinsic activity of active sites within a Zr-promoted catalyst using the same experimental methods.[18] However, the catalysts used for these studies were not prepared with the intention of depositing ZrO_2 over the surface of the Co nanoparticles, and the reported H_2 chemisorption data do not show clear signs that the Co nanoparticle surfaces were covered by the promoter. If the active sites at the interface between Co and ZrO_2 were to exhibit enhanced activity for FTS, then these catalysts may have been unsuitable for identifying this phenomenon. In the present study, the lower apparent activation energy for FTS suggests that ZrO_2 plays a role in facilitating the rate determining step of CO dissociation.

4.4.4 Relationship between Zr Promotion and Product Selectivity

The shift of the product distribution toward higher molecular weight hydrocarbons follows from the larger CO adsorption constant for the Zr-promoted catalyst. With a stronger interaction between CO and the catalyst surface when the Zr promoter is present, a higher coverage of CO on the catalyst surface should occur on the promoted catalyst compared to the unpromoted catalyst, provided that the promoter does not also strengthen the adsorption of H. This phenomenon would also decrease the availability of H on the catalyst surface, and in turn suppress the formation of methane and decreases the probability of chain termination to paraffins by α-hydrogen addition. The secondary hydrogenation of olefins to paraffins would become slower with less H availability, which would result in a higher olefin to paraffin ratio at a fixed CO conversion. These effects are also achieved by increasing total pressure owing to competitive adsorption between CO, which adsorbs molecularly, and H_2, which adsorbs dissociatively.[41] As pressure increases, the surface coverage of adsorbed CO will increase, which decreases the H availability and leads to a more olefinic product distribution having a higher average molecular weight. Accordingly, Zr promotion is analogous to operating at a higher pressure, at least with respect to its effects on product selectivity.

Increasing the total pressure improves the product selectivity of the Zr-promoted catalyst, but the promoted catalyst is less sensitive to the pressure changes than is the unpromoted catalyst. This is understandable considering that product selectivity is heavily related to the coverage of the Co surface by CO, which has an upper limit dictated by saturation. The Zr-promoted catalyst, with its larger CO adsorption constant, starts with a higher CO surface coverage at low pressure than does the unpromoted catalyst. As pressure increases, the CO surface coverages for both catalysts increase and converge toward unity, which also causes the product selectivities of the catalysts to converge. Operating at higher CO conversions leads to further product selectivity improvements, but only when at elevated pressure (Figure 4.11). These results can be explained by the same principles that account for the connection between turnover frequencies and CO conversion (Figure 4.8). For a given CO conversion, reactors operated at higher pressure will have higher water partial pressure. Along with increasing catalyst activity, elevated water concentrations have been documented to yield more C_{5+} and less methane.[50] Furthermore, the suppression of olefin secondary hydrogenation at high pressure permits olefins to re-adsorb and to reinitiate chain growth. The beneficial effects of higher CO conversion on product selectivity also apply to the unpromoted catalyst.[41] Consequently, the C_{5+} selectivities for both catalysts would probably be quite similar at pressures and CO conversions near 10 bar and 50%, respectively. For this reason, it may be more appropriate to consider Zr promotion as a tool for achieving a target product selectivity at a lower operating pressure rather than as a means for improving dramatically the highest attainable C_{5+} selectivity.

4.4.5 Interaction between Zr and the Co Active Sites

The dependence of the catalyst selectivity on the Zr loading can be rationalized with the following model. It is assumed, as shown in Scheme S4.2 of the Supporting Information, that the surface of Co comprises two types of sites, Co atoms on the perimeter of ZrO_2 moieties covering the Co surface and Co sites that are not adjacent to the ZrO_2. The sites on the perimeter of the ZrO_2 moieties are assumed to be more active and have a higher affinity toward CO than those located farther away. As the coverage of Co by ZrO_2 increases, the number of the less active Co sites unaffected by ZrO_2 will decrease monotonically, whereas the number of more active Co sites adjacent to ZrO_2 will increase. Given the highly dispersed nature of the ZrO_2, it is reasonable to assume that Zr might deposit randomly on the catalyst surface. Under this assumption, the total number of active sites along the ZrO_2 perimeter would be maximized when the ZrO_2 covers half the Co surface.[51] The fraction of active Co sites that are adjacent to the ZrO_2 would be close to unity at this level of coverage. Higher loading of ZrO_2 would decrease the number the sites available for catalysis by covering up the remainder of the Co surface.

Since the observed product selectivity is the average of the selectivities of all active sites weighted their activity, the product distribution will improve as the fraction of sites adjacent to the ZrO_2 becomes larger. This behavior is observed for catalysts prepared with Zr/Co ratios between 0 and 1.0 where the product distribution shifts toward higher molecular weight and the olefinic content of the light hydrocarbon product fraction increases as the Zr loading increases (Figure 4.9). Once all Co sites are adjacent to ZrO_2, the observed product selectivity will be equivalent to the intrinsic selectivity of an active site at the Co-ZrO_2 interface, which represents an upper limit to the product selectivity improvements resulting from Zr promotion. This onset

of the insensitivity of product selectivity toward Zr loading occurs at a Zr/Co ratio of 1.0. The percentage of the Co nanoparticle surface that is covered by ZrO_2 at this loading is about 50%, which agrees with the theoretical expectation for the ZrO_2 perimeter to be maximized at half monolayer coverage of the catalyst surface. Additional Zr did not alter the product selectivity, which is consistent with most active sites being adjacent to the ZrO_2 and the additional promoter depleting the number of such sites by covering the nanoparticle surface.

The same conclusion was reached in our recent work with Mn-promoted Co, which demonstrated that the optimal amount of Mn promoter corresponds to the loading required to form a half monolayer of the promoter on the Co nanoparticle surface.[23] A key difference between the two promoters is that the optimal loading for the Zr promoter is Zr/Co = 1.0 whereas the Mn-promoted catalysts only require Mn/Co = 0.1. This difference is attributable to the different level of spatial association between the two promoters and Co. Mn has a strong probability of associating with the Co such that a half monolayer of MnO on the Co nanoparticle surfaces is established before Mn deposits elsewhere. In the Zr-promoted catalysts, the Zr disperses randomly over the catalyst such that a half monolayer on the Co nanoparticles is reached at a loading that places a half monolayer over the entire catalyst surface. These results demonstrate the importance of controlling for differences in the degree of contact between the Co and the promoter when comparing different metal oxide promoter elements.

The differences between MnO and ZrO_2 promoters extend beyond performance-loading relationships. The highest attainable C_{5+} selectivity at low pressure, where the promotion effects were most apparent, was higher for ZrO_2 (59%) than for MnO (48%). Moreover, the apparent rate coefficient and CO adsorption constant for the Zr-promoted catalyst were larger than those of the Mn-promoted catalysts. These comparisons, made under conditions for which the interface between Co and the promoter was maximized, suggest that Zr is intrinsically a more effective promoting element. A periodic trend that likely accounts for the higher performance of the Zr-promoted catalyst is the higher Lewis acidity of Zr(IV), which is largely a result of the higher oxidation state of the Zr compared to the Mn under FTS.[52] Metal oxide promoters functioning as Lewis acids has been hypothesized in the literature.[21,53] In this proposal, the CO is envisioned to be adsorbed onto the Co through the C atom while interacting simultaneously with the nearby promoter cation via the O atom, which helps to bind and weaken the carbonyl bond. Although it is difficult to find direct evidence for this intermediate, there are findings in the present work that support this hypothesis. The CO TPD profile for the Zr-promoted catalyst (Figure 4.5) contains a high temperature CO desorption peak, which may be related to chemisorbed CO that interacts with the Zr. Additionally, the pre-exponential factor of the CO adsorption constant for the Zr-promoted catalyst was two orders of magnitude smaller than that for the unpromoted catalyst. This is consistent with the hypothesis of simultaneous interaction of the adsorbed CO with both the Co and Zr, which should result in the adsorbed CO being more vibrationally constrained leading to a significant decrease in entropy.

4.5 Conclusion

The present work establishes that Zr promotion can be an effective tool for improving the activity and product selectivity of Co-based FTS catalysts. Higher turnover frequencies were

observed for the Zr-promoted catalysts at most operating conditions, which resulted from the larger FTS apparent rate coefficient and CO adsorption constant for the promoted catalysts. Adding Zr to the catalyst suppressed the formation of methane and shifted the product distribution in favor of the C_{5+} hydrocarbons. The effects of pressure on the product selectivity of the promoted and unpromoted catalysts demonstrate that Zr promotion was analogous to operating at a higher pressure owing to the larger CO adsorption constants of the promoted catalysts. Stronger interactions between CO and the catalyst surface would increase the ratio of CO to H on the catalyst surface. With less H availability at the active sites of the Zr-promoted catalysts, termination to paraffins is suppressed and the growth of longer hydrocarbon chains can occur.

Structurally, the Zr promoter formed highly dispersed ZrO_2 under reaction conditions. Furthermore, it appears that Zr did not form mixed alloys or oxides with the Co. Instead, the ZrO_2 existed as a near monolayer dispersed over the catalyst surface with limited preference for associating spatially with the Co nanoparticles versus the support. The relationship between catalyst selectivity and Zr loading is consistent with the formation of enhanced active sites at the interface between the Co metal and the ZrO_2 promoter. As ZrO_2 begins to cover the catalyst nanoparticles as Zr loading increases, the fraction of active sites adjacent to the promoter increases. Eventually, the fraction of active sites that are promoted approaches unity, with evidence suggesting that this occurs near a Zr/Co atomic ratio of 1, and no further improvements to the product selectivity result from higher Zr loading. The structure and catalytic behavior of the Zr-promoted catalysts are very similar to those of Mn-promoted catalysts, but for catalysts in which the Co-promoter interfaces were maximized, Zr promotion results in stronger enhancements to the CO dissociation rates and adsorption. Accordingly, these findings support the hypothesis that the Lewis acidity of the promoter is the relevant descriptor for metal oxide promotion effects.

Acknowledgements

The funding for this study was provided by BP through the XC^2 catalysis program and by the Director, Office of Science, Office of Basic Energy Sciences and by the Division of Chemical Sciences, Geosciences, and Biosciences of the U.S. Department of Energy at Lawrence Berkeley National Laboratory under Contract No. DE-AC02-05CH11231. Work at the Molecular Foundry was supported by the Office of Science, Office of Basic Energy Sciences, of the U.S. Department of Energy under Contract No. DE-AC02-05CH11231. This research used resources of the Advanced Photon Source, a U.S. Department of Energy (DOE) Office of Science User Facility operated for the DOE Office of Science by Argonne National Laboratory under Contract No. DE-AC02-06CH11357. Portions of this work were performed at the DuPont-Northwestern-Dow Collaborative Access Team (DND-CAT) located at Sector 5 of the Advanced Photon Source (APS). DND-CAT is supported by Northwestern University, E.I. DuPont de Nemours & Co., and The Dow Chemical Company. MRCAT operations are supported by the Department of Energy and the MRCAT member institutions. The authors would like to thank Dr. Konstantinos Goulas for his assistance with the XAS experiments.

Table 4.1 Physical characterization data for the Co-ZrO_2 catalysts.

Zr/Co Atomic Ratio	Co Loading[a] (wt %)	d(Co)[b] (nm)	O_2 Uptake (mmol g_{cat}^{-1})	H_2 Uptake (mmol g_{cat}^{-1})
0	9.8	11 ± 3	1.0	0.063
0.01	9.8	10 ± 2	0.96	0.067
0.05	9.7	11 ± 3	0.90	0.060
0.10	9.5	10 ± 4	0.86	0.060
0.25	9.4	10 ± 3	0.82	0.053
0.5	8.9	9 ± 3	0.72	0.037
1.0	7.7	10 ± 3	0.57	0.017
2.0	6.6	9 ± 4	0.43	0.008

[a] Compositions were determined by ICP-OES, and the Co wt % were approximately constant at 10 wt% with respect to mass of Co and SiO_2.

[b] Surface mean diameter.

Table 4.2 Co extents of reduction, nanoparticle dispersions, and coverages of the nanoparticle surfaces by ZrO_2.

Zr/Co Atomic Ratio	Co(0)[a] (%)	Dispersion[b] (%)	ZrO_2 Coverage[c] (%)
0	87	9.1	–
0.01	82	9.5	0 ± 10
0.05	76	8.7	0 ± 10
0.10	73	9.3	0 ± 10
0.25	69	9.4	0 ± 10
0.5	63	10.8	30 ± 10
1.0	54	9.3	50 ± 10
2.0	44	10.2	70 ± 20

[a] Percentage of Co in the metallic state after reduction.

[b] Determined by particle sizes assuming a site density of 14.6 Co atoms/nm^2.

[c] Percentage of the metallic Co nanoparticle surface area covered by ZrO_2.

Table 4.3 Fitted kinetics parameters for the Zr-promoted and unpromoted catalysts.

Zr/Co Atomic Ratio	A (bar^{-1} s^{-1})	E_A (kJ/mol)	$K_{CO,0}$ (bar^{-1})	Q_{CO} (kJ/mol)
0	7×10^7	84	3×10^{-4}	35
1.0	6×10^6	68	1×10^{-6}	62

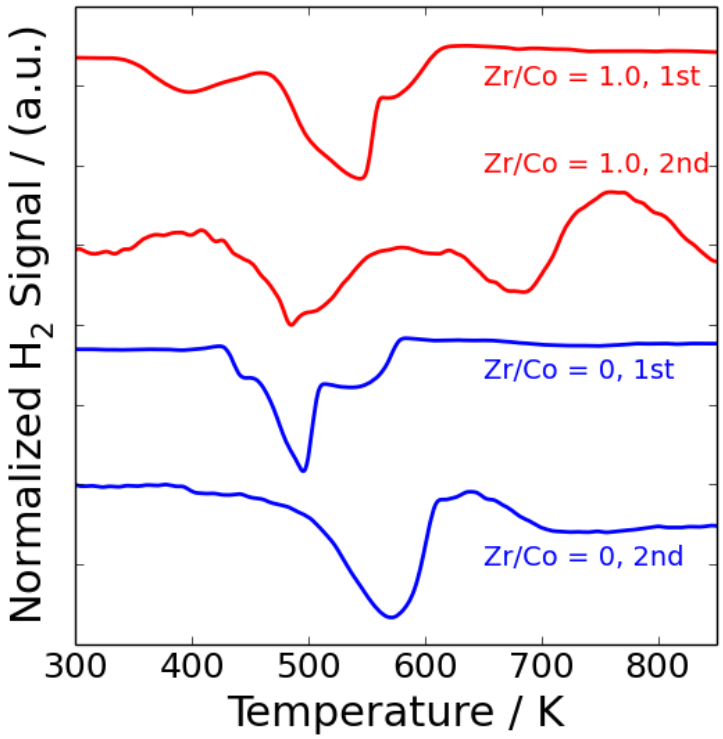

Figure 4.1 TPR profiles of the Co and Co-ZrO_2 (Zr/Co = 1.0) catalysts. The curves labeled "1st" correspond to the initial decompositions of the dried catalyst precursors. The curves labeled "2nd" correspond to the second reductions of the passivated catalysts that would occur prior to conducting FTS reactions. The catalyst synthesis process and its relation to these TPR data is illustrated in Scheme S4.1 of the Supporting Information.

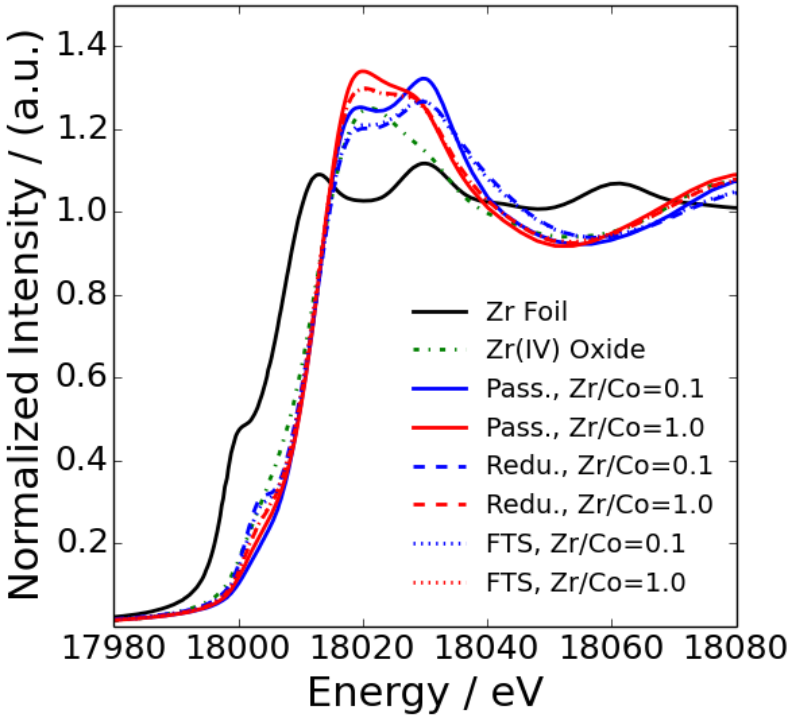

Figure 4.2 In situ XANES spectra of the Co-ZrO_2 catalysts collected at the Zr K-edge. Spectra for catalysts prepared with low (Zr/Co = 0.1) and high (Zr/Co = 1.0) promoter loadings were collected at three conditions: passivated state at ambient temperature (Pass.), after reduction with H_2 at 723 K for 2 h and cooling to 493 K (Redu.), and in 2/1 H_2/CO syngas at 493 K (FTS). A more detailed view of the effect of Zr loading on the spectra is included in Figure S4.2 of the Supporting Information.

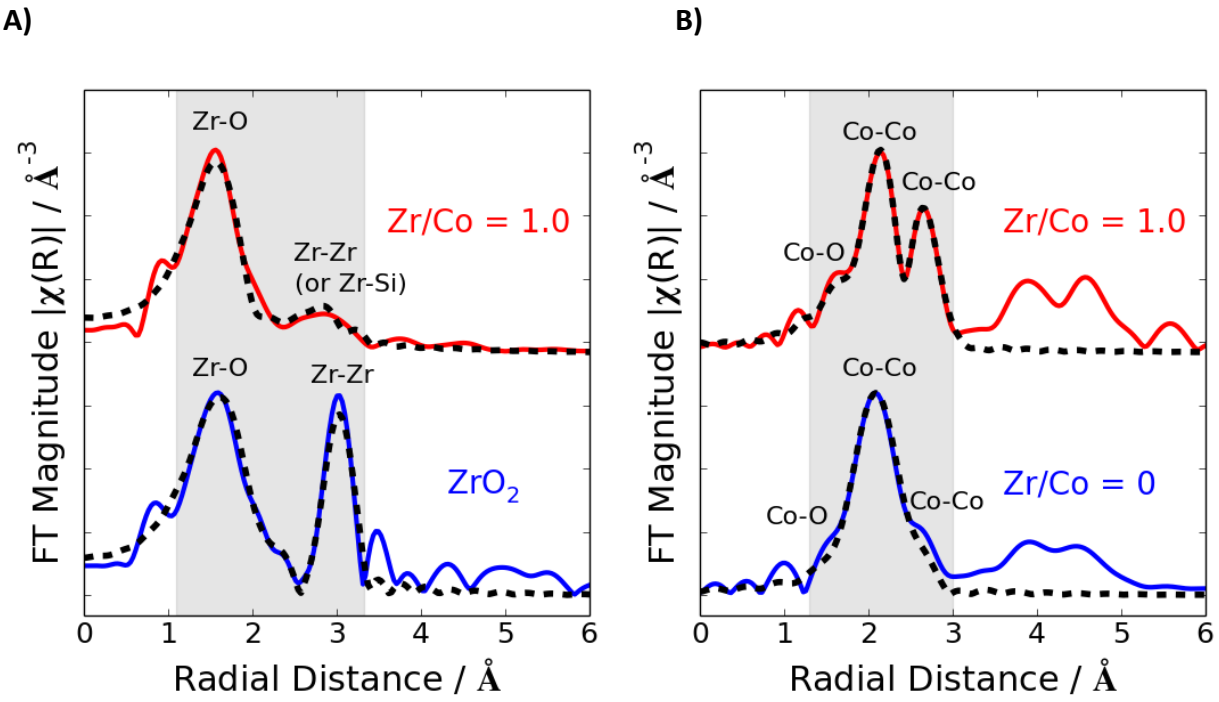

Figure 4.3 EXAFS spectra of Co and Co-ZrO_2 catalyst samples at the (A) Zr K-edge and (B) Co K-edge. The spectra were measured at ambient temperature and pressure in He. Before collecting the spectra, the catalyst samples were reduced in H_2 at 723 K (the ZrO_2 reference was used without pretreatment). The solid colored lines in the plots are the k^2-weighted Fourier transforms of the EXAFS spectra, and the dashed black lines are fits to these data within the shaded gray region.

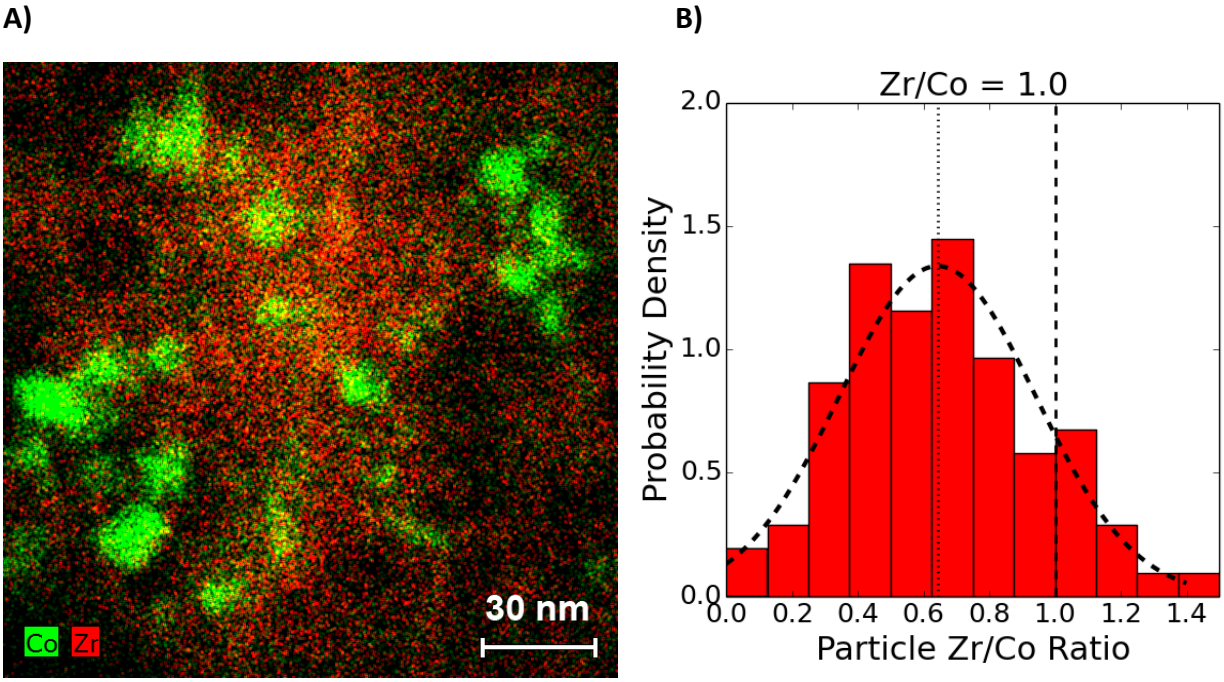

Figure 4.4 STEM-EDS elemental map (A) and nanoparticle composition histogram (B) of the Co-ZrO_2 catalyst prepared with a Zr/Co = 1.0 atomic ratio. The dashed curve in the histogram is a Gaussian function fitted to the data, and the vertical lines in the histogram indicate the mean nanoparticle composition (dotted) and the bulk catalyst composition (dashed).

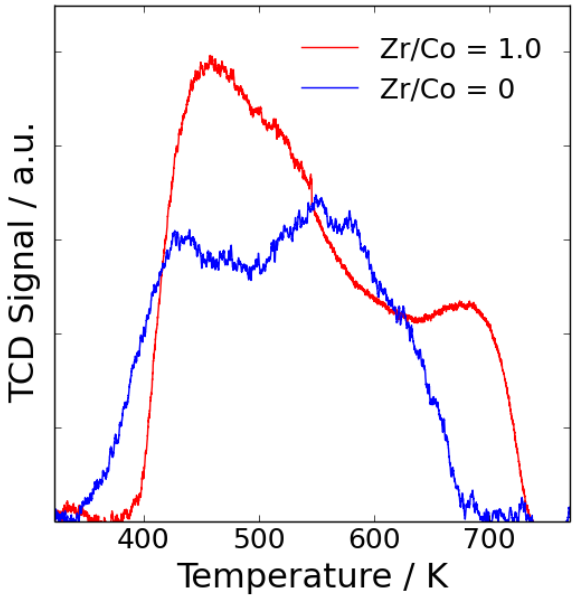

Figure 4.5 CO temperature-programmed desorption spectra for the Zr-promoted (Zr/Co = 1.0) and unpromoted (Zr/Co = 0) catalysts. The CO adsorption took place at 323 K and the desorption temperature ramp rate was 10 K/min. The plotted data are the instrument thermal conductivity signals as a function of sample temperature.

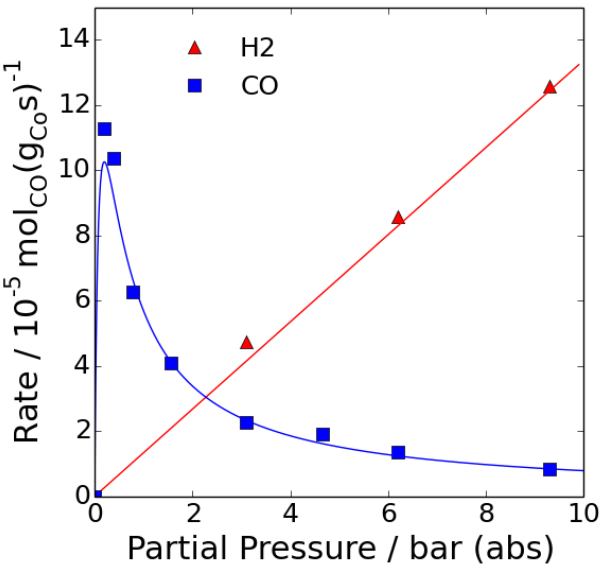

Figure 4.6 Dependence of the CO consumption rate for the Zr-promoted catalyst (Zr/Co = 1.0) on (A) H_2 and (B) CO partial pressures. The variation of H_2 partial pressure was done with a constant CO partial pressure of 1.55 bar; the variation of CO partial pressure was done with a constant H_2 partial pressure of 3.1 bar. The data for both figures were collected at 493 K and were extrapolated to 0% conversion. The curves in the plot correspond to the rate law from eq. 4.6 fitted to the data.

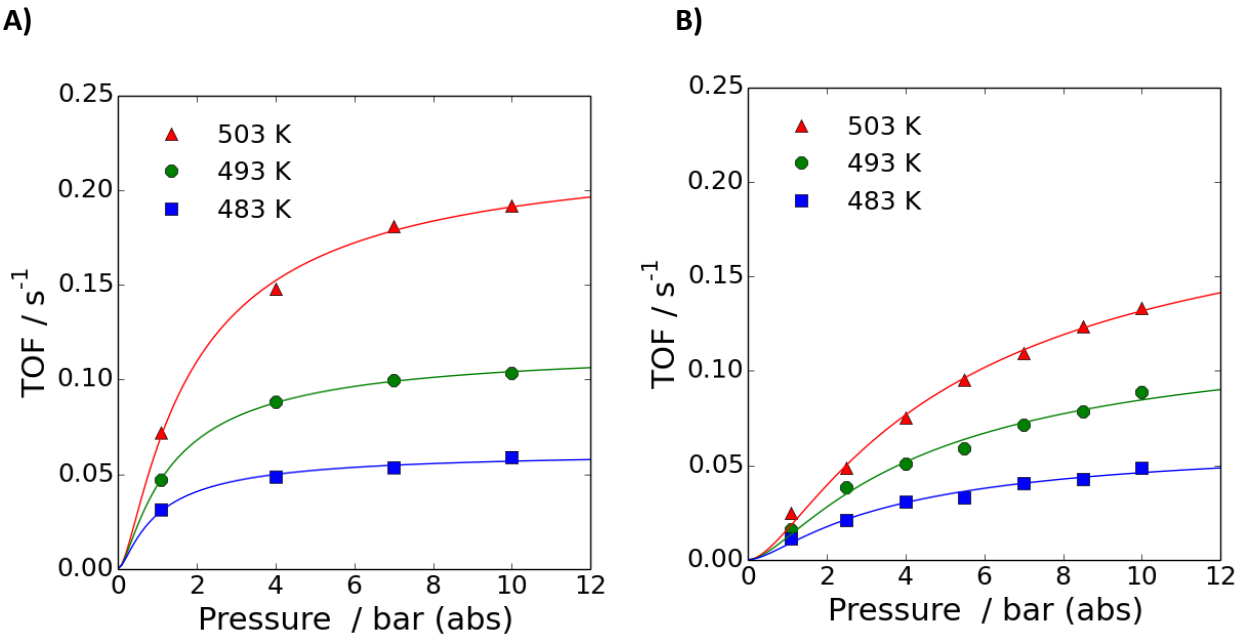

Figure 4.7 Dependence of FTS turnover frequencies on temperature and pressure for (A) Zr-promoted (Zr/Co = 1.0) and (B) unpromoted (Zr/Co = 0) catalysts. These data were collected using a 7% Ar, 31% CO, and 62% H_2 reactor inlet feed composition, and the data points were extrapolated to 0% conversion. The curves in the plots are fits to the data using eq. 4.6.

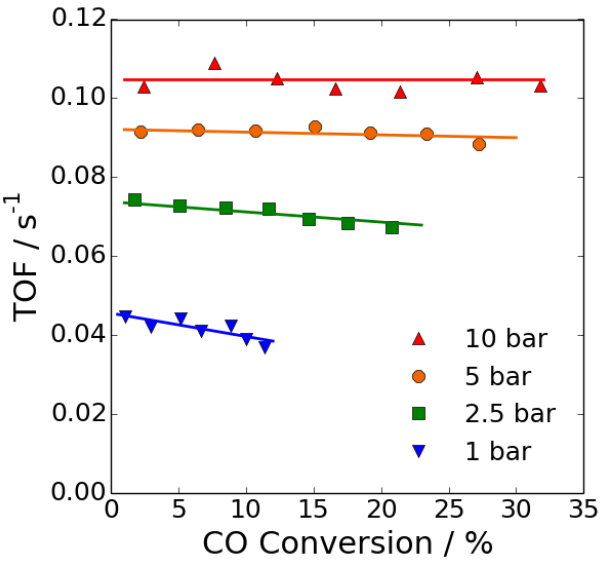

Figure 4.8 FTS turnover frequencies as a function of CO conversion for the catalyst prepared with Zr/Co = 1.0. These data were collected at 493 K with a 7% Ar, 31% CO, and 62% H_2 reactor inlet feed composition. The lines in the plot are for visual aid.

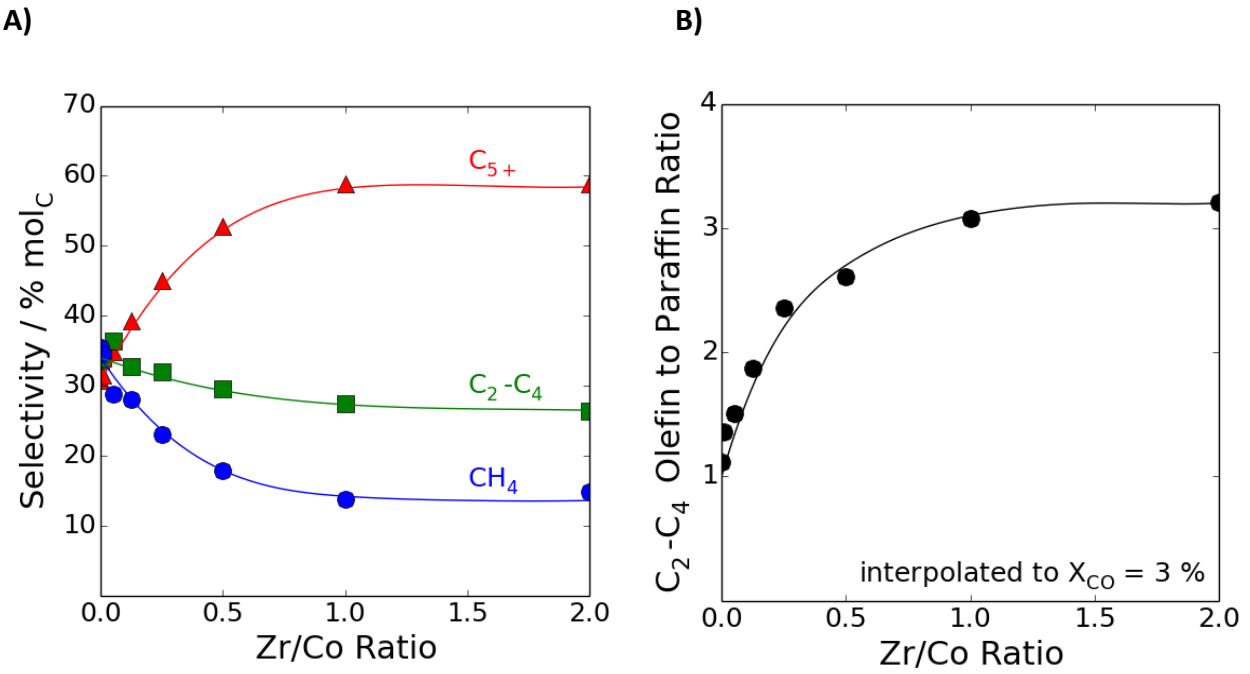

Figure 4.9 Effect of Zr loading on product selectivities at 1 bar and 493 K. (A) Methane, C_2–C_4, and C_{5+} selectivities at 0% conversion as a function of Zr loading. (B) Olefin to paraffin ratio within the C_2–C_4 product fraction interpolated to 3% CO conversion as a function of Zr loading. All data points were collected with a reactor inlet feed composition of 7% Ar, 31% CO, and 62% H_2. The curves in each plot are cubic splines added for visual aid.

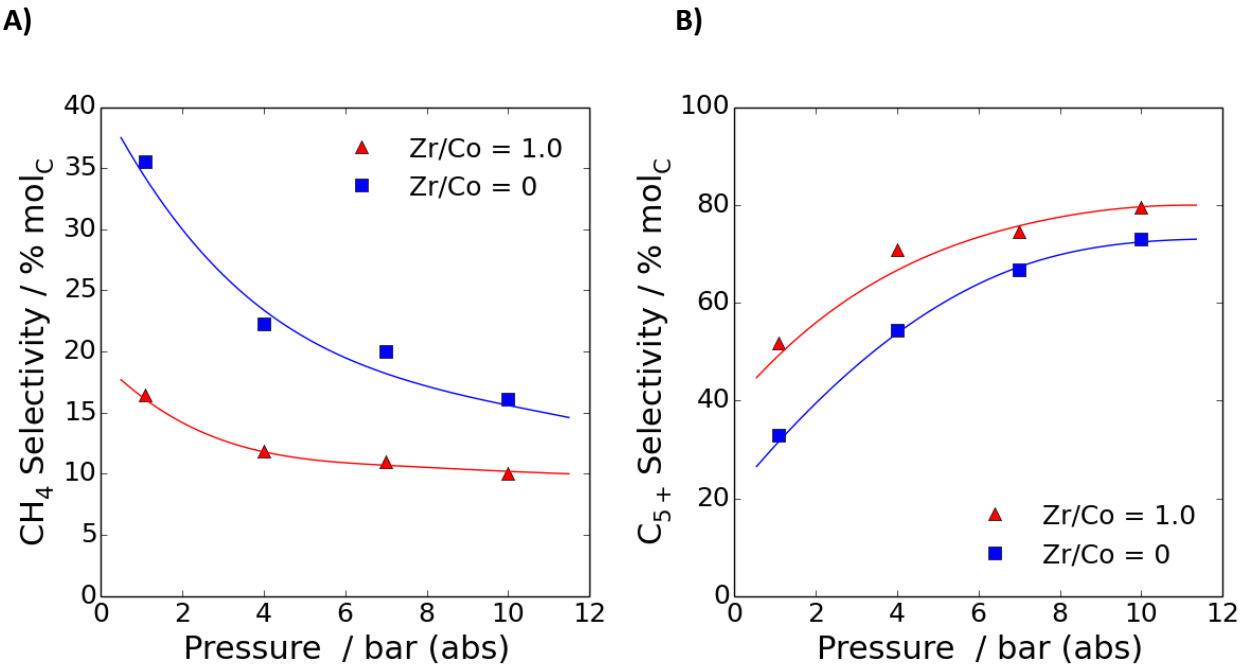

Figure 4.10 Comparison of (A) methane and (B) C_{5+} selectivities as a function of pressure for Zr-promoted (Zr/Co = 1.0) and unpromoted (Zr/Co = 0) catalysts. The data were collected at 493 K with a 7% Ar, 31% CO, and 62% H_2 reactor inlet feed composition. The plotted data points were extrapolated to 0% conversion. The curves in each plot are cubic splines added for visual aid.

A) B)

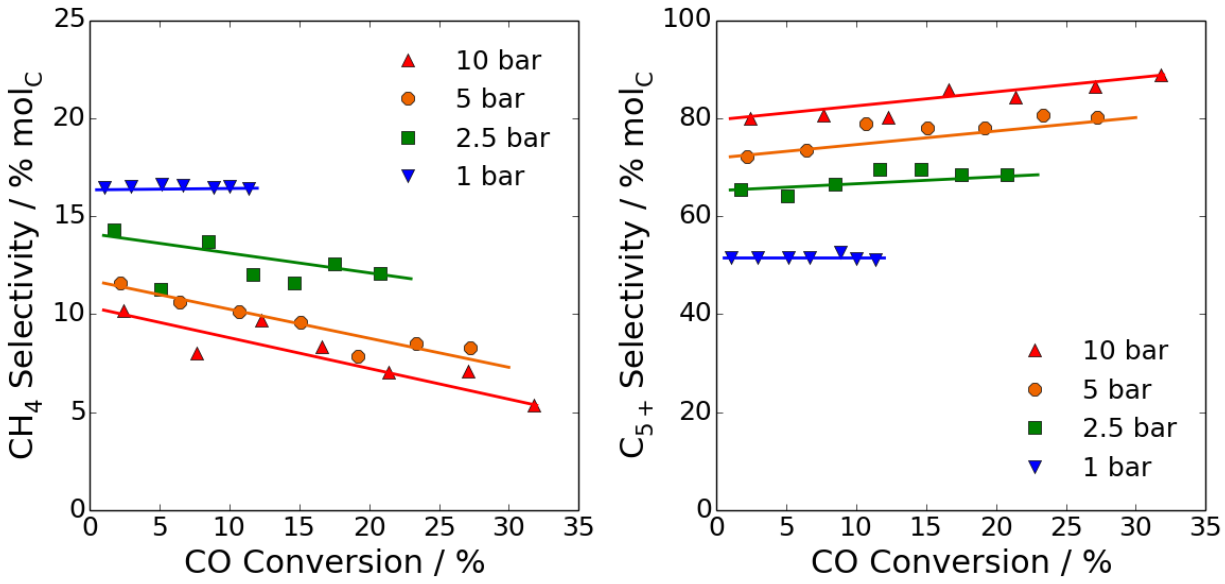

Figure 4.11 Selectivities toward (A) CH_4 and (B) C_{5+} for the catalyst prepared with Zr/Co = 1.0 as a function of CO conversion. These data were collected at 493 K with a 7% Ar, 31% CO, and 62% H_2 reactor inlet feed composition. The lines in the plot are for visual aid.

Supporting Information

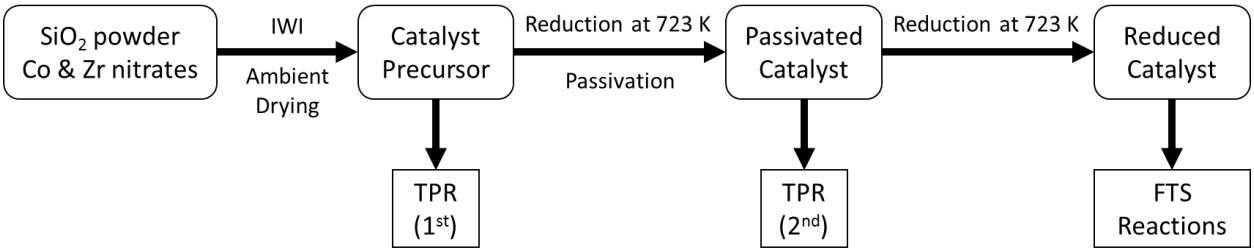

Scheme S4.1 Sequence of steps involved in the synthesis of the Co-Zr catalysts. The states of the catalysts are represented by the boxes with rounded corners. Examples of experiments using the catalysts in a particular state are represented by rectangles. The TPR spectra labeled "1st" and "2nd" in Figure 4.1 were collected using the catalyst precursor and passivated catalyst, respectively, as sample material.

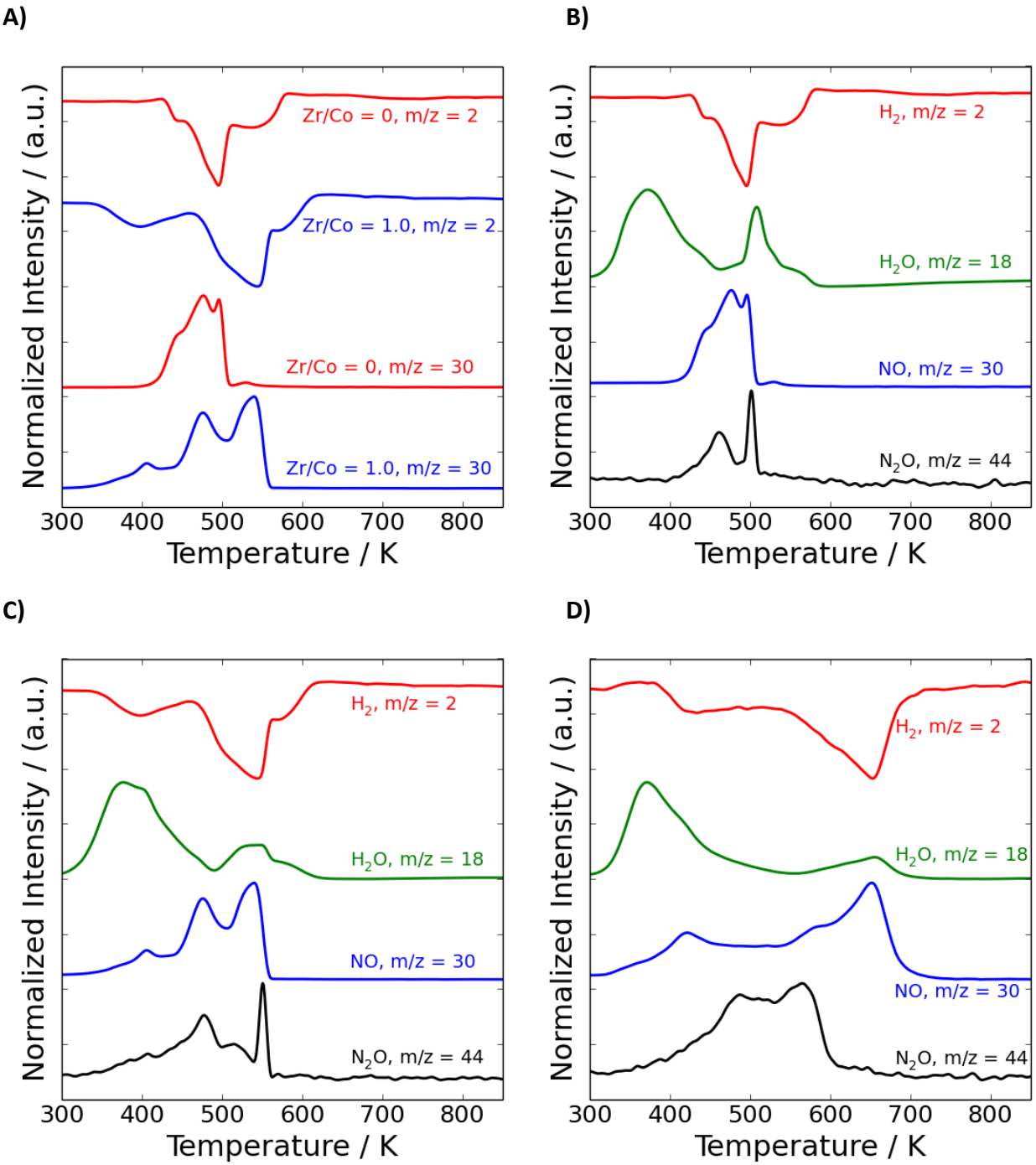

Figure S4.1 TPR spectra of catalyst precursors. (A) Comparison of H_2 consumption and NO production for the unpromoted (Zr/Co = 0) and Zr-promoted catalyst (Zr/Co = 1.0) precursors. Signals for the (B) Zr/Co = 0 catalyst precursor, (C) Zr/Co = 1.0 catalyst precursor, and (D) dried Zr precursor on SiO_2 support.

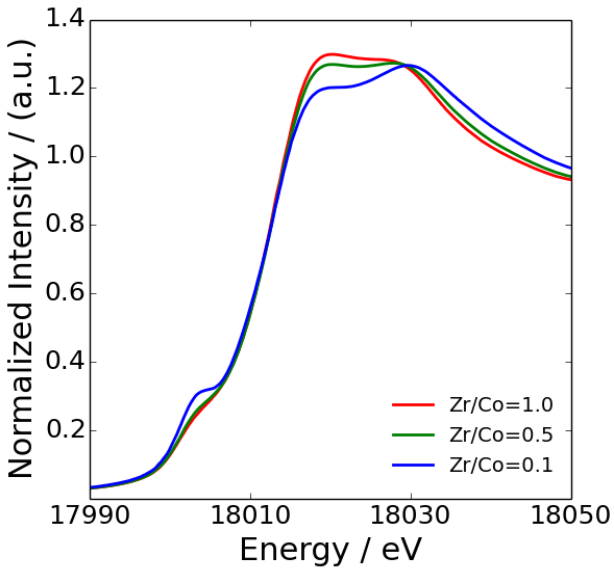

Figure S4.2 In situ XANES spectra of the reduced Co-Zr catalysts collected at the Zr K-edge for different loadings of Zr. The spectra were measured at 493 K after reducing the catalysts in H_2 at 723 K. While the spectra for the Zr/Co = 0.5 and Zr/Co = 1.0 are consistent with that of monoclinic ZrO_2, the spectrum for the Zr/Co = 0.1 catalyst most closely matches that of tetrahedral ZrO_2.

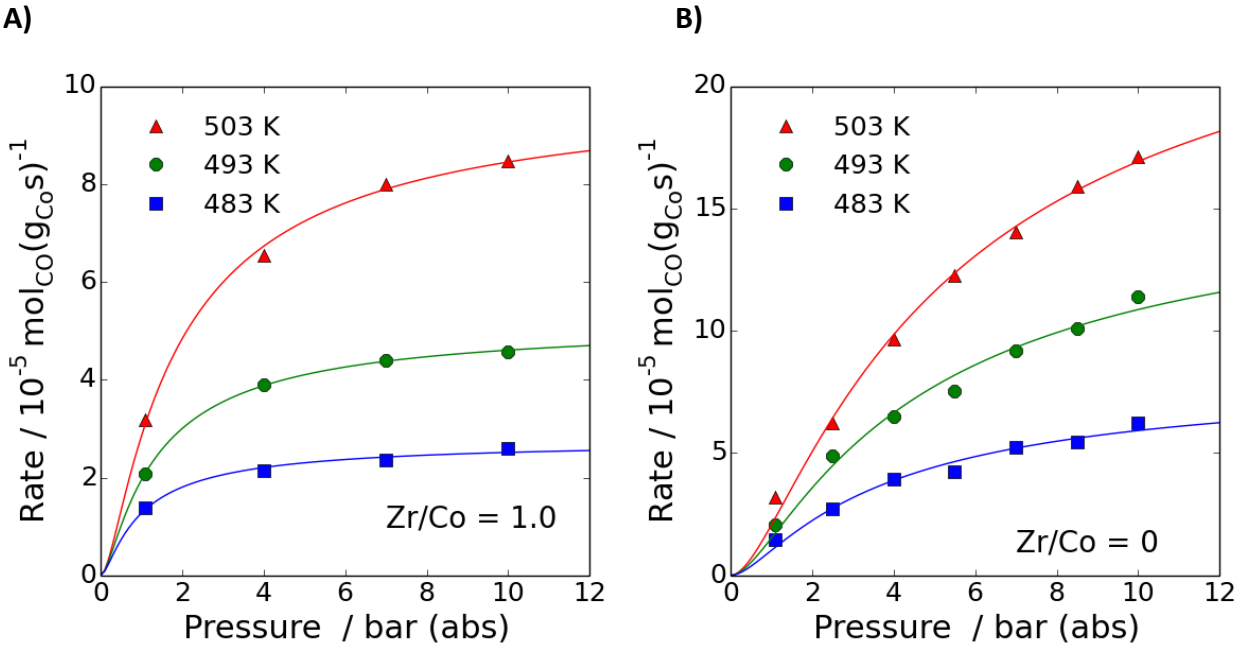

Figure S4.3 Rates of CO consumption per gram Co as functions of temperature and pressure for (A) Zr-promoted (Zr/Co = 1.0) and (B) unpromoted (Zr/Co = 0) catalysts. These data were extrapolated to 0% conversion. The curves in the plots are fits to the data using eq. 4.6.

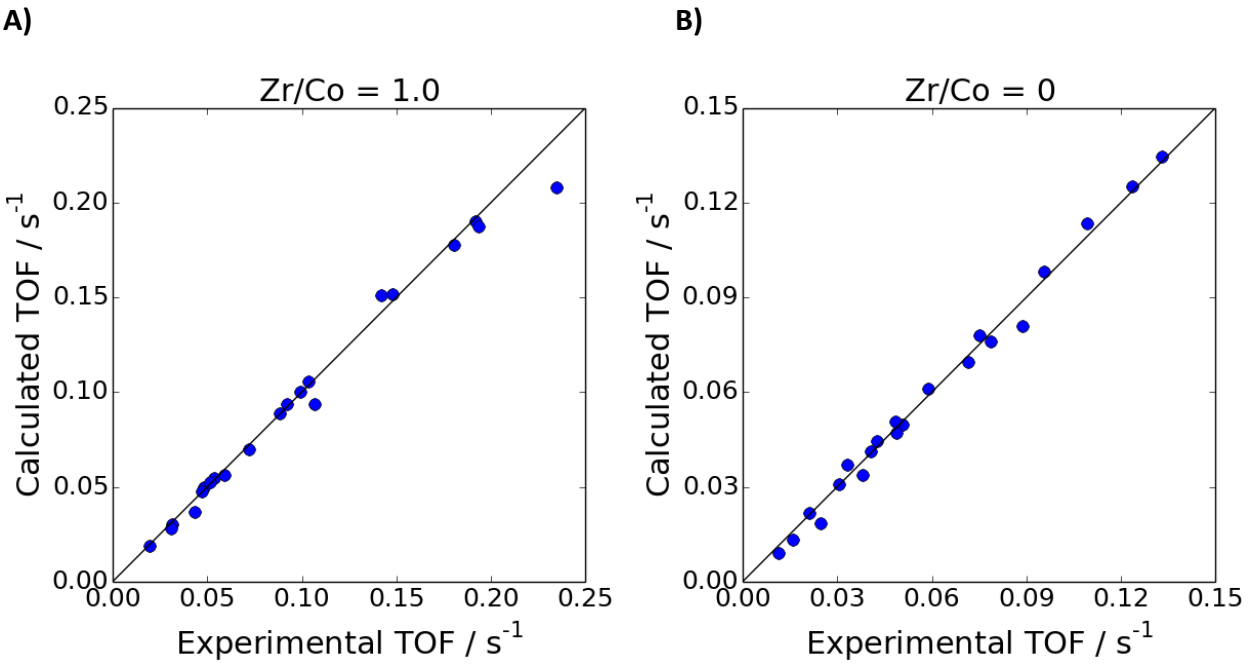

Figure S4.4 Parity plots for the (A) Zr-promoted (Zr/Co = 1.0) and (B) unpromoted (Zr/Co = 0) catalysts. Only the turnover frequencies extrapolated to 0% conversion were used in these plots. The calculated turnover frequencies were derived from the rate law from eq. 4.6 using the fitted parameters from Table 4.3.

Table S4.1 Fitted parameters for the catalysts prepared with Zr/Co = 0 and Zr/Co = 1.0 using the rate law given as eq. 4.6.

Zr/Co Atomic Ratio	T (K)	*a* (bar^{-1} s^{-1})	*b* (bar^{-1})
0	483	0.056	1.7
0	493	0.090	1.4
0	503	0.13	1.2
1.0	483	0.21	6.8
1.0	493	0.30	5.1
1.0	503	0.42	3.6

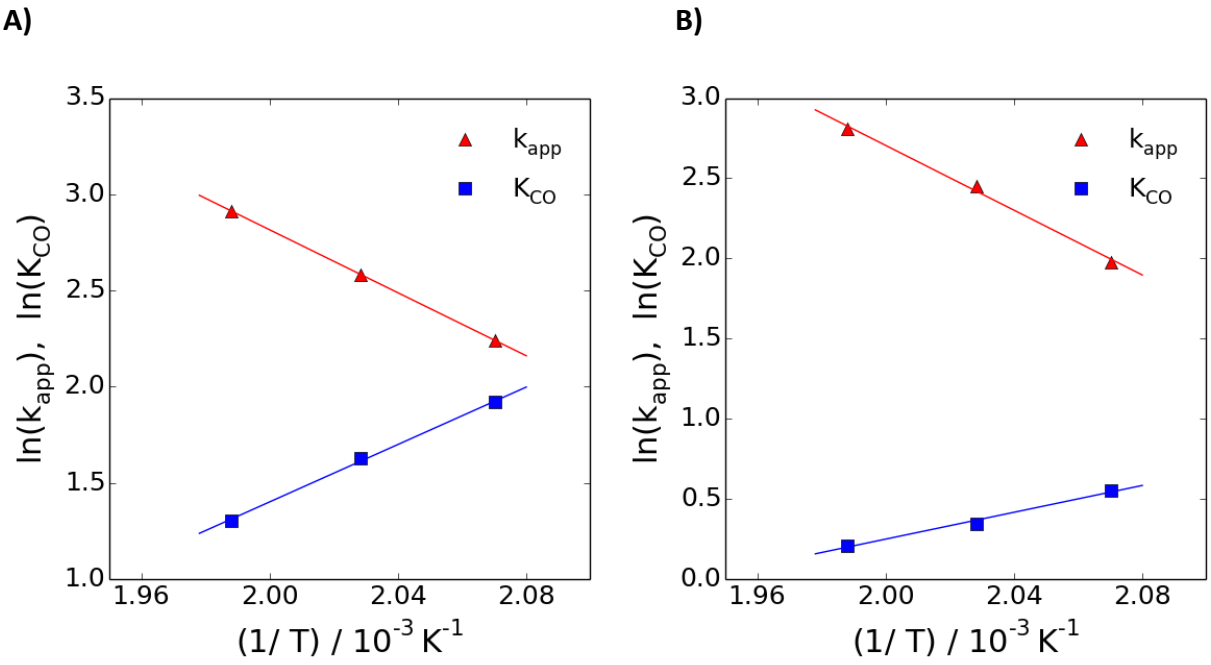

Figure S4.5 Arrhenius plots for the (A) Zr-promoted (Zr/Co = 1.0) and (B) unpromoted (Zr/Co = 0) catalysts. k_{app} and K_{CO} correspond to the constants a and b in eq. 4.6, respectively. Here, the rate constant k_{app} was used with units of 10^{-5} mol_{CO} g_{Co}^{-1} s^{-1}.

A)

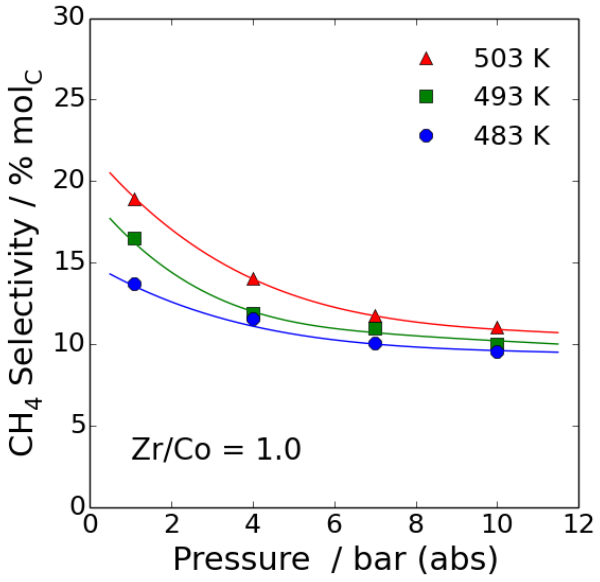
503 K
493 K
483 K
Zr/Co = 1.0
CH4 Selectivity / % molC
Pressure / bar (abs)

B)

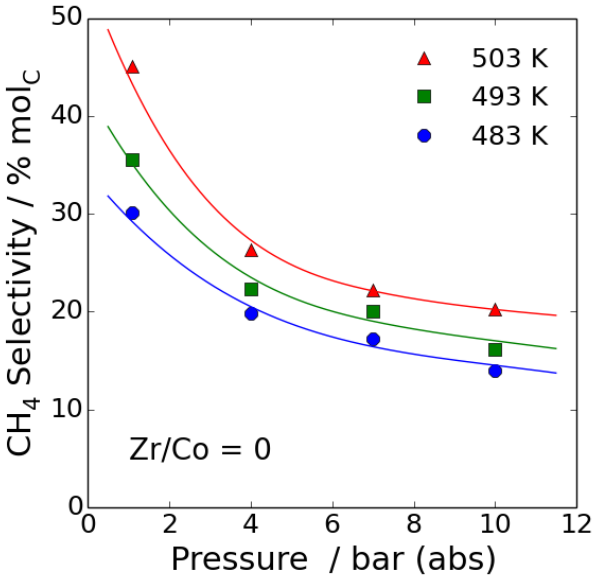
503 K
493 K
483 K
Zr/Co = 0
CH4 Selectivity / % molC
Pressure / bar (abs)

C)

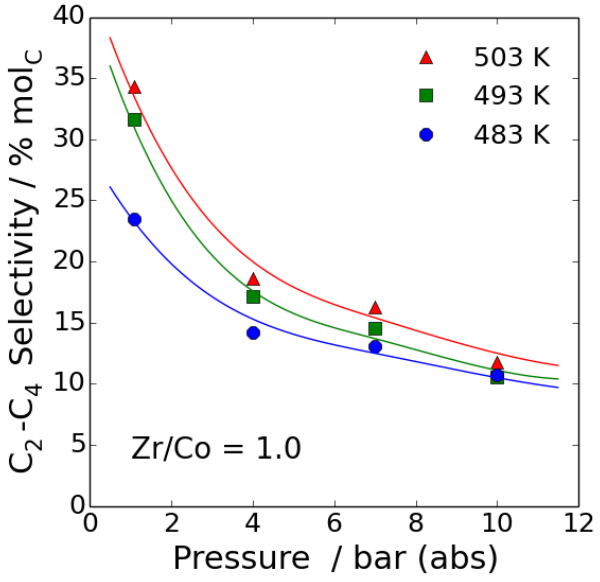
503 K
493 K
483 K
Zr/Co = 1.0
C2-C4 Selectivity / % molC
Pressure / bar (abs)

D)

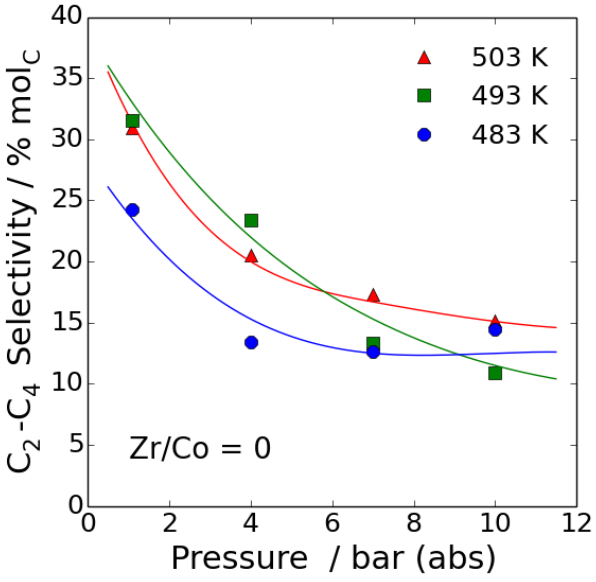
503 K
493 K
483 K
Zr/Co = 0
C2-C4 Selectivity / % molC
Pressure / bar (abs)

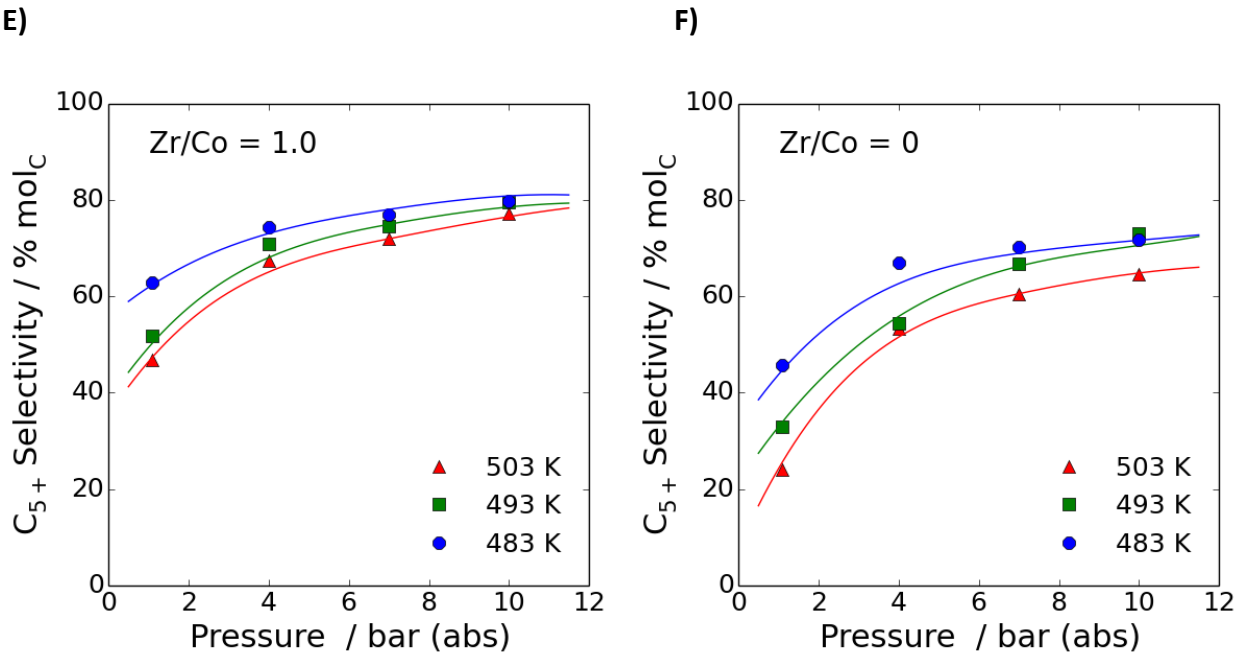

Figure S4.6 Effect of pressure and temperature on product selectivities for the Zr-promoted (Zr/Co = 1.0) and unpromoted (Zr/Co = 0) catalysts. (A) Methane, (C) C_2-C_4, and (E) C_{5+} selectivities for the Zr-promoted catalyst. (A) Methane, (C) C_2-C_4, and (E) C_{5+} selectivities for the unpromoted catalyst. These data were collected at with a 7% Ar, 31% CO, and 62% H_2 reactor inlet feed composition. The plotted data points were extrapolated to 0% conversion. The curves in each plot are cubic splines added for visual aid.

BLACK = ZrO2

BLUE = unpromoted active sites (not adjacent to ZrO2)

RED = promoted active sites (near the Co-ZrO2 interface)

A) Zr/Co = 0

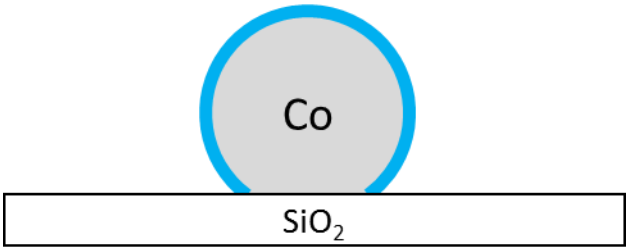

- All active sites exhibit the intrinsic active of unpromoted Co (shown in blue).

B) Zr/Co = 0.25

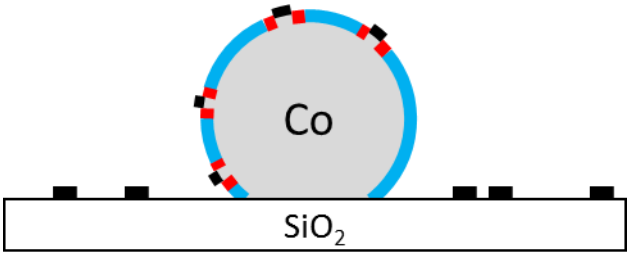

- ZrO_2 deposits onto the Co nanoparticle and SiO_2 support surfaces with equal preference.
- Active sites that are near the interface (shown in red) exhibit enhanced FTS activity and selectivity.
- The majority of active sites remain unpromoted because the ZrO_2 loading is too low to saturate the Co nanoparticle surface.

C) Zr/Co = 1.0

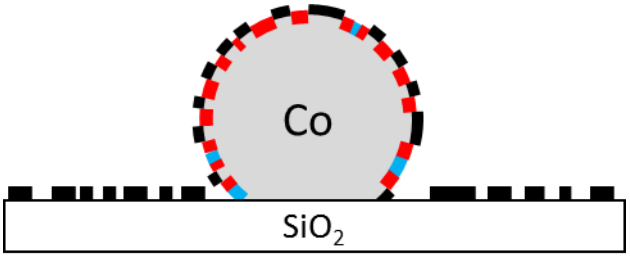

- The ZrO2 loading is high enough to achieve half monolayer coverage of the catalyst surface
- Nearly all active sites are adjacent to ZrO_2 and exhibit the enhanced FTS activity and higher affinity to CO

Scheme S4.2 Hypothesized structures an (A) unpromoted Co nanoparticle, (B) Zr-promoted nanoparticle with Zr/Co = 0.25, and (C) Zr-promoted nanoparticle with Zr/Co = 1.0.

References

1. Dry, M.E. *Catal. Today* **2002**, *71*, 227-241.

2. Huber, G.H.; Iborra, S.; Corma, A. *Chem. Rev.* **2006**, *106*, 4044-4098.

3. Khodakov, A.Y.; Chu, W.; Fongarland, P. *Chem. Rev.* **2007**, *107*, 1692-1744.

4. Mauldin, C.H.; Davis, S.M.; Arcuri, K.B. Cobalt Catalysts for the Conversion of Methanol and for Fischer-Tropsch Synthesis to Produce Hydrocarbons. U.S. Patent 4,663,305. May 5, 1987.

5. Minderhoud, J.K.; Post, M.F.M.; Sie, S.T.; Sufholter, E.J.R. Process for the Preparation of Hydrocarbons. European Patent ZA8308672 (A). July 25, 1984.

6. Eri, S.; Goodwin, J.G., Jr.; Marcelin, G.; Riis, T. Catalyst for production of hydrocarbons. U.S. Patent 4,801,573. Jan 31, 1989.

7. Oukaci, R.; Singleton, A.H.; Goodwin, J.G., Jr. *Appl. Catal., A* **1999**, *186*, 129-144.

8. Enache, D.I.; Roy-Auberger, M.; Revel, R. *Appl. Catal., A* **2004**, *268*, 51-60.

9. Panpranot, J.; Taochaiyaphum, N.; Jongsomjit, B.; Praserthdam, P. *Catal. Commun.* **2006**, *7*, 192-197.

10. Wei, M.; Okabe, K.; Arakawa, H.; Teraoka, Y. *Catal. Commun.* **2004**, *5*, 597-603.

11. Liu, Y.; Murata, K.; Okabe, K.; Hanaoka, T.; Sakanishi, K. *Chem. Lett.* **2008**, *37*, 984-985.

12. Tao, C.; Li, J.; Zhang, Y.; Liew, K.Y. *J. Mol. Catal. A: Chem.* **2010**, *331*, 50-57.

13. Ali, S.; Chen, B.; Goodwin, J.G., Jr. *J. Catal.* **1995**, *157*, 35-41.

14. Feller, A.; Claeys, M.; van Steen, E. *J. Catal.* **1999**, *185*, 120-130.

15. Moradi, G.R.; Basir, M.M.; Taeb, A.; Kiennemann, A. *Catal. Commun.* **2003**, *4*, 27-32.

16. Xiong, H.; Zhang, Y.; Liew, K.; Li, J. *J. Mol. Catal. A: Chem.* **2005**, *231*, 145-151.

17. Jongsomjit, B.; Panpranot, J.; Goodwin, J. G., Jr. *J. Catal.* **2003**, *215*, 66-77.

18. Rohr, F.; Lindvåg, O.A.; Holmen, A.; Blekkan, E.A. *Catal. Today* **2000**, *58*, 247-254.

19. Ma., W.-P.; Ding, Y.-J.; Lin, L.-W. *Ind. Eng. Chem. Res.* **2004**, *43*, 2391-2398.

20. Sachtler, W.M.; Ichikawa, M. *J. Phys. Chem.* **1986**, *90*, 4752-4758.

21. Boffa, A.B.; Lin, C.; Bell, A.T.; Somorjai, G.A. *Catal. Lett.* **1994**, *27*, 243-249.

22. Johnson, G.R.; Werner, S.; Bustillo, K.C.; Ercius, P.; Kisielowski, C.; Bell, A.T. *J. Catal.* **2015**, *328*, 111-122.

23. Johnson, G.R.; Werner, S.; Bell, A.T. *ACS Catal.* **2015**, *5*, 5888-5903.

24. Reuel, R.C.; Bartholomew, C.H. *J. Catal.* **1984**, *85*, 63-77.

25. Kropf, A.J.; Katsoudas, J.; Chattopadhyay, S.; Shibata, T.; Lang, E.A.; Zyryanov, V.N.; Ravel, B.; McIvor, K.; Kemner, K.M.; Scheckel, K.G.; Bare, S.R.; Terry, J.; Kelley, S.D.; Bunker, B.A.; Segre, C.U. *AIP Conf. Proc.*, **2009**, 299-302.

26. Ravel, B.; Newville, M. *J. Synchrotron Radiat.* **2005**, *12*, 537-541.

27. Newville, M. J. Synchrotron Radiat. **2001**, *8*, 96-100.

28. Cliff, G.; Lorimer, G.W. *J. Microsc.* **1975**, *103*, 203-207.

29. Weisz, P.B.; Prater, C.D. *Adv. Catal.* **1954**, *6*, 143-196.

30. Inoue, S.; Ōki, H.; Hagiwara, Z. *J. Inorg. Nucl. Chem.* **1975**, *37*, 929-936.

31. Girardon, J.-S.; Lermontov, A.S.; Gengembre, L.; Chernavskii, P.A.; Griboval-Constant, A.; Khodakov, A.Y. *J. Catal.* **2005**, *230*, 339-352.

32. Arnoldy, P.; Moulijn, J.A. *J. Catal.* **1985**, *93*, 38-54.

33. Rhodes, M.D.; Pokrovski, K.A.; Bell, A.T. *J. Catal.* **2005**, *233*, 210-220.

34. Satoh, N.; Hayashi, J.-i.; Hattori, H. *Appl. Catal., A* **2000**, *202*, 207-213.

35. McTaggart, F.K. *Nature* **1961**, *191*, 1192.

36. Meneghetti, F.; Wendel, E.; Mascotto, S.; Smarsly, B.M.; Tondello, E.; Bertagnolli, H.; Gross, S. *CrystEngComm* **2010**, *12*, 1639-1649.

37. Redhead, P.A. *Vacuum* **1962**, *12*, 203-211.

38. Papp, H. *Surf. Sci.* **1983**, *129*, 205-218.

39. Patanou, E.; Tveten, E.Z.; Chen, D.; Holmen, A.; Blekkan, E.A. *Catal. Today* **2013**, *214*, 19-24.

40. Yates, I.C.; Satterfield, C.N. *Energy Fuels* **1991**, *5*, 168-173.

41. Dinse, A.; Aigner, M.; Ulbrich, M.; Johnson, G.R.; Bell, A.T. *J. Catal.* **2012**, *288*, 104-114.

42. Das, T.K.; Conner, W.A.; Li, J.; Jacobs, G.; Dry, M.E.; David, B.H. *Energy Fuels* **2005**, *19*, 1430-1439.

43. Lögdberg, S.; Boutonnet, M.; Walmsley, J.C.; Järås, S.; Holmen, A.; Blekkan, E.A. *Appl. Catal., A* **2011**, *393*, 109-121.

44. Iglesia, E. *Appl. Catal., A* **1997**, *161*, 59-78.

45. Bezemer, G.L.; Bitter, J.H.; Kuipers, H.P.C.E.; Oosterbeek, H.; Holewijn, J.E.; Xu, X.; Kapteijn, F.; van Dillen, A.J.; de Jong, K.P. *J. Am. Chem. Soc.* **2006**, *128*, 3956-3964.

46. Zeng, B.; Hou, B.; Jia, L.; Wang, J.; Chen, C.; Sun, Y.; Li, D. *ChemCatChem* **2003**, *5*, 3794-3801.

47. Borer, A.L.; Brönnimann, C.; Prins, R. *J. Catal.* **1994**, *145*, 516-525.

48. Jiang, Y.; Fu, T.; Lü, J.; Li, Z. *J. Energy Chem.* **2013**, *22*, 506-511.

49. Adams, D.L. *Surf. Sci.* **1974**, *42*, 12-36.

50. Storsæter, S.; Borg, Ø.; Blekkan, E.A.; Holmen, A. *J. Catal.* **2005**, *231*, 405-419.

51. Williams, K.J.; Boffa, A.B.; Lahtinen, J.; Salmeron, M.; Bell, A.T.; Somorjai, G.A. *Catal. Lett.* **1990**, *5*, 385-394.

52. Tanaka, K.; Ozaki, A. *J. Catal.* **1967**, *8*, 1-7.

53. Sachtler, W.M.H.; Shriver, D.F.; Hollenberg, W.B.; Lang, A.F. *J. Catal.* **1985**, *92*, 429-431.

Chapter 5

Connections between the Lewis Acidity of Metal Oxide Promoters and the Catalytic Properties of Co-Based Fischer-Tropsch Synthesis Catalysts

Abstract

Elements that form metal oxides (Ce, Gd, La, Mn, and Zr) were investigated as promoters for improving the activity and selectivity of Co-based FTS catalysts. The extent to which these promoters decrease the selectivity toward CH_4 and increase the selectivity toward C_{5+} hydrocarbons depends on both the loading and the identity of the promoter element. Elemental mapping by STEM-EDS revealed that the propensity for a given element to associate with Co is connected to the sensitivity of the product distribution toward changes in promoter loading. For all promoters, a sufficiently high loading resulted in the product distributions becoming insensitive to further increases in promoter loading, very likely due to the formation of a half monolayer of promoter oxide over the Co surface. Simulations suggest that the fraction of Co active sites that are adjacent to the promoter moieties approaches unity at this degree of coverage. The oxidation states of the promoters under reaction conditions, determined by in situ XANES measurements, were used to calculate relative Lewis acidities of the promoters based on Sanderson electronegativities. The strong positive correlation between the C_{5+} product selectivity and the Lewis acidity of the promoter oxide suggests that the promotional effects are a consequence of Lewis acid-base interactions between the reaction intermediates and the catalyst surface. Kinetics data obtained at different pressures were used to obtain estimates for the apparent rate coefficient and the CO adsorption constant appearing in the Langmuir-Hinshelwood expression that describes the CO consumption kinetics for both the unpromoted and the metal oxide-promoted catalysts. Both parameters had positive correlations with the promoter Lewis acidity. These results are consistent with the hypothesis that the promoter acts as a Lewis acid interacting with the O atom of adsorbed CO to facilitate CO adsorption and dissociation.

5.1 Introduction

Fischer-Tropsch synthesis (FTS) over Co-based catalysts has been a widely studied chemical process for converting feedstocks such as biomass, coal, and natural gas into synthetic transportation fuels. Although modern FTS catalysts largely produce C_{5+} hydrocarbons, the production of light hydrocarbons by these catalysts remains a significant obstacle for achieving favorable FTS process economics.[1] To shift the product distribution toward higher molecular weight hydrocarbons as well as to increase catalyst activity, promoters are often added to Co-based FTS catalysts.[2] A variety of elements have been identified as having promotional effects on the activity and selectivity of these catalysts, and elements that form metal oxides have been most consistently reported as being capable of improving the FTS product distribution. Research concerning metal oxide promotion originates from investigations into the effects of oxide supports on catalytic properties.[3] At present, most research focuses on systems where the

promoter precursor is deposited as an additive onto the catalyst, which affords more control over the interactions between the active Co metal and the metal oxide promoter.

This approach has been explored thoroughly for catalysts promoted with early transition metals and lanthanides. Studies by de Jong et al.[4,5] and Weckhuysen et al.[6-10] have demonstrated that promotion with MnO enhances CO consumption rates and C_{5+} selectivity. Moreover, it is now well-established that these promotional effects require contact between the Co and MnO[11,12]. Multiple researchers have reported that ZrO_2 promotion increases FTS turnover frequencies and results in higher selectivity to long-chain hydrocarbons[13-16]. Similar observations were made for Co catalysts promoted with La,[17-20] Ce,[21,22] and Gd.[23] Despite the abundance work on metal oxide promotion, there have been limited efforts to compare promoter elements directly and rationalize any differences in terms of periodic trends.

For many metal nanoparticle-based catalysts, active sites at the interface between the metal and an oxide exhibit altered reactivity. This phenomenon is well-known for various metals supported on oxide supports,[24,25] but these effects can also be exploited via promotion. Rate enhancements for CO methanation over Pd have been observed for catalysts that were promoted with La_2O_3 moieties.[26] Using Rh catalysts, multiple researchers have demonstrated that CO hydrogenation rates are improved when the Rh is partially covered by metal oxide overlayers.[27,28] These findings have led to the hypothesis that metal oxide interfaces assist CO dissociation during FTS.[29] Specifically, it has been proposed that metal cations act as Lewis acids that interact with the O atom of CO adsorbed onto Co, thereby facilitating the cleavage of the C–O bond.[30] This reasoning suggests that the magnitude of metal oxide-based promotional effects should be related to the Lewis acidity of the promoter. Recently, we have reported the existence of correlations between the C_{5+} selectivity of Co-based FTS catalysts and promoter Lewis acidity.[31,32] Similarly, a study by Prieto et al. has found connections between both FTS turnover frequency and C_{13+} selectivity and the Lewis acidity of oxide supports.[33] These results identify the role of Lewis acidity in understanding promotional effects, but the importance of interface formation between the Co and the metal oxide and the effects of Lewis acidity on the rate law parameters have not been clearly defined.

In this study, a variety of metal oxide promoters (Ce, Gd, La, Mn, and Zr) were investigated for their effects on the catalytic properties of Co-based FTS catalysts. These promoters were found to form highly dispersed oxide structures over the surface of the Co nanoparticles. Relationships between catalyst performance and the degree of coverage of the nanoparticles by the promoter strongly suggest that the formation of an interface between the Co and the promoter oxide is responsible for the promotional effects. The active sites in the promoted catalysts are presumed to occur at the metal-metal oxide interface, and evidence is found that such sites enhance CO adsorption and dissociation of the C–O bond. The strength of these promotional effects is found to correlate with the Lewis acidity of the promoter, supporting the hypothesis that Lewis acid-base interactions are responsible for metal oxide promotion of FTS on Co.

5.2 Experimental Section

5.2.1 Catalyst Synthesis

Catalysts synthesis was carried out as described previously.[34] For the unpromoted catalyst, incipient wetness impregnation was used to deposit $Co(NO_3)_2$ (Sigma-Aldrich, 99.999% purity) onto porous SiO_2 (PQ Corporation, CS-2129). The promoted catalysts were prepared by co-impregnation whereby the aqueous impregnation solution included both the $Co(NO_3)_2$ and the precursor of the promoter element. For this work, the promoted catalysts were prepared using either Mn acetate or nitrate salts of Ce, Gd, La, or Zr (Sigma-Aldrich, 99.999% purity). $Mn(CH_3CO_2)_2$ was used because this precursor has previously been shown to yield the desired catalyst structure.[35] After the metal precursors were deposited onto the SiO_2, the sample was dried overnight at ambient temperature and then heated at 5 K/min to 723 K under flowing H_2 (100 mL/min) and held at 723 K for 2 h. After this step, the reduced catalyst was cooled to ambient temperature under flowing He (100 ml/min). The catalyst was then exposed to 500 ppm O_2 (100 mL/min) to passivate the Co.

5.2.2 Temperature-Programmed Reduction

The reduction profiles for the passivated catalysts were obtained by heating the samples from ambient temperature to 850 K at 5K/min in a quartz tube reactor under flowing 1% H_2, 1% Ar, and 98% He (30 mL/min). The composition of the reactor effluent was monitored by an MKS Minilab quadrupole mass spectrometer. Corrections for variations in the reactor effluent flow rate were made using the Ar signal as an internal standard.

5.2.3 O_2 Titration

O_2 titrations of the reduced catalysts were performed using a Micromeritics AutoChem II 2920 instrument. In a typical measurement, a sample of passivated catalyst was loaded into a quartz U-tube, which was then inserted into the instrument. The sample was reduced by heating it at 5 K/min to 723 K under flowing H_2 (100 mL/min) and then holding it at 723 K for 2 h. The sample tube was subsequently flushed with He (100 mL/min) until the thermal conductivity detector (TCD) in the instrument achieved a stable baseline signal. Pulses of 20% O_2 in He (3.1 µmol O_2/pulse) were then injected into the He carrier gas flow every 6 min in order to titrate the reduced catalyst. The final O_2 uptake was determined by the number of pulses required to achieve TCD peaks of equal area.

5.2.4 H_2 Chemisorption

Static H_2 chemisorption was performed using a Micromeritics 3Flex surface characterization analyzer. Passivated catalyst samples were loaded into a quartz U-tube and then reduced by heating at 5 K/min to 723 K under flowing H_2 and holding at 723 K for 2 h. The sample tube was then evacuated for 2 h at 723 K and cooled to 373 K. An H_2 adsorption isotherm was then collected by dosing a fixed quantity of H_2 into the sample tube and allowing the pressure to equilibrate. Based on work by Reuel and Bartholomew,[36] it was assumed that the total H_2 uptake from a single isotherm collected at 373 K corresponds most closely to 1/1 H/Co adsorption stoichiometry, neglecting any H_2 spillover onto the promoter oxide. As described in the Results

section, severe H_2 spillover occurred on the lanthanide-promoted catalysts, which prevented the H_2 uptake data from being used to determine the quantity of surface Co metal for these catalysts.

5.2.5 X-Ray Absorption Spectroscopy

X-ray absorption spectroscopy (XAS) measurements were conducted at beamlines 5-BM (DND-CAT) and 10-BM (MRCAT)[37] at the Advanced Photon Source synchrotron at Argonne National Laboratory. All spectra were acquired in transmission mode with the energy of the incident X-rays controlled by a Si(111) monochromator. The samples were placed between two gas ionization detectors to measure the absorption of X-rays, and a reference metal foil was placed between the second and a third detector to calibrate the X-ray energies and align the spectra. Catalyst samples were pressed into pellets and placed inside a cell that was heated by a tube furnace and connected to a gas inlet manifold. X-ray absorption near-edge structure (XANES) spectra of the passivated catalysts were collected at the Co K-edge and promoter L_3-edge before reducing the catalysts by heating the cell at 5 K/min to 723 K under flowing H_2 and holding at 723 K for 2 h. Following the reduction step, the catalysts were cooled to ambient temperature under flowing He and extended X-ray absorption fine structure (EXAFS) spectra were collected at the Co K-edge along with XANES spectra at the promoter L_3-edge. The cell temperature was then increased to 493 K and the catalysts were exposed to a 2/1 H_2/CO synthesis gas mixture. After 6 h of aging under synthesis gas, a final set of XANES spectra were collected. The Demeter software family,[38] which uses IFFEFIT internally,[39] was used to process and analyze the XAS spectra. Fits of the EXAFS region of the spectra were done following the procedures described in our recent study of Zr-promoted catalysts.[34]

5.2.6 STEM Imaging and Elemental Mapping

Samples for electron microscopy were prepared by drop-casting ethanol suspensions of ground catalyst particles onto lacey carbon-covered Cu TEM grids (Ted Pella). The TEM grids were dried in a vacuum oven at 383 K for 1 h to evaporate the solvent. All microscopy work was conducted at the National Center for Electron Microscopy at the Molecular Foundry of the Lawrence Berkeley National Laboratory using an FEI Titan electron microscope that was operated with an accelerating voltage of 200 kV. Co nanoparticle size distributions were obtained by high-angle, annual dark-field scanning transmission electron microscopy (HAADF-STEM). Energy dispersive spectroscopy (EDS) with a Bruker, four-segment, silicon drift detector was used to obtain elemental maps of the Co and promoter elements. For these measurements, the fluorescent X-ray spectrum from 0-20 keV was collected with an energy resolution of 140 eV and a dispersion of 10 eV per channel. The electron micrographs and elemental maps were analyzed by the ImageJ and Bruker Esprit software programs, respectively. Nanoparticle compositions were determined from the elemental map data by the Cliff-Lorimer method[40] using the Ce L_α (4.839 keV), Co K_α (6.931 keV), Gd L_α (6.053 keV), and La L_α (4.647 keV) X-ray peaks. Peak deconvolution was performed by the software to obtain accurate areas for the Co K_α and Gd L_α peaks, which were close in energy, and to remove Fe and Cu background signals. The mapped regions were estimated to be thin enough such that self-absorption and secondary X-ray fluorescence would be negligible.

5.2.7 Catalytic Reactions

Catalyst activity and selectivity were assessed by conducting FTS reactions in packed-bed reactors. For these experiments, a sample of passivated catalyst diluted with calcined SiO_2 was loaded into either a quartz or stainless steel reactor (1 cm inner diameter) for reactions for atmospheric and elevated pressure, respectively. The reactor was heated by a tube furnace, and mass flow controllers were used to regulate the flow of gases to the reactor. A diaphragm back-pressure regulator controlled the pressure within the stainless steel reactor. Immediately downstream of the reactors were sample collection vessels, heated to 403 K, that collected the liquid wax products. An Agilent 6890N gas chromatograph was used for online analysis of the gaseous products leaving the sample collection vessels. All tubing downstream of the sample collection vessels was maintained at 503 K to prevent product condensation.

In a typical experiment, the catalyst was first reduced by heating the reactor at 5 K/min to 723 K under flowing H_2 (100 mL/min) and holding it at 723 K for 2 h. The reactor was then flushed with He and cooled to 493 K, the temperature used for all FTS reactions in this study. Over the course of 10 min, synthesis gas composed of 7% Ar, 31% CO, and 62% H_2 was gradually introduced into the reactor while the He flow was gradually stopped to prevent runaway conditions. The catalyst was then aged for 12 h under differential conversion conditions, after which the catalyst activity was stable to within 10% for the duration of the experiments. Measurements were then conducted at different pressures and space velocities. The reactor and SiO_2 support were found to have negligible background activity, and the system was determined to satisfy the Weiss-Prater criterion[41] so that transport limitations could be ruled out. The conversion and activity of the catalysts were calculated as previously reported.[34] At atmospheric pressure, the sum of the C-containing products was used to calculate activity; at elevated pressure where liquid wax production can be significant, the CO consumption was used to determine activity. The product selectivities were calculated according to the methods used by Dinse et al.[42] On a molar carbon basis, CO_2 and oxygenates were less than 1% of the product distribution.

5.3 Results

5.3.1 Effects of Metal Oxide Promotion on Co Reduction

Temperature-programmed reduction (TPR) profiles for the unpromoted and metal oxide-promoted catalysts are shown in Figure 5.1. For the unpromoted catalyst and the catalysts promoted with Ce, Gd, La, and Mn, a single Co reduction peak was observed between 555 and 585 K. Most literature studies of Co catalysts propose a two-step reduction consisting of Co_3O_4 reducing to CoO followed by CoO reducing to Co metal.[43,44] These two reduction events can occur with very little temperature separation as reported by Martínez et al. for the reduction of Co supported on SBA-15.[45] The temperature range for the peaks observed in the present study is close to that reported by Martínez et al. for the reduction of Co_3O_4 to CoO (560 to 580 K) and CoO to Co metal (580 to 610 K). Given that the catalysts in the present study are active for FTS after reduction as low as 673 K, it is likely that the observed reduction peak consists of overlapping contributions from the reduction of Co_3O_4 to CoO and the reduction of CoO to Co metal. A second broad peak appears in most of these profiles centered near 723 K, which may

correspond to the partial reduction of Co species associated with the support or promoter.[46,47] Increasing the reduction temperature from 673 to 723 K did not affect catalyst activity substantially. Even if this additional reduction event corresponds to further Co formation, it does not appear to result in the formation of additional catalytically active sites. The TPR profile for the Zr-promoted catalyst was more complex, with reduction peaks appearing at 475 and 675 K. Based on these temperatures, it is plausible to assign the first and second peaks to the reduction of Co_3O_4 to CoO and the reduction of CoO to Co metal, respectively; however, it remains unclear as to why Zr alters the phase of the passivated Co and whether this initial phase incorporates Zr. The area of the first peak is close to that of the second peak, which is consistent with the results from O_2 titration indicating that the Co_3O_4 reduces to CoO and only about half of the CoO reduces further to Co metal.

Most of the promoter oxides did not undergo partial reduction during the catalyst pretreatment, but both Ce and Mn exhibited signs of reduction. For the Mn-containing catalyst, a shoulder in the TPR profile near 480 K exists, which possibly corresponds to the reduction of MnO_2 to MnO. Although the temperature for this reduction step is substantially lower than that for the first reduction step for bulk MnO_2,[48] in situ XANES measurements confirmed that the Mn in the passivated catalysts had an apparent oxidation state of 4+, which reduced to 2+ after reduction. Similar observations were made for the Ce-promoted catalyst in which the oxidation state of Ce reduced from 4+ to 3+. The small peak at 690 K in the TPR profile possibly corresponds to this reduction step and is about 70 K above the reported temperature at which bulk CeO_2 undergoes partial reduction.[49] The TPR profile for the Gd-promoted catalyst contains a broad peak centered at 700 K, but the persistence of Gd^{3+} after reduction suggests that this peak is not related to the reduction of Gd. Documenting these oxidation state changes is important because these events lead to higher O_2 titration uptakes, which need to be taken into account when calculating the extent of Co reduction.

O_2 titration uptakes for the reduced catalysts are listed in Table 5.1. These values were used to determine the extents of Co reduction, given in Table 5.2. XANES measurements of the Co apparent oxidation states suggested that the reduced catalysts consisted of a mixture of Co metal and CoO. Based on phase diagrams for Co and O, the Co metal and CoO were assumed to fully oxidize to Co_3O_4 during the O_2 titration measurements.[50] The contribution of the promoter oxidation state change to the O_2 uptake was included in the calculation assuming that Mn changes from 2+ to 4+ and that Ce changes from 3+ to 4+, as indicated by XANES measurements. These assumptions appear in eq. 5.1 where $f_{Co,metal}$ is the fraction of Co in the metallic state after reduction, U_{O_2} is the molar uptake of O_2, N_{Co} is the moles of Co, N_P is the moles of promoter, and γ is the stoichiometric factor for the oxidation of the promoter. There appears to be a weak relationship between the extent of Co reduction and the temperature of the main TPR reduction peak. The promoted catalysts exhibited increasing temperatures of Co reduction and decreasing extents of reduction in the order Mn < Gd < Zr. The Ce-promoted Co was unusual in that it had a lower temperature of Co reduction than the unpromoted catalyst and yet its extent of Co reduction was lower than that for the unpromoted catalyst. This suggests that a portion of the Co was associated with the promoter in an irreducible phase dispersed over the support.

$$f_{Co,metal} = \frac{2U_{O_2} - \left(\frac{4}{3} - 1\right)N_{Co} - \gamma N_P}{N_{Co}} \quad (5.1)$$

5.3.2 Effects of Metal Oxide Promotion on Co Nanoparticle Size

To make meaningful comparisons between the unpromoted and metal oxide-promoted catalysts, it is important to establish whether the addition of the promoters resulted in changes in the mean Co nanoparticle diameters. Nanoparticles with diameters less than 6 to 10 nm have been shown to have lower turnover frequencies and higher selectivities toward CH_4 than larger particles.[51,52] Consequently, similarly sized Co nanoparticles must be present in the metal oxide-promoted catalysts to assume the absence of promoter-induced Co particle size effects on catalyst activity and selectivity. Based on our prior work with Mn-[35] and Zr-promoted[34] catalysts, for which the nanoparticle diameters were close to 10 nm and largely independent of promoter loading, all catalysts in the present study were prepared with the same Co weight loading with respect to the sum of Co and SiO_2 and pretreated by directly reducing the catalyst precursors in H_2. This strategy was found to yield similarly sized Co nanoparticles for the lanthanide promoters as shown in Table 5.1.

The surface mean diameters[53] reported in Table 5.1 were obtained by examining about 300 nanoparticles from different regions in the HAADF-STEM images of the catalysts. Since the visual contrast between the Co nanoparticles and the SiO_2 is often poor, STEM-EDS elemental maps were used to confirm which features corresponded to Co nanoparticles as opposed to concentrated regions of SiO_2. This approach is represented by the green highlighting in the images included in Figure S5.1 of the Supporting Information. The Co nanoparticles frequently appeared in clusters, which is particularly evident in Figures S5.1B and S5.1C of the Supporting Information. Accordingly, the diameters were extracted from the HAADF-STEM images, which had higher spatial resolution than the elemental maps. The diameters reported in Table 5.1 were corrected for the density difference between Co metal and CoO because Co within the passivated catalysts was predominantly in the form of CoO prior to reduction. These procedures resulted in estimates for the mean nanoparticle diameters of between 9 and 12 nm, which means that the Co particle sizes lie outside the regime where size effects on catalyst activity and selectivity might occur. The standard deviations of the nanoparticle size distributions ranged from 2 to 4 nm and were also not affected by the promoter.

5.3.3 Effects of Metal Oxide Promotion on Co Nanoparticle Structure

With regard to Co nanoparticle structure, no evidence for the presence of mixed phases of Co and the promoter was observed. The Co K-edge EXAFS spectra of the reduced catalysts shown in Figure 5.2 are consistent with each catalyst consisting of a mixture of Co metal (presumed to be in the hexagonal close-packed crystal structure) and CoO. To provide context for these results, the spectrum of Co metal exhibits a peak at R = 2.18 Å, corresponding to the first coordination shell of neighboring Co atoms. The spectrum of the CoO reference sample contains peaks R = 1.61 and 2.61 Å for Co-O and Co-Co scattering paths, respectively. The EXAFS spectrum of the unpromoted catalyst is composed of metallic Co peaks principally, although contributions from CoO are also visible. The ratio of the intensity of the CoO peaks to that of the metallic Co peak increased with the promoters in the order La < Ce < Mn. This feature is also

present in the peaks corresponding to the higher order coordination shells that were not fit (i.e., between R = 3 and 6 Å). Qualitatively, these results match the ordering for the extents of Co reduction (Table 5.2) in which the unpromoted catalyst had the highest extent of reduction followed by the La-, Ce-, and Mn-promoted catalysts in that order. Of the elements considered in this study, the Zr-promoted catalyst had the lowest extent of Co reduction. The EXAFS spectrum of this catalyst, which was reported previously,[34] contains the highest CoO peak intensities relative to the Co metal peak intensity. Owing to the proximity of the energies for the Co K-edge and Gd L_2-edge, it was not possible to analyze the EXAFS region of the XAS spectrum of the Gd-promoted catalyst.

Without signs for the formation of metallic alloys or mixed oxides composed of the Co and the promoters, it is reasonable to conclude that any promoter in contact with the Co would decorate the surface of the Co nanoparticles. Coverage of the Co surface by the promoter oxide should result in the fraction of the nanoparticle surface that is accessible to chemisorption being smaller for the promoted catalysts compared to the unpromoted catalyst. This hypothesis was tested by means of H_2 adsorption experiments. For the unpromoted catalyst, a close agreement was found between the nanoparticle dispersion determined by TEM, 8.3%, and the dispersion determined by H_2 uptake, 8.5%. For the promoted catalysts, TEM particle sizes and H_2 uptake data were used to estimate the fraction of the nanoparticle surface covered by the promoter according to the procedure reported previously.[35] As shown in Table 5.2, the Mn- and Zr-promoted catalysts both had H_2 uptakes equivalent to about half of the Co nanoparticle surface assuming 1/1 H/Co adsorption stoichiometry, suggesting that the promoter formed a half monolayer over the metallic Co. Ce and Gd promotion led to comparatively large H_2 uptakes that exceeded the upper limit of surface Co determined by TEM particle sizes. These results are clear indicators for the occurrence of H_2 spillover from the Co onto the promoter occurring in these catalysts. As a consequence, the fractional coverage of the Co surface by the promoter cannot be calculated for these catalysts. It is less clear whether the La-promoted catalyst was also subject to H_2 spillover since its calculated dispersion by H_2 chemisorption was less than the dispersion determined by TEM. However, given the chemical similarity of La to other lanthanides, it would be reasonable to consider the estimated 10% promoter coverage of the La-promoted Co as being underestimated.

5.3.4 Promoter Oxidation States and Structure

The oxidation states of the promoters under reaction were determined by in situ XANES measurements. Figure 5.3 shows the promoter L_3-edge XANES spectra of the lanthanide-promoted catalysts in the passivated state, after reduction, and after 6 h exposure to synthesis gas. In Figure 5.3A, the spectrum of the La/Co = 0.1 catalyst is very similar to that of La_2O_3, suggesting that the apparent oxidation state of the La promoter was 3+ and did not change during the pretreatment or FTS reaction. The spectrum of the passivated Ce-promoted catalyst most closely resembles that of CeO_2 (Figure 5.3B). After reduction at 723 K in H_2, the edge energy of the spectrum of the Ce-promoted catalyst shifted to lower energy and resembled those of the Ce(III) references. Here, $Ce(NO_3)_3$ and $Ce_2(SO_4)_3$ were used as reference samples in place of Ce_2O_3 which oxidizes under ambient conditions. Exposing the reduced catalyst to FTS reaction conditions caused minimal changes to the spectrum. These results demonstrate that the

apparent oxidation of Ce was 4+ in the passivated state, underwent reduction to the 3+ oxidation state following reduction of the catalyst in H_2, and then remained at 3+ under reaction conditions. The spectra of the Gd-promoted catalyst were all similar to that for the Gd_2O_3 reference sample, indicating that Gd adopted a 3+ apparent oxidation state.

Although the metal oxidation states are essential for estimating Lewis acidities, the crystal structure and local environment of the promoter also need to be considered because they can affect the Lewis acidity of oxides.[54] Owing to the highly dispersed nature of the promoters, it was not possible to identify their crystal structures by means of X-ray diffraction. Instead, XAS measurements were used to make inferences about the promoter coordination environments. Prior measurements of the Zr-promoted catalyst indicated that the promoter most closely resembled monoclinic ZrO_2 at high loadings where the promotional effects were maximal.[34] Additionally, it was determined that the promoter was highly dispersed over the catalyst surface. Similar findings were obtained for the Mn-promoted catalyst used in the present study. The positions of the first two peaks in the EXAFS spectrum of the reduced Mn-promoted catalyst closely match those for the Mn-O and Mn-Mn scattering paths in MnO with the rock-salt structure (Figure S5.2 of the Supporting Information). A notable difference between the spectrum of the catalyst and that of MnO is that the relative intensities of these peaks are inverted. This is a consequence of the Mn being more highly dispersed within the catalyst such that a central Mn atom is surrounded by fewer neighboring Mn atoms than is the case for bulk MnO. The high dispersion of the Mn promoter also contributes to the lower intensity of the EXAFS peaks between R = 3.3 and 6 Å, resulting from next-nearest neighboring atoms located farther from the central absorbing atom.

Unfortunately for the Ce, Gd, and La promoters, the close energy overlap of their L edges prevents EXAFS analysis of the corresponding spectra. However, recent work by Asakura et al. has reported that a correlation exists between the full width at half maximum (FWHM) of the white line of the La L_3-edge and the La coordination number.[55] Following their procedure of fitting an arctangent and pseudo-Voigt function to the edge, it was determined that the widths of the La L_3-edge white lines for the L_2O_3 reference and the La-promoted catalyst were similar (4.7 eV), which suggests similar coordination environments for the La atoms in both samples. Following these trends, it was assumed that the Ce and Gd promoters adopted crystal structures consistent with their bulk oxides.

5.3.5 Spatial Association between Co and the Metal Oxide Promoters

The ability of the lanthanide promoters to associate with Co was evaluated by elemental mapping. Representative STEM-EDS maps of these catalysts prepared with promoter loadings high enough such that the product selectivity was insensitive to promoter loading are shown in Figure 5.4. Visual inspection of these maps reveals that different promoters exhibited different degrees of association with the Co. For the La-promoted catalyst prepared with a La/Co atomic ratio of 0.1 (Figure 5.4A), a high degree of spatial overlap is observed between the La and Co channels (red and green, respectively). Here, yellow nanoparticles are clearly visible, which indicates the copresence of both elements at the nanoparticle locations. Also, the relatively low intensity of the La signal over the catalyst support indicates that most of the La was associated with the Co nanoparticles. By contrast, an absence of preferential association between the

promoter and Co occurred for the Ce-promoted catalyst. Figure 5.4B shows an extreme example for the catalyst prepared with Ce/Co = 2.0 in which segregation is clearly visible between the Co nanoparticles and the CeO_2. Although not all elemental maps of the Ce-promoted catalyst exhibited such segregation, the CeO_2 was always found to be highly dispersed over the catalyst surface. The Gd-promoted catalyst prepared with a Gd/Co ratio of 1.0 also appeared to lack a preferential association for the Co, which is seen in Figure 5.4C in which the Gd is highly dispersed over the catalyst surface. For all catalysts, the promoters appears to be well dispersed over the catalysts support, and no features attributable to promoter oxide nanoparticles larger than nanometer scale were observed.

The elemental maps in Figure 5.4 suggest that La has a much stronger affinity for Co than Ce and Gd. This conclusion is reinforced by the analysis of nanoparticle compositions in the promoted catalysts. Figure 5.5 shows nanoparticle composition histograms for the Ce-, Gd-, and La-promoted catalysts at low and high promoter loadings. These data were obtained from the elemental maps by combining the X-ray spectra from all pixels within 1 nm of a nanoparticle and calculating the composition of this region using the Cliff-Lorimer method. Between 100 and 200 nanoparticles were quantified for a given catalyst sample to obtain a composition histogram. A summary of the means and standard deviations of the nanoparticle compositions distributions for each promoter, including Mn and Zr, at low and high loadings is presented in Table S5.1 of the Supporting Information.

In accordance with Figure 5.4A, the nanoparticle composition distribution for the catalyst prepared with La/Co = 0.1 (Figure 5.5A) had a mean value of 0.094, which is very close to the bulk La/Co ratio. By a material balance, this agreement between the mean nanoparticle composition and the bulk composition suggests that nearly all La was associated with the Co. The mean nanoparticle compositions for the Ce- and Gd-promoted catalysts at the same loading were only 0.027 and 0.052, respectively. These values are significantly lower than the bulk promoter/Co ratio of 0.1, indicating that a substantial fraction of the promoter was not associated with the Co nanoparticles for both catalysts. Interestingly, the histograms for the La- (Figure 5.5A) and Gd-promoted (Figure 5.5E) catalysts were modeled accurately by Gaussian functions whereas the composition distribution for the Ce-promoted (Figure 5.5C) catalyst had a shape that was closer to an exponential distribution. This difference may be a consequence of the Ce spatial distribution being negatively correlated with the Co. At higher loadings, the mean nanoparticle compositions for all the lanthanide-promoted catalysts were substantially lower than the catalyst bulk compositions (Figures 5.5B, 5.5D, and 5.5F). This is evidence that La in excess of an amount required to fully cover the surface of the Co deposits onto the support. A similar pattern was observed for the catalysts promoted by Ce and Gd.

Elemental maps and nanoparticle histograms for the Mn- and Zr-promoted catalysts were reported in our previous studies.[34,35] Briefly, the Mn exhibited a strong preference for associating with the Co at loadings below Mn/Co = 0.1. At Mn/Co = 0.5, the mean nanoparticle composition was 0.38, indicating that the additional Mn was dispersed over the support more so than on the Co nanoparticles. The location of the Zr did not appear to be correlated with the Co nanoparticles at low and high loadings, and the mean nanoparticle compositions for the Zr-promoted catalysts

were similar to those of the Gd-promoted catalysts prepared with the same promoter/Co atomic ratios.

5.3.6 Catalytic Activity

For catalysts in which the surface of the active phase is partially covered by another material, it is important to compare catalytic activity on the basis of turnover frequencies. For Co-based FTS catalysts this is typically done by considering the number of Co atoms accessible to H_2 chemisorption. While this technique has proven adequate for quantifying the surface Co atoms in unpromoted systems,[56] the presence of various metal oxide promoters in contact with the Co surface may complicate the analysis. In the present study, there is strong evidence that H_2 spillover occurred onto the lanthanide oxides, making it impossible to quantify the number of surface Co atoms. Using the H_2 uptake data to compute the turnover frequencies may grossly underestimate the values for the catalysts on which heavy spillover occurred. Based on our prior studies of Mn and Zr catalysts, for which H_2 spillover did not appear to have a large contribution, we propose the following workaround. Together, H_2 chemisorption uptakes and TEM particle size analysis suggest that Mn promotion effects are maximized when the Mn covers half the Co surface.[35] These results were also found to apply for Zr promotion.[34] Although these conclusions are empirically based, they are also consistent with theoretical expectations based on the simulated deposition of particles onto a surface.[57] Assuming that the particles decorating the surface are randomly deposited, the number of surface sites adjacent to, but not covered by, the particles would be maximized when the surface is half-covered by the particles (Figure S5.4 of the Supporting Information). Accordingly, if active sites at the interface between the Co and the promoter are responsible for the promotion effects, it is reasonable to hypothesize that for the lanthanide promoters, the loading at which the full effects of the promoter are achieved should occur when a half monolayer of the promoter is established on the Co surface.

Using the assumption that at the optimal promoter loading, the Co surface was half covered by the promoter oxide, the CO consumption rates were normalized to obtain estimated turnover frequencies. Figure 5.6 shows the dependence of turnover frequency on reactor pressure at 493 K in the regime of differential CO conversion. For all catalysts, the turnover frequencies increased with pressure, which is an expected consequence of increasing surface intermediate concentrations. However, as the pressure increased, the turnover frequencies also became less sensitive to pressure, which results from CO inhibition due to increasing CO surface coverage.[42] The turnover frequencies for the Gd-, Mn-, and Zr-promoted catalysts were about twice as high as those for the unpromoted catalyst and the Ce- and La-promoted catalysts. As a comparison, the turnover frequencies based on total H_2 uptake are shown in Figure S5.3 of the Supporting Information. In this figure, the turnover frequencies for the lanthanide-promoted catalysts are substantially lower than even the unpromoted catalyst due to H_2 spillover inflating the estimated number of active sites for the promoted catalysts.

To understand the effects of the promoters on CO adsorption and dissociation under FTS, a model was fit to the rate data using nonlinear least-squares regression. Previously, we have shown that a two-parameter Langmuir-Hinshelwood expression (eq. 5.2) was suitable for describing the CO consumption rates for the unpromoted, Mn-promoted, and Zr-promoted catalysts.[34,35] In this expression, $-r_{CO}$ is the rate of CO consumption, P_{H_2} is the partial pressure

of H_2, and P_{CO} is the partial pressure of CO. While this rate law was arrived at empirically,[58] the equation can also be derived assuming H-assisted CO dissociation as the rate determining step.[59] Using this mechanism, the parameters a and b in the rate law correspond to the apparent rate coefficient for CO consumption and the CO adsorption constant, respectively. In the present work, it was assumed that this rate law also applies to the lanthanide-promoted catalysts.

$$-r_{CO} = \frac{abP_{H_2}P_{CO}}{(1+bP_{CO})^2} \quad (5.2)$$

The fits to the rate data, represented by the curves through the turnover frequency data points in Figure 5.6, accurately described the dependence of the turnover frequencies for CO consumption on total pressure. A parity plot for all catalysts (Figure S5.5 of the Supporting Information) is highly linear, which confirms that the chosen rate law is suitable for describing the reaction kinetics. Values for the parameters a and b for each catalyst are given in Table 5.3. Both the apparent rate coefficient and the CO adsorption constant are larger for the metal oxide-promoted catalysts compared to the unpromoted catalyst. These results are consistent with there being facilitated C–O bond cleavage and higher CO surface coverages with the presence of the promoter. Although the estimates for the apparent rate coefficients depend on the total number of catalytically active sites, the CO adsorption constants were not affected by the site count. Consequently, the assumption of a half monolayer coverage of the Co surface did not influence the fitting of the CO adsorption constants.

5.3.7 Catalytic Selectivity

As shown in Figure 5.7, the selectivities to CH_4 and C_{5+} decreased and increased, respectively, for all promoted catalysts as the promoter loading increased. At a high enough loading, the selectivities plateaued and became insensitive to further increases in the promoter/Co ratio. The onset of the plateau occurred at different promoter/Co ratios for different elements. Moreover, the maximal improvement in the product distribution achieved at high promoter loading varied depending on the promoter element. Both La and Mn promotion caused rapid onsets of the promotional effects with CH_4 selectivity sharply decreasing and C_{5+} selectivity sharply increasing for these catalysts in the regime where the promoter/Co ratio was less than 0.1. By contrast, the product selectivities changed gradually with promoter loading for the catalysts promoted with Ce, Gd, and Zr. Only at a promoter/Co ratio of 1.0 for the Gd-promoted and Zr-promoted catalysts and 2.0 for the Ce-promoted catalyst did the selectivities cease to depend on promoter loading. These different sensitivities of selectivity toward the promoter loading were not related to the maximal selectivity improvements that could be achieved with each promoter element. In ascending order, the C_{5+} selectivities of the optimally-loaded catalysts increased with the promoter element as follows: La < Ce, Mn < Gd < Zr. The selectivities toward CH_4 and C_2-C_4 decreased with the identity of the promoter element in the same order.

At elevated pressure, the product distribution for all catalysts shifted toward higher molecular weight hydrocarbons, consistent with what is generally observed for Co-based FTS catalysts.[60] This is shown in Figure 5.8 for the CH_4 and C_{5+} selectivities. While the ordinal ranking of the promoters with respect to selectivity was generally preserved as pressure increased, the product selectivities of the catalysts converged as pressure increased. Whereas the C_{5+} selectivity

for the Zr-promoted catalyst was 95% larger than that for the unpromoted catalyst at atmospheric pressure, there was only a 13% improvement in the C_{5+} selectivity with Zr promotion at 10 bar. The carbon number selectivities for the lanthanide-promoted catalysts were not dependent on CO conversion at atmospheric pressure; however, at pressures above 5 bar, CH_4 selectivity decreased and C_{5+} selectivity increased slightly as CO conversion increased. Both of these phenomena were observed for the Mn-[35] and Zr-promoted[34] catalysts.

5.4 Discussion

5.4.1 Lewis Acidity of the Promoter Oxides

Several approaches exist for quantifying the Lewis acidity of metal oxides. At the simplest level, the oxidation state-adjusted Pauling electronegativity of the metal cation can be used as a proxy for Lewis acidity, which was the approach taken by Boffa et al. in their work relating the Lewis acidity of metal oxides deposited on Rh foil to CO and CO_2 hydrogenation rates.[28] More commonly, the spectroscopic signatures of basic probe molecules, such as CO and pyridine, are used as qualitative metrics for the Lewis acidity of surfaces.[61] Recent work by Jeong et al. has sought to bridge these approaches by creating a quantitative Lewis acidity scale for metal oxides based on Sanderson electronegativities.[62] The definition of relative Lewis acidity proposed by these researchers is given by eq. 5.3 in which N_M is the oxidation state of the metal cation and δ_M is the Sanderson partial charge[63] of the metal cation. It was found that eq. 5.3 exhibits a strong linear correlation with the energy of the intramolecular charge transfer (IMCT) band of alizarin (1,2-dihydroxy-9,10-anthracenedione), a sensitive probe molecule that coordinates with the cations present on the surface of metal oxides.

$$rel.\,Lewis\ acidity = N_M - 2\delta_M \tag{5.3}$$

This Lewis acidity scale proposed by Jeong et al. was chosen for comparing promoters in the present work because of its validation by probe molecule spectroscopy and its applicability toward a wide range of metal oxides, including lanthanide oxides. The suitability of this scale for catalytic studies has been demonstrated recently by Prieto et al. in their studies of synthesis gas chemistry over Rh[64] and Co-Ru[33] catalysts. In these studies, the Lewis acidity of oxide monolayer supports was related to catalyst activity and selectivity using the scale developed by Jeong et al. The shifts in the IMCT bands of alizarin adsorbed onto the oxide monolayers measured by Prieto et al. followed the same order with respect to oxide adsorbent as that reported by Jeong et al. for adsorption onto bulk oxides. Given the apparent insensitivity of Lewis acidity toward oxide thickness and the evidence that the promoters had coordination environments similar to those of their bulk counterparts, it was assumed that this Lewis acidity scale would be appropriate for the metal oxides in the present work. The Lewis acidity of the unpromoted catalyst, which serves as the point of reference, is not clearly defined by the scale because the characteristic feature of this catalyst is the lack of a metal oxide overlayer. To make comparisons between this catalyst and the metal oxide promoted catalysts, it was assumed that the lack of a promoter would be equivalent to a promoter with an oxidation state and Sanderson partial charge of 0. Hence, the unpromoted catalyst was assigned a value of 0 on the relative Lewis acidity scale. A list of the relative Lewis acidity values for the catalyst promoters is provided in Table 5.3 and, with more detail, in Table S5.2 of the Supporting Information.

5.4.2 Dependence of Catalytic Properties on Promoter Loading

Although higher loadings of the promoters were always associated with improvements in the product distributions, the sensitivity of these promotional effects to promoter loading for each element were markedly different. There appears to be no relationship between the promoter Lewis acidity or the maximal C_{5+} selectivity that can be achieved with a given element and the sensitivity of the product distribution toward the loading of that element. However, a strong connection exists between the promoter loading effects and the spatial association between the Co and the promoter. Analysis of the La- and Mn-promoted Co nanoparticle compositions revealed that these promoters associate preferentially with the Co up to a loading corresponding to a promoter/Co atomic ratio of about 0.1. The maximal C_{5+} selectivities for these promoters is also reached with a promoter/Co ratio of about 0.1. As the promoter loading increases above this critical ratio, the product selectivity does not change, and deposition of the additional promoter occurs onto the catalyst support separate from the Co nanoparticles. The insensitivity of the product distribution toward promoter loading is not a simple consequence of the additional promoter not being near the Co. The mean nanoparticle promoter/Co ratio still increases with promoter loading when the loading exceeds the critical ratio. Hence, rationalizing these effects requires a subtler explanation.

For the La- and Mn-promoted catalysts, the critical atomic ratio is close to the quantity of promoter that would be required to form a half monolayer of the promoter on the surface of the Co. With patches of metal oxide decorating the Co surface, metal-metal oxide interfaces will form between the Co and the promoter. This phenomenon results in two ensembles of Co active sites: those that are separate from the promoter interface and those that are adjacent to the interface. The overall product selectivity of a promoted catalyst will be the average of the selectivities of these two ensembles weighted by the product of the site turnover frequencies and the number of sites in each ensemble. A catalyst in which all active sites are located at an interface with the promoter will exhibit the intrinsic selectivity of the promoted sites, whereas a promoted catalyst in which no Co is in contact with the promoter will perform the same as an unpromoted catalyst. Supposing that sites at the metal-metal oxide interface yield less CH_4 and more C_{5+} than unpromoted sites, this model explains why the product selectivities improve with increasing promoter loading up to a critical loading at which few Co sites remain that are not adjacent to the promoter oxide overlayer. Increasing the promoter/Co ratio above the critical ratio will result in lower specific activity owing to the Co surface becoming covered by the promoter so as to decrease the total number of sites. This effect underlies the higher activity per gram Co for the unpromoted catalyst compared to the metal oxide promoted catalysts (Figure S5.6 of the Supporting Information).

The findings of the present study on La- and Mn-promoted Co are consistent with those reported earlier. In their studies of La-promoted catalysts, Haddad et al. also found that the chain propagation probability and C_{2+} selectivity reached their maximal values with a La/Co ratio of 0.1.[20,65] Vada et al. concluded that for a catalyst prepared with La/Co = 0.1, the Co nanoparticle surface was about 33% covered by the promoter, which is close to our expectation for a surface covered by approximately a half monolayer.[18] The observation of a plateau in the product selectivity as a function of Mn loading found in the course of our study agrees well with what had

been reported earlier for Mn-promoted catalysts by den Breejen et al.[5] Together, these results suggest that our observation of close spatial association between the Co and both the La and Mn may be related to intrinsic properties of these elements more than to our catalyst preparation method. Moreover, the appearance of a plateau in the product selectivity at high promoter loadings for multiple promoter elements is consistent with our proposal that the effects of the promoter are related to coverage of the Co nanoparticle surface by the promoter.

The hypothesis that promoted active sites occur at the metal-metal oxide interface is also consistent with the selectivity data and elemental maps for the Ce-, Gd-, and Zr-promoted catalysts. For these elements, a more gradual onset of the promotion effects occurs in response to increasing promoter loading. As reported previously, the critical Zr/Co ratio of 1.0 corresponds to a loading that would form a half monolayer of ZrO_2 over the entire catalyst surface, which is corroborated by Co nanoparticle sizes and H_2 uptake data.[34] Assuming that patches of metal oxide are randomly distributed over the Co surface, the interfacial perimeter between the Co and the oxides should be maximized when the oxide loading is equivalent to a half monolayer.[57] Accordingly, it is reasonable to propose that the Co-ZrO_2 interface is maximized at Zr/Co = 1.0 and the fraction of sites that are promoted is near unity, which results in the product selectivity not improving with higher Zr loadings. Similar to Zr, the Gd promoter showed no correlation with the locations of the Co nanoparticles, which explains why the critical Gd/Co ratio was also 1.0. The larger critical ratio for Ce of 2.0 may be the result of a weak negative correlation between the Ce and Co spatial distributions. If Ce has a preference for segregating from the Co, then a higher loading of the promoter would be required for the Co surface to become optimally saturated by the oxide.

The relationship between the promoter identity and the value of the critical atomic ratio is likely related to the strength of the interactions between the promoter, Co, and SiO_2. Expanding on this concept, the ability of Co to form mixed oxides with the promoter during the initial precursor decomposition and pretreatment steps may be important. MnO adopts a rock salt crystal structure similar to CoO and the formation of mixed oxides containing the two metals is well-known.[66,67] Although Zr has an ionic radius similar to that of Co, Zr is tetravalent and ZrO_2 adopts a monoclinic crystal structure. Mixed oxides of Co and Zr have been reported,[68] but it is unclear whether these phases can undergo reduction so as to release the Co and form metallic nanoparticles. Mixed oxides containing Co and either Ce,[69] La,[70] and Gd[71] have been reported, typically with perovskite crystal structures, but it is challenging to conclude from existing data why the La appears to associate so readily with the Co after reduction, whereas Ce and Gd have greater tendencies to segregate.

It is important to note that the preference of a given promoter element to associate with Co is not necessarily applicable to catalysts outside this study. The degree of element association depends heavily on the manner by which the catalysts are prepared. In contrast to the present work, Feltes et al. found that for Mn-promoted catalysts that supported on TiO_2, the C_{5+} selectivity did not plateau below a Mn/Co atomic ratio of at least 0.3.[11] Other researchers have found that C_{5+} selectivity can pass through a maximum at intermediate Zr[14] loadings. These examples illustrate the variability in catalytic properties resulting as a consequence of catalyst preparation method. Therefore, in order to compare the effects of different metal oxide

promoters, it is important to monitor and control for variations in spatial association between the Co and the promoter.

5.4.3 Influence of Promoter Lewis Acidity on Catalyst Activity and Selectivity

In their studies of Rh-based catalysts, Sachtler et al. observed enhancements in the CO hydrogenation rate when metal oxides were added to the Rh surface.[72] By analogy to coordination complexes in which carbonyls bond simultaneously to two metal atoms through both the C and O atoms,[73] these researchers speculated that CO may adsorb onto Rh in a tilted configuration so as to interact with nearby metal oxides. These findings were extended by Boffa et al., who determined that a positive correlation exists between both CO and CO_2 hydrogenation rates and the Lewis acidity of metal oxide particles deposited onto Rh foil.[28] Presumably, a stronger interaction between the O atom of adsorbed CO and the promoter results in a weaker C–O bond that can be cleaved more readily. Similar mechanisms have been proposed for FTS over Co catalysts promoted with metal oxides.[74] While there is ample evidence for improved FTS activity and selectivity in the presence of metal oxides,[2] there has been limited effort to conduct a controlled comparison of promoters from the perspective of Lewis acidity effects.

A key prediction for the hypothesis that the cations within the promoter oxides serve as Lewis acids is that the magnitude of the promotional effects should scale with the Lewis acidity of the promoter. In addition to enhancing the rate of CO consumption through facilitated CO dissociation, the higher concentration of reaction intermediates on the promoted catalyst would accelerate chain growth and lead to a higher molecular weight product distribution. The FTS activity data reported here was examined for evidence of these effects, but a comparison between the FTS turnover frequencies with the promoter Lewis acidities did not reveal any clear trends. This is because promotion affects the rate law in a manner that creates both rate-enhancing and rate-inhibiting effects on the turnover frequencies. As shown in Figure 5.9, both the apparent rate coefficient for CO consumption and the CO adsorption constant correlate positively with promoter Lewis acidity. The correlation for the apparent rate coefficient is affected by the assumption that the Co nanoparticles were covered by a half monolayer of the promoter, but even if H_2 uptakes are used as the basis for rate normalization, the correlation persists (Figure S5.7 of the Supporting Information). The CO adsorption constant is not affected by the number of active sites, which may explain the greater linearity in the relationship between this parameter and the promoter Lewis acidity. Similar results are found for the relationship between product selectivity and promoter Lewis acidity. In Figure 5.10, the selectivities to CH_4, C_2-C_4 hydrocarbons, and C_{5+} hydrocarbons are plotted as a function of promoter Lewis acidity. Here, a negative relationship is evident between the light hydrocarbon selectivity and promoter Lewis acidity, and with higher promoter Lewis acidity, higher C_{5+} selectivities are achieved.

Together, these correlations between both catalyst activity and selectivity and the promoter Lewis acidity support the interpretation that Lewis acid-base interactions occur between the promoter and the reaction intermediates on the Co surface. While the higher apparent rate coefficients for the promoted catalysts unambiguously contribute to higher activity, the effect of the higher CO adsorption constant is more complex. In the low pressure regime, the higher CO adsorption constant results in higher rates due to the increasing surface coverage of CO; however, at high pressures where the surface is nearly saturated by CO, the

higher CO adsorption constant inhibits the reaction. Consequently, the turnover frequency for CO consumption is optimized with a promoter of intermediate Lewis acidity that balances the competing effects from the apparent rate coefficient and the CO adsorption constant. As shown in Figure S5.8 of the Supporting Information, this optimum occurs with Gd_2O_3 and MnO when the reaction is conducted at 493 K and 10 bar. With respect to product selectivity, the best-performing promoter was ZrO_2, which has the highest relative Lewis acidity of the elements considered in this study. Since the selectivity improvements are largely attributed to the larger adsorbed CO/H ratio on the promoted catalyst surface,[42,75] it would be reasonable to predict that oxides with even higher relative Lewis acidities would result in yet higher C_{5+} selectivities.

It is important to compare the findings of the present study with those Prieto et al. who recently reported positive correlations between both turnover frequency and C_{13+} selectivity and the Lewis acidity of metal oxide supports.[33] To a first approximation, the results of the present study are in agreement with those of Prieto et al.; however, there are two notable differences. First, the turnover frequencies reported by these authors increased monotonically with the relative Lewis acidity of the support, whereas in the present study an optimum at intermediate Lewis acidity was found. Although Prieto et al. controlled for nanoparticle size and pore size effects, the partial coverage of the Co nanoparticles by the metal oxide was not controlled, and catalysts prepared with WO_x exhibited more surface decoration by the metal oxide than catalysts prepared with oxides of lower Lewis acidity. If sites at the metal-metal oxide interface are responsible for the enhancements in the turnover frequency, then the turnover frequency for the catalyst with the highest relative Lewis acidity in the study by Prieto et al. (i.e., the catalyst prepared with WO_x) could have been overestimated, which could account for the monotonicity of the turnover frequency as a function of promoter Lewis acidity. However, we must concede that the assumption in the present study of half coverage of the Co surface by the promoter is imprecise and introduces uncertainty in our estimated turnover frequencies for the lanthanide-promoted catalysts.

The second difference between the two studies is that Prieto et al. observed the selectivity toward long-chain hydrocarbons to exhibit a volcano dependence with the optimal selectivity being achieved with either TiO_2 or Ta_2O_5. This is not experimentally inconsistent with the present study because we did not test elements with relative Lewis acidities greater than those for TiO_2 and Ta_2O_5. However, this finding does not follow from the assumptions that the CO adsorption constant increases monotonically with higher promoter Lewis acidity and that the product distribution shifts to higher molecular weights due to increases in the adsorbed CO/H ratio resulting from the larger CO adsorption constant. A plausible explanation for the trend observed by Prieto et al. relates to electron withdrawal from the Co metal to the oxide support, which is distinct from the proposed direct interaction between adsorbed CO and the promoter. Supports having stronger electronegativity have been found to decrease the electron density of Co nanoparticles more substantially than supports having weaker electronegativity.[76] This effect results in adsorbed CO being less strongly bound to Co when the oxide support is more electronegative. Consequently, the oxide may contribute toward two opposing effects: strengthening of CO adsorption due direct interactions with adsorbed CO and weakening of CO adsorption due to electron withdrawal from the Co. To rationalize the findings of Prieto et al. with our own, we speculate that for promoters with very high relative Lewis acidities, the effects

of lower Co electron density may outcompete the direct interaction between the promoter and the adsorbed CO so as to result in a lower adsorbed CO/H ratio on the Co surface. Hence, a promoter that is too Lewis acidic, specifically with a relative Lewis acidity higher than that of ZrO_2, may be detrimental to the product distribution.

5.5 Conclusion

The promotion of Co-based FTS catalysts by metal oxides can result in improvements to both catalyst activity and selectivity, and the effectiveness of these promoters depends heavily on the loading of the promoter. For catalysts promoted with either Ce, Gd, La, Mn, or Zr, the selectivity toward CH_4 decreases and the selectivity toward C_{5+} increases as the promoter/Co ratio increases, but eventually a critical loading is reached above which the product selectivities are insensitive to further increases in the promoter loading. This phenomenon is attributed to the formation of a metal-metal oxide interface between the Co and the promoter. STEM-EDS imaging suggests that a connection exists between the critical loading and the degree of association between the Co and promoter. For elements that exhibit strong preferential association with Co, such as La and Mn, only a small amount of the promoter (promoter/Co ≈ 0.1) is required to achieve the full promotional effects. Elements that appear to be dispersed over the catalyst support with no correlation with the Co nanoparticle locations, such as Ce, Gd, and Zr, require promoter/Co ratios of at least unity before product selectivities become insensitive to promoter loading. Assuming that La and Mn promotion represent the extreme case of complete spatial association of the promoter with the Co and that Ce, Gd, and Zr promotion represent the counterpart where no spatial correlation exists, these different critical promoter/Co ratios all correspond to approximately half monolayer coverage of the Co nanoparticle surfaces. This finding is consistent with the hypothesis that active sites along the interface with the promoter oxide are responsible for the promotional effects.

Along with promoter loading, the identity of the promoter element exerts a significant effect on the magnitude of the promotional effects. For catalysts prepared with the critical promoter/Co ratios, C_{5+} hydrocarbon selectivity increases with the Lewis acidity of the promoter element. Although strongest at atmospheric pressure, this effect persists at pressures up to 10 bar. A strong positive correlation exists between the apparent rate coefficient for CO consumption and the promoter Lewis acidity, which implies that the promoter facilitates cleavage of the C–O bond, most likely from adsorbed CHOH. Relatedly, the CO adsorption constant correlates strongly with the promoter Lewis acidity, which suggests that the promoter increases the surface coverage of the catalyst by CO under reaction conditions. This increase in the extent of CO adsorption shifts the product distribution toward higher molecular weight hydrocarbons, but greater CO surface coverage also inhibits the reaction rate. This interplay between the rate enhancing effect of a higher apparent rate coefficient and the rate inhibiting effect of a higher CO adsorption constant results in the turnover frequency at 10 bar being optimized by promoters with an intermediate Lewis acidity, such as Gd_2O_3 or MnO. These present results support the hypothesis that the role of the metal oxide promoter is to participate in Lewis acid-base interactions with adsorbed CO. Furthermore, these findings establish a periodic trend that can be used to rationally select candidate promoter elements that have yet to be tested for their effects on catalyst performance.

Acknowledgements

The funding for this study was provided by the Director, Office of Science, Office of Basic Energy Sciences and by the Division of Chemical Sciences, Geosciences, and Biosciences of the U.S. Department of Energy at Lawrence Berkeley National Laboratory under Contract No. DE-AC02-05CH11231. Work at the Molecular Foundry was supported by the Office of Science, Office of Basic Energy Sciences, of the U.S. Department of Energy under Contract No. DE-AC02-05CH11231. This research used resources of the Advanced Photon Source, a U.S. Department of Energy (DOE) Office of Science User Facility operated for the DOE Office of Science by Argonne National Laboratory under Contract No. DE-AC02-06CH11357. Portions of this work were performed at the DuPont-Northwestern-Dow Collaborative Access Team (DND-CAT) located at Sector 5 of the Advanced Photon Source (APS). DND-CAT is supported by Northwestern University, E.I. DuPont de Nemours & Co., and The Dow Chemical Company. MRCAT operations are supported by the Department of Energy and the MRCAT member institutions. We acknowledge assistance with the XAS measurements from Dr. Qing Ma, Dr. Konstantinos Goulas, Lin Louie, John Howell, Adam Grippo, and Julie Rorrer.

Table 5.1 Physical characterization data for the metal oxide-promoted catalysts.

Promoter Element	Promoter/Co Atomic Ratio[a]	Co Loading[b] (wt %)	d(Co)[c] (nm)	O_2 Uptake (mmol g_{cat}^{-1})	H_2 Uptake (mmol g_{cat}^{-1})
Unpromoted	N/A	9.8	12 ± 3	0.97	0.059
La	0.1	8.9	12 ± 4	0.80	0.040
Ce	2.0	6.4	9 ± 2	1.1	0.088
Mn	0.1	9.4	11 ± 3	0.82	0.022
Gd	1.0	7.3	10 ± 3	0.53	0.067
Zr	1.0	7.7	10 ± 4	0.55	0.017

[a] Composition at which selectivity becomes insensitive to promoter loading.

[b] Compositions were determined by ICP-OES.

[c] Surface mean diameter of Co metal nanoparticles.

Table 5.2 Extents of Co reduction, nanoparticle dispersions, and coverages of the nanoparticle surfaces by the metal oxide promoters.

Promoter Element	Promoter/Co Atomic Ratio[a]	Co(0)[b] (%)	Dispersion[c] (%)	Promoter Coverage[d] (%)
Unpromoted	N/A	83	8.3	N/A
La	0.1	73	8.2	10 ± 20
Ce	2.0	69	11	–
Mn	0.1	59	8.7	50 ± 20
Gd	1.0	52	9.7	–
Zr	1.0	52	9.2	40 ± 30

[a] Composition at which selectivity becomes insensitive to promoter loading.
[b] Percentage of Co in the metallic state after reduction.
[c] Determined by particle sizes assuming a site density of 14.6 Co atoms/nm^2.
[d] Percentage of the metallic Co nanoparticle surface area covered by the promoter.

Table 5.3 Fitted kinetics parameters for the unpromoted and Zr-promoted catalysts.

Promoter Oxide	Promoter/Co Atomic Ratio[a]	Rel. Lewis Acidity ($N_M - 2\delta_M$)	a^b (bar^{-1} s^{-1})	b (bar^{-1})
Unpromoted	N/A	0	0.085	1.4
La_2O_3	0.1	0.85	0.14	2.9
Ce_2O_3	2.0	0.96	0.13	3.1
MnO	0.1	1.4	0.26	3.3
Gd_2O_3	1.0	1.4	0.32	3.8
ZrO_4	1.0	2.5	0.32	5.0

[a] Composition at which selectivity becomes insensitive to promoter loading.
[b] Assuming that the Co nanoparticle surface is covered by a half monolayer of the promoter.

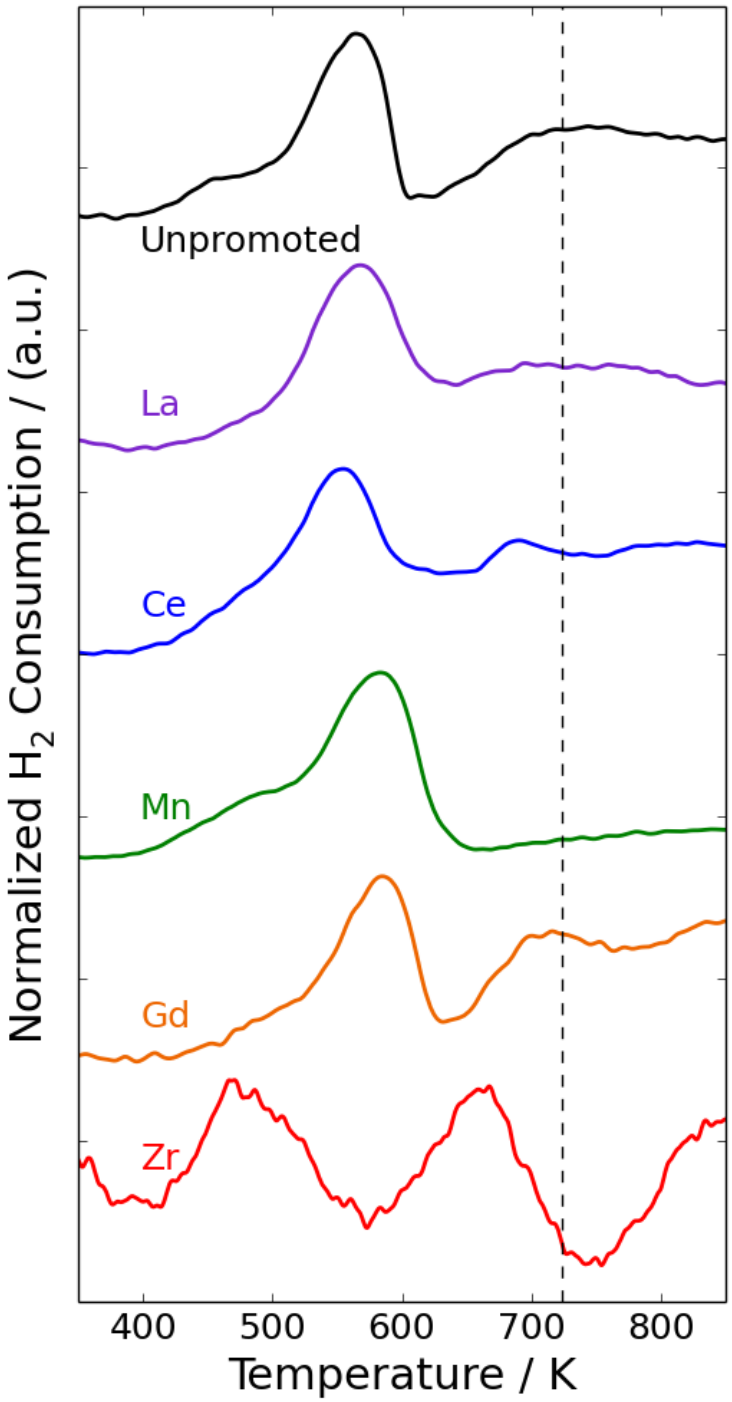

Figure 5.1 TPR profiles of the unpromoted and metal oxide-promoted catalysts. The samples were heated at 5 K/min from 298 to 873 K under flowing carrier gas (30 mL/min) composed of 1% H_2, 1% Ar, 98% He. The vertical dashed line indicates the temperature at which the catalysts were reduced prior to conducting FTS reactions (723 K).

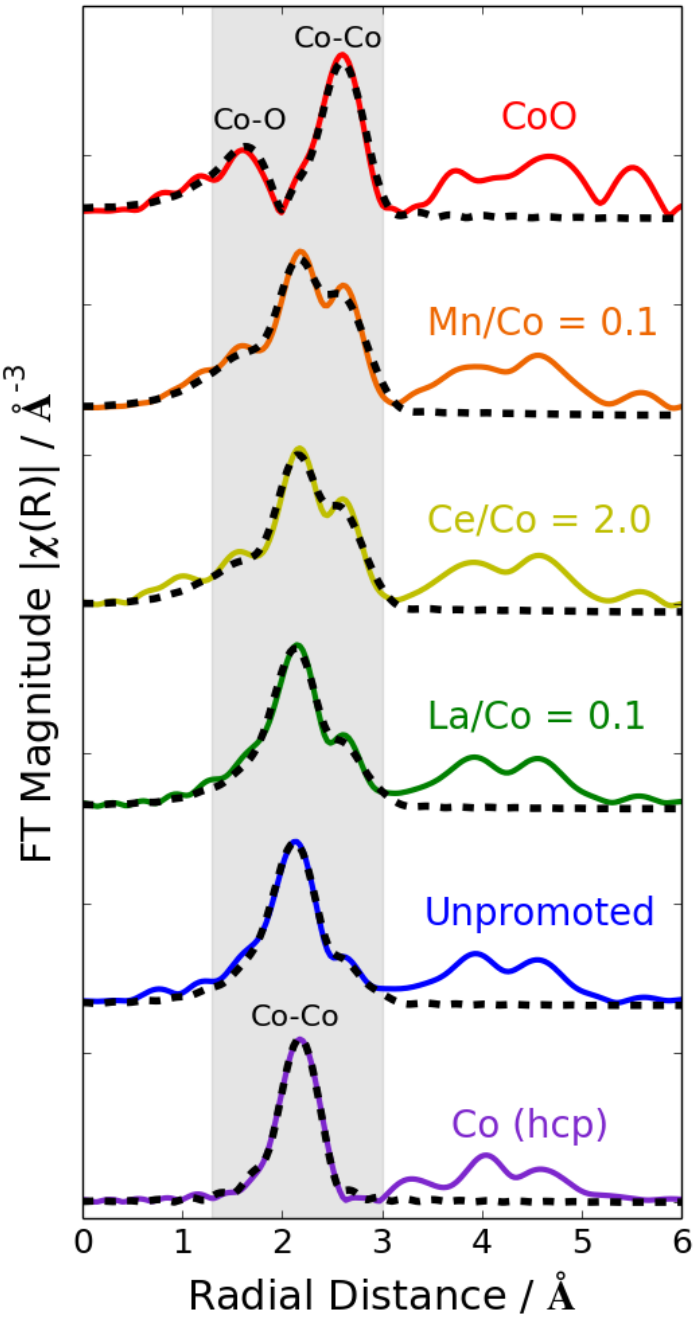

Figure 5.2 EXAFS spectra of the Co and metal oxide-promoted catalyst samples at the Co K-edge. The catalysts were reduced under flowing H_2 at 723 K for 2 h prior to collecting the spectra at ambient temperature and pressure under He. The Co metal and CoO references were measured without pretreatment. The solid colored lines in the plots are the k^2-weighted Fourier transforms of the EXAFS spectra, and the dashed black lines are fits to these data within the shaded gray region.

A)

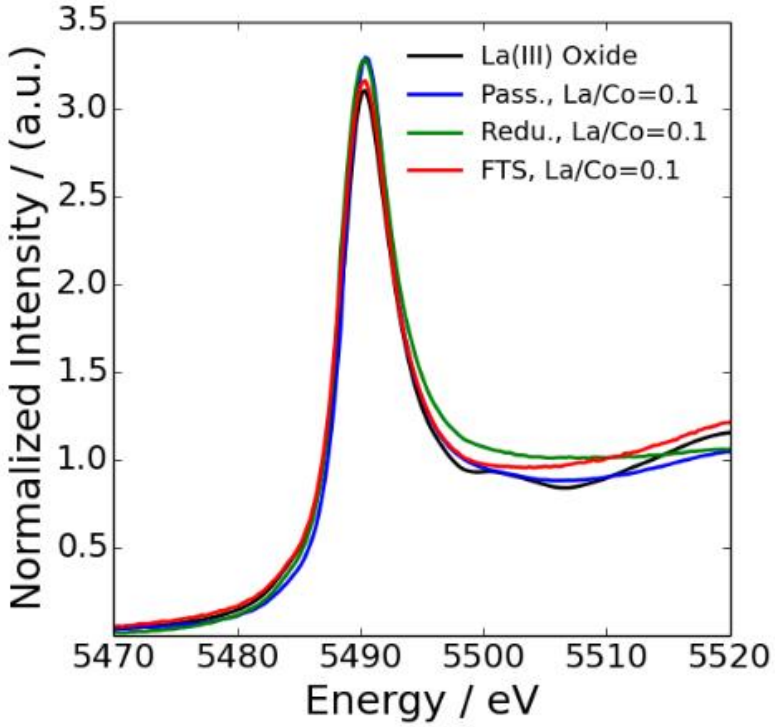
La(III) Oxide
Pass., La/Co=0.1
Redu., La/Co=0.1
FTS, La/Co=0.1
Normalized Intensity / (a.u.)
Energy / eV
3.5
3.0
2.5
2.0
1.5
1.0
0.5
5470
5480
5490
5500
5510
5520

B)

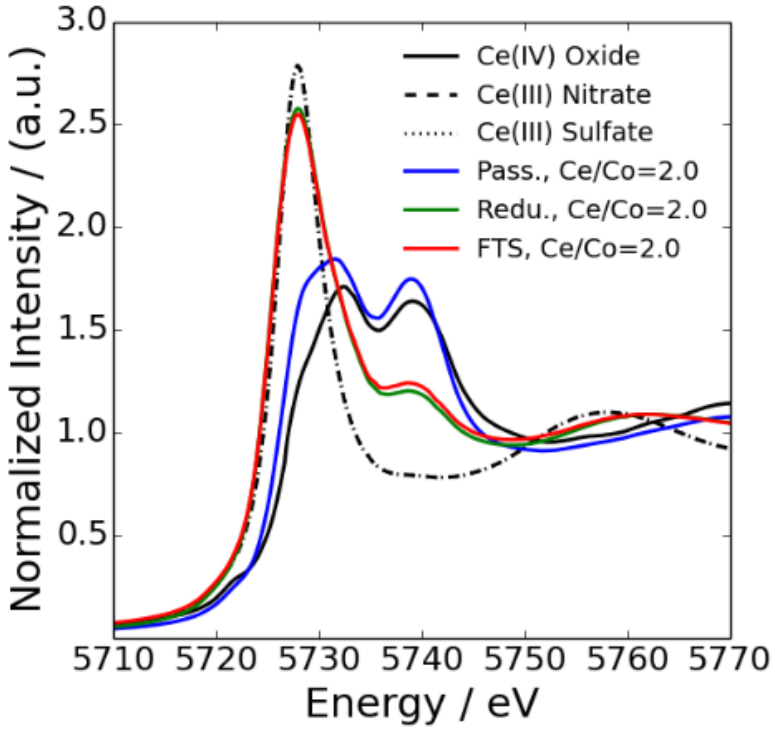
Ce(IV) Oxide
Ce(III) Nitrate
Ce(III) Sulfate
Pass., Ce/Co=2.0
Redu., Ce/Co=2.0
FTS, Ce/Co=2.0
Normalized Intensity / (a.u.)
Energy / eV
3.0
2.5
2.0
1.5
1.0
0.5
5710
5720
5730
5740
5750
5760
5770

C)

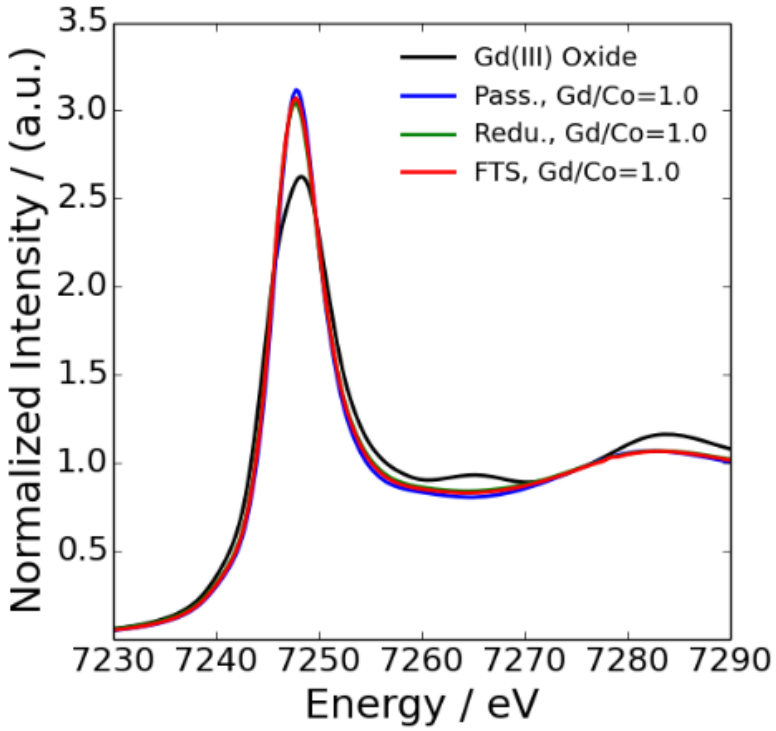

Figure 5.3 In situ XANES spectra of the catalysts prepared with (A) La/Co = 0.1, (B) Ce/Co = 2.0, and (C) Gd/Co = 1.0. The spectra were collected at the L_3-edges for the promoter element at three conditions: passivated at ambient temperature (Pass.), after reduction with H_2 at 723 K for 2 h and cooling to 493 K (Redu.), and under 2/1 H_2/CO synthesis gas at 493 K (FTS).

A)

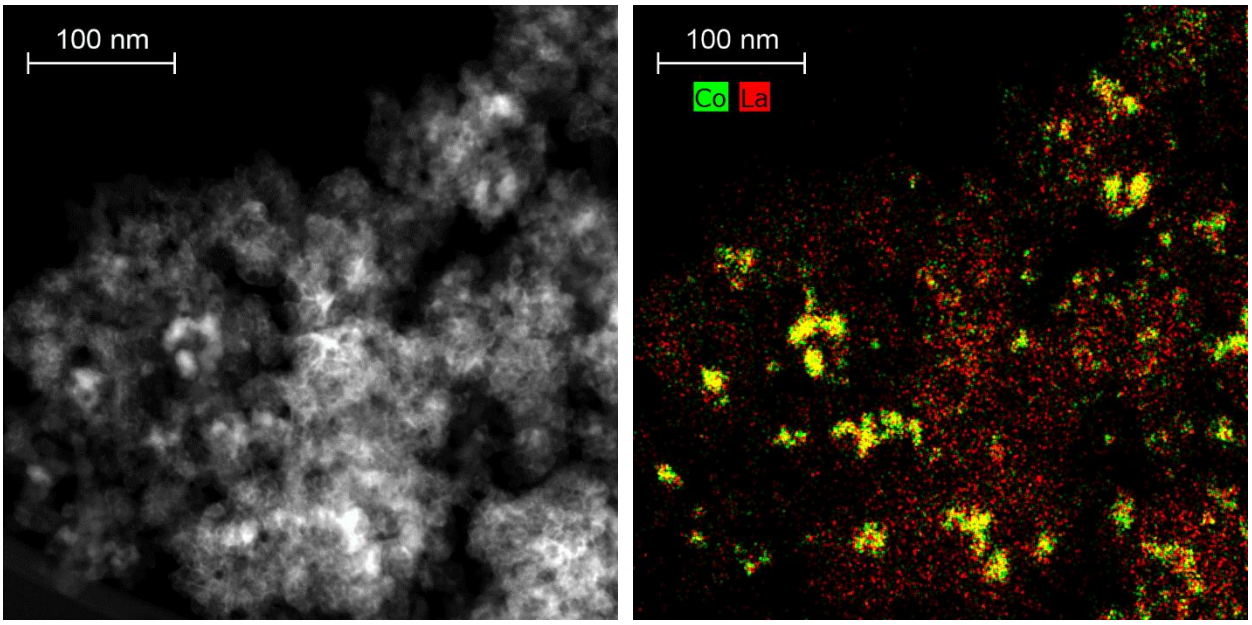

B)

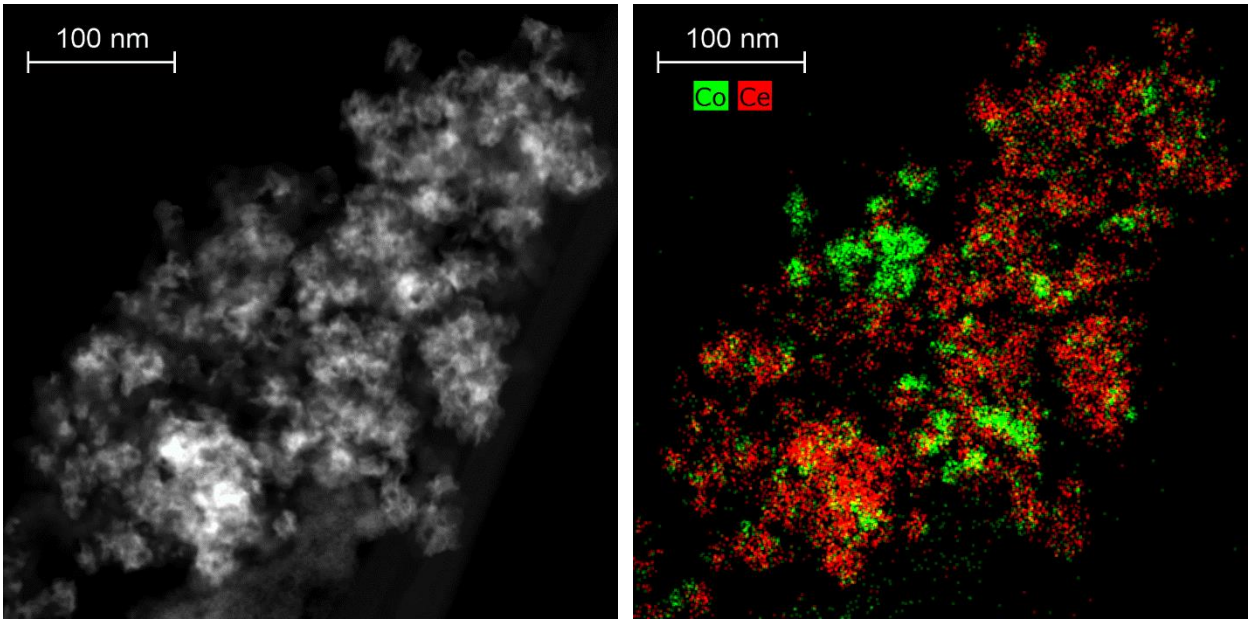

C)

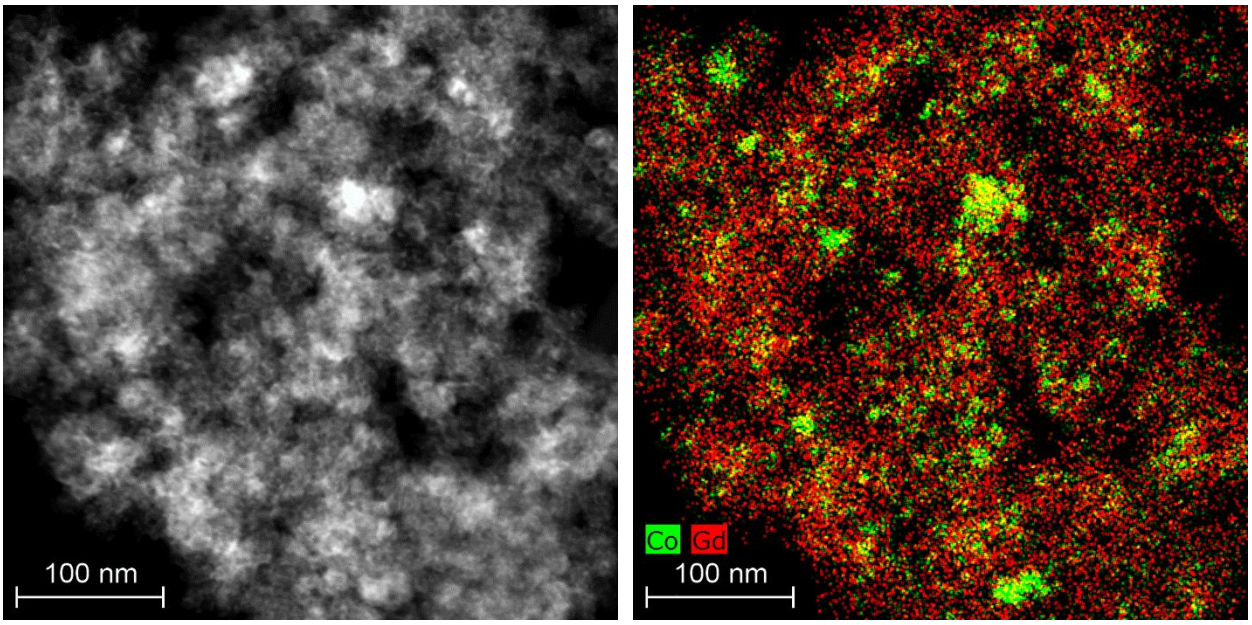

Figure 5.4 Representative HAADF-STEM images and STEM-EDS elemental maps for the catalysts prepared with (A) La/Co = 0.1, (B) Ce/Co = 2.0, and (C) Gd/Co = 1.0. In each elemental map, the Co and promoter signals are normalized separately to the pixels with the highest Co and promoter X-ray counts, respectively.

A)

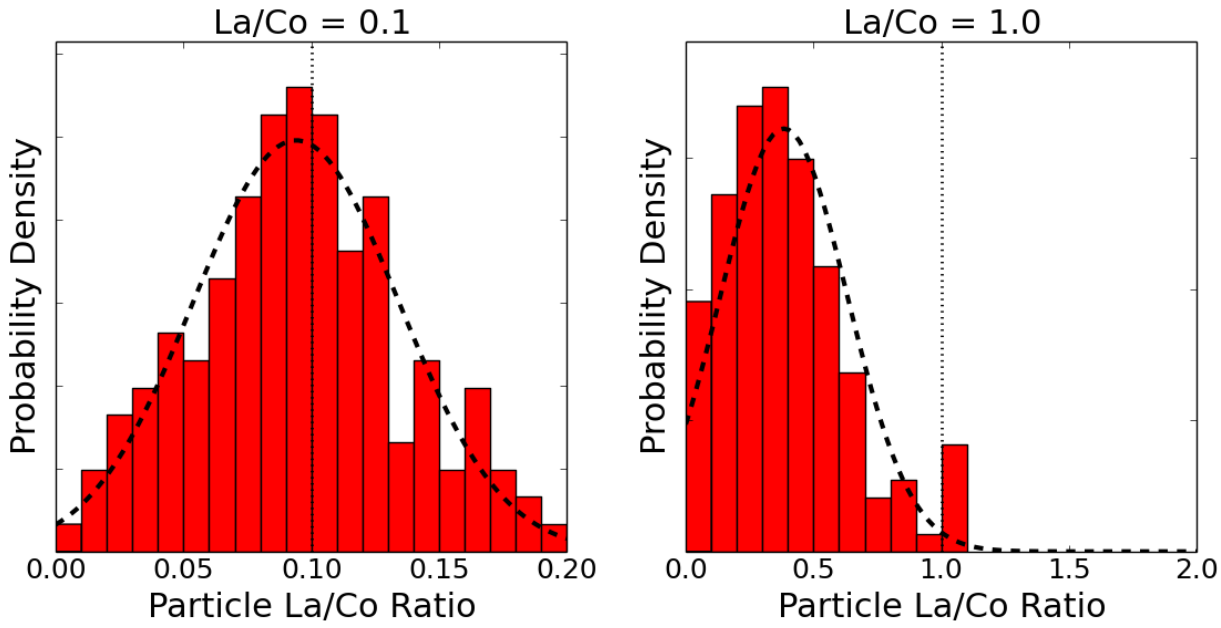
La/Co = 0.1
Probability Density
0.00
0.05
0.10
0.15
0.20
Particle La/Co Ratio
La/Co = 1.0
Probability Density
0.0
0.5
1.0
1.5
2.0
Particle La/Co Ratio

B)

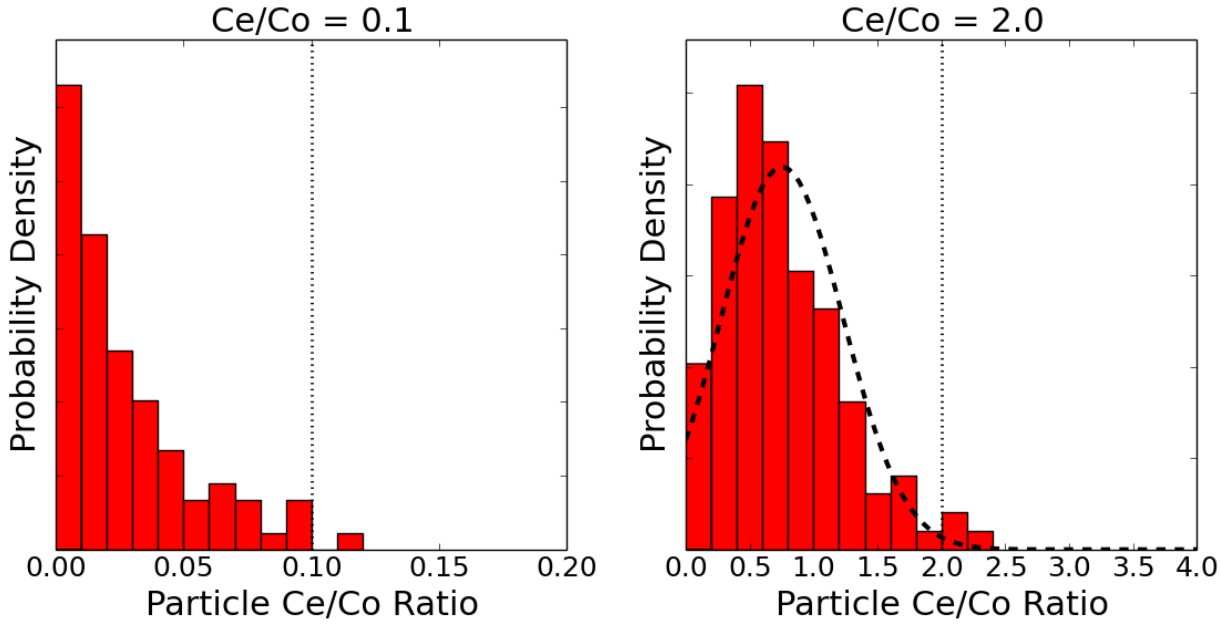
Ce/Co = 0.1
Probability Density
0.00
0.05
0.10
0.15
0.20
Particle Ce/Co Ratio
Ce/Co = 2.0
Probability Density
0.0
0.5
1.0
1.5
2.0
2.5
3.0
3.5
4.0
Particle Ce/Co Ratio

C)

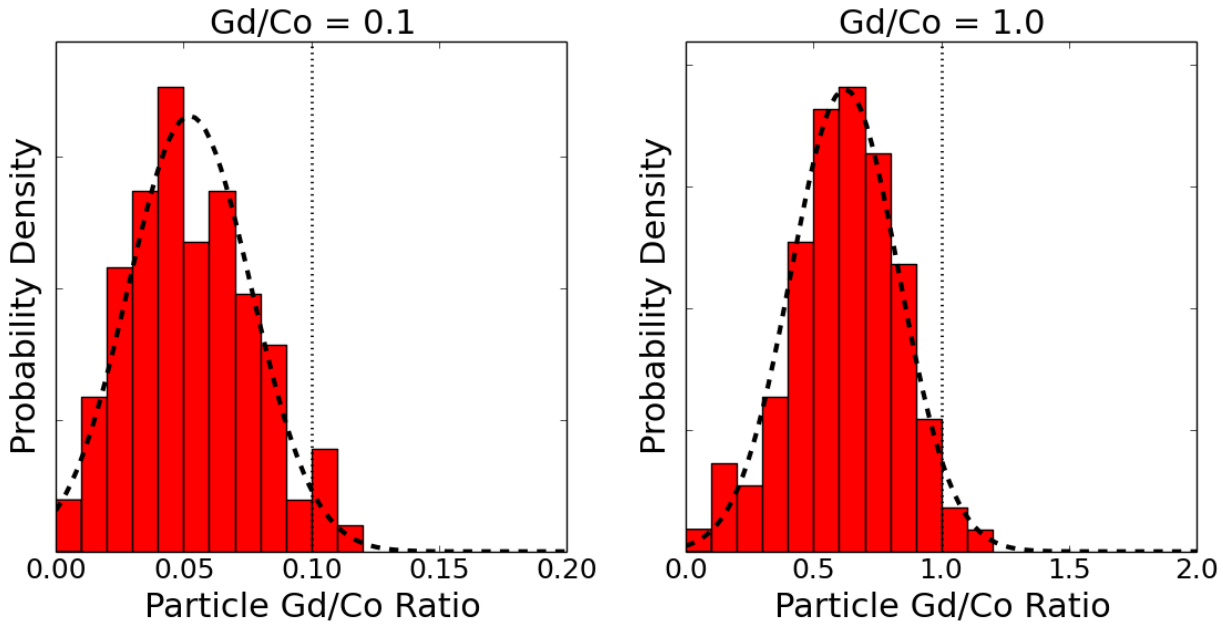

Figure 5.5 Nanoparticle composition histograms for catalysts prepared with (A) La, (B) Ce, and (C) Gd promoters with promoter/Co ratios of (first column) 0.1 and (second column) 1.0. The dashed curves in the histograms are Gaussian functions fitted to the data. The dotted vertical lines indicate the bulk catalyst compositions.

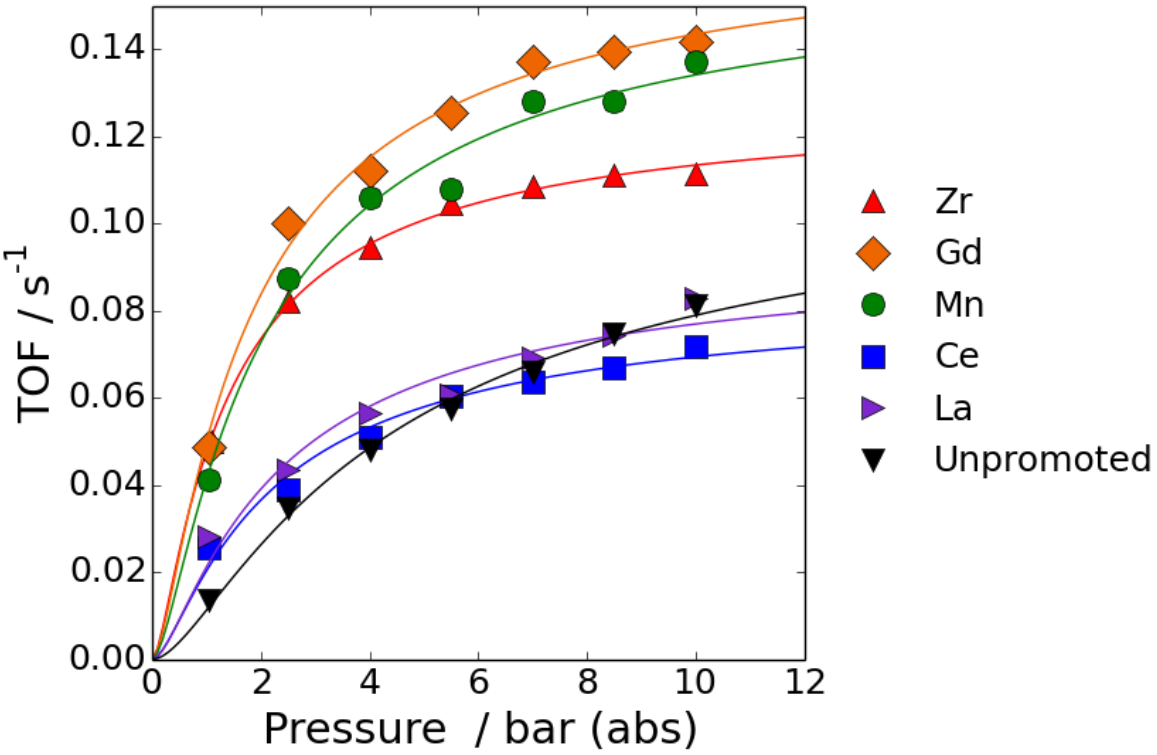

Figure 5.6 FTS turnover frequencies as a function of pressure for the unpromoted and metal oxide-promoted catalysts. The catalyst compositions correspond to those in Table 5.1, and it was assumed that the Co nanoparticles were covered by a half monolayer of the promoter. The data were collected at 493 K with a reactor inlet feed of 7% Ar, 31% CO, and 62% H_2. All datapoints were extrapolated to 0% CO conversion. The curves in each plot are fits to the data using the rate law given by eq. 5.2.

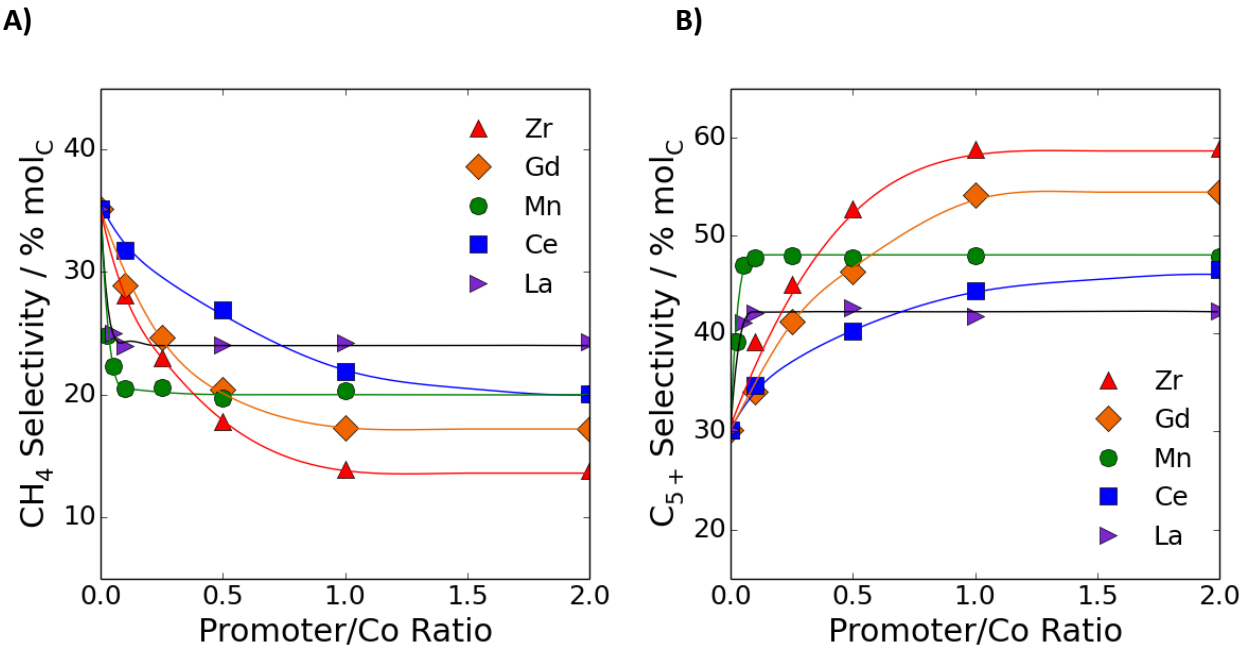

Figure 5.7 Effects of promoter loading on the selectivity toward (A) CH_4 and (B) C_{5+} hydrocarbons at 493 K and 1 bar. The data were collected with a reactor inlet feed of 7% Ar, 31% CO, and 62% H_2. All datapoints were extrapolated to 0% CO conversion. The curves in each plot are cubic splines included for visual aid.

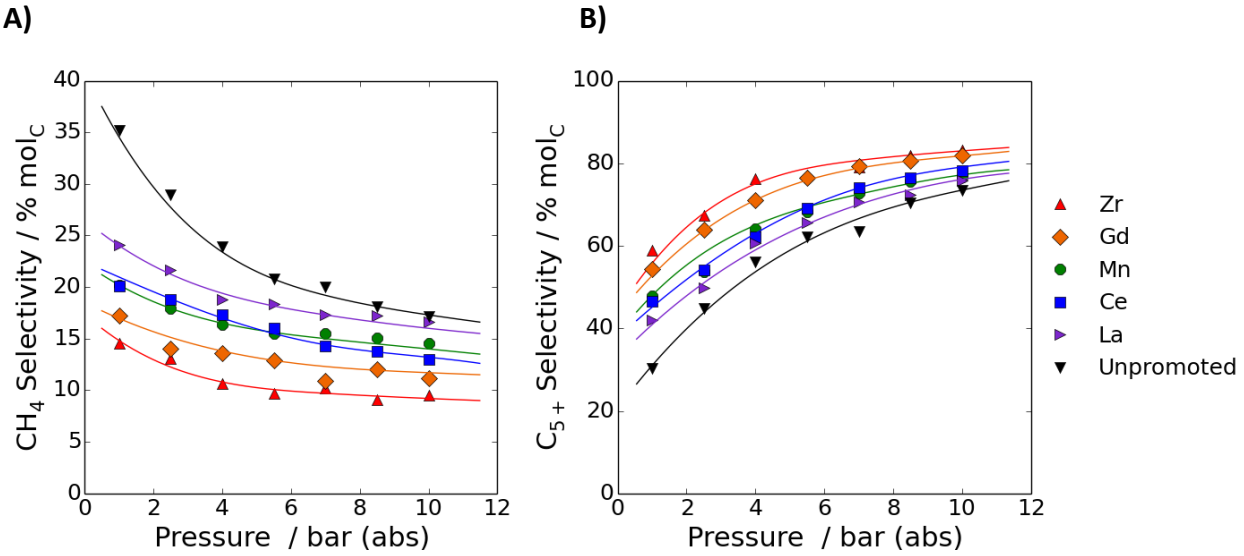

Figure 5.8 Selectivities toward (A) CH_4 and (B) C_{5+} hydrocarbons as a function of pressure for the unpromoted and metal oxide-promoted catalysts. All data were collected at 493 K with a 7% Ar, 31% CO, and 62% H_2 reactor inlet feed. The data points in the figure were extrapolated to 0% CO conversion. The catalyst compositions correspond to those in Table 5.1. The curves in each plot are cubic splines included for visual aid.

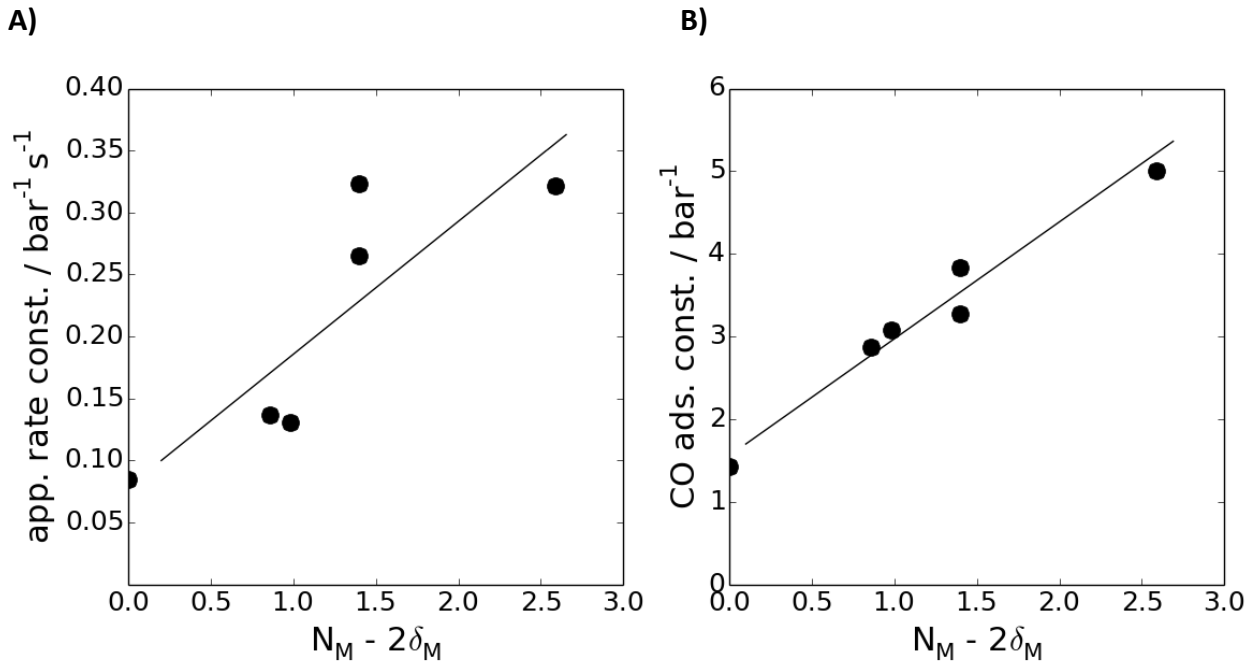

Figure 5.9 Correlations of (A) the apparent rate coefficient and (B) the CO adsorption constant with the relative Lewis acidity of the promoter oxide, represented by $N_M - 2\delta_M$. The apparent rate coefficient and CO adsorption constant correspond to parameters a and b in eq. 5.2, respectively. The turnover frequency data from Figure 5.6, where it was assumed that the Co nanoparticles were covered by a half monolayer of the promoter, were used to fit these parameters. The CO consumption rate data used for the fits were collected at 493 K at pressures between 0 and 10 bar with a 7% Ar, 31% CO, and 62% H_2 reactor inlet feed and were extrapolated to 0% CO conversion.

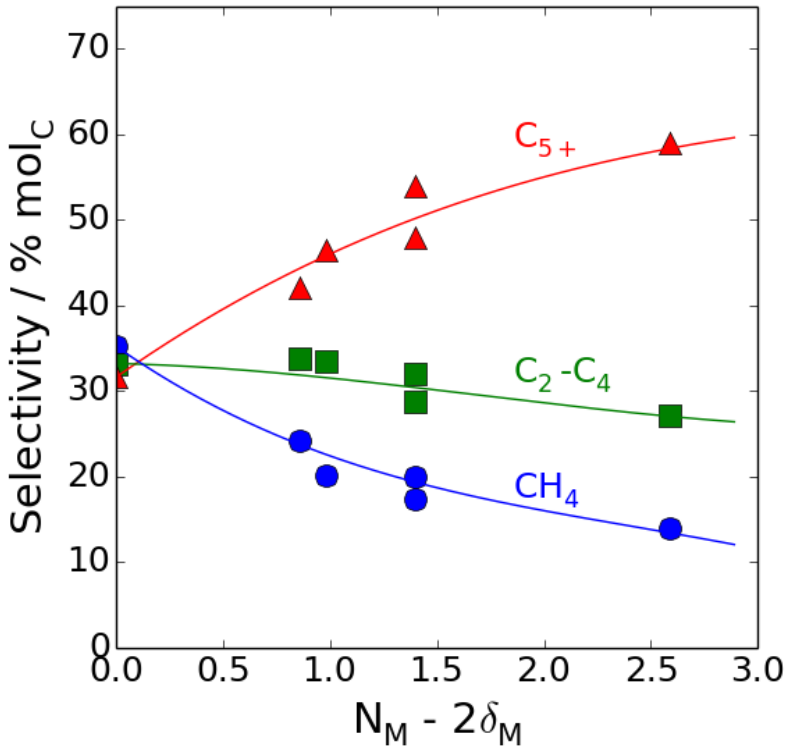

Figure 5.10 Selectivities toward CH_4, C_2-C_4, and C_{5+} as a function of the promoter Lewis acidity. Here, $N_M - 2\delta_M$ is used as a proxy for the relative Lewis acidity of the promoter oxide, and the unpromoted catalyst was assigned a value of 0. An index of these values for each promoter is provided in Table 5.3. The selectivities correspond to those Figure 5.7 where the promoter loading was high enough such that the product selectivities were insensitive to promoter loading. The data were collected at 493 K at atmospheric pressure with a 7% Ar, 31% CO, and 62% H_2 reactor inlet feed and were extrapolated to 0% CO conversion.

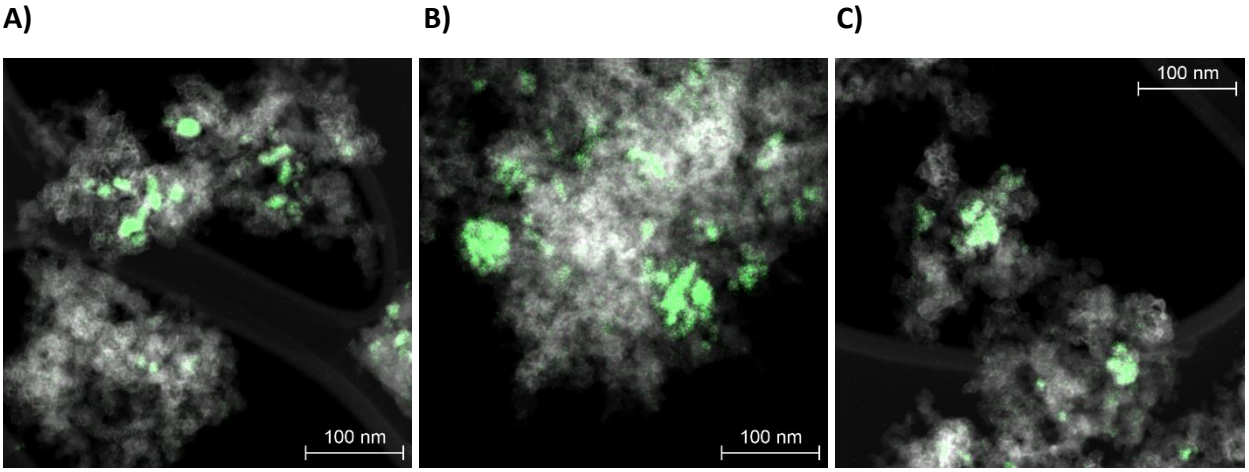

Figure S5.1 HAADF-STEM images of the catalysts prepared with (A) La/Co = 0.1, (B) Ce/Co = 2.0, and (C) Gd/Co = 1.0. The green highlighting in these images is the Co EDS channel, which was used to assist in locating the Co nanoparticles.

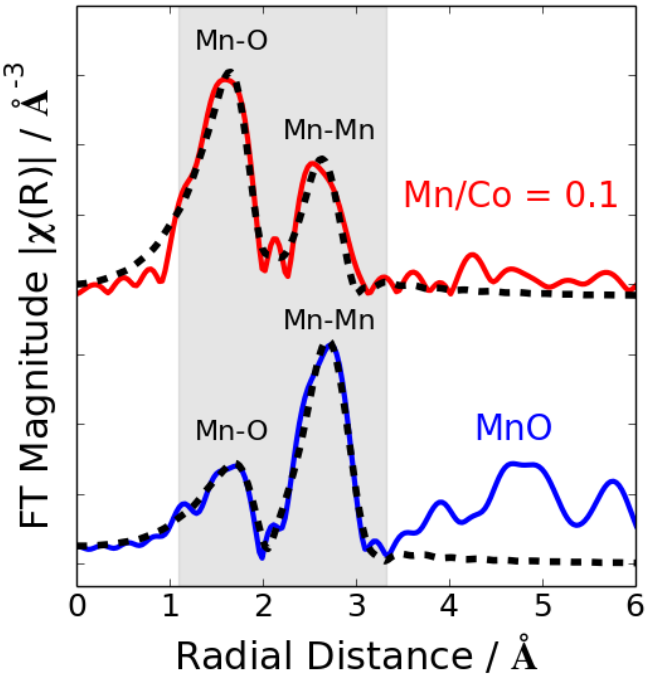

Figure S5.2 EXAFS spectra for the Mn-promoted catalyst and a MnO reference sample at the Mn K-edge. The catalyst was reduced under flowing H_2 at 723 K for 2 h prior to collecting the spectra at ambient temperature and pressure under He. The MnO was measured without pretreatment. The solid colored lines in the plots are the k^2-weighted Fourier transforms of the EXAFS spectra, and the dashed black lines are fits to these data within the shaded gray region.

Table S5.1 Mean nanoparticle compositions for the metal oxide-promoted catalysts.

Promoter Element	Bulk Promoter/Co Atomic Ratio	Mean Nanoparticle Promoter/Co Atomic Ratio	Std. Dev. of Nanoparticle Promoter/Co Atomic Ratios
La	0.1	0.094	0.040
La	1.0	0.38	0.25
Ce	0.1	0.027	0.026
Ce	2.0	0.75	0.48
Mn	0.1	0.086	0.018
Mn	0.5	0.38	0.097
Gd	0.1	0.052	0.024
Gd	1.0	0.62	0.21
Zr	0.1	0.058	0.027
Zr	1.0	0.63	0.27

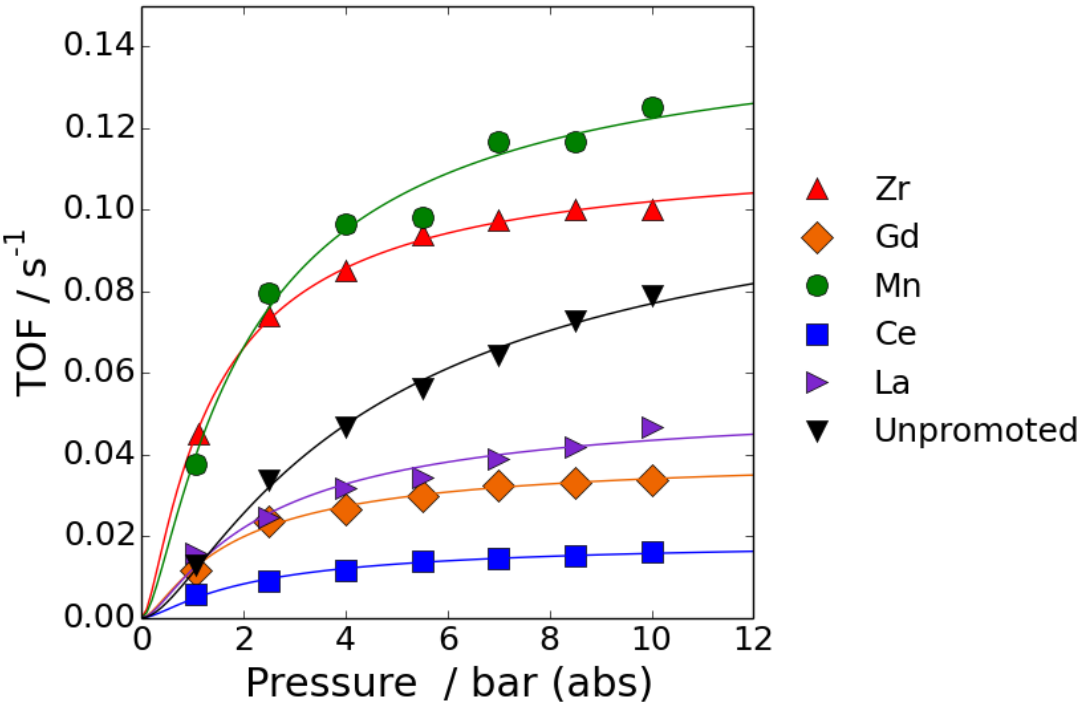

Figure S5.3 FTS turnover frequencies as a function of pressure for the unpromoted and metal oxide-promoted catalysts at 493 K. The catalyst compositions correspond to those in Table 5.1, and the H_2 uptake was used to normalize the rates assuming a 1/1 H/Co adsorption stoichiometry. The data were collected with a reactor inlet feed of 7% Ar, 31% CO, and 62% H_2. All datapoints were extrapolated to 0% CO conversion. The curves in each plot are fits to the data using the rate law given by eq. 5.2.

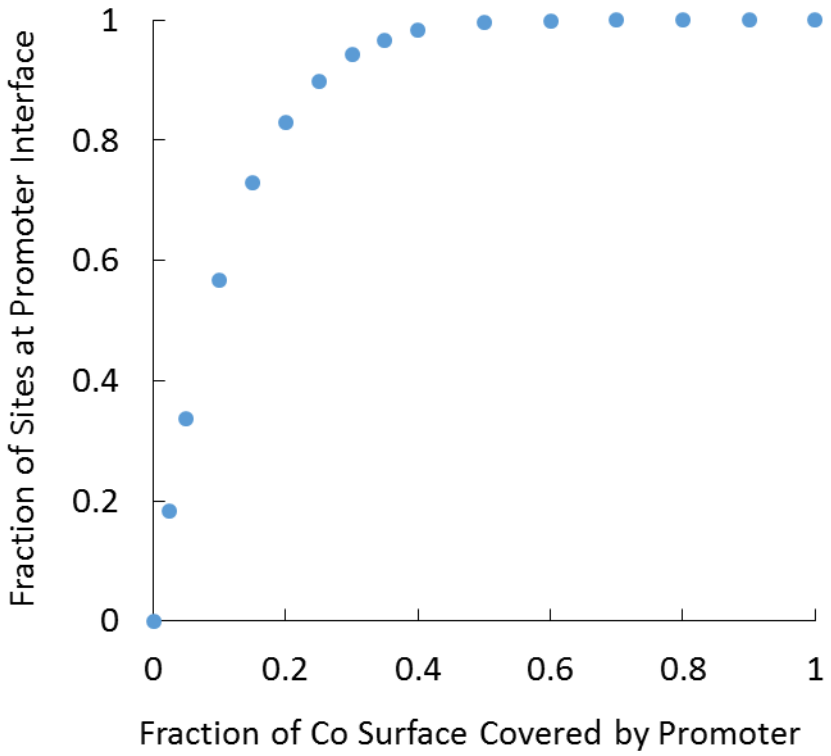

Figure S5.4 Fraction of active sites interfacing with the promoter determined by simulated deposition of promoter moieties onto Co. For this simulation, a 2D lattice of Co sites was created. Promoter moieties were assumed to be the same size as an active site (i.e., one cell in the lattice). The promoter was assumed to deposit as a partial monolayer over the Co surface before forming multilayer structures (i.e., promoter moieties could not be assigned to a given cell more than once). After the target number of promoter moieties was randomly assigned to the cells, the remaining cells that were not covered by the promoter (i.e., the active sites) were examined. Active sites that were adjacent to a cell covered by the promoter were considered to be at the interface with the promoter. Here, adjacency was defined as including diagonal adjacency. Periodic boundary conditions were used to handle sites at the edges of the lattice.

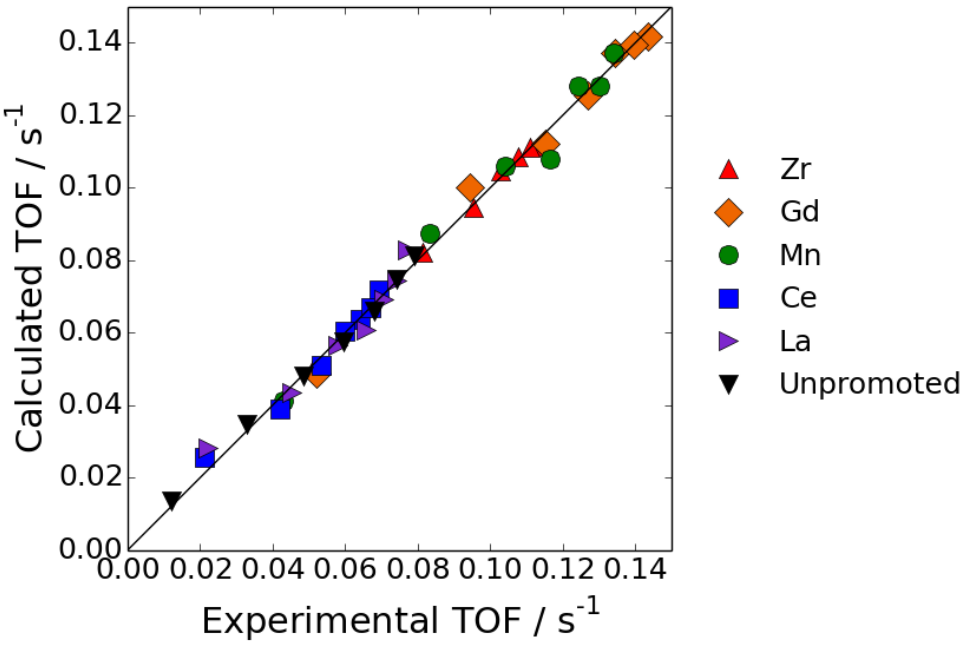

Figure S5.5 Parity plot for the unpromoted and metal oxide-promoted catalysts. The catalyst compositions correspond to those in Table 5.1, and the CO consumption rates were normalized assuming a half monolayer coverage of the catalyst by the promoter. The data were collected at 493 K with a reactor inlet feed of 7% Ar, 31% CO, and 62% H_2. All datapoints were extrapolated to 0% CO conversion. The calculated turnover frequencies were calculated using eq. 5.2 and the fitted parameters from Table 5.3.

Table S5.2 Relative Lewis acidities of the promoter elements.

Promoter Element	N_M [a]	$S_{M^{n+}}$ [b]	δ_M [c]	Rel. Lewis Acidity $(N_M - 2\delta_M)$
La	3	0.154	1.08	0.85
Ce	3	0.203	1.02	0.96
Mn	2	1.66	0.315	1.4
Gd	3	0.469	0.819	1.4
Zr	4	0.900	0.731	2.5

[a] Oxidation state of the metal cation confirmed by in situ XANES.

[b] Sanderson electronegativity of the metal cation reported by Sanderson[1] and Jeong et al.[2]

[c] Sanderson partial charge of the metal cation defined by eq. S5.1 for the metal oxide M_xO_y where S_O is the Sanderson electronegativity for oxygen ($S_O = 3.654$).[2]

$$2\delta_M = \frac{\sqrt[x+y]{S_{M^{n+}}{}^{x} S_O{}^{y}} - S_{M^{n+}}}{\sqrt[2.08]{S_{M^{n+}}}} \quad \text{(S5.1)}$$

[1] Sanderson, R.T. *Inorg. Chem.* **1986**, *25*, 3518-3522.

[2] Jeong, N.C.; Lee, J.S.; Tae, E.L.; Lee, Y.J.; Yoon, K.B. *Angew. Chem. Int. Ed.* 2008, *47*, 10128-10132.

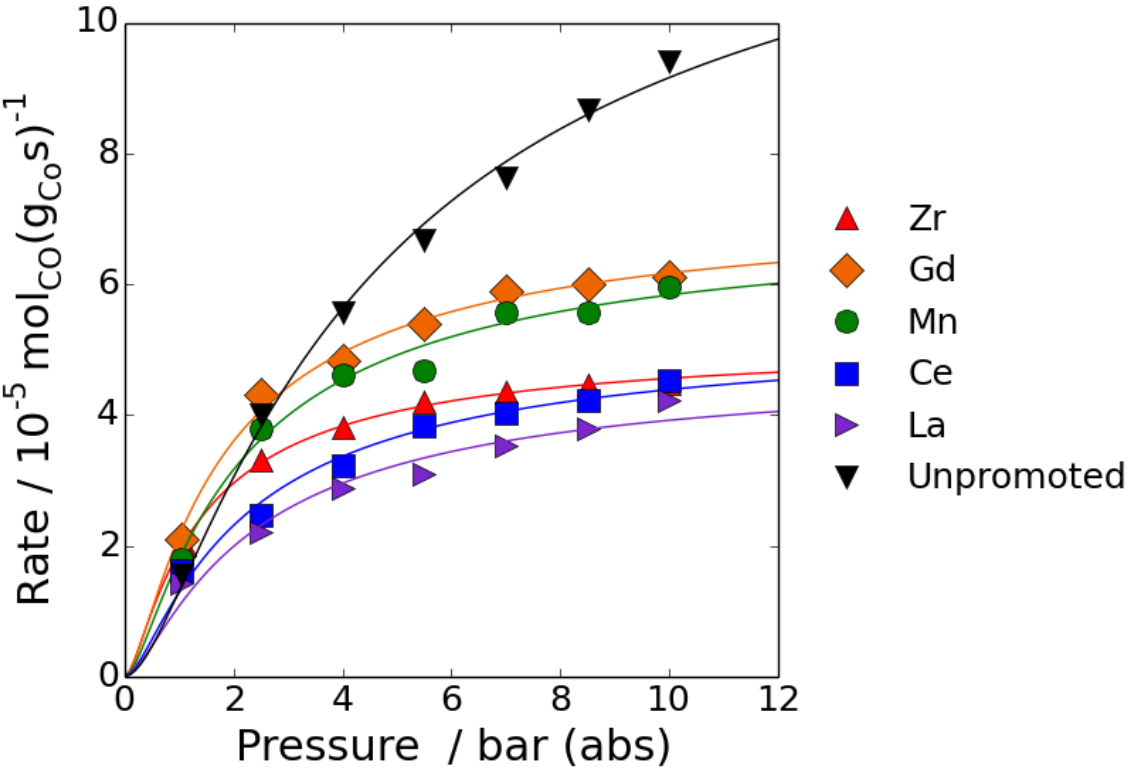

Figure S5.6 Rates of CO consumption per gram Co as a function of pressure for the unpromoted and metal oxide-promoted catalysts. The catalyst compositions correspond to those in Table 5.1. The data were collected at 493 K with a reactor inlet feed of 7% Ar, 31% CO, and 62% H_2. All datapoints were extrapolated to 0% CO conversion. The curves in each plot are fits to the data using the rate law given by eq. 5.2.

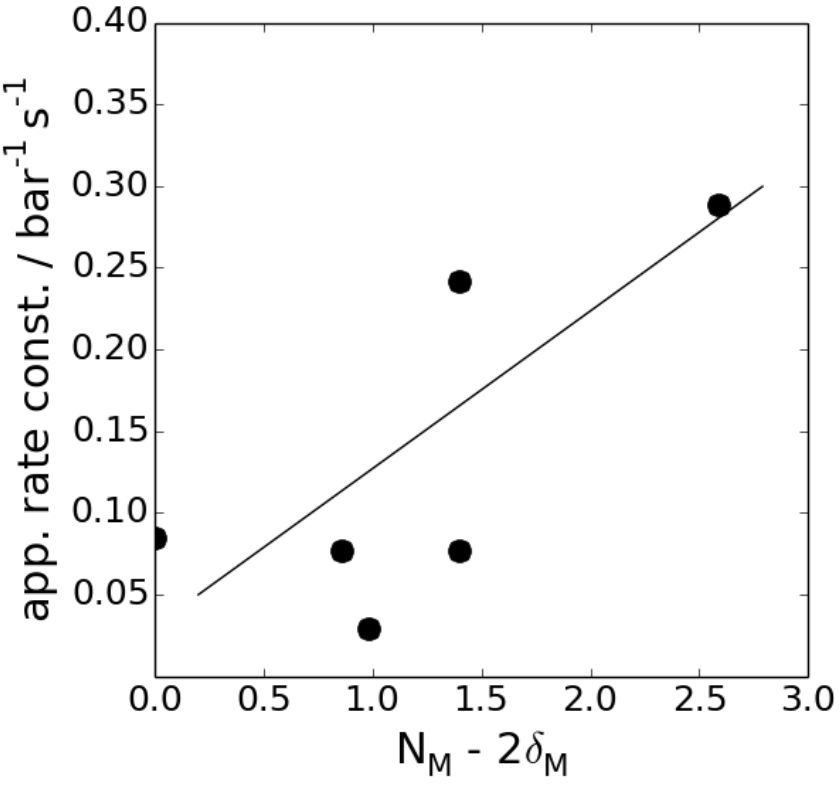

Figure S5.7 Correlation between the apparent rate constant and the relative Lewis acidity of the promoter oxide, represented by $N_M - 2\delta_M$. The apparent rate constant and CO adsorption constant correspond to parameters a and b in eq. 5.2, respectively. The turnover frequency data from Figure S5.3, where the H_2 uptake was used to normalize the rate data, were used to fit these parameters.

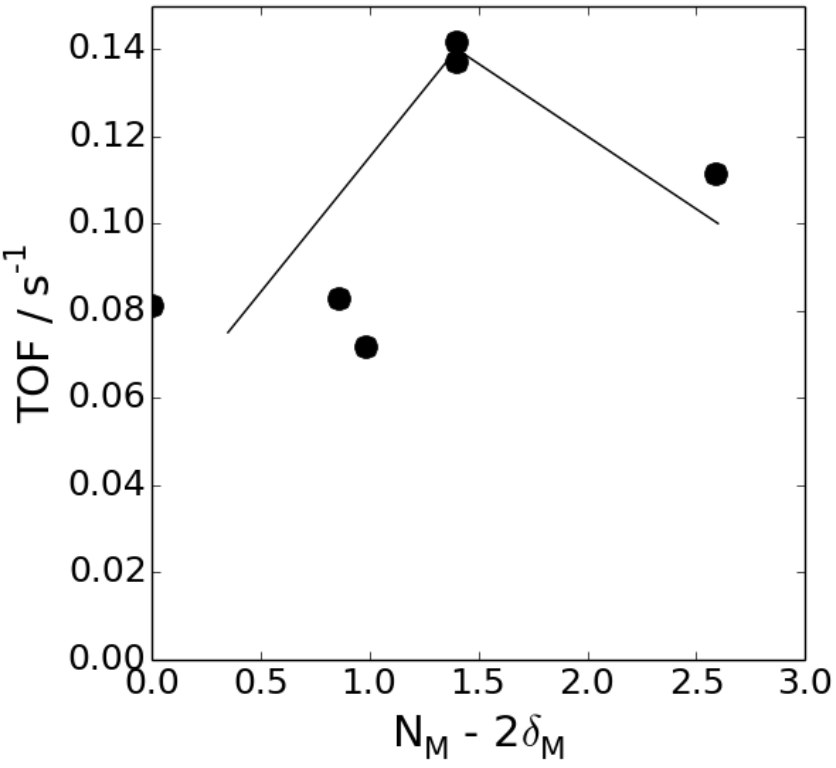

Figure S5.8 FTS turnover frequencies for the unpromoted and metal oxide-promoted catalysts demonstrating that the optimal turnover frequency occurs with promoters of intermediate Lewis acidity. The data were collected at 493 K and 10 bar with a reactor inlet feed of 7% Ar, 31% CO, and 62% H_2. All datapoints were extrapolated to 0% CO conversion. It was assumed that the Co nanoparticles were covered by a half monolayer of the promoter.

References

1. Zhang, Q.; Kang, J.; Wang, Y. *ChemCatChem* **2010**, *2*, 1030-1058.

2. Khodakov, A.Y.; Chu, W.; Fongarland, P. *Chem. Rev.* **2007**, *107*, 1692-1744.

3. Oukaci, R.; Singleton, A.H.; Goodwin, J.G., Jr. *Appl. Catal., A* **1999**, *186*, 129-144.

4. Bezemer, G.L.; Radstake, P.B.; Falke, U.; Oosterbeek, H.; Kuipers, H.P.C.E.; van Dillen, A.J.; de Jong, K.P. *J. Catal.* **2006**, *237*, 152-161.

5. den Breejen, J.P.; Frey, A.M.; Yang, J.; Holmen, A.; van Schooneveld, M.M.; de Groot, F.M.F.; Stephan, O.; Bitter, J.H.; de Jong, K.P. *Top. Catal.* **2011**, *54*, 768-777.

6. Morales, F.; de Groot, F.M.F.; Glatzel, P.; Kleimenov, E.; Bluhm, H.; Hävecker, M.; Knop-Gericke, A.; Weckhuysen, B.M. *J. Phys. Chem. B* **2004**, *108*, 16201-16207.

7. Morales, F.; de Groot, F.M.F.; Gijzeman, O.L.J.; Mens, A.; Stephan, O.; Weckhuysen, B.M. *J. Catal.* **2005**, *230*, 301-308.

8. Morales, F.; Grandjean, D.; de Groot, F.M.F.; Stephan, O.; Weckhuysen, B.M. *Phys. Chem. Chem. Phys.* **2005**, *7*, 568-572.

9. Morales, F.; Grandjean, D.; Mens, A.; de Groot, F.M.F.; Weckhuysen, B.M. *J. Phys. Chem. B* **2006**, *110*, 8626-8639.

10. Morales, F.; de Smit, E.; de Groot, F.M.F.; Visser, T.; Weckhuysen, B.M. *J. Catal.* **2007**, *246*, 91-99.

11. Feltes, T.E.; Espinosa-Alonso, L.; de Smit, E.; D'Souza, L.; Meyer, R.J.; Weckhuysen, B.M.; Regalbuto, J.R. *J. Catal.* **2010**, *270*, 95-102.

12. Johnson, G.R.; Werner, S.; Bustillo, K.C.; Ercius, P.; Kisielowski, C.; Bell, A.T. *J. Catal.* **2015**, *328*, 111-122.

13. Ali, S.; Chen, B.; Goodwin, J.G., Jr. *J. Catal.* **1995**, *157*, 35-41.

14. Feller, A.; Claeys, M.; van Steen, E. *J. Catal.* **1999**, *185*, 120-130.

15. Moradi, G.R.; Basir, M.M.; Taeb, A.; Kiennemann, A. *Catal. Commun.* **2003**, *4*, 27-32.

16. Xiong, H.; Zhang, Y.; Liew, K.; Li, J. *J. Mol. Catal. A: Chem.* **2005**, *231*, 145-151.

17. Ledford J.S.; Houalla, M.; Proctor, A.; Hercules, D.M.; Petrakis, L. *J. Phys. Chem.* **1989**, *93*, 6770-6777.

18. Vada, S.; Kazi, A.M.; Bedu-Addo, F.K.; Chen, B.; Goodwin, J.G., Jr. La Promotion of Co Fischer-Tropsch Catalysts. In *Natural Gas Conversion II*; Curry-Hyde, H. E., Howe, R. F., Eds.; Elsevier: Amsterdam, The Netherlands, 1994; Vol. Studies in Surface Science and Catalysis 81, pp 443-448.

19. Adachi, M.; Yoshii, K.; Han, Y.Z.; Fujimoto, K. *Bull. Chem. Soc. Jpn.* **1996**, *69*, 1509-1516.

20. Haddad, G.J.; Chen, B.; Goodwin, J.G., Jr. *J. Catal.* **1996**, *161*, 274-281.

21. Guerrero-Ruiz, A.; Sepúlveda-Escribaano, A.; Rodríguez-Ramos, I. *Appl. Catal., A* **1994**, *120*, 71-83.

22. Zeng, S.; Du, Y.; Su, H.; Zhang, Y. *Catal. Commun.* **2011**, *13*, 6-9.

23. Huber, G.W.; Butala, S.J.M.; Lee, M.L.; Bartholomew, C.H. *Catal. Lett.* **2001**, *74*, 45-48.

24. Wu, Y.Y.; Mashayekhi, N.A.; Kung, H.H. *Catal. Sci. Technol.* **2013**, *3*, 2881-2891.

25. Cargnello, M.; Doan-Nguyen, V.V.T.; Gordon, T.R.; Diaz, R.E.; Stach, E.A.; Gorte, R.J.; Fornasiero, P.; Murray, C.B. *Science* **2013**, *341*, 771-773.

26. Rieck, J.S.; Bell, A.T. *J. Catal.* **1985**, *96*, 88-105.

27. van den Berg, F.G.A.; Glezer, J.H.E.; Sachtler, W.M.H. *J. Catal.* **1985**, *93*, 340-352.

28. Boffa, A.B.; Lin, C.; Bell, A.T.; Somorjai, G.A. *Catal. Lett.* **1994**, *27*, 243-249.

29. Nonneman, L.E.Y.; Ponec, V. *Catal. Lett.* **1990**, *7*, 197-204.

30. Sachtler, W.M.H.; Shriver, D.F.; Hollenberg, W.B.; Lang, A.F. *J. Catal.* **1985**, *92*, 429-431.

31. Johnson, G.R.; Werner, S.; Bell, A.T. A Systematic Study of Mn and Zr Oxide Promoters for Fischer-Tropsch Synthesis Using Alumina Nanosphere-Supported Model Catalysts. *Proceedings of the 2014 AIChE Annual Meeting,* Atlanta, GA, November 16-21, 2014.

32. Johnson, G.R.; Werner, S.; Bell, A.T. Metal Oxide Promotion of Cobalt Fischer-Tropsch Catalysts: Relating Effects to Periodic Trends. *Proceedings of the 24th Meeting of the North American Catalysis Society*, Pittsburgh, PA, June 14-19, 2015.

33. Prieto, G.; De Mello, M.I.S.; Concepcíon, P.; Murciano, R.; Pergher, S.B.C.; Martínez, A. *ACS Catal.* **2015**, *5*, 3323-3335.

34. Johnson, G.R.; Bell, A.T. The Role of ZrO_2 in Promoting the Activity and Selectivity of Co-Based Fischer-Tropsch Synthesis Catalysts. *ACS Catal.* Submitted for publication.

35. Johnson, G.R.; Werner, S.; Bell, A.T. *ACS Catal.* **2015**, *5*, 5888-5902.

36. Reuel, R.C.; Bartholomew, C.H. *J. Catal.* **1984**, *85*, 63-77.

37. Kropf, A.J.; Katsoudas, J.; Chattopadhyay, S.; Shibata, T.; Lang, E.A.; Zyryanov, V.N.; Ravel, B.; McIvor, K.; Kemner, K.M.; Scheckel, K.G.; Bare, S.R.; Terry, J.; Kelley, S.D.; Bunker, B.A.; Segre, C. U. AIP Conf. Proc., 2010; pp 299-302.

38. Ravel, B.; Newville, M. *J. Synchrotron Radiat.* **2005**, *12*, 537-541.

39. Newville, M. *J. Synchrotron Radiat.* **2001**, *8*, 96-100.

40. Cliff, G.; Lorimer, G.W. *J. Microsc.* **1975**, *103*, 203-207.

41. Weisz, P.B.; Prater, C.D. *Adv. Catal.* **1954**, *6*, 143-196.

42. Dinse, A.; Aigner, M.; Ulbrich, M.; Johnson, G.R.; Bell, A.T. *J. Catal.* **2012**, *288*, 104-114.

43. Khodakov, A.Y.; Lynch, J.; Bazin, D.; Rebours, B.; Zanier, N.; Moisson, B.; Chaumette, P. *J. Catal.* **1997**, *168*, 16-25.

44. Jacobs, G.; Ji, Y.; Davis, B.H.; Cronauer, D.; Kropf, A.J.; Marshall, C.L. *Appl. Catal., A* **2007**, *333*, 177-191.

45. Martínez, A.; López, C.; Márquez, F.; Díaz, I. *J. Catal.* **2003**, 486-499.

46. Girardon, J.-S.; Lermontov, A.S.; Gengembre, L.; Chernavskii, P.A.; Griboval-Constant, A.; Khodakov, A.Y. *J. Catal.* **2005**, *230*, 339-352.

47. Arnoldy, P.; Moulijn, J.A. *J. Catal.* **1985**, *93*, 38-54.

48. Stobbe, E.R.; de Boer, B.A.; Geus, J.W. *Catal. Today* **1999**, *47*, 161-167.

49. Laachir, A.; Perrichon, V.; Badri, A.; Lamotte, J.; Catherine, E.; Lavalley, J.C.; Fallah, J.E.; Hilaire, L.; Normand, F.L.; Quéméré, E.; Sauvion, G.N.; Touret, O. *J. Chem. Soc., Faraday Trans.* **1991**, *87*, 1601-1609.

50. Chen, M.; Hallstedt, B.; Gauckler, L.J. *J. Phase Equilib.* **2003**, *24*, 212-227.

51. Bezemer, G.L.; Bitter, J.H.; Kuipers, H.P.C.E.; Oosterbeek, H.; Holewijn, J.E.; Xu, X.; Kapteijn, F.; van Dillen, A.J.; de Jong, K.P. *J. Am. Chem. Soc.* **2006**, *128*, 3956-3964.

52. Melaet, G.; Lindeman, A.E.; Somorjai, G.A. *Top. Catal.* **2014**, *57*, 500-507.

53. Datye, A.K.; Xu, Q.; Kharas, K.C.; McCarty, J.M. *Catal. Today* **2006**, *111*, 59-67.

54. Pokrovski, K.; Jung, K.T.; Bell, A.T. *Langmuir* **2001**, *17*, 4297-4303.

55. Asakura, H.; Shishido, T.; Teramura, K.; Tanaka, T. *Inorg. Chem.* **2014**, *53*, 6048-6053.

56. Bartholomew, C.H. *Catal. Lett.* **1990**, *7*, 27-52.

57. Williams, K.J.; Boffa, A.B.; Lahtinen, J.; Salmeron, M.; Bell, A.T.; Somorjai, G.A. *Catal. Lett.* **1990**, *5*, 385-394.

58. Yates, I.C.; Satterfield, C.N. *Energ. Fuel* **1991**, *5*, 168-173.

59. Ojeda, M.; Nabar, R.; Nilekar, A.U.; Ishikawa, A.; Mavrikakis, M.; Iglesia, E. *J. Catal.* **2010**, *272*, 287-297.

60. Zennaro, R.; Tagliabue, M.; Bartholomew, C.H. *Catal. Today* **2000**, *58*, 309-319.

61. Kung, H.H. Transition Metal Oxides: Surface Chemistry and Catalysis; Elsevier: New York, 1989.

62. Jeong, N.C.; Lee, J.S.; Tae, E.L.; Lee, Y.J.; Yoon, K.B. *Angew. Chem. Int. Ed.* **2008**, *47*, 10128-10132.

63. Sanderson, R.T. Chemical Bonds and Bond Energy; Academic Press: New York, 1976.

64. Prieto, G.; Concepción, P.; Martínez, A.; Mendoza, E. *J. Catal.* **2011**, *280*, 274-288.

65. Haddad, G. J.; Chen, B.; Goodwin, J.G., Jr. *J. Catal.* **1996**, *160*, 43-51.

66. Lavela, P.; Tirado, J.L.; Vidal-Abarca, C. *Electrochim. Acta* **2007**, *52*, 7986-7995.

67. Liang, Y.; Wang, H.; Zhou, J.; Li, Y.; Wang, J.; Regier, T.; Dai, H. *J. Am. Chem. Soc.* **2012**, *134*, 3517-3523.

68. Zavaliy, I.Y.; Denys, R.V.; Černý, R.; Koval'chuck, I.V.; Wiesinger, G.; Hilscher, G. *J. Alloy Compd.* **2005**, *386*, 26-34.

69. Faria, P.C.C.; Monteiro, D.C.M.; Órfão, J.J.M.; Pereira, M.F.R. *Chemosphere* **2009**, *74*, 818-824.

70. Ito, T.; Zhang, Q.; Saito, F. Powder Technol. **2004**, *143-144*, 170-173.

71. Ivas, T. Cerium-Gadolinium-Cobalt-Oxides: Phase Equilibria and Defect Chemistry in Bulk and Grain Boundaries; PhD Thesis; ETH Zurich: Zürich, Switzerland, 2013.

72. Sachtler, W.M.; Ichikawa, M. *J. Phys. Chem.* **1986**, *90*, 4752-4758.

73. Horwitz, C.P.; Shriver, D.F. *Adv. Organomet. Chem.* **1984**, *23*, 219-305.

74. Barrault, J.; Guilleminot, A. *Appl. Catal.* **1986**, *21*, 307-312.

75. den Breejen, J.P.; Radstake, P.B.; Bezemer, G.L.; Bitter, J.H.; Frøseth, V.; Holmen, A.; de Jong, K.P. *J. Am. Chem. Soc.* **2009**, *131*, 7197-7203.

76. Ishihara, T.; Eguchi, K.; Arai, H. *J. Molec. Catal.* **1992**, *72*, 253-261.